# Fluorescence and random lasing in disordered media

By

Wan Zakiah Binti Wan Ismail

A thesis submitted to Macquarie University for the

Degree of Doctor of Philosophy

Faculty of Science and Engineering

February 2016

MACQUARIE
University

# Contents

# Statement of candidate

Fluorescence and random lasing in disordered media is an experimental-based research project that has been supported and funded by Macquarie University, the Australian Government (Endeavour Scholarship) and the ARC Centre of Excellence Centre for Ultrahigh Bandwidth Devices for Optical Systems (CUDOS).

The preparation of random laser materials and the optical measurements were done in the Wet-chemistry and Optics laboratories at Macquarie University. The characterization of random laser materials (dynamic light scattering, transmission electron microscopy and scanning electron microscopy) were performed in the Wet-chemistry and Microscopy laboratories supervised by Ms. Debra Birch, Dr. Regina Dunford and Dr. Susan Law.

This thesis is submitted to fulfil the requirement of the degree of Doctor of Philosophy at Macquarie University and has not been submitted for a degree at any other university or institution. I certify that the thesis is an original manuscript and has been written by me. To the best of my knowledge, all sources used in the preparation of this thesis have been appropriately acknowledged in the customary manner.

---

Wan Zakiah Wan Ismail

# Acknowledgements

I truly thank my principal supervisor, Professor Judith Dawes for her encouragement, support and guidance in doing my PhD research. I value her commitment and experience in handling many issues to finish this research. I am also grateful to gain the supervision from experienced and skilled scientists, Professor Ewa Goldys and Professor David Coutts. Their help and comments to solve the scientific and technical problems have been important in completing this thesis.

I would like to thank Professor Michael Withford for his support as the ARC Centre of Excellence Centre for Ultrahigh Bandwidth Devices for Optical Systems (CUDOS) Macquarie University node director. I acknowledge the Plasmonics group (Vincent Ng, Alireza Maleki and Thanh Phong Vo), CUDOS (Peter Dekker) and MQ Biofocus members (Deming Liu, Sandhya Clement, Guozhen Liu, Wan Aizuddin and Kai Zhang) for their help in my research areas. Peter Dekker helped me in maintaining and fixing the pump laser source, Thanh Phong helped me in setting up the optical measurements while the others assisted me in preparing and characterizing random laser materials. I also thank Debra Birch and Nicole Vella for giving me training on scanning electron microscopy and transmission electron microscopy.

For scholarship and research funding, I make a special acknowledgement to the Australian Government (Endeavour Scholarship), Islamic Science University of Malaysia (USIM), MQ Photonics and CUDOS. I also acknowledge the administrative staff of the Department of Physics and Astronomy for their assistance.

In the end, I would like to thank my family especially my husband, Syafiq Isa for their invaluable love and support to help me finish my PhD research.

# List of publications

Work in this thesis has been published in a number of peer-reviewed journals and presented in many national and international conferences.

## Peer-reviewed Journal Articles

1. W. Z. Wan Ismail, D. Liu, S. Clement, D. W. Coutts, E. M. Goldys and J. M. Dawes, "Spectral and coherence signatures of threshold in random lasers," Journal of Optics, **16**, 105008 (2014). **(Chapter 3)**
2. W. Z. Wan Ismail, T. P. Vo, E. M. Goldys and J. M. Dawes, "Plasmonic enhancement of Rhodamine dye random lasers," Laser Physics, **25**, 085001 (2015). **(Chapter 5)**
3. W. Z. Wan Ismail, G. Liu, K. Zhang, E. M. Goldys and J. M. Dawes "Dopamine sensing and measurement using threshold and spectral measurements in random lasers," Optics Express, **24** (2), A85-A91 (2016). **(Chapter 7)**
4. W. Z. Wan Ismail, E. M. Goldys and J. M. Dawes "Extended emission wavelength of random dye lasers by exploiting radiative and non-radiative energy transfer," Applied Physics B:Lasers and Optics, **122,** 1-9 (2016). **(Chapter 4)**

## Conference Papers

1. W. Z. Wan Ismail, H. Liu, T. P. Vo and J. M. Dawes, "Investigation of scattering and random lasing phenomena using dielectric and metal

nanoparticles," 20th Australian Institute of Physics Congress (Sydney, Australia) (2012).

2. W. Z. Wan Ismail, T. P. Vo, D. W. Coutts, E. M. Goldys and J. M. Dawes, "Comparison of random lasing threshold for dielectrics and metal nanoparticles," Australian and New Zealand Conference on Optics and Photonics (Fremantle, Australia) (2013) [Award for Best Student Poster at the conference].
3. W. Z. Wan Ismail, T. P. Vo, P. Stark, D. W. Coutts, E. M. Goldys and J. M. Dawes, "Plasmonic enhancement of coherence in random lasers," International Conference on Nanoscience and Nanotechnology (Adelaide, Australia) (2014).
4. W. Z. Wan Ismail, T. P. Vo, D. W. Coutts, E. M. Goldys and J. M. Dawes, "Plasmonic enhancement of gain in random lasers," OptoElectronics and Communication Conference (Melbourne, Australia) (2014).
5. W. Z. Wan Ismail, W. A. Wan Razali, A. Zyagin, D. W. Coutts, E. M. Goldys and J. M. Dawes, "Ruby-Nanocrystal-Enhanced Random Dye Lasers," CLEO: Science and Innovations (San Jose, United States) (2015).
6. W. Z. Wan Ismail, E. M. Goldys and J. M. Dawes, "Fluorescence resonance energy transfer (FRET) in random dye lasers," CLEO Pacific Rim (Busan, Korea) (2015).
7. J. M. Dawes, W. Z. Wan Ismail, E. M. Goldys, D. W. Coutts, "Enhancing the Performance of Random Lasers: Effects of Localised Surface Plasmons and Resonance Energy Transfer", 4th International Conference on Photonics, Optics and Laser Technology (Rome, Italy) (2016).

# Abstract

Random lasers have fascinating and useful properties, and may be applied in fields such as sensing, imaging, spectroscopy, material processing, optical displays and new lighting systems. This thesis, ‘‘Fluorescence and random lasing in disordered media” aims to provide an experimental study of incoherent random lasers and to demonstrate a new sensing application for these lasers.

In this thesis, we study the spectral and coherence signatures of threshold in random lasers using alumina and Rhodamine 6G under nanosecond-pulsewidth pumping. We compare coherence properties (temporal and spatial coherence) with emission spectra and study the effects of particle concentration and scattering length for the weakly scattering and diffusive random laser regimes. The threshold, as defined by changes in the visibility of the interference fringes, is consistent with that defined by changes in the emission peak intensity or in the emission linewidth.

We investigate radiative and non-radiative energy transfer processes from Rhodamine 6G (donor) to Methylene blue (acceptor) to fabricate efficient infra-red random dye lasers (> 700 nm). The energy transfer efficiency is influenced by acceptor concentration, pump energy density and spectral overlap, and the optimum random laser performance is achieved when the concentration of Methylene blue is 6 times the concentration of Rhodamine 6G. A Stern-Volmer analysis is used to quantify the radiative and non-radiative energy transfer.

Colloidal-solution and solid-state random dye lasers (Rhodamine 6G and Rhodamine 640 with alumina and gold nanoparticles) are characterized based on the wavelength shift of the emission peak, local field enhancement, fluorescence

quenching, absorption and scattering properties. The improved performance of metal-based random lasers is attributed to localized surface plasmons.

We also investigate the effects of metal-fluorophore distance and surface roughness of nanoparticles on the characteristics of random lasers. The surface plasmon resonance of silver changes with increased silver-fluorophore distance, and is also affected by the surface roughness of silver-gold bimetallic nanoparticles. Increased silver-fluorophore distance increases the lasing threshold and slightly blue-shifts the emission peak due to self-absorption. Random lasing for Rhodamine 640 / lumpy bimetallic (silver and gold) nanoparticles is compared to random lasing for Rhodamine 640 / silver nanoparticles.

We investigate the possibilities of random lasing from active nanoscatterers, ruby and zinc oxide, but these systems operate below threshold and emit fluorescence and amplified spontaneous emission only.

Finally, we demonstrate a new dopamine measurement technique using threshold and spectral measurements in gold/dye random lasers. The presence and concentration of dopamine is detected through the random laser emission peak shift, emission linewidth, emission peak-to-background ratio and random lasing threshold. Considering these parameters, dopamine is most sensitively detected by a change in the emission linewidth with a limit of detection of $1 \times 10^{-7}$ M. Potential future work is to develop the random laser measurement technique to be suitable for clinical use.

# Chapter 1

# Introduction and Background

Research on light propagation in disordered media has enabled new phenomena such as random lasers, in which lasing relies on random multiple light scattering. Light scattering is considered detrimental in a regular laser as the scattering can possibly remove photons from the lasing mode of the laser cavity whereas in random lasers, multiple light scattering increases the path length of light in the active medium, leading to enhanced light amplification by stimulated emission [1, 2]. While regular lasers can be used in barcode scanners, laser printers, laser surgery and in optical disk drives, random lasers also have brought benefits in medical, military, security and communication fields [2, 3]. The advantages of these lasers are; random laser materials can be produced economically and simply on a large scale with flexible geometries and they have different coherence and emission properties than regular lasers [2].

In this thesis, we aim to understand the behavior of random lasers at threshold, and the factors which contribute to the efficient operation of random lasers. Lasing is based on fluorescence emission and amplified spontaneous emission (ASE) which are introduced in this chapter. We hypothesized that lasing threshold can be identified by the presence of spectral narrowing and a ‘kink’ in the emission peak intensity and coherence measurement. Scattering and gain play important roles to determine the threshold. We hypothesized that lasing threshold and emission intensity are influenced

by resonant energy transfer, plasmonics, nanoparticle-dye distance and surface roughness. By studying the behavior of random lasers, we have identified a new application of random lasers for biomedicine.

## 1.1 Fluorescence emission

Fluorescence is a form of luminescence, the emission of light by a substance (fluorophore or fluorescent dye) that absorbs excitation light. The process can be illustrated by a Jablonski diagram, shown in figure 1.1 [4, 5].

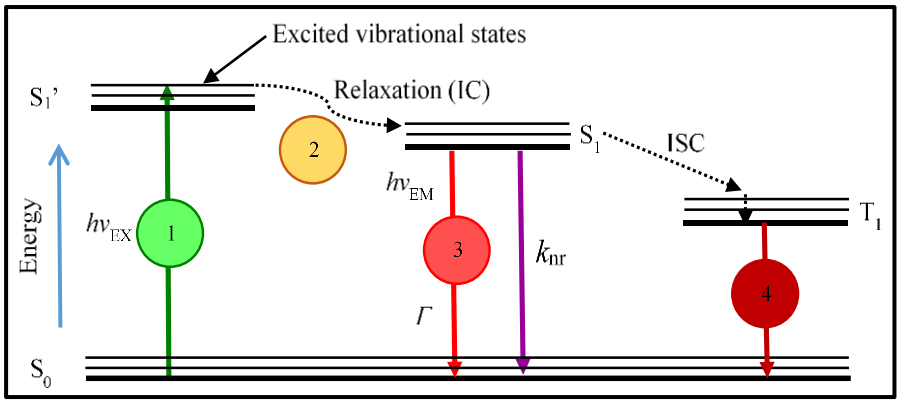


Figure 1.1 A Jablonski diagram that shows the processes involved in the creation of an excited electronic singlet state by optical absorption and subsequent emission of fluorescence. $hv_{EX}$ and $hv_{EM}$ are excited and emitted photon energies. Straight lines represent transitions involving photons, dotted lines represent vibrational or thermal transitions. $S_o$ and $S_1$' are the ground state and excited electronic singlet states, $T_1$ is the excited triplet state while steps 1, 2, 3 and 4 correspond to excitation, relaxation or internal conversion (IC), fluorescence emission and phosphorescence. ISC corresponds to intersystem crossing whereas $k_{nr}$ and $\Gamma$ correspond to non-radiative decay and emissive rates of the fluorophore. The diagram is redrawn based on [4, 6].

At step 1, the external source, a lamp or laser, excites a fluorophore by supplying a photon of energy, $hv_{EX}$ ($h$ = Planck's constant and $v$ = frequency of light), creating an excited electronic singlet state. At step 2, the energy of $S_1$' is partially dissipated, generating a relaxed singlet excited state ($S_1$), from which fluorescence emission originates. The fluorophore returns to its ground state, $S_0$, by emitting a photon ($hv_{EM}$). However, not all excited $S_1$ molecules return to the ground state ($S_0$)

by fluorescence emission since some molecules undergo intersystem crossing, collisional quenching and fluorescence resonance energy transfer (FRET). The energy of the emitted photon is lower than that of the exciting photon due to energy dissipation in step 2 and it is emitted at a longer wavelength.

A single fluorophore can produce many detectable photons as the same fluorophore can be repeatedly excited and can re-emit unless photobleaching occurs. The discrete electronic transitions are broadened due to vibrational and rotational effects. The fluorescence emission spectrum is a plot of the fluorescence intensity versus wavelength; it depends upon the chemical structure of the fluorophore, the solvent in which it is dissolved and the excitation wavelength selected [5].

Fluorescence intensity quantitatively depends on the fluorescence quantum yield of the molecules, the excitation source intensity and fluorescence collection efficiency of the instrument and the absorbance parameters (molar extinction coefficient, optical path length and solvent concentration). Fluorescence intensity is linearly proportional to excitation intensity, but the relationship becomes nonlinear when the sample absorbance exceeds about 0.05 in a 1 cm path length [4].

Fluorescence (Step 3 in Figure 1.1) is a different process from phosphorescence (Step 4). Phosphorescence occurs between excited and ground states with different spin multiplicities. After excitation to a vibrational level of S', intersystem crossing (ISC) to an electronic triplet excited state occurs. As a result, in contrast to fluorescence, in phosphorescence, light is emitted over a longer period of time (of the order of seconds or minutes) since the excited molecule undergoes a transition to a different excited state [6].

### 1.1.1 Fluorescence quantum yield and lifetime

The fluorescence quantum yield and lifetime are important for quantifying fluorescence. The fluorescence quantum yield refers to the number of emitted photons relative to the number of absorbed photons, indicating the efficiency of the fluorescence process [4, 5]. The maximum fluorescence yield is 100 %, where each absorbed photon produces an emitted photon [5, 7]. The fluorescence lifetime is the average time the molecule stays in its excited state prior to return to the ground state [5]. The fluorescence parameters (fluorescence quantum yield, $Q$, and lifetime, $\tau$) are related to the emissive rate of the fluorophore ($\Gamma$) and non-radiative decay to $S_0$ ($k_{nr}$), given by [5];

$$Q = \frac{Number\ of\ photons\ emitted}{Number\ of\ photons\ absorbed} = \frac{\Gamma}{\Gamma + k_{nr}} \tag{1.1}$$

$$\tau = \frac{1}{\Gamma + k_{nr}} \tag{1.2}$$

where the quantum yield, Q and the lifetime, $\tau$ can be modified by a number of factors. The quantum yield is close to unity if the radiative decay rate is much larger than the radiationless decay rate [5]. The parameters, $\Gamma$ and $k_{nr}$ are shown in figure 1.1. Rhodamine 6G has a quantum yield approaching unity, with bright emission, as a result of large $\Gamma$, and its fluorescence lifetime in methanol solution is short, ~ 4 ns [8].

### 1.1.2 Fluorescence quenching and energy transfer

Fluorescence quenching arises from short-range interactions between the fluorophore and the local molecular environment, such as collisional quenching, resonant energy transfer, excited state reactions and complex formation [4, 5].

Photobleaching refers to the destruction of the excited fluorophore, for example, due to photosensitized generation of reactive oxygen species. Photobleaching can cause irreversible loss of fluorescence signal if there is no replenishment of the bleached fluorophore population and the extent of photobleaching depends on the duration and intensity of exposure to excitation light [4]. We may observe decreased Rhodamine 6G emission if the dye has been exposed to pump light for a long time.

Collisional quenching of fluorescence refers to the deactivation of the excited-state fluorophore upon collisions with other molecules in solution. The fluorophore returns to the ground state after an encounter with collisional quenchers such as oxygen, amines, halogens and electron-deficient molecules like acrylamide [5]. For example, if an oxygen molecule collides with a fluorophore in the excited state, then the fluorophore may return to the ground state without emitting a photon [5].

Aside from diffusive collisions, fluorescence quenching arises due to resonance energy transfer from long-range multipole coupling such as dipole-dipole, dipole-quadrupole and quadrupole-quadrupole coupling. It is a non-radiative energy transfer as the transfer does not involve any emission of light by the donor. Rather, it is due to the interaction between the donor and the acceptor molecules during the excitation lifetime of the donor [5, 9]. This mechanism, also known as Förster Resonant Energy Transfer (FRET) is determined by a spectral overlap between the emission spectrum of a fluorophore (the donor) with the absorption spectrum of the acceptor [5, 10] . Such overlap is shown in figure 1.2.

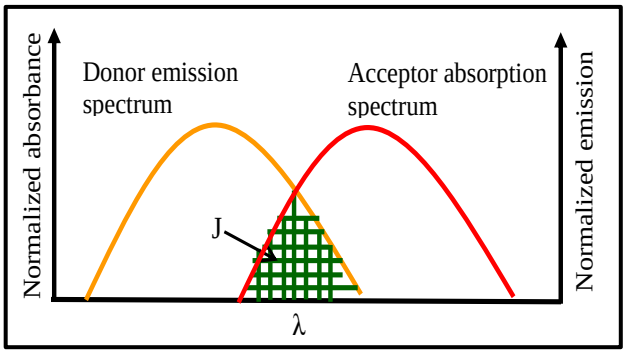


Figure 1.2 Spectral overlap (shaded J) between emission of the donor and absorption of the acceptor indicates rate of the resonant energy transfer.

The spectral overlap and the distance between the donor and the acceptor affect the rate of energy transfer. The rate of energy transfer, $P_{DA}$ is given by [5];

$$P_{DA} = \frac{1}{\tau_D}\left(\frac{R_0}{R}\right)^6 \tag{1.3}$$

where $R_o$ is the Förster distance, $\tau_D$ is the donor fluorescence lifetime without energy transfer and $R$ is the distance between the donor (D) and acceptor (A). $R_o$ is proportional to spectral overlap. Hence, the efficiency of Förster energy transfer, $\eta_{nr}$ for a single donor-acceptor pair at a fixed distance, $R$ is [5];

$$\eta_{nr} = \frac{R_0^6}{R_0^6+R^6} \tag{1.4}$$

Radiative energy transfer also affects fluorescence as it involves the emission of a photon by the donor molecule and its subsequent absorption by the acceptor molecule. It is dominant in dilute solutions and the radiative energy transfer efficiency, $\eta_r$ can be estimated through [9];

$$\eta_T = \eta_r + \eta_{nr} \tag{1.5}$$

where $\eta_T$ is the total energy transfer efficiency.

Quenching may also occur if the fluorophores form non-fluorescent complexes with quenchers before excitation occurs. A complex-formation process corresponds to static quenching since it does not depend on diffusion or molecular collisions. Dye

aggregation is an example of complex formation, where the dye molecules stack together to minimize contact with the solvent. Dye aggregation can be minimized by adding surfactant or increasing the temperature [5].

Fluorescence quenching of dye by gold nanoparticles was studied by Tapasi Sen *et al.* [11], who observed a decrease in the photoluminescence and the lifetime of the Rhodamine 6G dye with gold nanoparticles. They suggested that the decrease was due to a surface energy transfer process as the distance between the donor and acceptor was large and the energy transfer followed a $1 / R^4$ distance dependence. Dulkeith *et al.* [12] studied radiative and non-radiative effects in time-resolved fluorescence experiments on lissamine molecules (donor) chemically attached to gold nanoparticles (acceptor). They deduced that the radiative rate of lissamine dye molecules decreased by more than an order of magnitude while the non-radiative rate increased by more than an order of magnitude when the lissamine was attached to gold nanoparticles [12].

### 1.1.3 Fluorescence enhancement

Fluorescence enhancement corresponds to an increase of emission intensity due to plasmonic or other effects.

#### 1.1.3.1 Plasmonic effects on fluorescence

Plasmonic enhancement of fluorescence by nanostructured metals occurs due to two main factors: (1) Concentrating the incident light into local electromagnetic 'hot spots' which leads to increased absorption of the incident light by the fluorophores. (2) Changing the radiative and non-radiative decay rates of nearby fluorophores affecting the fluorescence lifetime and quantum yield [13, 14].

Metals are defined by their quasi-free electrons in the ground state, and these electrons are responsible for their high electric conductivity and reflectivity. The free electrons of the metal behave like a gas of free charge carriers (a plasma) and can be excited to produce longitudinal electromagnetic charge density waves [15]. The quantum of plasma oscillations (plasmons) that can be derived directly from Maxwell's equations plays an important role in the optical properties of metals. The dielectric function of the free electron gas is given as [16-18];

$$\varepsilon(\omega) = 1 - \frac{\omega_p^2}{\omega^2 + i\gamma\omega} \tag{1.6}$$

where $\omega_p$ is the plasma frequency and $\gamma$ is the collision frequency ($\gamma = 1/\tau$). $\tau$ is the relaxation time of the free electron gas which is normally on the order of $10^{-14}$ s at room temperature, corresponding to $\gamma$ = 100 THz . Light with a frequency below the plasma frequency is reflected, since the electric field of the photons is screened by the metallic electrons. However, light with a frequency above the plasma frequency is transmitted since the electrons cannot respond fast enough to screen it [16-18].

Plasmons can be grouped into three distinct categories as volume plasmons, propagating surface plasmons and localized surface plasmons. Volume plasmons are also known as bulk plasmons as they normally occur in bulk metal. The bulk plasmons cannot be excited by a transverse field of photons since they are longitudinal propagating modes. Surface plasmons (SPs) are oscillations of surface conduction electrons near a metal surface which are excited by electromagnetic radiation at a metal surface [15, 16]. Here, we are concerned with propagating surface plasmons and localized surface plasmons.

Propagating surface plasmons are confined at a metal surface, and interact strongly with photons, and are also termed as surface plasmon polaritons (SPPs). SPPs

propagate along a metal surface and exist as bound surface modes at the boundary between a dielectric and a metal film. Figure 1.3 illustrates a schematic of SPPs where plasmons propagate in the *x*- and *y*-directions along the metal-dielectric interface and decay evanescently in the *z*-direction [19]. The refractive index of the surrounding medium, and the dielectric function and structure of the metals influence the resonance condition for exciting these plasmons. SPPs generally do not exist in metal nanoparticles but can be found in metal films [16, 19, 20].

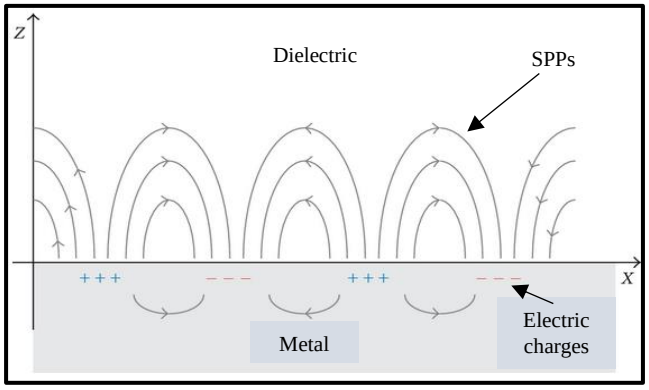


Figure 1.3 Propagation of surface plasmon polaritons (SPPs) along a metal surface [19].

In contrast, localized surface plasmons (LSPs) are excited in a bound geometry of metal nanoparticles and do not propagate. They decay either non-radiatively or radiatively, giving rise to scattering and / or absorption of light. The resonance condition and the wavelength of the incident light both affect the coupling of light to LSPs. The electron charges cannot propagate; they merely oscillate in the metal nanoparticles [16, 19, 20]. A schematic of localized surface plasmons is depicted in figure 1.4. The electron cloud displaced relative to the nuclei produces a Coulomb attraction which develops a restoring force that causes the electron cloud to oscillate relative to the nuclei. In other words, a spherical metal nanoparticle irradiated by light

creates an oscillating electric field that results in coherent oscillation of conduction electrons. Light interacts with particles much smaller than the incident wavelength and this leads to a plasmon that oscillates locally around the nanoparticle at the localized surface plasmon resonance (LSPR) [19].

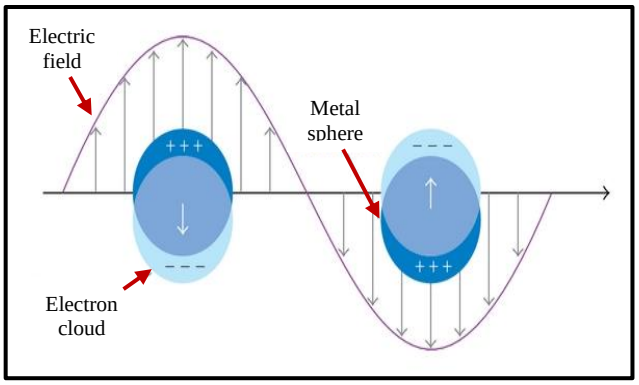


Figure 1.4 Localization of surface plasmons on metal spheres when light illuminates the metal particles with displacement of conduction electron cloud relative to the nuclei [19].

Mie theory can be used to understand the surface plasmons arising on spherical metal nanoparticles in terms of scattering and absorption of light by using the quasistatic and dipole approximations [15, 20]. The local field surrounding metal nanoparticles is enhanced by excited surface plasmons and is strongly wavelength dependent. The strongest interaction with surrounding fluorophores occurs when the nanoparticle plasmon resonance has a good overlap with the excitation and / or emission spectra of the fluorophore [14, 21]. The highest excitation rate can be achieved when the localized surface plasmon resonance peak directly overlaps with the maximum of the dye absorption spectrum [13, 14]. The metal causes changes in the radiative decay rate due to changes in the local photonic mode density and there is also an increase in the non-radiative decay rate due to energy transfer from the dye

molecules to the metal. Fluorescence enhancement arises when the radiative rate increases more than the non-radiative decay rate [13, 14].

#### *1.1.3.2 Modified structure effects on fluorescence*

Aside from plasmonic effects, modified structures with zinc oxide, quantum dots, silica and photonic crystals can also enhance the fluorescence. For example, a photonic crystal was designed as an optical resonator to enhance florescence emission [22]. Enhanced fluorescence is also observed due to surface scattering, and the redistribution of the electromagnetic fields from nanostructured aluminium oxide [23]. Wang *et al.* [24] observed broadband fluorescence enhancement from zinc-oxide nanoflower arrays and ZnO nanorods, which was comparable with that from metal-enhanced fluorescence.

## 1.2 Random lasing in disordered media

The term "random lasing" was originally introduced since the light experiences a random walk and scatters in an active gain medium before being emitted as a laser beam. Random lasing works on the same principle as a regular laser.

In a regular laser, a laser gain medium consists of laser-active atoms or ions which have different energy states and a mechanism to put the atoms into a certain excited state. Spontaneous emission occurs when an atom in the excited state spontaneously decays into a lower energy level, releasing energy in the form of a photon which is emitted in a random direction (figure 1.5) [25]. Under normal conditions, fewer atoms are in the higher energy state but there are certain conditions (such as the presence of an upper energy state that has long lifetime) in which more atoms occur in an upper energy state than is expected under normal thermodynamic

equilibrium. Such process is known as a population inversion. Excited atoms emit photons of the proper wavelength and decay to the ground state. These spontaneously emitted photons can stimulate the emission of other photons via stimulated emission of radiation, allowing many photons with similar characteristics (wavelength, frequency and phase) to be generated in a short time (figure 1.5) [25]. The stimulated emission photon goes in the same direction as the incoming photon and the resulting photons bounce back and forth a gain material being amplified between two mirrors to produce the laser beam.

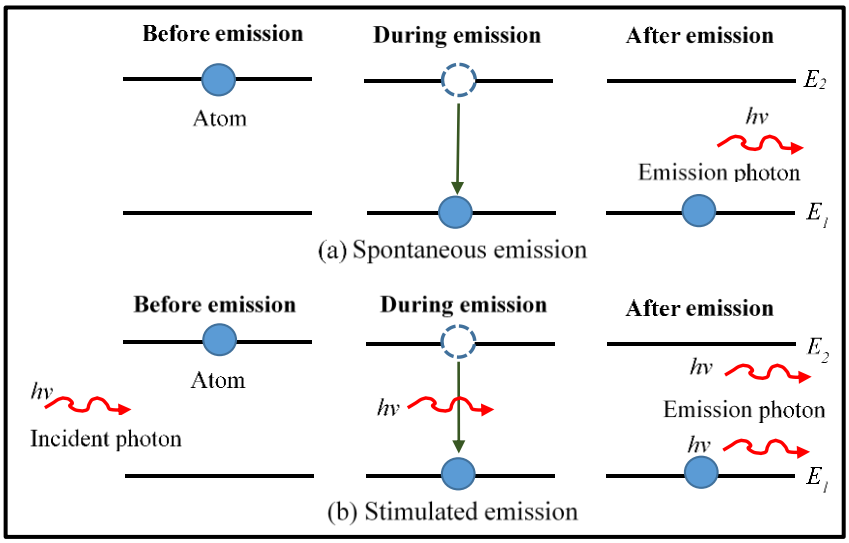


Figure 1.5 (a) Spontaneous emission and (b) Stimulated emission of photon. $E_1$ and $E_2$ are the ground and excited energy states while $hv$ represents the photon energy ($h$ is the Planck's constant and $v$ is the frequency). In spontaneous emission, atom is excited to the higher energy state and decays to the ground state, releasing a photon. In stimulated emission, an incident photon stimulates the emission of another photon which has similar characteristics with the incident photon.

In the case of random lasing, multiple light scattering by particles in the disordered material traps the light long enough for efficient amplification, and the resulting laser light emerges in random directions (figure 1.6) [2, 26]. Thus, the feedback mechanism in random lasing is provided by disorder-induced scattering, not by a cavity formed by mirrors. Two basic criteria to define a random laser are, (i) Light

is scattered by particles / structures due to randomness and amplified by stimulated emission, (ii) There is a threshold when the total gain exceeds the total loss in the system which also can be observed in regular lasers [2, 26].

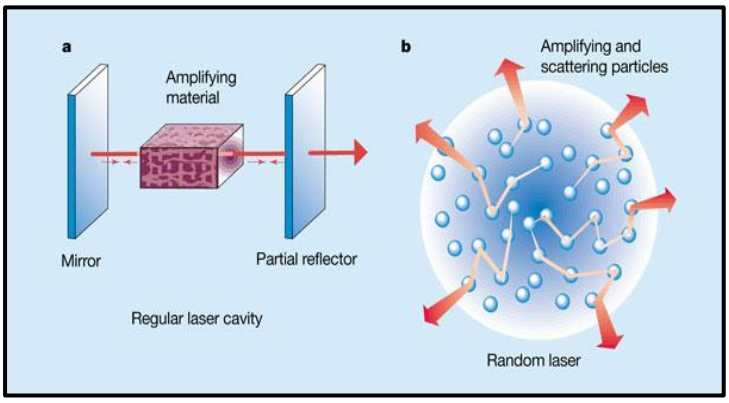


Figure 1.6 (a) Regular lasers (b) Random lasers. Regular lasers use mirrors to form a cavity for the feedback mechanism while random lasers use multiple light scattering for feedback. Both lasers need a gain medium to amplify the light [26].

### 1.2.1 History of random lasers

In the last few decades, random lasers have captured researchers' attention due to their potential applications as cheap miniature laser sources in many fields including medical image processing, metrology, communications and others. The history of random lasers dates to the mid twentieth century when Ambartsumyan *et al.* [27] made an experiment which consisted of two ruby crystals as the active gain medium and the feedback mechanism was achieved by a mirror and a volume / surface filled scatterer. They had invented a new type of laser that generated light from a scattering medium. In the experiment, excited atoms or molecules in a scattering medium emitted photons spontaneously, then the photons experienced multiple scattering and underwent random walks before leaving the medium. The photons could cause stimulated emission of additional photons when they travelled

in the gain medium [27, 28]. A few years later, researchers used laser crystal powders to create lasing in random media known as powder lasers [29]. Similarly, Lawandy *et al.* [30] demonstrated random lasers with spectrally narrow, high intensity and laser-like light emission through non-resonant optical feedback from multiple scattering. This triggered further theoretical and experimental studies [31-34] on light amplification in diffusive media before the term "random laser" appeared.

## 1.2.2 Principle of random lasing in disordered media

The principle of lasing in disordered media (random lasing) is different from that of fluorescence since fluorescence occurs without feedback (see Section 1.1). Fluorescence is spectrally broad while random lasing produces a narrow emission peak or multiple emission peaks with a threshold above which the emission intensity increases nonlinearly with the pump energy density. Random lasing needs multiple light scattering for feedback, and a suitable energy pump source to excite the gain medium.

### *1.2.2.1 Multiple light scattering*

Light scattering is a phenomenon in which light is redirected by interactions with a particle [35]. When a particle is illuminated by light, electric charges in the particle oscillate with the electric field of the incident wave. The oscillating electric charges radiate electromagnetic waves in all directions, resulting in scattering. The energetic electrons convert part of the absorbed energy into other forms such as thermal energy. The interaction of light with a single particle is the simplest case, but it is more subtle when the scattering medium has many particles. Each particle scatters

the incident light and also scatters light from the other particles resulting in multiple light scattering. An important parameter in multiple light scattering theory is the mean free path. The scattering mean free path, $l_s$ refers to the average distance that light travels between two successive scattering events while the transport mean free path, $l_t$ corresponds to the average distance the light propagates in the sample before the propagation is randomized [1].

Scattering in random and disordered media involves relevant equation specifying directional effects (figure 1.7). In random and disordered media, $l_s \sim l_t$ for isotropic scattering (scattering is similar in all directions) while for anisotropic scattering (scattering depends on direction), the transport mean free path, $l_t$ is [1, 3];

$$l_t = \frac{l_s}{1-\langle cos\theta \rangle} \tag{1.7}$$

where $l_s$ is the scattering mean free path and $\langle cos\theta \rangle$ is the average cosine of the scattering angle [1, 3]. The scattering angle is shown in figure 1.7, redrawn from ref. [36]. Further explanation of scattering can be found in [36].

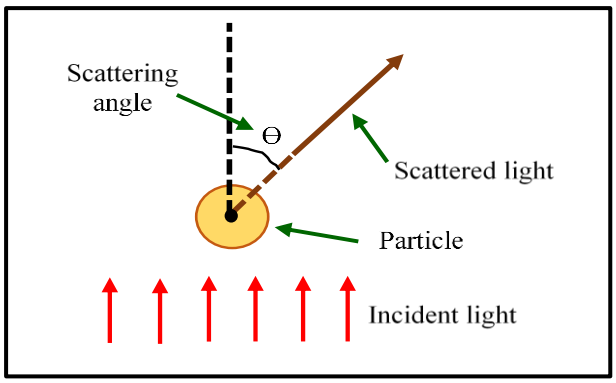


Figure 1.7 Definition of scattering angle. In this figure, the incident light is from below. The figure is redrawn based on ref. [36].

The scattering mean free path is given by [3, 28, 36-38];

$$l_s = \frac{1}{\rho \sigma_s} \tag{1.8}$$

where $\rho$ and $\sigma_s$ are the number density of scatterers and the scattering cross section respectively. The scattering cross section can be defined as an effective area of the incident light at the position of a particle that measures the probability of a scattering event [35, 36]. There are three regimes for multiple light scattering [1, 3, 39] in the isotropic scattering media ($l_s \sim l_t$);

(i) Localization regime: $l_t \leq \lambda$

(ii) Diffusive regime: $\lambda < l_t < L$

(iii) Ballistic regime: $l_t \geq L$

where $\lambda$ is the light wavelength and $L$ is the sample size in which the lasing takes place. This governs the total length available for the photon to scatter. In the localization regime, interference of the scattered light stops the light propagation and the light is spatially localized, while in the diffusive regime, the light diffuses through the strongly scattering medium. The electromagnetic wave propagation of the diffusive regime can be modelled as the random walk of photons with a step length equal to the scattering length [1, 40]. The ballistic regime corresponds to a regime that has low number density of scatterers, so light photons travel 'ballistically'. This is also known as the weakly scattering regime [1, 40].

In this study, we are concerned with elastic light scattering where the direction of light propagation is modified and the energy of the photon is conserved. Elastic scattering can be described by different models depending on the size of the nanoparticles. Rayleigh scattering refers to elastic scattering of light from particles whose diameters are much smaller than the wavelength of the scattered light. The scattering cross section based on Rayleigh scattering, $\sigma_{sR}$ is given as [41];

$$\sigma_{sR} = \frac{8\pi}{3}\left(\frac{2\pi n_m}{\lambda}\right)^4 a^6 \left(\frac{m^2-1}{m^2+2}\right)^2 \tag{1.9}$$

where $\lambda$ is the light wavelength, $a$ is the particle radius and $m = n_p/n_m$ is the ratio of the refractive index of the particles to that of the surrounding medium. The Rayleigh scattering cross section is proportional to $1/\lambda^4$ as indicated in eq. (1.9).

The Mie scattering model arises from a solution of Maxwell's equations for homogenous, isotropic and dielectric spheres [41]. The Mie scattering cross section, $\sigma_{sM}$ is given as [41];

$$\sigma_{sM} = \left(\frac{2\pi}{k_m^2}\right) \sum_{n=1}^{\infty} (2n+1)\,(|a_n|^2 + |b_n|^2) \tag{1.10}$$

where $k_m = 2\pi\, n_m/\lambda$. The $a_n$ and $b_n$ are the scattering coefficients which can be found in ref. [41]. Mie scattering theory is an accurate model to analyse the scattering properties of nanoparticles for spherical nanoparticles with size close to the light wavelength [41]. If the particle radius is much larger than the wavelength, geometrical optics can be used to estimate the scattering cross section, $\sigma_{sG}$ from [41];

$$\sigma_{sG} = \pi a^2 \tag{1.11}$$

where $a$ is the particle radius.

Aside from the Rayleigh, Mie and Geometric Optics modelling, coherent backscattering (CBS) experiments can be used to estimate the effect of scattering in disordered media. CBS of light is a photon self-interference effect which leads to an enhanced intensity cone in the backscattering direction [42]. Photons which are incident on a dense colloidal particle suspension undergo Brownian motion. The photons propagate through a scattering medium and endure many scattering events until they are absorbed or leave the medium. Any random path of light inside a scattering medium can be time-reversed [43]. Two photons which are counter-propagating along the same optical path may have similar phase delays. Therefore, if two partial waves enter the same optical path from the opposite ends, the two partial

waves can be in phase when they leave the sample. This leads to constructive light interference in the backscattering direction [43]. Theoretical and experimental studies of coherent backscattering yield the transport mean free path from the backscattering cone graph [44-46]. The CBS experimental set up and coherent backscattering cone are shown in figure 1.8 [45]. The width of the backscattering cone is predicted to be proportional to $\lambda$ / $l_t$ where $\lambda$ is the light wavelength and $l_t$ is the transport mean free path [44-46]. The width of the backscattering cone, $\theta_w$ can be defined as [42];

$$\theta_w \approx \frac{\lambda}{\sqrt{2} l_t} \tag{1.12}$$

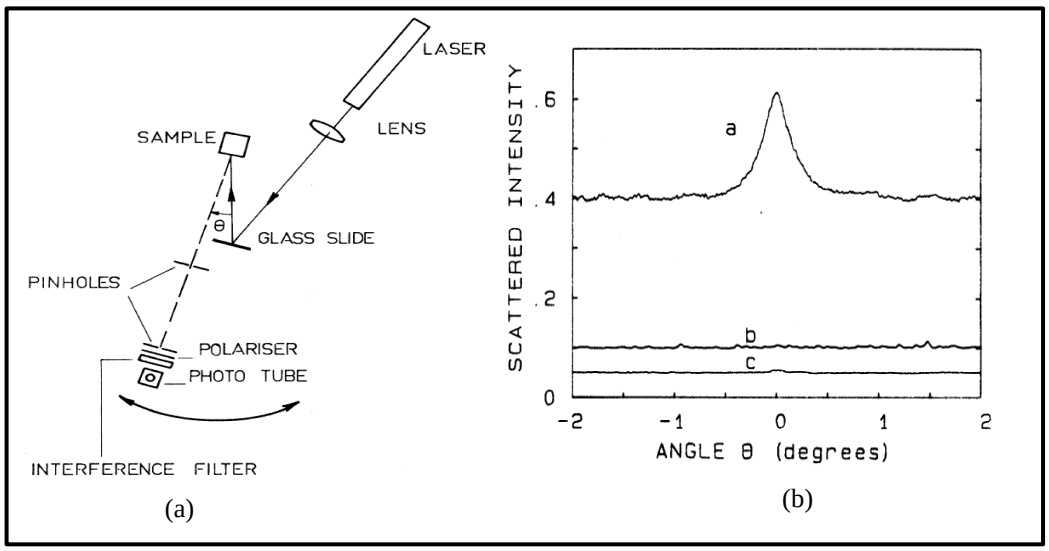


Figure 1.8 (a) Coherent backscattering experiment set up and (b) Measured coherent backscattering cone for an aqueous suspension of 460 nm polystyrene beads (curve a) in a cell, a cell filled with water without polystyrene (curve b) and in the absence of any cell (curve c) [45].

In this thesis, the scattering mean free path, $l_s$ was estimated using eq. (1.8) while the transport mean free path, $l_t$ was measured by coherent backscattering (CBS) experiments.

### *1.2.2.2 Optical gain*

Apart from multiple light scattering, a source of optical gain is needed in the random lasing system. A gain material (consisting of scatterers or non-scatterers) becomes active when it is excited by a high energy pump source. In an amplifying disordered medium, the light waves are multiply scattered and amplified. The gain length, $l_g$ and amplification length, $l_{amp}$ describe the amplification process. The gain length refers to the path length over which the intensity is amplified by a factor *e* and the amplification length is defined as the (rms) average distance between the beginning and ending point for paths of length, $l_g$ [1, 33]. Light travels in a straight line in a transparent solution (a medium without scattering), thus, $l_{amp} = l_g$. In a three-dimensional system, $l_{amp}$ is related to $l_g$ as given by [1];

$$l_{amp} = \sqrt{\frac{l_t l_g}{3}} \tag{1.13}$$

Within the active gain region, emitted photons propagate and are amplified until they escape from the region. A necessary condition of random lasing is $l_s$ (scattering mean free path) $\geq l_g$, so that the light is adequately amplified to balance the loss before it escapes the random medium [1, 3]. The photon residence time (the average time interval spent by a photon in the medium) in the gain region depends on the probability of scattering back into the active gain region and the diffusion length of the pump photons. Thus, the necessary conditions for random lasing are: (i) sufficient scattering to trap the light in a gain medium and (ii) The scattered light is amplified enough to balance the loss before it leaves the gain medium.

## 1.2.3 Characteristics of random lasing in disordered media

### *1.2.3.1 Random lasing threshold*

The lasing thresholds in regular lasers are determined at the onset of the nonlinear increase of the output power as a function of the input power whereas the lasing threshold in random lasers is usually reached when the pump transition is bleached which can be determined at the onset of the nonlinear increase of emission intensity as a function of pump energy density [47-50].

The lasing threshold can be affected by the particle and dye concentrations [49, 51, 52], refractive index contrast between scatterers and the surrounding media [53], excitation spot diameter [32], energy transfer and plasmonics effects [54-56]. Cao *et al.* [52] studied random lasers using zinc oxide and found that when the scattering mean free path of photons in zinc oxide was less than the stimulated emission wavelength, the lasing threshold reduced. The lasing threshold was reduced when the concentration of dielectric scatterers (titania) [51] was increased, due to increased scattering and feedback. The random laser threshold decreased when the Rhodamine 6G concentration was increased to 10 g/L due to the higher available gain [49]. The lasing threshold reduced with a larger refractive index contrast between the scatterers and the surrounding medium [53]. Wang *et al.* [56] found that the FRET (from zinc oxide to titania) reduced the lasing threshold of random lasers with zinc oxide (nanorod) / titania (nanoparticles). The titania nanoparticles as the scatterers enhanced the efficiency of the zinc oxide random lasers. Metal nanoparticles also affect the random lasing threshold through surface plasmon resonance (SPR) and absorption loss [54, 55]. Plasmonic scattering is strongest when the surface plasmon resonance

wavelength matches the lasing emission wavelength, leading to the lowest lasing threshold [3].

#### *1.2.3.2 Random laser emission, multi-directional emission and tunability*

One signature of random laser operation is that the emission intensity increases and one or more narrow emission peaks appear when lasing is achieved which can also be observed in regular lasers [55, 57, 58]. When a photon propagates in a gain medium, it can stimulate the emission of a second photon. The gain length at frequencies near the maximum of the gain spectrum approaches the average path length of the photons in the gain medium. Hence, the probability of a photon generating a second photon before escaping from the gain medium approaches one and the emission intensity suddenly increases. An abrupt increase of the emission intensity at the maximum of the gain spectrum leads to a significant narrowing of the emission peak [57].

For random lasers excited by picosecond-pulsewidth pump lasers, multiple emission peaks (emission peak linewidth less than 1 nm) appear on top of the broad fluorescence background when the scattering increases [57]. A closed loop path forms a laser resonator, and for sufficient gain, laser oscillation can occur in the loop. The oscillation frequency is determined by the actual path length. Discrete narrow emission peaks appear, resulting from the random closed loop paths acting as resonators [57]. In the weakly scattering regime, multiple emission peaks can be observed from random changes of the refractive index inducing waveguiding and resonant modes with large transport mean free paths [3]. However, the observation of spiky emission may be limited by the resolution of the detection system, pump pulse duration and characteristics of the nanostructures [2, 58-61].

The lasing frequency is determined by the peak of the available gain. The control of lasing frequency is important in lasers but it is hard to achieve in disordered media due to the absence of a well-defined cavity in comparison with regular lasers. The cavity determines the laser emission characteristics in regular lasers. In random lasers, the emission wavelength can be tuned by varying the particle / structure size and absorption which changes the gain curve and mode selection. For example, resonance effects can affect the emission wavelength [62] and the emission wavelength was shifted 37 nm when the particle (photonic glass) diameters were changed by 10 %, due to resonant scattering [63]. The random laser emission wavelength was tuned by changing the size of scattering gold nano-islands, due to the plasmon resonance shift [47]. Furthermore, the emission wavelength can be shifted by modifying the absorption, for example by adding nonfluorescent dye (Quinaldine Blue) to the gain media (Rhodamine 640) with titania scatterers [64]. Additionally, the absorption of zinc oxide was modified in zinc oxide / alumina nanopowder lasers by varying the weight fraction of alumina to shift the ZnO emission wavelength [65].

As well as the physical characteristics of the particle scatterers, the emission wavelength may also be tuned by varying other parameters such as temperature, electric field and pump beam distribution. When the temperature changes, the laser feedback changes due to changes in the refractive index of the disordered media [3, 66]. The emission wavelength of a random laser with liquid crystal can be tuned by applying a small voltage to the sample to shift the wavelength by changing the refractive index of the liquid crystal [67].

Random laser emission is observed in all directions, resulting in multidirectional lasers, due to the random scattering events. However, directional

control in random lasers may be desirable for applications that require a uni-directional output. The emission direction of a random laser can be controlled by providing directional confinement using waveguides. Liang *et al.* [68] used a rib waveguide to produce the directional and controllable edge-emitting random laser diodes by burying a p-GaN / annealed i-ZnO: Al (3%) / n-ZnO : Al (5%) heterojunction diode with a 2 μm rib waveguide. The strong electrical and optical confinement of the buried heterojunction rib waveguide structure produces excellent electrical-to-optical conversion efficiency that can enhance the emission intensity [68]. Plasmonic waveguides can also produce enhanced random lasing with low threshold and directional output. [47].

#### *1.2.3.3 Coherence*

Coherence is a key property of lasers. Optical coherence is defined as the ability of light to produce interference effects [69, 70]. Coherent light in a field exists when there is a fixed phase relationship between the electric field values at disparate locations or times whereas partially coherent light exists when there is partial correlation between phase values [69, 70].

Coherence enables the laser beam to have a very narrow spectrum (temporal coherence) and to focus to a tight spot (spatial coherence). Coherent and incoherent sources can be characterized by their photon statistics so that a coherent source has a Poisson photon distribution whereas an incoherent source may have a Bose-Einstein photon distribution [3]. Cao *et al.* [71] measured the photon number distribution, and showed a change from Bose-Einstein distribution to Poisson distribution when the lasing threshold was achieved. Zacharakis *et al.* [72] showed that random lasers with incoherent feedback produced both Poisson and Bose-Einstein distributions leading to

partially coherent light. If a large gain is provided, the intensity increases until it completely depletes the gain medium leading to suppression of intensity fluctuations. Then, the characteristics of the Poisson distribution can be observed [2]. Studies of coherence in random lasers include spatial coherence using Young's two slit interferometric scheme [73] and temporal coherence using a Twyman-Green interferometer [74] and a Michelson interferometer set up [75].

#### *1.2.3.4 Polarization*

Polarization can be controlled by intracavity Brewster windows or Lyot filters in a regular laser, but in random lasers, multiple light scattering and optical gain affect the spectro-polarimetric properties of random laser modes [76]. Methods to realize polarized emission from disordered media, include introducing anisotropic components. Linearly-polarized random lasing emission can be realized by choosing a linear pump polarization, a suitable dye with a preferred absorption axis and molecular alignment in the gain medium to force the laser emission to be highly polarized and a highly viscous solvent or polymer host to 'freeze' the dye molecules in position and orientation [76]. Linearly polarized lasing is observed in dye-doped nematic liquid crystals. A schematic diagram of the experimental set up for investigation of lasing emission from the dye-doped nematic liquid crystals [77] is shown in figure 1.9. The polarization orientation approximates the bisection between the direction for maximal scattering in nematic liquid crystals and the nematic director. The polarization can be tuned by rotating the nematic liquid crystal [3, 77]. The sample could be rotated in the x–y plane to form any arbitrary angle between the nematic director and the x axis. The x–y plane is perpendicular to the optical table [77].

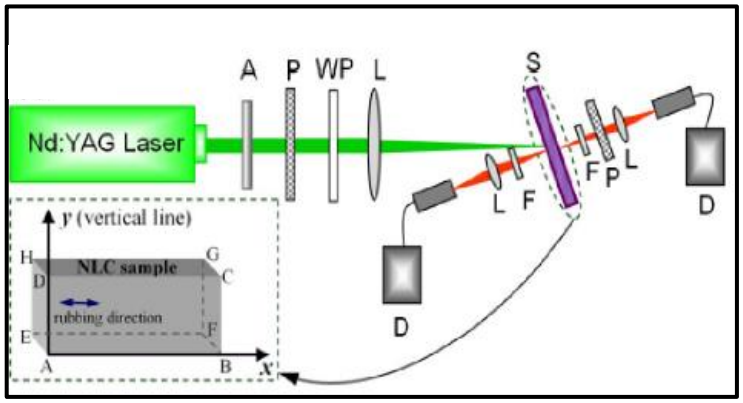


Figure 1.9 Schematic diagram of the experimental setup. A, P, WP, L, F, and D are the attenuator, polarizer, wave plate (including quarter-wave/half-wave plates), lens, bandpass filter centered at 630 nm and high-speed photodetector respectively. S is the dye-doped NLC cell [77].

## 1.2.4 Types of random lasing

Random lasing can be categorized into two types based on the form of the feedback; coherent and incoherent feedback [1, 78].

### *1.2.4.1 Random lasing with incoherent / diffusive feedback*

Incoherent feedback corresponds to the instability of light amplification along open trajectories where the light does not return to its original scatterer but remains within the gain volume. During this time, there are no spatial resonances of the electromagnetic field, the phase of the scattered light can be ignored and the dwell time of the light is insensitive to frequency. The feedback mechanism returns a fraction of the photons or energy to the gain medium and hence, is known as energy feedback [1, 3]. For these lasers, the amplification line of the gain medium is the only resonant element and the mean frequency of the emission depends on the centre frequency of the emission band of the gain media and not on the dimensions of laser cavity.

Interference effects occur in all random laser materials since the multiple light scattering process is elastic but the effects are not clearly observed in random lasing with incoherent feedback [2]. The interference effects may be averaged out if long

excitation pulses are used or several laser shots are averaged leading to a smooth narrowing of the spectrum instead of emission spikes on top of the spectrum [2]. Random lasing with incoherent feedback characterized by a narrow emission peak and nanosecond-pulsewidth pump lasers based on dielectric [49, 64] or metal scatterers [47, 54, 55, 79] was well studied. However, Wang *et al.* [60] and Dominguez *et al.* [61] observed multiple emission peaks from disordered media consisting of silver nanowires and nanospheres.

Random lasing with incoherent feedback may appear analogous to amplified spontaneous emission (ASE), a phenomenon in which photons that are emitted spontaneously by excited atoms are subsequently amplified by stimulated emission. ASE does not need input 'seed' light to emit photons and it occurs in high-gain active materials without scattering particles if the rays can propagate freely, the excitation is strong and there is sufficient excitation volume [2]. ASE light can be emitted even without feedback from scattering, but in incoherent feedback random lasers, multiple light scattering plays an important role for lasing.

In random lasers with incoherent feedback, the lasing threshold can be determined when a narrow emission peak appears on top of the fluorescence background. The emission intensity increases nonlinearly with the pump energy density and the emission linewidth decreases below 10 nm when the lasing threshold is reached [47-49].

#### *1.2.4.2 Random lasing with coherent feedback*

Coherent feedback refers to the instability of light amplification along closed loop paths where the scattered light returns to the same position in phase [1]. Closed loop paths can be formed by recurrent light scattering where the light scatters from a

particle, propagates through a gain medium and returns to the original particle [1]. These events become more frequent when scattering in the medium becomes stronger and the scattering mean free path, $l_s$ decreases. When $l_s \sim \lambda$ (light wavelength), diffusion of light ceases completely and localized photon modes are obtained from interference of the recurrent scattered light [1]. Scattering can create modes with a high spatial confinement in the photon localization region, where the scattered light travels in a path that eventually forms a closed loop. Along the closed loop path, interference leads to standing-wave patterns with a high degree of light confinement and spatial resonance. Modes are derived from the spatial resonance when the spontaneously emitted photons are amplified through stimulated emission [1, 3]. Due to the interference in the closed loop, laser spikes in the emission can be observed [52].

Laser spikes in regular lasers are associated with threshold lasing modes which inside the cavity are similar to the resonances or quasi-bound states of the passive system [80]. In the localized regime, quasi-bound states are nearly identical to the threshold lasing modes whereas in the diffusive regime, quasi-bound states and lasing modes are quite different. In lasers with arbitrarily complex and open cavities such as random lasers, the quasi-bound states are distinct from the threshold lasing modes in which the system can be described as constant-flux states [80]. These constant flux states can describe threshold lasing modes both inside and outside the scattering medium for any scattering strength. This theory can be used to study the multimode regime in diffusive random lasers in which constant flux states can provide a better approximation for finding the threshold lasing modes of random lasers and coincides with the exact lasing modes of uniform index cavities [80].

Laser spikes are the main characteristics of random lasing with coherent feedback as distinct from random lasing with incoherent feedback. In random lasers with coherent feedback, the lasing threshold is achieved when multiple emission peaks appear. The emission intensity increases nonlinearly with the pump energy density and the emission linewidth of the spike decreases to < 1 nm when the lasing threshold is reached. The characteristics of the lasing thresholds for random lasers with coherent and incoherent feedback are shown in figure 1.10. Figure 1.10 (d) shows the difference between the ASE and the random lasing threshold. The ASE threshold follows an exponential curve (shown as a dashed line) while the random lasing threshold is determined through a sharp 'kink' of the emission intensity versus pump energy graph [50, 81, 82].

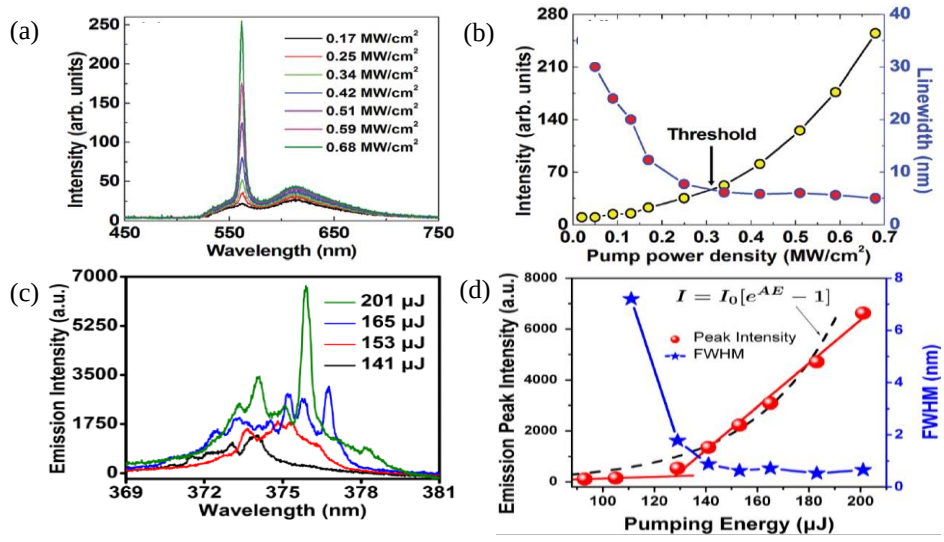


Figure 1.10 (a) A narrow emission peak appears on top of the fluorescence (incoherent random laser) [48]; (b) A nonlinear increase of emission intensity and a drastic decrease of emission linewidth when the random lasers incoherent feedback reaches the threshold (incoherent random laser) [48]; (c) Multiple emission peaks appears on top of the fluorescence (coherent random laser) [50]; (d) A nonlinear increase of emission intensity and a drastic decrease of emission linewidth when the random lasers coherent feedback reaches the threshold (coherent random laser). The dashed line is an exponential fit for ASE (*A* is a constant, *E* is the pumping energy) [50].

In addition, the transition from incoherent random lasers to coherent random lasers was previously observed in ref. [57] by varying the scattering in the random

medium, in ref. [61] using a high resolution spectrometer, in ref. [60] using silver nanowires as the scatterers and in ref. [58] using nano-rubbing cavities on a polymeric layer. Cao *et al.* [57] used a picosecond-pulsewidth pump laser while other studies [58, 60, 61] used a nanosecond-pulsewidth pump laser to excite the samples. Table 1 shows the comparison between random lasing with coherent and incoherent feedback.

Table 1 Comparison or random laser properties between incoherent and coherent random lasing

| Properties | Incoherent Random Lasing | Coherent Random Lasing |
|---|---|---|
| Feedback | Intensity or energy feedback | Field or amplitude feedback |
| Frequency | Frequency independent and phase insensitive | Frequency dependent and phase sensitive |
| Light paths | Light amplification along open loops | Light amplification along closed loop paths |
| Light paths | Light only returns back to the gain volume | Light returns back to the first scatterer that scatters the light in a loop |
| Interference effects | Interference effect is not observed | Interference is used to localize the light |
| Type of scattering | Weak scattering of light with less particle concentration. | Strong scattering of light with more concentrated particles. |
| Lasing mode | No discrete lasing mode | Discrete lasing modes |
| Effects of multiple scattering | Multiple scattering only increases the light optical path in the gain medium and the light phase is ignored ($l_s >> \lambda$) | Multiple scattering can exhibit recurrent light scattering events that forms closed loop paths ($l_s \sim \lambda$) |
| Linewidth | Produce nanometre spectral peak linewidth (FWHM) | Produce sub-nanometre spectral peak linewidth (FWHM) |

## 1.2.5 Geometries of random lasing in disordered media

Two important elements in random lasing are (i) scatterers, which consist of particles or disordered structures such as dielectric / metal nanoparticles, nematic liquid crystals and others and (ii) the gain material such as laser dye, quantum dots and others. Scatterers and gain materials are used to form different geometries of random lasers. Different geometries of random lasers include colloidal solutions, embedding the scatterers and gain on a surface or in a film or doping scatterers with a gain material.

### *1.2.5.1 Active scatterers*

Active scatterers are particles or disordered structures which provide both multiple light scattering and optical gain. Semiconductors and rare-earth-doped crystals can act as active scatterers. Semiconductors including zinc oxide (ZnO) [52, 65, 83-85], zinc sulphide (ZnS) [86], zinc selenide (ZnSe) [87] and gallium arsenide (GaAs) [88] were used to realize random lasing due to their wide bandgap. Cao *et al.* [52] observed coherent and multidirectional random lasing by depositing zinc oxide powder onto indium tin oxide (ITO) coated glass substrates. Upconversion ZnO random lasers excited by femtosecond pulsed lasers through multi-photon excitation were reported [83, 85]. Incoherent feedback random lasing due to band-to-band excitation processes was achieved in ref. [85] at ~ 390 nm through ZnO nanostructured films fabricated on a silicon substrate whereas ultraviolet coherent feedback random lasing was achieved from ZnO powder, attributed to direct three-photon absorption [83]. Additional scattering influences the lasing threshold of ZnO random lasers and affects the laser emission wavelength by varying the extent of self-absorption by ZnO nanopowder (varying the photon-transport mean free path) [84]. Raman mode random

lasing at 517 nm and 527 nm was observed in ZnS-β-carotene random gain media [86]. The random gain medium was prepared by extracting β-Carotene molecules from pale green leaves using acetone and incorporating into ZnS random gain media. The spectral overlap of the absorption and emission bands produced lasing emission at the desired wavelengths [86]. Blue- (475 nm) and infra-red (880 nm) random lasing emission was achieved using ZnSe [87] and GaAs [88] respectively.

Rare-earth doped crystals or glasses can also provide both scattering and gain. Early studies of lasing using neodymium powders by Noginov *et al.* [74, 89] characterized lasing threshold, slope efficiency and coherence properties of the laser emission. Random lasing has also been realized from a diamond nanoparticle film [90]. Monocrystalline synthetic diamond nanoparticles were annealed and dispersed in a hexane solution. The dried diamond film was excited with a picosecond-pulsewidth laser with a spot size ~ 200 μm. UV random lasing was observed from the film when the nanodiamond annealing temperature was 400-700 $^{o}$C [90]. A recent report on diamond random lasers used boron-doped p-type diamonds as a hole source [91].

#### *1.2.5.2 Passive scatterers in a gain medium*

Passive scatterers are particles which provide scattering but no absorption, for example titania, alumina, biological tissues and nematic liquid crystals. Lasing with passive scatterers requires a gain medium, such as Rhodamine laser dye. By using separate scatterers and gain media, the scattering effect and the optical gain in the system can be varied independently. The first experimental study of random lasers mixed titania with Rhodamine 640 dye and observed a narrow emission peak [30]. Varying the particle concentration and dyes separately affects the emission spectra and

lasing threshold of the random lasers [49, 51]. We observed that by varying the particle concentration, the spatial and temporal coherence were also affected (Chapter 3).

Biological tissues are effective scattering media due to their disordered nanostructures and they can produce random lasing when the tissues are infiltrated with dye. Vardeny *et al.* [92] and Song *et al.* [93] observed random lasing from colon tissues and bone tissues. In their studies, the tissues multiply scattered the light to create feedback whereas gain was provided by laser dyes. Another recent experiment used butterfly wing structures to provide an effective biological resonance cavity with ZnO nanoparticles emitting light [94].

Mixing dyes can extend the wavelength range of random lasing emission through energy transfer from donor molecules to acceptor molecules [62, 95]. The energy transfer includes both radiative and non-radiative processes, influenced by the spectral overlap between the absorption spectrum of the donor with the fluorescence spectrum of the acceptors. Dye-doped polymer nanoparticles provide both scattering and gain; for example Rhodamine 6G-doped latex nanoparticles [96] and Pyrromethene 567-doped polyhedral oligomeric silsesquioxanes nanoparticles [97].

Periodic structures such as photonic crystals can provide scattering due to defects and imperfections. Electron-beam lithography and metal-organic chemical vapor deposition can be used to fabricate photonic crystal structures and to grow the host material on a substrate [3]. Coherent random lasing in the localization regime was observed in ref. [98] by using embedded quantum wells in optically-pumped photonic crystal waveguides.

Quantum dots are useful as gain materials because of their size-dependent emission wavelength over a broad wavelength range (colour tunability). Scattering

arises due to the disorder in the quantum dots, spatial positioning and size and is enhanced by introducing surface roughness [99]. Colloidal solutions of CdSe quantum dots with Rhodamine 6G ($10^{-4}$ M) were pumped by a frequency-doubled Q-switched Nd:YAG laser (532 nm, 7 ns) to produce coherent lasing [100].

#### *1.2.5.3 Passive and lossy scatterers in a gain medium*

Metal nanoparticles induce absorption loss through energy transfer and lead to fluorescence quenching [12, 101]. However, metal nanoparticles increase the gain through plasmonic effects [14, 15, 19, 20]. These effects influence the emission and lasing threshold of random lasers balancing effects due to fluorescence quenching and plasmonic enhancement [39, 54, 55].

##### *1.2.5.3.1 Plasmonic effects and absorption loss in random lasers*

As explained in section 1.1.3.1, plasmonics can enhance fluorescence and thus can improve the performance of random lasers by enhancing the optical gain. Metal nanoparticles have the potential to enhance lasing in disordered media due to their large scattering strength, whereas dielectric nanoparticles are lossless scatterers. Metal nanoparticles exhibit surface plasmon resonance (SPR) and localize the excitation light near the surface to yield high gain for lasing. The optical scattering of metal nanoparticles is adjustable by varying the particle size, shape and surrounding medium. Hence, metal nanoparticles can enhance excitation of dye emitters locally through surface plasmon resonance while scattering the light with high efficiency [3, 39].

Dice *et al.* [55, 102] introduced the first metal-based random laser using silver nanoparticles with Rhodamine 6G in methanol. Spectral narrowing was observed with a lasing threshold lower than for equivalent random lasers with dielectric scatterers.

Gold nanoparticles were subsequently used with Rhodamine 6G for improved performance [39, 54]. The overlap between the surface plasmon resonance wavelength of the gold nanoparticles and the laser emission wavelength of Rhodamine 6G can optimize the performance of metal-based random lasers by enhancing the local electric field through localized surface plasmons [14, 21]. The enhancement effect of surface plasmons [47, 54, 61] produced incoherent random lasing with directional output.

The plasmonic effect depends on the distance between the metal nanoparticles and fluorophores (metal-fluorophore distance) and influences the laser threshold. However, at shorter distances, quenching also increases the threshold. The trade-off between plasmonic enhancement and absorption loss was discussed in refs. [37, 39] by varying the metal-dye spacing by varying the silica thickness on metal core shell nanoparticles and in ref. [55] by varying the concentration of metal nanoparticles.

The combination of metal nanoparticles with a gain medium can produce stimulated emission of surface plasmons, known as surface plasmon amplification by stimulated emission of radiation (SPASER). SPASER is the nanoplasmonic counterpart of a laser: it consists of a medium with an optical gain in close vicinity to a metallic nanostructure that can generate surface plasmon excitation [103]. In a SPASER, the resonant cavity is replaced by a metallic nanostructure to support plasmonic modes and photons are replaced by surface plasmons. When the active (gain) medium is excited externally, the energy source transfers the excitation to generate surface plasmon modes [103].

### *1.2.5.4 Other geometries of random lasers*

Other random laser geometries have been developed for enhanced performance. Most random lasers use spherical particles as the scatterers due to ease of fabrication and analysis. However, scattering particles with other shapes such as rods [104], wires [60] and irregular shapes [81, 105] are also suitable. Coherent random lasing using ZnO nanorods was observed in ref. [104] when the ZnO nanorod arrays were embedded in the ZnO epilayers (Magnesium Oxide (MgO) buffer layer and a ZnO thin film. No lasing was obtained from ZnO nanorod arrays due to low density. Thus, the ZnO epilayers increased the optical gain and reduced the scattering mean free path. Wang *et al.* [60] obtained two random lasing thresholds for incoherent and coherent feedback when Rhodamine 6G was used with silver nanowires. Nanowires can have large electromagnetic (EM) field enhancement and high light-scattering efficiencies due to the localized plasmon resonance and can act as antennas to radiate emission from fluorophores [106, 107]. Comparison of different shapes of gold found that gold nanostar-based random lasers outperformed nanosphere- and nanorod-based random lasers [105] due to the huge field enhancements at the spiky tips of the nanostars. Figure 1.11 presents different shapes of scatterers which were used in random lasers previously.

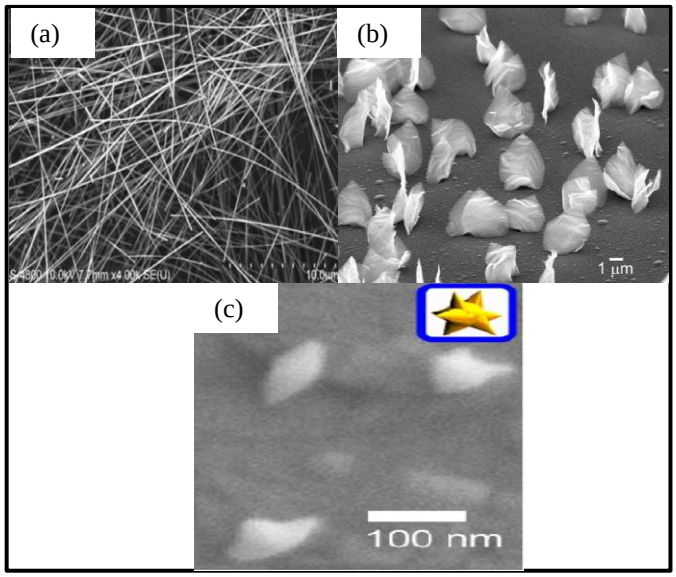


Figure 1.11 Different shapes of nanoparticles which are used in random lasers (a) Silver nanowires [60]; (b) Titania nanomembranes [81] and (c) Gold nanostars [105].

The performance of random lasers is also affected by the surface roughness of the random laser scatterers, which may have micron-scale grooves [99], gold–silver bimetallic porous nanowires [108] and nano-rubbing-induced cavities [58]. The grooves and the nano-rubbing processes enhance the scattering effect and increase the feedback. Gold-silver bimetallic porous nanowires produced broad surface plasmon spectra which gave strong feedback and supported coherent random lasing over the whole visible range in dye lasers [108].

Flexible photonic devices are developed for displays as optical sources. The effects of flexible structures on random lasers were demonstrated in refs. [48, 109, 110]. Viola *et al.* [109] demonstrated random lasers from a fluidic paper-based device. The device was fabricated using soft-lithography techniques by producing microfluidic porous channels in cellulose fibres impregnated with Rhodamine B. The confinement induced by the lithographic process was used to tailor the threshold and spectral position. A flexible bacterial cellulose (BC) membrane was used as the host material for the random laser instead of water or polymer film [110]. The BC

membranes were immersed in a colloidal solution of silver nanoparticles before infiltrating the gain medium (Rhodamine 6G) and incoherent random lasing was observed from the BC membranes. Zhai *et al.* [48] developed a technique to tune the emission wavelength of a random laser by stretching a soft substrate containing a solution of polydimethylsiloxane doped with rhodamine 6G organic dye and silver nanowires to obtain tuning from 558 to 565 nm. Stretching changed the random polarization to partial polarization and caused reorientation and breakage of the silver nanowires to tune the emission wavelength while the embedded silver nanowires provide plasmonic feedback to enhance the random laser performance [48].

Recently, random lasing has been applied in fibre lasers with feedback provided by scattering from disordered nanostructures in the fibres. The first demonstration of a random fibre laser was made by de Matos *et al.* [111]. The hollow-core microstructured fibre filled with dye and titania colloid solution was transversely pumped and produced random lasers with incoherent feedback, generated from stimulated emission due to scattering from the nanoparticles in the axial direction. The scatterers provided axial feedback whereas the fibre geometry gave the transverse confinement. This study encouraged further developments to enhance the performance of random fibre lasers such as using metal nanoparticles [112-114], holes [115] and fibre Bragg grating (FBG) [116] to provide multiple light scattering. Hu *et al.* [113] compared gold-based random dye lasers in a cuvette with gold-based random lasers in a liquid-core optical fibre and observed coherent random lasing in the liquid-core optical fibre. Instead of nanoparticles, Yonenaga *et al.* [115] used holey photonic crystal fibre (PCF) filled with laser dye solution. Figure 1.12 presents the design of random fibre lasers for transverse and longitudinal pumping.

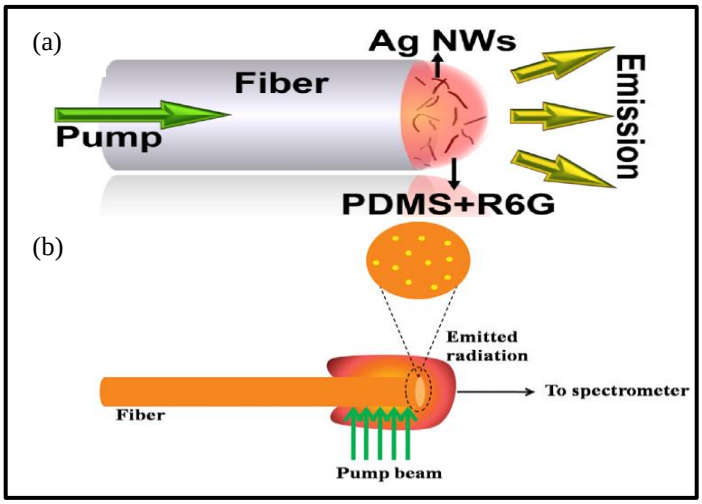


Figure 1.12 Schematics of random fibre lasers for (a) longitudinal excitation [112] and (b) tranverse excitation [114].

### 1.2.6 Applications of random lasers

Random lasers can be used as "laser paint" as light sources for holography for medical applications, imaging, sensing, photonic barcode, optomicrofluidics, optical batteries, displays, spectroscopy and new lighting systems [3, 43].

Polson and Vardeny [117] successfully used random lasers to map cancerous tissues following their prior work [92] in which they showed that spectral emission was affected by the scattering properties of the cancerous tissues. Healthy and cancerous tissues were soaked separately in Rhodamine 6G dye and flattened between two parallel microscope slides. The samples were pumped with Nd:YAG laser (532 nm, 100 ps and 800 Hz) and the emission spectra were recorded. A power Fourier transform (PFT) of the emission spectra was used to distinguish between the tissues.

Random lasers can be used for sensing as reported by Song *et al.* [93]. Nanoscale structural alterations in a mechanical or structural biosensor can be detected through the characteristics of random lasing in bone specimens. Light at 690 nm was used to excite samples of bone, soaked with a dye emitting at 800 nm. The bone

specimens were placed under tension for mechanical testing, resulting in shifts to the emission peak wavelengths of the random laser. Pre-failure damage in bone at very small strains was detectable due to the large detection area and the ultrasensitive random laser behaviour.

As mentioned, random lasing is enhanced when optical fibre is used due to better confinement inside the fibre. Wang *et al.* [118] used random fibre lasers to achieve long-distance fibre-optic remote sensing through 100 km of fibre with a fibre Bragg grating (FBG) as the sensing element. Due to the mode-selection effect by the FBG, a single highly pronounced emission peak was observed which shifted with the temperature [118].

Redding and colleagues [119, 120] developed novel applications of random lasing as a light source for bioimaging [119] and a compact on-chip random spectrometer [120]. Redding *et al.*[119] demonstrated that random lasers can produce high-intensity, speckle-free light, suitable for bioimaging. The random laser performance was compared with other light sources through speckle generation tests, image quality tests and contrast-to-noise ratio (CNR) tests. In the speckle generation tests, both random lasers and LEDs generated non-speckle patterns while in the CNR tests, both also produced higher CNR. In the image quality tests, random lasers outperformed all other light sources [119]. In ref. [120], a random spectrometer with a spectral resolution of 0.75 nm at a wavelength of 1500 nm in a 25 μm by 50 μm random structure was designed and fabricated on a silicon wafer. The spectral resolution was increased by enhancing the spectral decorrelation of speckle patterns which can be increased by increasing the optical path length through multiple

scattering in the random structure [120]. Reviews for applications and future prospects of random lasers also can be found in refs. [3, 43].

## 1.3 Chapter 1 Summary

A general introduction to fluorescence emission and random lasing in disordered media has been presented in this chapter as a guide for the experiments reported in the remainder of the thesis. This chapter summarized the main elements of random laser materials, characteristics of fluorescence, amplified spontaneous emission and coherent random lasing, types and properties of random lasing and geometries of random lasers. Finally, some applications of random lasers were reviewed.

# Chapter 2

# Emission of active nanoparticles in disordered media

Active scatterers such as ruby, zinc oxide (ZnO), diamond nanoparticles have potential for random lasers. In this chapter[1], we discuss emission from ruby and ZnO nanoparticles. The emission spectra of these nanoparticles were analyzed in terms of the angular dependence of the emission, scattering strength and excitation energy. The aims of Chapter 2 are (i) To understand the suitability of active nanoparticles for random lasers, (ii) To study the effect of scattering and gain due to active nanoparticles for random lasers and (iii) To develop techniques to characterize emission spectra and measure random laser properties. We did not observe random lasing from the ruby and zinc oxide nanoparticles. There are a number of reasons for this:

(i) Three level laser system for ruby nanocrystals - the laser medium needs to be strongly pumped to ensure a sufficient population of atoms are excited from the ground state to obtain a population inversion;

[1] We learned synthesis and characterization techniques of the active nanoparticles from Wan Aizuddin Wan Razali, Deming Liu and Sandhya Clement (PhD students from the MQ Biofocus Research Centre), Philipp Stark (an internship student, Master in Science from Ulm University), and staff of the Microscopy Unit and the Department of Earth and Planetary Sciences, Macquarie University.

(ii) Insufficient scattering and gain - the active nanoparticles provide scattering and gain simultaneously, so there is possibility that the light is scattered out of the pumped region instead of being absorbed by the nanoparticles;

(iii) Insufficient pump lasers - the pump lasers should have sufficient pulse energy to adequately excite the atoms for the population inversion.

This chapter consists of two main sections: 2.1 Ruby nanocrystals and 2.2 Zinc Oxide nanoparticles and nanorods. An estimate of the absorbed pump energy and gain for the ruby nanocrystal solution is provided at the end of section 2.1. The emission from diamond nanocrystals is attached in the appendix.

## 2.1 Ruby nanocrystals

### 2.1.1 Introduction

Ruby consists of an alumina ($Al_2O_3$) host crystal, doped with a small concentration of chromium (Cr) ions that are responsible for the absorption and emission characteristics of ruby. Ruby was the first laser: Maiman *et al.* [121, 122] irradiated a ruby crystal coated on two parallel faces with silver using a high power flash lamp. The $Cr_2O_3$:$Al_2O_3$ composition was 0.0515 ± 0.0005 weight percent (pink ruby). A high-pulse-intensity flash tube (1.67 Joules/$cm^2$) was needed to produce stimulated emission in the ruby, yielding a narrow emission peak at 694.3 nm when the lasing threshold was achieved. The ruby laser is a three level laser scheme. Ruby has very broad excitation bands in the visible spectra (400 and 500 nm). The upper state lifetime of ruby is relatively long (3 ms), allowing for very high energy pumping. The chromium content influences the emission [123]. Recently, fluorescence from both a film of ruby [123] and ruby nanocrystals [124] have been demonstrated. Ruby

nanoparticles present new opportunities for applications in fluorescent imaging and sensing.

This section presents the preparation of ruby nanocrystals and the characteristics of the emission of ruby nanocrystals as a function of the chromium concentration, gain and scattering effects and angular dependence of the emission. However, we did not observe any spectral narrowing or spikes as a signature of random lasing from the ruby nanocrystals.

### 2.1.2 Sample preparation and experimental set up

Ruby nanocrystals were produced by crushing the bulk ruby crystal and reducing the resulting ruby powder to nanometer size using a high-energy ball milling (HEBM) method. Three types of synthetic ruby crystals with different chromium concentrations (figure 2.1) were used. Table 2.1 lists the concentration of chromium in parts per million (ppm) and the percentage of chromium to aluminium atomic ratio for the 3 types of ruby crystals used[2].

Figure 2.1 Three types of synthetic ruby crystals with different chromium concentrations: (a) Sample 1 (Dark rose), (b) Sample 2 (Rose) and (c) Sample 3 (Pink rose)

[2] The $Cr^{3+}$ doping level within the ruby crystal was measured using inductively coupled plasma mass spectrometry (ICP MS) under the supervision of Will Powell, Geochemical Evolution and Metallogeny of Continents (GEMOC) in the Department of Earth and Planetary Sciences. The ICP MS method is described in the Appendix.

Table 2.1 The concentration of chromium in parts per million and percentage of chromium to aluminium atomic ratio for different parts per million (ppm), measured by ICP MS.

| | Concentration of Chromium (ppm) | Cr:Al (%) |
|---|---|---|
| Sample 1 | 4640 | 0.88 |
| Sample 2 | 3360 | 0.63 |
| Sample 3 | 880 | 0.17 |

### 2.1.2.1 Crushing bulk ruby crystals and sieving

The bulk ruby crystal was crushed by a Hydraulic Rock press[3] for a period of several hours. The crushing process is shown in figure 2.2.

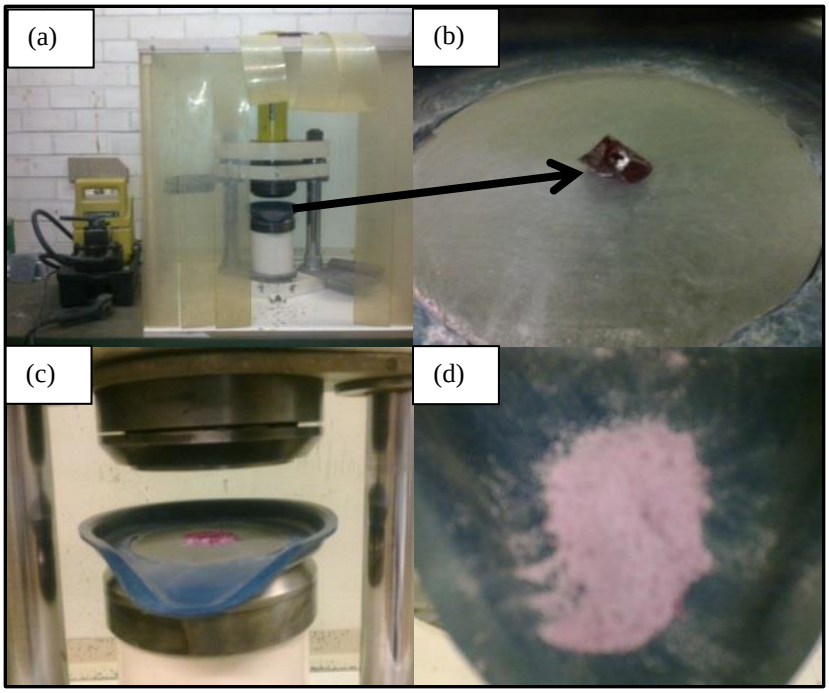


Figure 2.2 (a) Hydraulic Rock press; (b) Bulk ruby crystals on the Hydraulic Rock press plate; (c) The bulk ruby crystal was slowly pressed to crush it into powder and (d) Ruby powders after several pressings.

The bulk crystal was pressed several times to obtain ruby powder in micrometer size. The ruby powder was sieved by a 53 μm sieve (figure 2.3) before the ball milling process.

[3] The bulk ruby crystal was crushed at the Earth Science laboratory at the Department of Earth and Planetary Sciences

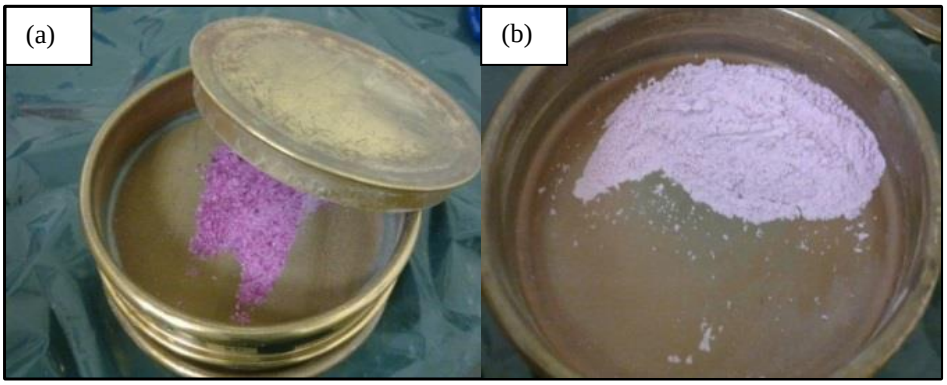


Figure 2.3 (a) Sieving by 53 µm sieve to eliminate the large ruby particles and (b) Ruby powders with < 53 µm size was used for ball milling process.

### 2.1.2.3 High-energy ball milling (HEBM) method

The high-energy ball milling method is suitable for the large-scale production of nanoscale particles [125-127] and is a low cost alternative to other approaches such as laser ablation [124], hydrothermal synthesis [128] and spray pyrolysis [129]. The ruby nanocrystals were prepared by using a Pulverisette-7 (Fritsch,Germany) high energy planetary ball mill. In this system, the starting powder particles are trapped between the inner surface of a grinding bowl and highly kinetic zirconia colliding balls which cause repeated deformation, re-welding and fragmentation of pre-mixed powders resulting in the formation of finely dispersed particles in the grain-refined matrix. Two processes affect the particle characteristics: (1) The cold welding process, which increases the average particle size of the composite and (2) The fragmentation process, which breaks up composite particles. Steady-state equilibrium is attained when a balance is achieved between these processes after a certain period of milling [125, 126].

For our experiments, 30 g of zirconium oxide ($ZrO_2$) balls (0.2 mm size) was placed into a grinding bowl with 3 g of ruby powder (< 53 µm) suspended in Milli-Q water. Wet milling produces smaller nanoparticles than dry milling and $ZrO_2$ balls

were shown to be compatible with wet milling with reduced contamination [127]. The bowl was covered by a lid and put into the milling machine. The speed of the ball milling machine was 1100 rpm, with a duty cycle consisting of 3 minutes milling time and 8 minutes cooling time. The process was repeated for 100 duty cycles. The nanocrystals were extracted by adding deionized water into the milling bowl. The bowl was shaken briefly and the colloidal ruby nanoparticles were sieved (0.08 mm metal sieve) and extracted by a syringe. In each extraction, 10 ml of deionized water was added until a clear extracted solution appeared. All operating parameters were taken from the ball milling system manual and some trial measurements. The ball milling process is shown in figure 2.4[4].

[4]The ball milling process was implemented in the Australian National Fabrication Facility (ANFF) lab

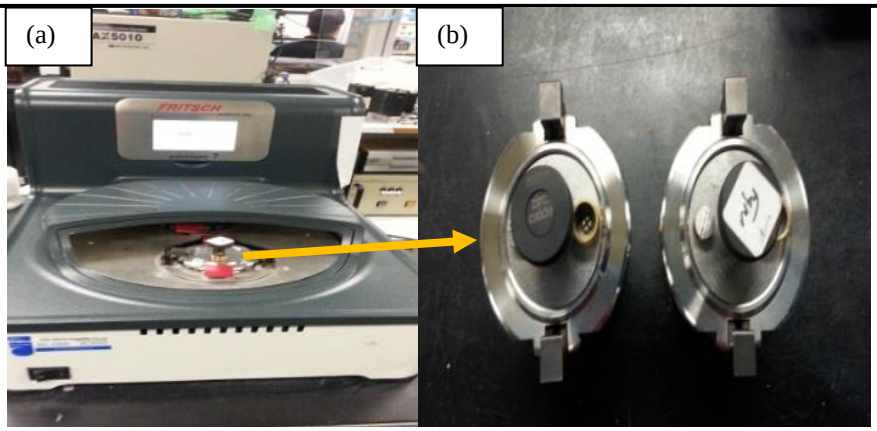


(a) A Pulverisette-7 (Fritsch,Germany) high energy planetary ball mill; (b) Two milling bowls were used to prepare two samples for each milling

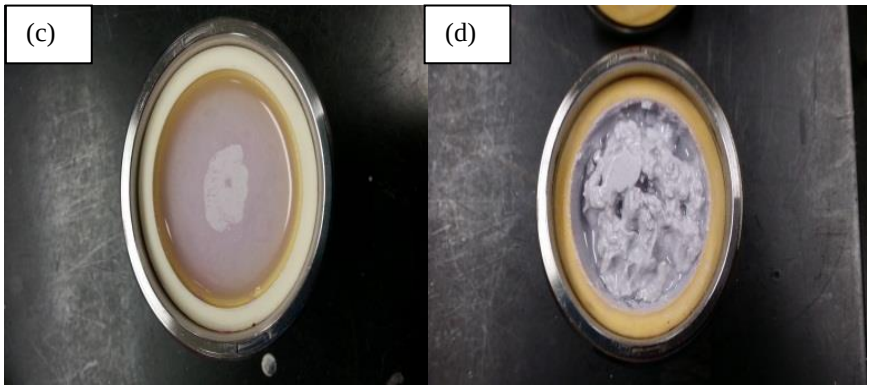


(c) 30 g of $ZrO_2$ balls with 3 g ruby powder were suspended in water before milling; (d) Ruby and $ZrO_2$ paste after milling.

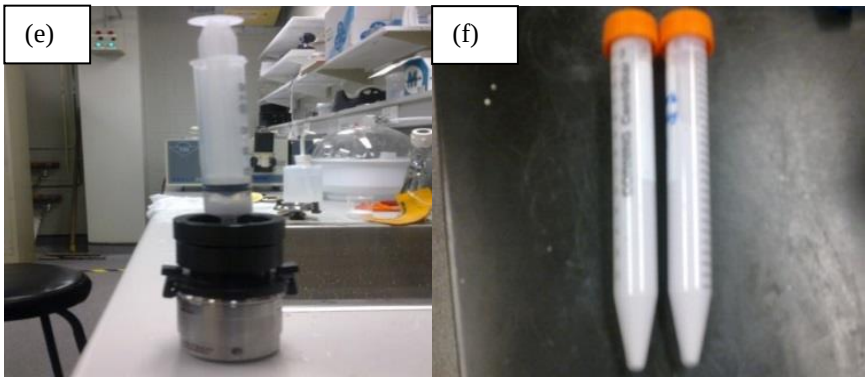


(e) Extraction process by a syringe; (f) Ruby nanocrystals after the extraction

Figure 2.4 Ball milling process

### 2.1.2.4 Characterization of ruby nanocrystals

Slight $ZrO_2$ contamination appeared in each sample due to ball erosion resulting from collisions with the ruby powder. Energy-Dispersive X-ray Spectroscopy (EDS)[5] showed the $ZrO_2$ contamination in the colloidal ruby nanocrystals was found to be ~ 5% for each sample (figure 2.5), resulting in similar scattering effects in each sample. EDS is an analytical technique used to characterize and analyse chemical elements of a sample. Here, EDS was implemented using an X-Ray spectroscopy detector JED-2300 (JEOL Ltd, Japan). A few drops of colloidal ruby nanocrystals were dried on a clean glass coverslip and transferred onto a sticky carbon stub. A blower removed excess sample grains from the carbon stub to avoid contamination of the EDS vacuum chamber during measurements.

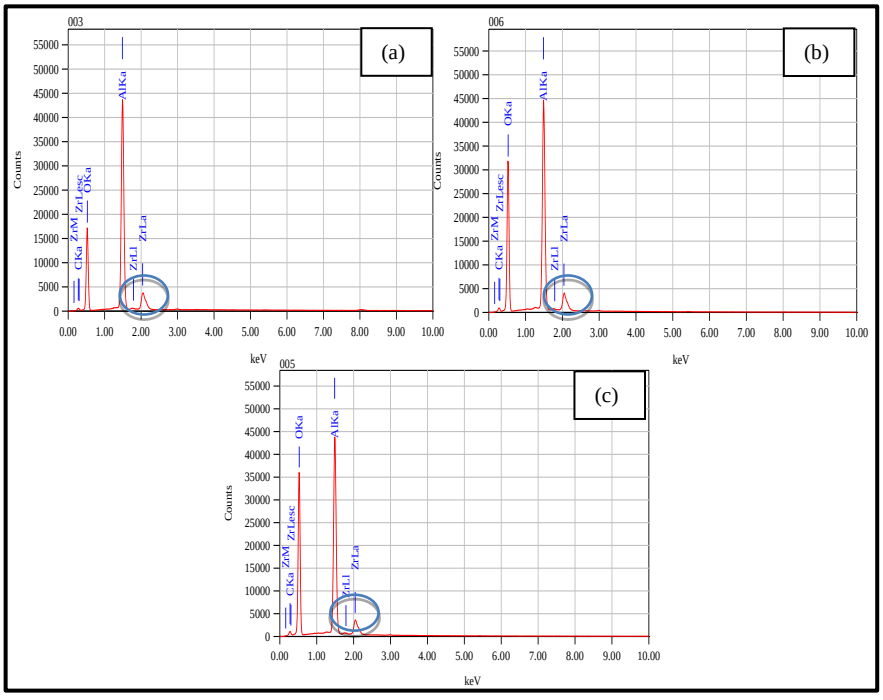


Figure 2.5 EDS analysis of (a) Sample 1 (Dark Rose), (b) Sample 2 (Rose) and (c) Sample 3 (Pink Rose). The $ZrO_2$ contamination is indicated by the blue circles.

[5]The EDS was done in the Microscopy Lab, after training by Debra Birch.

Transmission electron microscope (TEM) images (figure 2.6) suggest that the $ZrO_2$ particles are similar in size distribution to the ruby nanocrystals. The TEM[6] was obtained using a transmission electron microscope (Philips CM10 with Olympus SIS Megaview G2 Digital Camera, resolution ~ 1376 × 1032 pixels) at an accelerating voltage of 100 kV. The samples were prepared by dropping the diluted colloidal ruby nanocrystals on the surface of a copper grid and drying in vacuum.

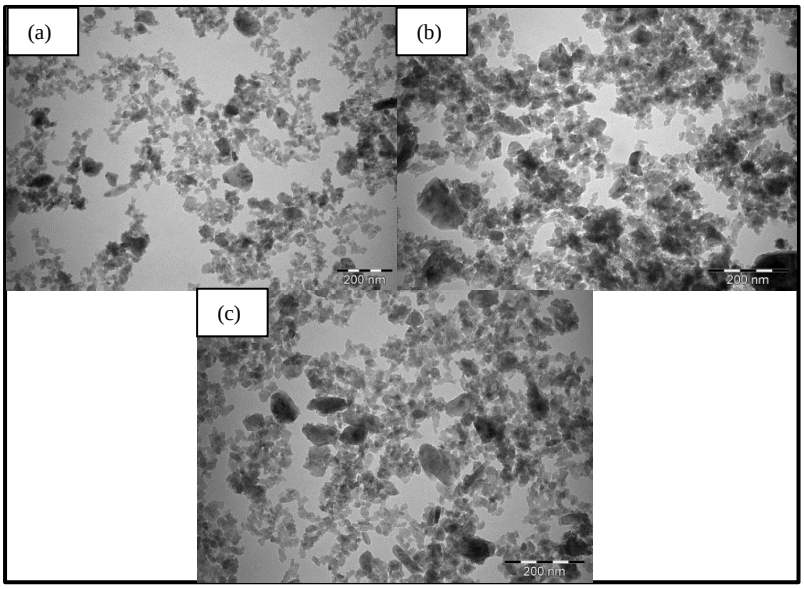


Figure 2.6 Transmission electron microscope (TEM) images of (a) Sample 1 (Dark Rose), (b) Sample 2 (Rose) and (c) Sample 3 (Pink Rose) with slight contamination from $ZrO_2$ balls. The $ZrO_2$ particles are similar in size distribution to the ruby nanocrystals and cannot be differentiated in the TEM image. The scale bar is 200 nm.

The colloidal solution was ultrasonically dispersed for 10 minutes to break up aggregated particles. Subsequently, the solution was centrifuged using an Eppendorf Mini-Spin micro-centrifuge at 500 rcf (relative centrifugal force) for 5 minutes and the supernatant was extracted for the optics experiments. The particle size in the supernatant was checked using a Zetasizer Nano ZSP (Malvern Instruments Ltd). The

[6] The TEM was done in the Microscopy Lab, after training by Nicole Vella.

Zetasizer uses dynamic light scattering (DLS) to determine the hydrodynamic diameter and polydispersity index of the ruby nanoparticles [130]. The colloidal ruby nanocrystals were diluted (100×) in aqueous solution, ultrasonically dispersed for 3 minutes and transferred to a plastic cuvette before the measurement. The average diameter of the ruby nanocrystals was estimated ~ 100 ± 15 nm based on DLS.

To estimate the number density of scatterers, the supernatant solution was centrifuged again at the highest speed (14.1 krcf) and the sediment was dried at room temperature. The dried ruby nanocrystals were weighed and mixed with Milli-Q water. The sample was ultrasonically treated for 10 minutes to prevent particle flocculation and aggregation just before the measurement. The suspensions had a ruby nanocrystal concentration (including $ZrO_2$) of 0.06 g/cm$^3$. The number density of scatterers was calculated to be in the range $2 \times 10^{13}$ to $5 \times 10^{13}$ cm$^{-3}$.

The transport mean free path, $l_t$ ~ 115 μm was estimated from eq. (1.12) in Chapter 1 ($\theta_w \approx \frac{\lambda}{\sqrt{2} l_t}$, where $\theta_w$ is the width of backscattering cone, $\lambda$ is the wavelength of HeNe laser and $l_t$ is the transport mean free path) using a standard coherent backscattering (CBS) experiment [44, 46, 131] as shown in figure 2.7. $\theta_w$ can be determined from the full width at half maximum (FWHM) of the emission intensity (figure 2.8). A collimated beam from a continuous wave (CW) HeNe Laser illuminated the ruby nanocrystal solution in a cuvette. The scattered light from the front of the cuvette was captured by a CCD camera and the image was analysed to obtain the coherent backscattering cone as shown in figure 2.8.

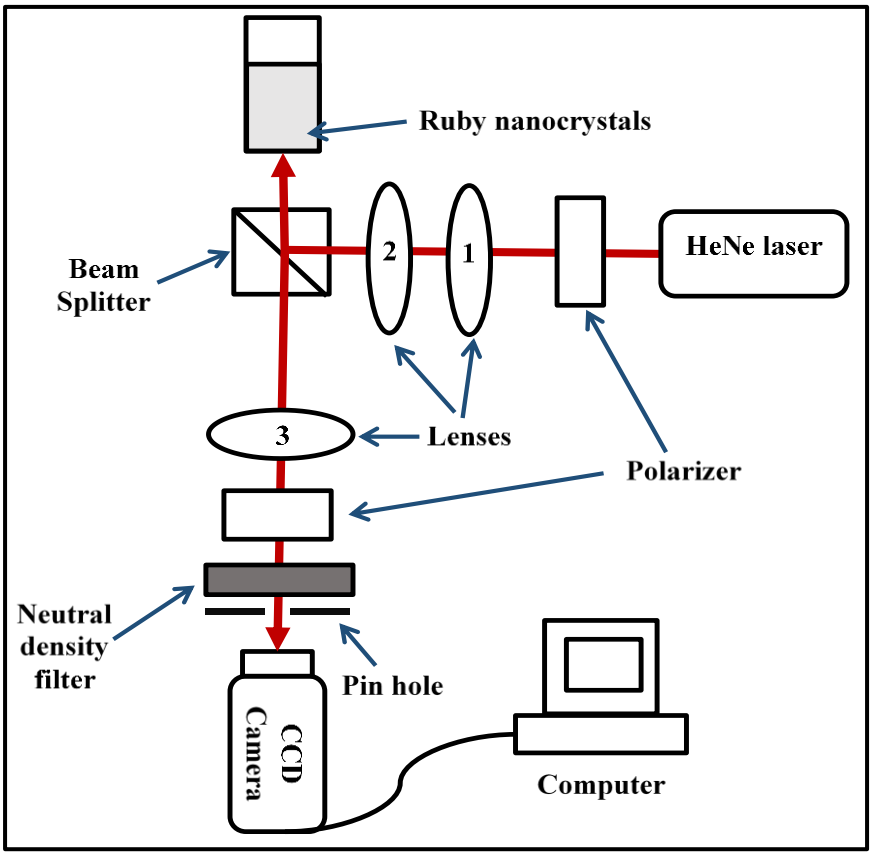


Figure 2.7 Coherent Backscattering (CBS) experiment based on [44, 46, 131]. Lenses ($f_1$ ~ 25.4 mm, $f_2$ ~ 100 mm, $f_3$ ~ 450 mm) were used and the distance from the CCD camera to the sample was 1000 mm and the CCD camera (DCC 1545 M, Thorlab) has a pixel size ~ 0.264 mm.

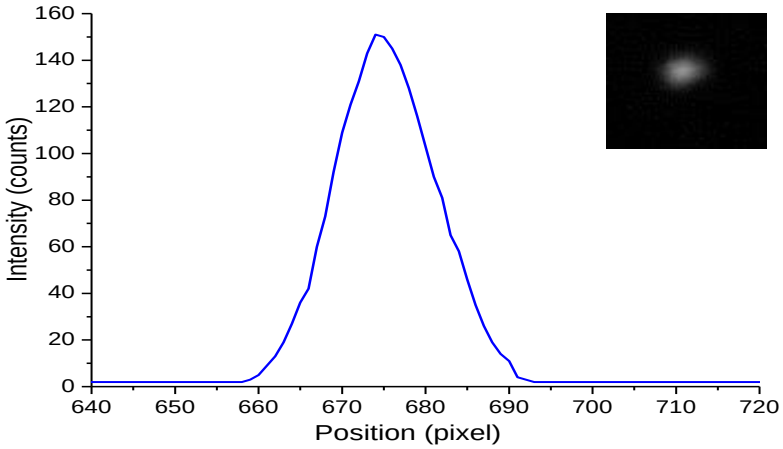


Figure 2.8 Coherent backscattering cone and the captured image (inset). Width of backscattering cone, $\theta_w$ ~ FWHM of the intensity graph / distance between the camera and the sample. The transport mean free path, $l_t$ measured from a CBS experiment is comparable with the scattering mean free path, $l_s$ calculated based on eq. (1.8).

#### 2.1.2.5 Optical measurements

The excitation of the ruby nanocrystal suspensions was performed using a Q-switched frequency-doubled Nd:YAG laser (532 nm, 4 ns, 10 Hz) aligned at 45$^{o}$ from the normal to the front face of a (1 cm × 1 cm) quartz cuvette. A fixed polarizer and rotatable half wave-plate were used to vary the laser excitation energy. A focusing lens with $f$ = 10 cm was used to focus the excitation energy into the ruby suspension with a pump spot diameter of 2 mm at the front face of the cuvette. The emission spectrum was measured by a fibre-coupled spectrometer (Ocean Optics USB2000+UV-VS-ES or Ocean Optics Maya 2000 Pro), which collected and displayed the emission spectra with a resolution of ~ 1 nm. The emission light from the front of the cuvette was collected by a lens ($f$ = 5 cm), 30$^{o}$ to the normal at the front of the cuvette and the emission intensity was collected for a single pulse unless otherwise stated and filtered by a 532 nm edge filter to prevent the pump light from entering the spectrometer. The excitation and fluorescence of active nanoparticles were measured by a Fluorolog spectrofluorometer (Horiba Jobin Yvon) with excitation $\lambda$ of 530 nm. Other optics experiments are explained in the later sections.

### 2.1.3 Results and discussion

The emission intensity, linewidth, variable gain and scattering effects and angular dependence of the emission of colloidal ruby nanocrystals were characterized. The nanocrystals fluoresce under green excitation and the emission spectrum of the ruby nanocrystals has an emission peak at ~ 693.1 nm, shown in figure 2.9. The optimum excitation wavelengths for the ruby nanocrystals are 405 nm and 550 nm.

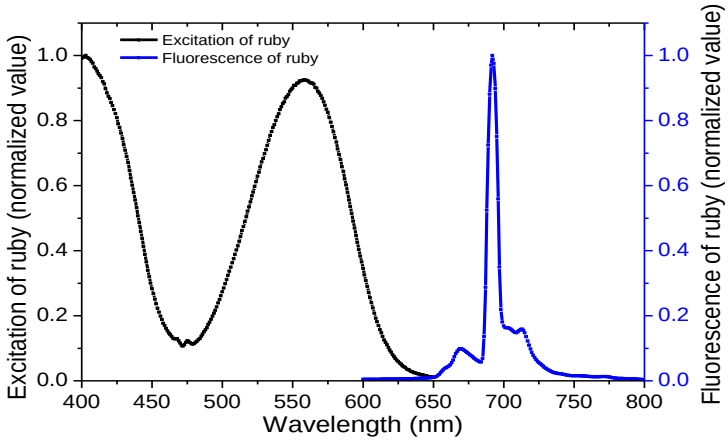


Figure 2.9 Excitation and emission spectra of ruby nanocrystals (sample 1). The sample was measured using a Fluorolog spectrofluorometer (1 nm spectral resolution).

### 2.1.3.1 Low resolution measurement of emission spectra

The emission spectra from the optics experiments for low resolution measurement (Ocean Optics USB2000, ~ 1 nm resolution) for all three samples of ruby nanocrystals are shown in figure 2.10. The figure shows that the emission peak intensity increases when more energy is introduced into the sample. Samples with a higher chromium concentration produce higher emission peak intensity due to increased light absorption. The results are consistent with those of Atakan *et al.* [123] who showed bulk ruby emission intensity reached a maximum value when the chromium concentration was increased to a Cr : Al ratio of order 1.1 %, and it decreased for a Cr : Al ratio above 3.6 %. The emission linewidth and emission peak wavelength remain the same for each excitation energy density in each sample. Atakan *et al.* [123] observed slight emission peak shifts (blue shifted ~ 0.4 nm) when the Cr:Al ratio ranged from 2-7%, but this is a significantly higher chromium concentration than our samples.

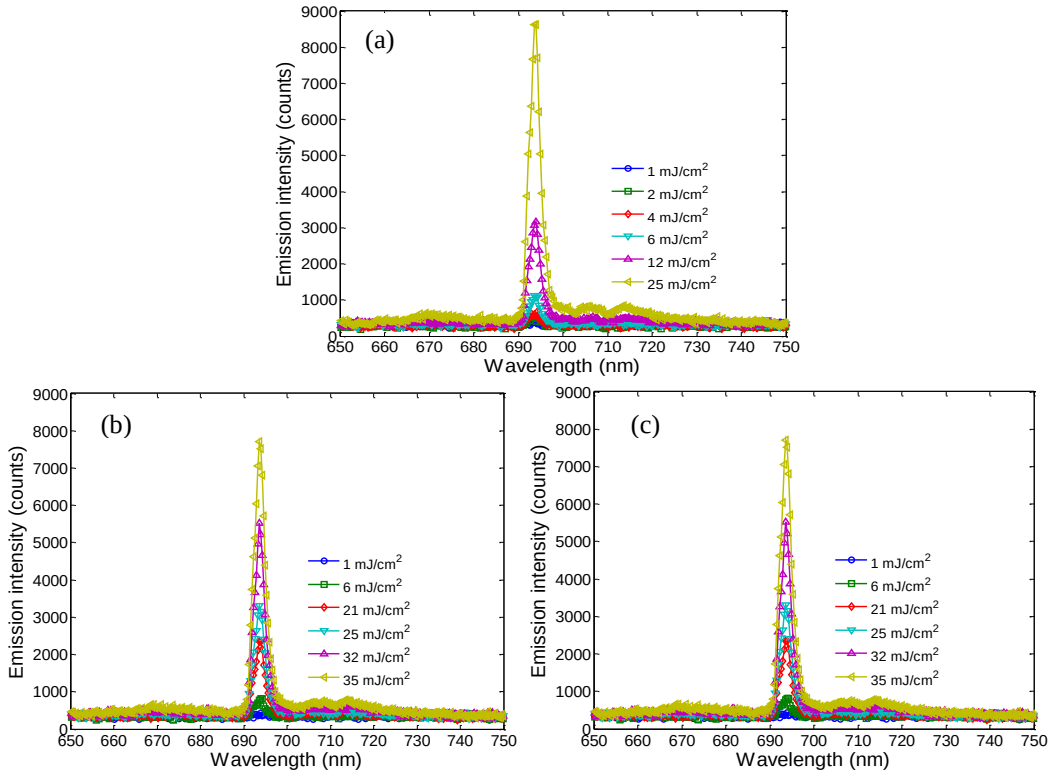


Figure 2.10 Emission spectra (raw data) from colloidal ruby nanocrystals for different samples; (a) Sample 1 (Dark Rose), (b) Sample 2 (Rose) and (c) Sample 3 (Pink Rose) excited by Nd:YAG pulsed laser. Higher excitation energy density gives higher emission and the spectral shape is maintained.

The emission spectra for sample 1 were averaged for 10 seconds to increase signal-to-noise ratio, the background was subtracted and the resulting spectra are plotted in figure 2.11.

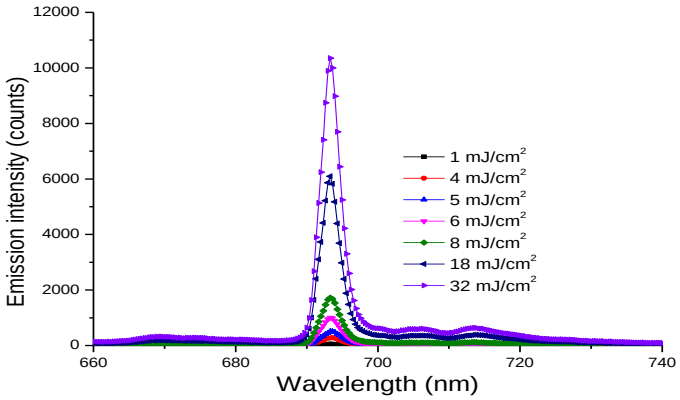


Figure 2.11 Emission spectra (averaged for 10 seconds with higher integration time and processed data) from colloidal ruby nanocrystals (sample 1) when the excitation energy density was increased. The background was subtracted and the emission spectra were averaged for 10 second. The emission linewidth (~ 3nm) remains the same for each excitation energy density.

The directional dependence of the emission was studied by varying the collection angle of the light from $0^o$ to $90^o$ to the normal of the front face of the cuvette. The distance from the front of the cuvette to the fibre input to the spectrometer was fixed at 6 cm. The emission peak intensity of the light from the colloidal ruby nanocrystals as a function of observation angle is plotted in figure 2.12. Figure 2.12 (a) shows that, as the angle of light collection increases, the emission peak intensity reduces gradually. The decrease in the emission intensity at larger angles is due to the light's longer optical path length within the excited pump volume. Greater amplification is achieved if the light experiences a shorter optical path length within the low excitation energy region and longer optical path length within the high excitation energy volume [132]. The emission spectra at different observation angles (for fixed energy excitation density) are shown in figure 2.12 (b), indicating that the spectral features of the emission are preserved regardless of the angle of observation. Thus, the light is uniformly amplified in the excitation volume [132]. No random lasing occurred in any samples as we did not observe spectral narrowing when the pump energy density was increased. This is due to the three level laser scheme of ruby, in which there is a large ground state absorption at the emission wavelength.

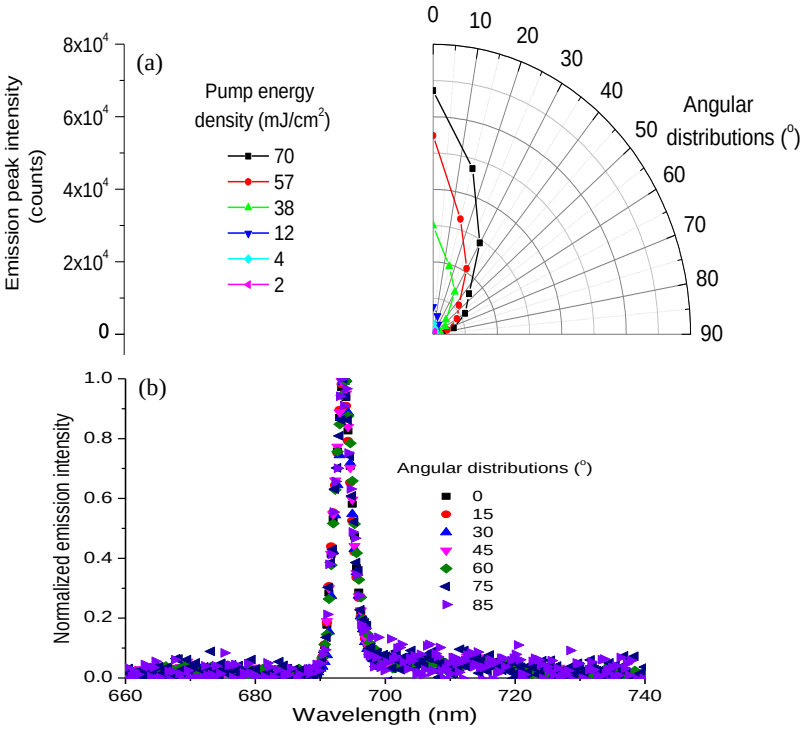


Figure 2.12 (a) Emission peak intensity versus angle distribution from normal to the front face of the cuvette for colloidal ruby nanocrystals (sample 1). The emission peak intensity reduces when the angle increases from normal; (b) Emission spectra of colloidal ruby nanocrystals for different angular distributions from normal to the front face of the cuvette, pumped with a fixed energy density 38 mJ/cm$^2$ for colloidal ruby nanocrystals (sample 1).

*2.1.3.1.1 Emission spectra of ruby nanocrystals with alumina and gold nanoparticles*

The ruby nanocrystal emission spectra were characterized in terms of scattering and gain by adding various concentrations of alumina (average diameter ~ 150 nm, Sigma Aldrich) or gold nanoparticles (average diameter ~ 60 nm, Ted Pella) to the fixed concentration of colloidal ruby nanocrystals. In this analysis, ruby nanocrystals with a concentration of 0.001 g/cm$^3$ (the number density of scatterers was estimated as $5 \times 10^{11}$ cm$^{-3}$ using an average particle diameter, 100 nm) were mixed with different concentrations of alumina ($3.3 \times 10^{10}$ to $9.9 \times 10^{13}$ cm$^{-3}$) or gold nanoparticles ($3 \times 10^{8}$ to $2 \times 10^{11}$ cm$^{-3}$) in an aqueous solution forming 1 ml of solution. All concentrations are quoted as final concentration in the random laser sample. 0.05 g of polyvinyl alcohol (PVA) was dissolved in the solution at 80 $^{o}$C. Then, the final solution was

dropped on a glass substrate (area ~ 4 cm × 2 cm) and dried at room temperature for 24 hours. The film thickness, ~ 50 µm was uniform as measured by an Alphastep 500 profiler (KLA Tencor). PVA was used in order to produce a viscous solution and prevent particle sedimentation after several hours. The dried sample was excited by single pulse pumping without using a focusing lens to avoid sample damage and the emission light was collected by the same spectrometer. The extinction / absorption spectra of the films containing gold and alumina nanoparticles are shown in figure 2.13.

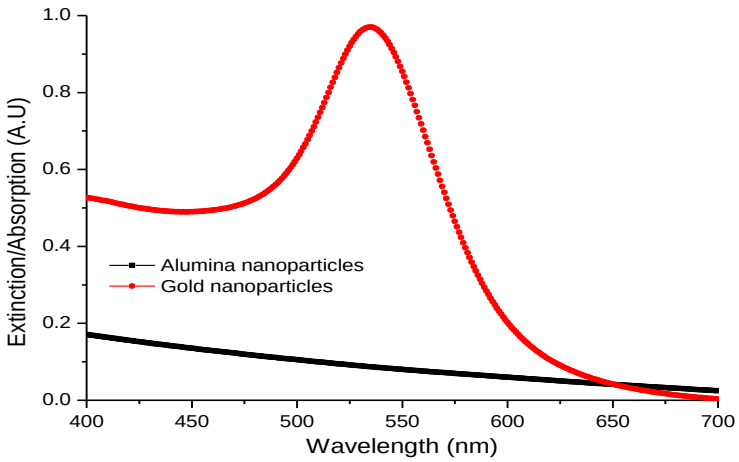


Figure 2.13 Extinction / Absorption spectra of gold nanoparticles (60 nm) and alumina nanoparticles (150 nm) in a PVA film measured by a Cary spectrophotometer. Gold nanoparticles absorb green light while alumina nanoparticles do not absorb visible light.

The alumina nanoparticles are elastic scatterers (minimal light absorption) whereas the gold nanoparticles absorb green light. Figure 2.14 shows the emission peak intensity for various concentrations of alumina with a fixed concentration of ruby nanocrystals for three different excitation energy densities. The emission intensity increases when more alumina is added until it reaches the optimum value at ~ $1.3 \times 10^{13}$ $cm^{-3}$ of alumina. Alumina nanoparticles act as scatterers that scatter the light inside the samples. Stronger scattering confines the pump light within the ruby-doped film resulting in higher emission intensity. Fluorescence emission enhancement from

gallium arsenide (GaAs) powder was observed when alumina was added [88] and Deng *et al.* [133] also claimed that high scattering efficiency of fluorophores can promote fluorescence emission enhancement. However, excessive scatterers prevent efficient absorption of pump light since the pump light is scattered out of the excited area. So, excessive alumina decreases the emission intensity as shown in figure 2.14.

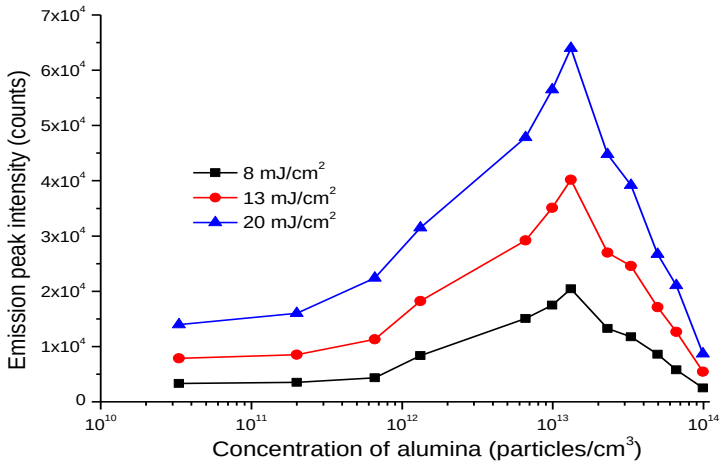


Figure 2.14 Emission peak intensity versus various concentrations of alumina for different excitation energy densities. The emission peak intensity increases with alumina concentration until it reaches the maximum value at ~ $1.3 \times 10^{13}$ $cm^{-3}$. Above this concentration, the emission decreases gradually.

Figure 2.15 shows the effect of mixing various concentrations of gold nanoparticles with ruby nanocrystals. The emission intensity increased gradually when more gold was added with a maximum value at $7 \times 10^{9}$ $cm^{-3}$ gold concentration. Addition of gold nanoparticles increases the light scattering and absorption concurrently leading to light confinement near the gold nanoparticles' surface. Gold nanoparticles localize the excitation light due to their surface plasmon resonance at 530 nm, resulting in increased pump light absorption and producing high emission intensity. Thus, the ruby nanocrystals reach the optimum emission intensity with a lower concentration of gold nanoparticles than of alumina. The emission peak intensity gradually drops with additional gold due to higher absorption losses. The

effects of metal nanoparticles on the emission of dyes [12, 14], quantum dots [134] and nanodiamonds [135] are consistent with our observations of the enhancement of nanoruby emission.

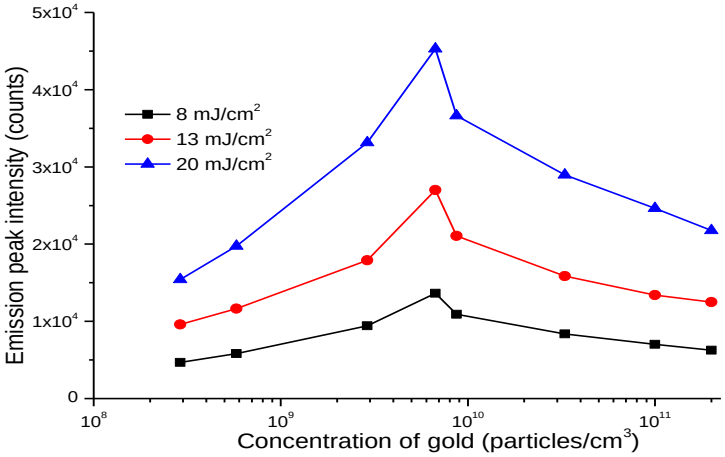


Figure 2.15 Emission peak intensity versus various concentrations of gold for different excitation energy densities. The emission peak intensity increases with the gold concentration to the maximum value at ~ $7 \times 10^9$ $cm^{-3}$, then decreases gradually.

### 2.1.3.2 High resolution measurement of emission spectra

The ruby nanocrystal emission spectra were also measured by a high resolution spectrometer (Ocean Optics Maya 2000 Pro, 0.4 nm resolution) to resolve the double emission peaks characteristic of ruby nanocrystals. The emission spectra were averaged for 10 seconds to increase the signal-to-noise ratio and reduce fluctuations. In this experiment, the ruby nanocrystals were placed in a quartz cuvette (1 cm × 1 cm). Figure 2.16 shows the emission spectra from colloidal ruby nanocrystals ($3 \times 10^{13}$ $cm^{-3}$) (Sample 1, Cr:Al:0.88%), measured by the Ocean Optics Maya 2000 Pro. There are two emission peaks at $R_1$ ~ 694.5 nm and $R_2$ ~ 693.1 nm as shown in figure 2.16 whereas only one peak at 693.1 nm is resolved by the Ocean Optics USB2000. The emission intensity increases linearly when higher excitation energy density is used. In figure 2.16, we observe a dip at $\lambda$ ~ 695.2 nm for the emission spectrum

excited by a low pump energy density (8 mJ/cm$^2$). We attribute it to noise as the dip is gone when the pump energy density increases.

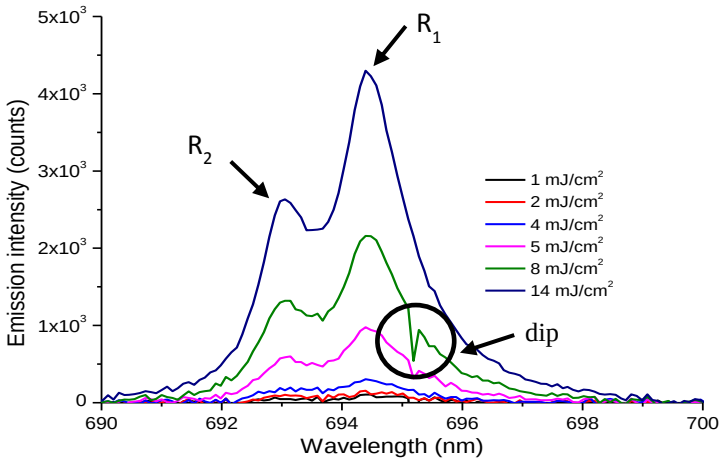


Figure 2.16 Emission spectra from colloidal ruby nanocrystals (Sample 1, Cr:Al:0.88%) versus wavelength for different excitation energy densities. Higher pump energy density gives higher emission. Two emission peaks ($R_1 \sim 694.5$ nm and $R_2 \sim 693.1$ nm) (shown by black arrows) are resolved using the Ocean Optics Maya 2000 Pro. A dip can be seen at $\lambda \sim 695.2$ nm as shown in the circle.

The emission spectra for low and high excitation energy densities are normalized, shown in figure 2.17 to observe any spectral changes. From that figure, we can see that both emission spectra resemble each other except that the emission spectrum for low excitation is quite noisy.

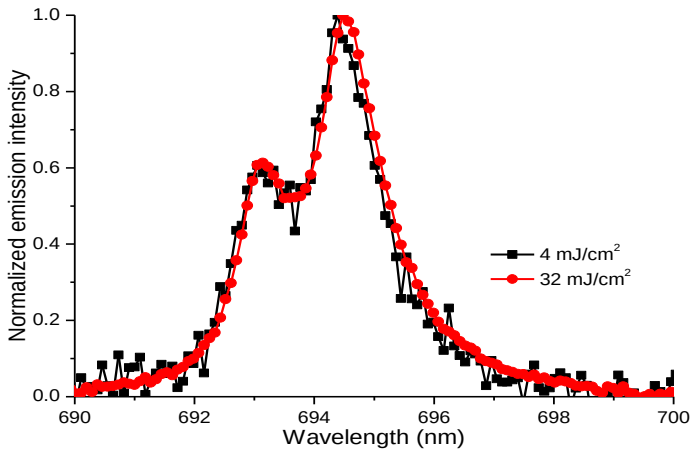


Figure 2.17 Normalized emission spectra versus wavelength of colloidal ruby nanocrystals (Sample 1, Cr:Al:0.88%) for different excitation energy densities (low and high excitation). The emission spectra have the same intensity ratio for both cases.

The emission spectra for all samples of ruby nanocrystals are compared in figure 2.18. The emission peak wavelengths and power ratios for the $R_1$ and $R_2$ peaks are similar for each sample. Small shifts in the emission peak wavelength can occur due to different chromium concentrations [123] but in the present system, we did not observe any wavelength changes.

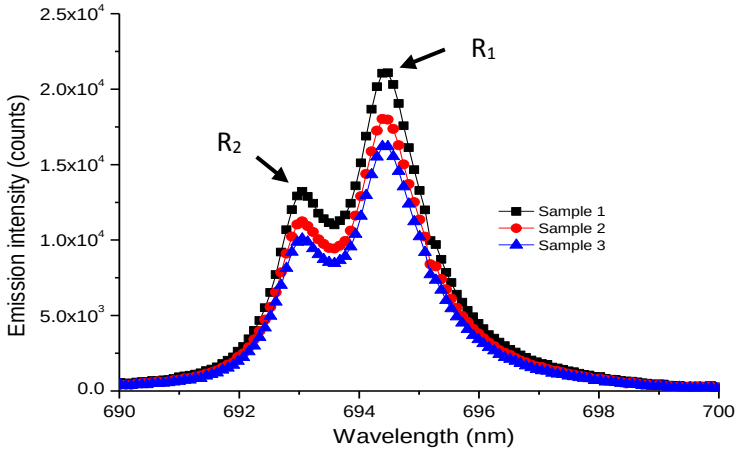


Figure 2.18 Emission spectra of 3 different samples of ruby nanocrystals pumped with similar excitation energy density measured by high resolution Maya 2000 Pro (0.4 nm resolution). The emission peak wavelengths and power ratios for both $R_1$ and $R_2$ (shown by black arrows) are constant in all samples.

Another Nd:YAG nanosecond-pulsewidth laser (Surelite Continuum laser, 532 nm, 10 Hz, 4 ns, maximum energy of 200 mJ, pump diameter of 7 mm) was used to compare the emission spectra with the previous lower energy pump laser (Minilite Continuum laser, 532 nm, 10 Hz, 4 ns, maximum energy of 12 mJ, pump diameter of 3 mm). Figure 2.19 shows the comparison of emission spectra from ruby nanocrystals (sample 1) pumped by two different nanosecond-pulsewidth lasers. The spectra are very consistent except the baseline for the emission spectrum excited by the Surelite pump laser is slightly off, possibly due to the large excitation spot size (7 mm).

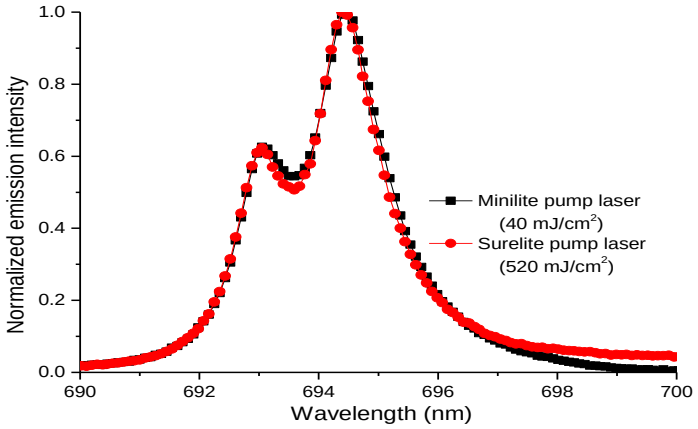


Figure 2.19 Normalized emission spectra of ruby nanocrystals (Sample 1, Cr:Al: 0.88%) for different nanosecond-pulsewidth pump laser versus wavelength. The spectral shape does not show any obvious changes.

From figures 2.16 to 2.19, it is clear that ruby nanocrystals can emit at two wavelengths ($R_1$ ~ 694.5 nm and $R_2$ ~ 693.1 nm). As reported in [121], the signature of lasing from a ruby crystal was when $R_1$ increased and narrowed and $R_2$ stopped increasing. However, we use ruby nanocrystals instead of bulk ruby crystals. Ruby is a three level system that requires higher excitation densities, otherwise the laser suffers high losses due to ground state absorption [33]. Considering figures 2.16 to 2.19, the emission intensity of $R_1$ is always higher than $R_2$ and their ratio is consistently ~ 0.4. Therefore, we determine that lasing was not observed from any nanoruby samples as the power ratio of $R_1$ and $R_2$ was consistently ~ 0.4. Random lasing was also not observed in ruby powder (results are not shown).

### 2.1.3.3 Analysis of emission from ruby nanocrystals

Koechner [136] studied the laser properties of bulk crystalline ruby incorporating 0.05 % chromium ions ($Cr^{3+}$). In this crystal, the population inversion can be achieved by pumping $Cr^{3+}$ optically. Ruby fluoresces on the $R_1$ and $R_2$ lines (as shown in figure 2.16) but the $R_1$ line lases before the $R_2$ line due to its higher population inversion [136]. The energy per unit volume which can be extracted from

the inverted ruby depends on the energy level populations, $n_2$ ($R_1$) and $n_2$ ($R_2$), provided that the pulse duration is sufficiently long for these two levels to remain in thermal equilibrium [136]. Then, the maximum energy for a complete inversion, $E_{ex(max)}$ can be calculated based on [136];

$$E_{ex(max)} = \frac{2h\nu n_{tot}}{3+K} \quad (2.1)$$

where $K$ (Boltzmann factor) = 0.87, $h$ (Planck's constant) = $6.6 \times 10^{-34}$ Js and $\nu$ (pump laser frequency) = $5.6 \times 10^{14}$ $s^{-1}$ and the $Cr^{3+}$ concentration of $n_{tot}$ ~ $1.58 \times 10^{19}$ $cm^{-3}$ for 0.05 % of $Cr^{3+}$ in bulk ruby crystals. Koechner [136] obtained the maximum gain coefficient, $g_{0(\max)}$, for complete inversion in a 0.05% Cr-doped rod as 0.2145 $cm^{-1}$ from;

$$g_{0(max)} = \frac{\sigma_{21} n_{tot}}{K+1} \quad (2.2)$$

where $\sigma_{21}$ is the stimulated emission cross section in ruby (~ $2.5 \times 10^{-20}$ $cm^2$). Laser action on the $R_2$ line can be achieved in ruby by using dielectrically coated resonator mirrors which have a higher transmission (increased loss) on the $R_1$ than the $R_2$ lines [136]. Therefore, the absorbed pump energy required to reach threshold, $E_{ab}$ can be calculated as [136];

$$E_{ab} \approx \frac{n_{tot} h \nu_p}{2 n_Q} \quad (2.3)$$

where $\nu_p$ (average frequency of the two main pump bands) = $6.25 \times 10^{14}$ $s^{-1}$ and $n_Q$ (quantum efficiency in ruby) ≈ 0.70.

To understand the experimental results, we considered the available gain from ruby nanocrystal-based random lasers by calculating $g_{0(\max)}$, $E_{ex(max)}$ and $E_{ab}$ using the approach of ref. [136]. Though Koechner [136] analyses the laser properties of a bulk ruby crystal, the model is still valid for ruby nanocrystals. Our experiments were

conducted at room temperature, which gives *K* (Boltzmann factor) = 0.87 [136] and in this experiment, the fraction of the ruby crystals in the ruby /zirconia mixture is 80%. We estimate the $n_{tot}$ for $Cr^{3+}$ of Sample 1, ~ $2.8 \times 10^{20}$ $cm^{-3}$ which gives $n_{tot}$ for ruby nanocrystals, ~ $3.6 \times 10^{18}$ $cm^{-3}$ (the average diameter and concentration of ruby nanoparticles are ~ 100 nm and ~ $3 \times 10^{13}$ $cm^{-3}$ respectively). $g_{0(\max)}$ for 0.05% Cr-doped rod is ~ 0.215 $cm^{-1}$ [136] whereas in our system, $g_{0(\max)}$ for 0.88% Cr-doped ruby nanocryatals is much smaller, ~ 0.05 $cm^{-1}$. We are unable to estimate the losses due to scattering and self-absorption in the ruby nanocrystals and we are not aware of any laser loss estimation from other studies of active scatterer-based random lasers. The $E_{ex(max)}$ and $E_{ab}$ for the 0.88 % Cr-doped ruby nanocrystals are estimated as ~ 0.7 $J/cm^3$ and ~ 1.1 $J/cm^3$. The maximum pump energy per unit volume used in our system is 0.5 $J/cm^3$, which is smaller than the $E_{ex(max)}$ and $E_{ab}$ estimated values. Therefore, the system is unlikely to be able to reach a population inversion. We did not observe lasing from the ruby nanocrystal solutions due to insufficient pump energy and resulting gain provided to the system.

Ruby crystal has a typical chromium concentration of $1.6 \times 10^{19}$ $atoms/cm^3$ and has a stimulated emission cross-section of $2.5 \times 10^{-20}$ $cm^2$ [136], whereas Rhodamine 6G (an efficient laser dye) with a typical concentration of $1 \times 10^{-3}$ M, or $6 \times 10^{17}$ $molecules/cm^3$, has a stimulated emission cross-section of $2 \times 10^{-16}$ $cm^2$ [8], so the available gain is higher for Rhodamine 6G dye compared to ruby. In addition, the losses in ruby due to its 3-level laser scheme create an additional challenge. Of course there are also likely to be surface states which may affect the lasing emission efficiency of the chromium ions on the surface of the ruby nanocrystals, and there are also losses of both pump and laser emission due to scattering from the nanocrystals.

## 2.2 Zinc oxide nanoparticles and nanorods

### 2.2.1 Introduction

Zinc oxide (ZnO) is useful in many applications such as fingerprint detection [137], optically targeted imaging of cancer cells [138] and as a laser source [139]. ZnO has a wide band-gap (3.37 eV) and high excitation binding energy (~ 60 meV) [139] which provides light amplification for emission and laser action.

In this section, we investigated the probability of random lasing from ZnO nanoparticles and ZnO nanorods. ZnO nanorods have better light confinement than ZnO nanoparticles [140]. We obtained broad emission spectra from both ZnO nanoparticles and nanorods which do not suggest random laser operation.

$1 \times 10^{12}$ $cm^{-3}$ of ZnO nanoparticles in deionized water was placed into a cuvette (1 cm × 1 cm) for laser excitation. To study the effect of plasmonics on emission of ZnO, $3 \times 10^{9}$ to $3 \times 10^{11}$ $cm^{-3}$ of silver nanoparticles (~ 60 nm, Sigma Aldrich) was mixed with a fixed concentration of ZnO nanoparticles ($1 \times 10^{12}$ $cm^{-3}$) in aqueous solution.

### 2.2.2 Synthesis and characterization of ZnO nanorods

The ZnO nanorods were prepared by a modified literature technique [141, 142] based on chemical bath deposition that consisted of spin-coating ZnO film seeds on a clean glass substrate. An air blower was used to remove dust / particles on the glass substrate before cleaning with ethanol and drying in an oven. The nanorods were grown on the ZnO film seeds [141, 142]. ZnO in ref. [141] was prepared by a sol-gel reaction but we used commercial ZnO nanoparticles (average diameter ~ 100 nm, Sigma Aldrich) to facilitate the sample preparation. To prepare the ZnO film seeds,

500 µl of ZnO nanoparticles in aqueous solution ($1 \times 10^{12}$ $cm^{-3}$) were spin-coated (first step at 500 rpm for 5 seconds and the second step at 3000 rpm for 30 seconds) on the glass substrate. The substrate was heated at 130 $^{o}$C for 5 minutes to evaporate the solvent. This process was repeated for five times to produce uniform coverage of ZnO seeds. To grow the ZnO nanorods, 0.025 M of zinc nitrate hexahydrate (ZNH) [$Zn(NO_3)_2.6H_2O$] was mixed with 0.0025 M of hexamethylenetetramine (HMT) [$C_6H_2N_4$] in 200 ml deionized water. The ZNH acts as a $Zn^{2+}$ ion source and the HMT acts as a pH buffer in the solution. The solution was heated and stirred with a magnetic stirrer at 90 to 95 $^{o}$C for 60 minutes to dissolve the ZNH and HMT. After stirring, the ZnO film seeds were submerged into the solution for the growth process. Three samples of ZnO nanorods were prepared by varying the growth chemical reaction time for 20, 60 and 90 minutes. Different lengths of ZnO nanorods can be produced by varying the chemical reaction times during the growth process [141]. The chemical reactions of the growth process can be expressed as [142];

$$(CH_2)_6N_4 + 6H_2O \rightarrow 6HCHO + 4NH_3 \quad (2.4)$$

$$NH_4^+ + OH^- \leftrightarrow NH_3 + H_2O \quad (2.5)$$

$$Zn^{2+} + 2OH^- \rightarrow Zn(OH)_2 \quad (2.6)$$

$$Zn(OH)_2 \rightarrow ZnO + H_2O \quad (2.7)$$

The ZnO nanorod films were rinsed with deionized water to remove residual salt on the surface and then dried in an oven at 90 °C for 5 minutes. A thin layer of PMMA was spin coated (2000 rpm for 30 seconds) on top of the ZnO nanorods to fill the free spaces between the nanorods to protect and stabilize them.

A similar optics experiment to that for ruby (see Chapter 2, section 2.1.2.5) was used except the samples were excited with a Q-switched Nd:YAG frequency-

tripled nanosecond-pulsewidth laser ( 355 nm, 10 Hz and 8 ns) instead of the Nd:YAG green laser. A focusing lens ($f$ = 10 cm) focused the pump light into the sample in the cuvette but no focusing lens was used for the ZnO nanorod films to prevent any sample damage. The thickness of the ZnO nanorod sample was ~ 500 nm, as measured by an Alphastep 500 profiler (KLA Tencor). The morphology and size of the ZnO nanorods were observed by field scanning electron microscopy (FE-SEM) using an electron microscope, JEOL 6480LV (JEOL Ltd, Japan). The ZnO nanorods were coated with a gold layer to avoid image charging. The SEM images of the ZnO seed layer and ZnO nanorods are shown in figures 2.20 and 2.21. Figure 2.20 shows that the ZnO nanoparticles are scattered and aggregated on the glass substrate with varied sizes and shapes.

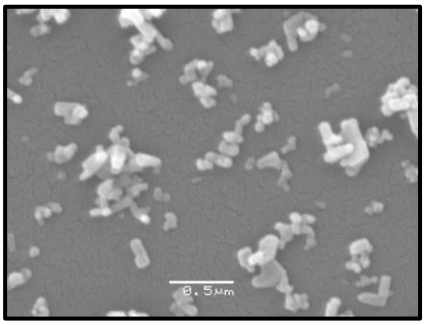


Figure 2.20 SEM image of ZnO seed layer. The scale bar is 500 nm.

Figure 2.21 shows the growth of ZnO nanorods from the ZnO seed layers for different reaction times; (a) 30 minutes, (b) 60 minutes and (c) 90 minutes. The three growth times indicate the changes for increased reaction times but the ZnO nanorods for all three samples did not grow and align as we expected. We attribute that to the non-uniformity of the commercial ZnO nanorods. However, it is evident that longer reaction times allow longer nanorods to grow and produce denser samples.

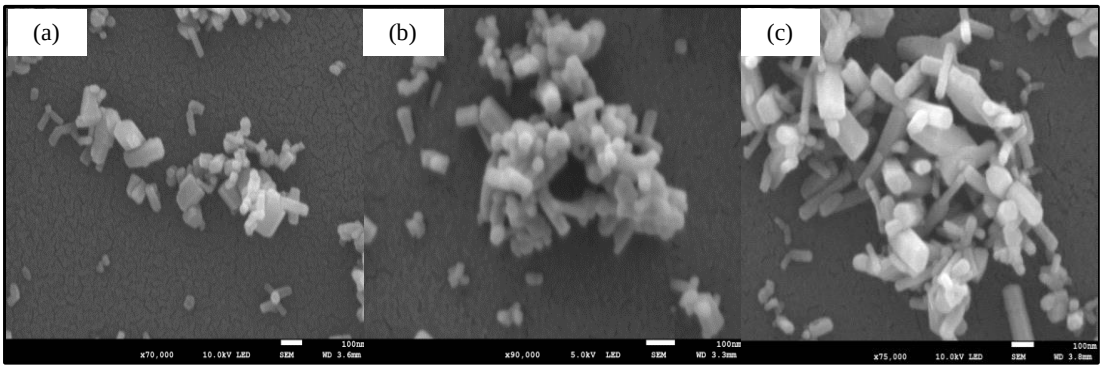


Figure 2.21 ZnO nanorods with different reaction times; (a) 30 minutes, (b) 60 minutes and (c) 90 minutes. Higher reaction times produce longer and denser ZnO nanorods. The scale bar is 100 nm.

### 2.2.3 Results and discussion

ZnO absorbs 355 nm light and emits at 385 nm while silver nanoparticles have an absorption peak at 425 nm (figure 2.22).

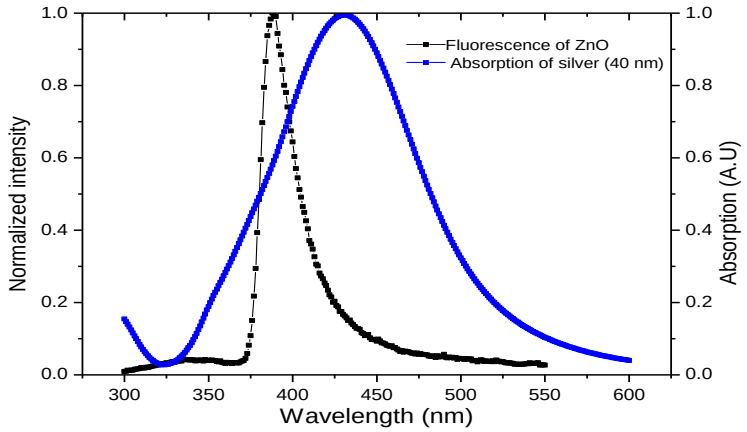


Figure 2.22 Normalized emission spectra from the fluorescence of ZnO and the absorption of silver indicating the possibility of localized surface plasmon effects. The fluorescence spectrum was measured by a Fluorolog spectrofluorometer (Horiba Jobin Yvon, ~ 1 nm resolution) while the absorption spectrum was measured by a Cary spectrophotometer.

The emission spectra of the ZnO nanorods with different growth times (20, 60 and 90 minutes) are shown in figure 2.23 (a). The emission peaks for all three samples are similar, ~ 385 nm. The emission peak intensity was higher for the longer nanorods due to the higher density of ZnO material.

Figure 2.23 (b) shows the emission spectra of the colloidal ZnO with silver nanoparticles. Various concentrations of silver nanoparticles were added to investigate

the plasmonic enhancement of the emission. The addition of silver nanoparticles to the colloidal ZnO nanoparticles increases the emission intensity due to surface plasmon resonance effects [143-145]. Localized surface plasmon effects occur when there is strong spectral overlap between the surface plasmon resonance peak of silver with the fluorescence of ZnO (figure 2.22). The ZnO emission is absorbed by the silver nanoparticles and creates localized excitation near the surface of the silver resulting in emission enhancement. However, an excess of silver nanoparticles reduces the intensity due to their increased absorption loss. Small emission wavelength shifts occur possibly due to increased scattering and absorption by the silver nanoparticles.

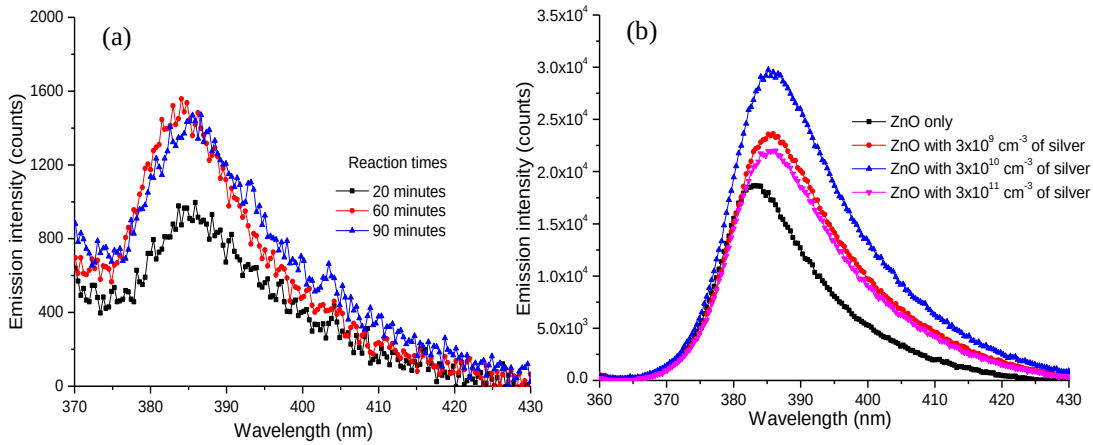


Figure 2.23 (a) Emission spectra of ZnO nanorods on glass substrates with different growth times (20, 60 and 90 minutes), excited by ~ 42 mJ/cm$^2$; (b) Emission spectra of ZnO nanoparticles without silver nanoparticles and with various concentrations of silver nanoparticles ($3 \times 10^9$ to $3 \times 10^{11}$ cm$^{-3}$). Emission enhancement occurs due to LSP while emission quenching occurs because of absorption loss. The emission spectra are averaged for 10 seconds to reduce the noise.

## 2.3 General discussion

In this chapter, the emission characteristics from active scatterers such as ruby and zinc oxide nanoparticles in disordered media were studied. The fluorescence lifetimes of samples were not measured due to lack of access to relevant equipment.

These active nanoparticles can absorb pump light and emit light at longer wavelengths, as well as scatter the pump light, to increase the pump absorption. Metal nanoparticles (gold and silver) can increase the emission intensity of ruby and zinc oxide nanoparticles due to local field enhancement and surface plasmon resonance effects. However, the concentration of metal nanoparticles should be chosen carefully to prevent excessive absorption loss. In our case, the limited contact of gold nanoparticles with ruby nanocrystals reduces the plasmonic effect. In a colloidal dye solution with metal nanoparticles, close contact between the metal nanoparticles and the dye is more probable, leading to coupling between the electromagnetic field concentrated close to the nanoparticle surface and the dye molecules. In our case, light scattering by metal nanoparticles is the only contribution to the fluorescence enhancement.

Each material studied has potential to exhibit gain (absorb the pump light) and scattering effects but no spectral narrowing (a signature of laser operation) was observed for any of the active scatterer samples in this study. As colloidal laser materials were used, the laser material is in a disordered medium. The pump light is not only absorbed but is scattered and experiences a random walk before leaving the excited medium. Other reasons are; too much scattering makes the excitation volume large and this pump light is insufficient to reach threshold. Therefore, a good balance between scattering and absorption is important to avoid pump light from being scattered out of the medium without being absorbed.

Bulk ruby crystals have been demonstrated to provide enough gain for laser operation when they are pumped effectively [121]. However, because ruby is a three level system with large ground state absorption at the emission wavelength, strong

excitation is needed to create a population inversion. In this experiment, we used two different pump lasers (Minilite Supercontinuum laser with maximum energy ~ 12m J and Surelite laser with the maximum energy ~ 200 mJ) to excite the ruby nanocrystals. We have tried the highest pump energy density (~ 500 mJ/cm$^2$), accessible to us to excite ruby nanocrystals but only fluorescence emission is observed. The 532 nm pump laser probably was not optimal to excite the ruby as the optimum excitation wavelength for ruby nanocrystals is either 405 nm or 550 nm (figure 2.9). A pump laser with a microsecond-pulsewidth may be preferable since ruby has a long excited state lifetime (3 ms). However, a high energy microsecond-pulsewidth pump source with either 405 nm or 550 nm excitation is not readily available.

To excite active scatterers where the gain coincides with the scatterers, high energy pumping with a suitable pulsewidth is needed. Most studies on random lasing using diamond [146] and zinc oxide nanoparticles [52, 147, 148] were done using picosecond-pulsewidth lasers to lie well within the fluorescence lifetime for zinc oxide nanoparticles, ~ 275 ps [148]. In this study, we used nanosecond-pulsewidth lasers, but did not obtain laser emission. However, nanosecond-pulsewidth pump lasers have been used to pump other laser materials such as Neodymium [29, 149] and $K_5PrLi_2F_{10}$ crystal powders [150].

Here, lack of laser operation is attributed to the relatively small gain of the materials and incompatible pump lasers. Alternative sample fabrication techniques such as vapor-solid growth to prepare ZnO nanorods [151] or forming a low-loss slab waveguide along the surface parallel to ZnO nanorod arrays [104] and hybrid nanocomposites of graphene oxide nanoflakes with ZnO [152] have been shown to produce random lasing. Yu *et al.* [104] also mentioned that it was difficult for ZnO

nanorods to support random lasing due to the low density of nanorods. In our system, the ZnO nanorods did not align as we expected, which would reduce the effective gain. With limited expertise in sample fabrication and limited access to appropriate pump lasers, we only obtained fluorescence emission. The sample fabrication and characterization techniques (ball milling, growth of zinc oxide by chemical bath deposition and embedding nanoparticles on films) and characterization of emission are described in this chapter to support future study. The techniques for sample characterization using the Zetasizer, TEM and CBS experiments were used in the following chapters.

## 2.4 Chapter 2 Summary

This chapter discussed the possibility of realizing random lasers from active nanoparticles, ruby and ZnO, but we only observed fluorescence enhancement. We believe laser action was inhibited by losses due to the three level laser system, insufficient scattering and gain and incompatible pump lasers. Thus, in the remainder of the thesis, we used dyes with passive nanoparticles. The concentration of passive nanoparticles and dyes to scatter and amplify the light, respectively, can be varied independently to control the random laser system (for example: for low concentration of passive nanoparticles, high concentration of dyes can be used to compensate for the weak scattering) and dyes with high quantum yield that can absorb green light are easily accessible. The random dye laser schemes are explained in the subsequent chapters.

# Chapter 3

# Spectral and coherence signatures of threshold in random lasers

Chapter 3 presents the spectral and coherence signatures of threshold in random lasers with incoherent feedback consisting of alumina colloidal nanoparticles suspended in Rhodamine 6G methanol solution (dyes with passive nanoparticles) under nanosecond-pulsewidth pumping, based on measurement of temporal and spatial coherence properties and comparison with emission spectra. Feedback in the random lasers was provided by multiple scattering from the alumina particles, and the effects of particle concentration and scattering length were studied for the weakly scattering and diffusive regimes. At threshold, in each regime, the visibility of the interference fringes jumped abruptly, coinciding with a substantial increase in emission peak intensity and decrease in the linewidth of a single dominant emission peak.

The results in Chapter 3 have been published as:

W. Z. Wan Ismail, D. Liu, S. Clement, D. W. Coutts, E. M. Goldys and J. M. Dawes, "Spectral and coherence signatures of threshold in random lasers," Journal of Optics **16**, 105008 (2014).

The first author (W. Z. Wan Ismail) set up and conducted the experiment, analyzed the experiment results and wrote the article. The second author (D. Liu) and the third author (S. Clement) gave advice in preparing and characterizing the samples. The other authors (D. W. Coutts, E. M. Goldys and J. M. Dawes) supervised the first author in setting up the experiment, analysing and discussing the results and revising the article.

## 3.1 Introduction

In conventional lasers, the output spectral, spatial and temporal features are controlled by an external cavity and / or waveguide resulting in well-defined threshold behavior such as the onset of a low order Gaussian beam. In random lasers, the output is controlled by inherently random scattering processes; hence the threshold behavior is potentially more subtle and complex. For example, a random laser does not produce a well-defined spatial mode even when pumped far above threshold. Here, I present measurements comparing the changes in the spatial and temporal coherence and emission spectrum in a random laser operating in the region around threshold.

As explained in Chapter 1 (Section 1.2.4: Types of random lasing), random lasers can be divided into two types: (i) Random lasers with incoherent feedback and (ii) Random lasers with coherent feedback. In random lasers with incoherent feedback, the feedback caused by multiple scattering returns light to the gain medium for amplification. As the pumping rate increases, the photon density grows quickly, and at threshold, produces a narrowed emission peak at the centre of the gain spectrum on a broad fluorescence background. In contrast, coherent feedback in random lasers corresponds to the situation where recurrent light scattering produces closed loop

paths of the scattered emission light. In this case, as the excitation energy increases, threshold is observed when several narrow spectral peaks emerge above the emission background [1, 78]. Wiersma noted that interference effects also occur in random lasers with incoherent feedback since the multiple scattering process is elastic [2]. Interference effects may be averaged out when using long excitation pulses or averaging over several laser pulses [2, 49, 59, 148]. This raises intriguing questions about the coherence and spectral characteristics of the emission near the onset of lasing in random lasers.

Optical gain and multiple light scattering are important principles in random lasers. As mentioned in Chapter 1 (Section 1.2.2: Principles of lasing in disordered media), the scattering strength can be measured using the scattering mean free path, $l_s$ ($l_s = 1/\rho\sigma_s$ where $\rho$ and $\sigma_s$ are the number density and the scattering cross-section of scattering particles respectively) [3, 28, 36-38]. $l_s \sim l_t$ (the transport length) for an isotropic medium. There are three regimes for light transport in isotropic media: the localization regime ($l_s \sim \lambda$), the diffusive regime ($L >> l_s >> \lambda$), and the weakly scattering regime ($l_s \geq L$) [1, 3]. In the weakly scattering regime, there is insufficient optical feedback for lasing as the scattering events are relatively rare, but in the diffusive regime, the light that is emitted in the active gain region undergoes multiple scattering events with a high probability of further amplification [102, 153]. With sufficient gain, laser oscillation occurs when the system reaches a threshold at which the gain exceeds the losses. Previous reports investigating the threshold for random lasers have focused on the characteristics of the emission spectra, [30, 49, 102, 148] whereas others investigated the coherence, without determining the lasing threshold [73-75].

This chapter presents the properties of random lasers composed of active media (Rhodamine 6G (Rh6G) in methanol pumped by a nanosecond-pulsed laser) with passive scatterers (alumina ($Al_2O_3$) nanoparticles). Above threshold, a narrow emission peak emerged above the emission background near the gain maximum, consistent with the incoherent feedback mechanism. The threshold behaviour of the random laser emission spectra was compared with the coherence properties for different scattering concentrations. The signature of lasing in random lasers at threshold determined from emission spectra was found to be consistent with that from coherence measurements. When the lasing threshold was achieved, the emission peak intensity increased substantially and high visibility interference fringes were observed. Random lasers with incoherent feedback exhibit partial temporal and spatial coherence.

## 3.2 Experimental methods

The random laser samples were pumped by a Q-switched frequency-doubled Nd:YAG laser, with a wavelength of 532 nm, 4 ns pulsewidth and pulse repetition rate of 10 Hz. The excitation energy was varied by a half waveplate before a fixed polarizer. A beam dump removed residual pump light. A focusing lens with $f$ = 10 cm, was used to focus the excitation energy into the dye / nanoparticle suspension within a quartz cuvette. The pump spot diameter throughout the experiment was 2 mm at the front face of the cuvette. Experiments for each sample were completed in less than 30 minutes to avoid problems with nanoparticles settling in the cuvette or photobleaching of the dye due to excessive pump light.

### 3.2.1 Sample preparation

Dielectric nanoparticles, alumina ($Al_2O_3$) with average diameter of 150 nm (Sigma Aldrich) were suspended in Rh6G (Sigma Aldrich) dissolved in methanol. The colloid solution changes colour when the concentrations of nanoparticles and dyes are varied (figure 3.1). The size of the nanoparticles was checked with a Zetasizer Nano ZSP (Malvern Instruments Ltd) using dynamic light scattering. $Al_2O_3$ was chosen as it is stable in methanol solution, has good refractive index contrast for scattering and does not absorb the excitation or emission light. The concentration of $Al_2O_3$ nanoparticles was varied from $3 \times 10^{10}$ to $1 \times 10^{12}$ $cm^{-3}$ and the Rh6G concentration was fixed at $1 \times 10^{-3}$ M in methanol. Each solution was ultrasonically dispersed for 30 minutes to break the aggregation of nanoparticles before placing into a cuvette (1 cm $\times$ 1 cm). A thin piece of teflon was positioned inside the cuvette to suppress lasing by reflection from the back and side faces of the cuvette. The scattering mean free path, $l_s$ for the random laser solutions ranged from 0.35 to 11.6 mm while $l_t \sim l_s$. Mie theory [35, 36, 41, 84, 154] is used to estimate the $\sigma_s$. The samples are in the diffusive and weakly scattering regimes.

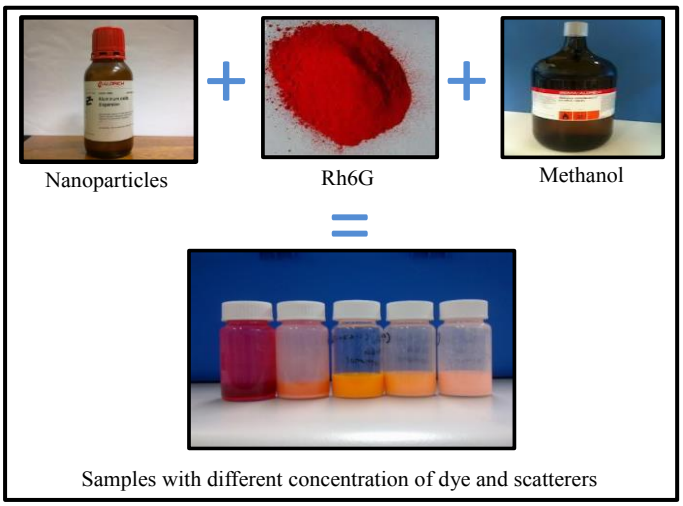


Figure 3.1 Preparation of colloid solution

### 3.2.2 Coherence measurements

The coherence of an optical field refers to the correlation between its parameters, including the ability of light to produce interference [70]. Spatial coherence corresponds to the correlation of the electric fields on the same wave front at two disparate positions while temporal coherence is the correlation of the electric field at two different times but at the same position [69, 70]. Noginov *et al.* [74] implemented experiments to study transverse and longitudinal coherence in nanosecond-pumped stimulated emission from ceramic powders. Temporal and spatial coherence measurements for random lasers have been separately reported by Papadakis *et al.* [75] and Redding *et al.* [73] respectively. Coherence can be measured by a mutual coherence function, $g_{12}$ that relates to the intensities of two light waves with field amplitudes $E_1$ and $E_2$, by eq. (3.1) [70, 155];

$$g_{12} = \langle E_1 * E_2 \rangle / \sqrt{I_1 I_2} \tag{3.1}$$

where $I_1 = |E_1|^2$ and $I_2 = |E_2|^2$. When the two light waves are superposed, the average intensity of their sum is given in eq. (3.2) [155];

$$I = I_1 + I_2 + 2\sqrt{I_1 I_2}\,|g_{12}| cos\varphi \tag{3.2}$$

where $\varphi = arg\{g_{12}\}$ is the phase of $g_{12}$. The degree of coherence is measured by $|g_{12}|$, where $|g_{12}|$ is zero for uncorrelated or incoherent waves and $|g_{12}|$ is 1 for fully coherent waves. Values in the range of $0 < |g_{12}| < 1$ refer to partially coherent light. The partially coherent light consists of a superposition of both the incoherent and the coherent components [3]. The degree of coherence can be indicated by the visibility, *V*, or the contrast of the interference pattern. *V* is obtained from the variation of minimum and maximum intensities, $I_{min}$ and $I_{max}$, as shown in eq. (3.3) [155];

$$V = (I_{max} - I_{min})/(I_{max} + I_{min}) \quad (3.3)$$

As explained in [73, 75], $V$ is proportional to $|g_{12}|$ when $I_1 = I_2$. In this chapter, the degree of spatial and temporal coherence was calculated based on measurements of *V*.

#### 3.2.2.1 Spatial coherence measurement

In this experiment, spatial coherence was measured using Young's double slit experiment [70, 155] as in figure 3.2. The random laser emission light was imaged onto a double slit ($s_1$ and $s_2$) with 40 µm slit width by two spherical lenses ($f$ = 5 cm and $f$ = 2.5 cm) with a magnification of 0.5 and a 532 nm edge filter to remove pump light. Light that passed through the slits overlapped and formed interference fringes. The interference fringes were observed by a CCD camera (PULNIX (TM-7CN)) at the back focal plane of a lens with focal length 5.0 cm. In addition, a neutral density (ND) filter reduced the light intensity to the CCD camera, resulting in clear fringes with less light saturation. A baffle was placed perpendicular to the double slit to block any pump light from entering the CCD camera. The interference fringes were captured for single pump pulse excitation.

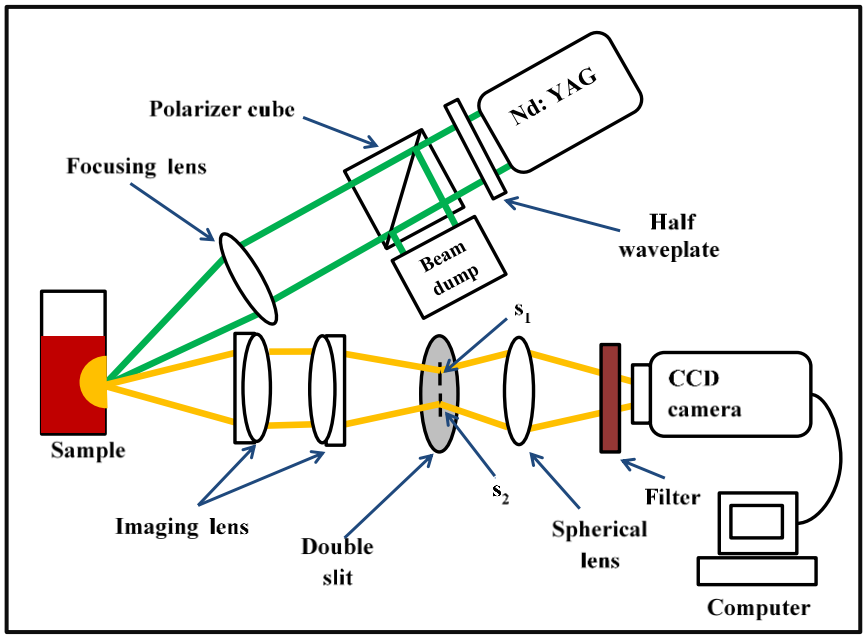


Figure 3.2 Experimental set up for spatial coherence measurement. The emission light from the front of the cuvette was collected by a spectrometer for the emission spectrum measurement.

### 3.2.2.2 Temporal coherence measurement

In a conventional Michelson Interferometer set up, one of the mirrors is moved backward gradually to introduce delay, resulting in reduced fringe visibility due to the difference in optical path length. Interference fringes with low visibility indicate reduced coherence. In this experiment, the two reflecting mirrors of a Michelson Interferometer were tilted, [75] to ensure both wavefronts reflected from the mirrors could interfere and interference fringes could be observed using a CCD camera. By tilting the mirrors, interference fringes were measured for every optical delay in a single pulse without any moving components. The optical path difference (OPD), $\Delta l$ between these wavefronts generated the optical delay, $\tau = \Delta l/c$ where $c$ represents the velocity of light.

The temporal coherence measurement set up is shown in figure 3.3. In this temporal coherence experiment, $I_1$ and $I_2$ are the intensity values of reflected light from the two tilted mirrors and $I_1 \sim I_2$. The fringe visibility for the tilted Michelson

Interferometer was calculated by using eq. (3.3). Thus, fringes from a single pump pulse were recorded with the temporal dimension being translated to a spatial dimension. The random laser emission was imaged to the entrance plane of the interferometer by using a lens, $f$ = 5 cm. A pinhole of 1 mm diameter at the entrance plane selected the central part of the emission. The end mirrors were tilted slightly at an angle of ~ $1^{o}$ and adjusted so that the images of the illuminated pinhole which were reflected by the mirrors were formed by a spherical lens at the interferometer exit. The two replicas formed by the spherical lens illuminated the CCD camera (PULNIX (TM-7CN)) and interference fringes were recorded. A 532 nm edge filter prevented scattered light from the excitation laser from entering the CCD camera. A neutral density (ND) filter was used to control the input light level.

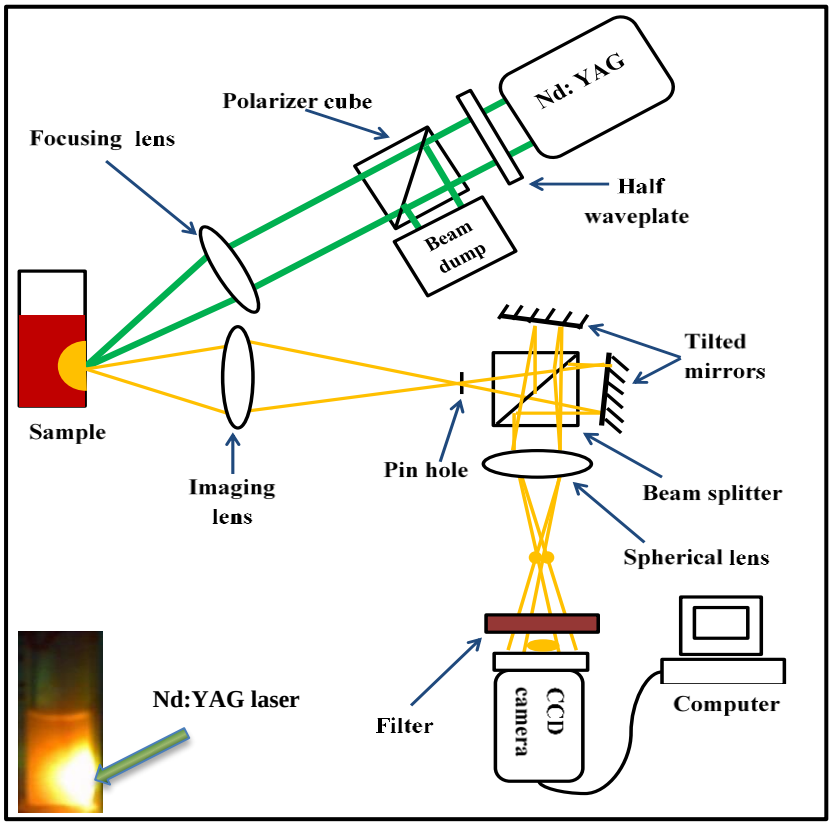


Figure 3.3 Experimental set up for temporal coherence measurement. The emission light from the front of the cuvette was collected by a spectrometer for the emission spectrum measurement. The inset shows the excited gain medium for Rh6G (1 mM) / alumina ($1 \times 10^{12}$ $cm^{-3}$) random lasers.

#### 3.2.2.3 Emission spectrum measurement

The emission spectrum was measured simultaneously for both coherence measurements by using a fibre-coupled spectrometer (Ocean Optics USB2000+UV-VS-ES). The emission light from the front of the cuvette was collected by a lens ($f$ = 5 cm), 30$^o$ from normal and filtered by a 532 nm edge filter to prevent the pump light from entering the spectrometer.

## 3.3 Results

### 3.3.1 Spectral measurement

In the spatial coherence measurements, emission spectra for Rh6G solutions with three concentrations of $Al_2O_3$ nanoparticles are shown in figures 3.4 to 3.6. For the lowest particle concentration ($3 \times 10^{10}$ cm$^{-3}$ and $l_s$ = 11.6 mm) shown in figure 3.4, the emission spectrum was dominated by a broad fluorescence spectrum. The sample was in the weakly scattering regime. The threshold occurs at 41 mJ/cm$^2$ where a narrow emission peak (3 nm) starts to appear on the top of the fluorescence spectrum.

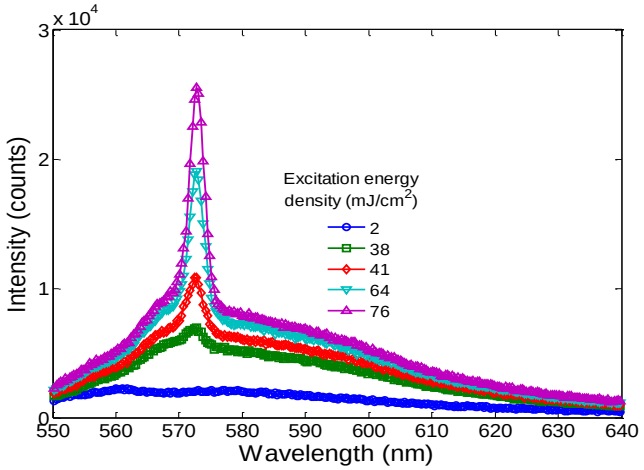


Figure 3.4 Emission intensity spectrum for random lasers containing Rh6G and $Al_2O_3$ nanoparticles ($3 \times 10^{10}$ cm$^{-3}$) with different excitation energy densities. A narrow lasing peak occurred at 41 mJ/cm$^2$. The lasing peak spectral width remained constant for lasing above threshold.

When the concentration was increased up to $3 \times 10^{11}$ cm$^{-3}$ corresponding to $l_s$ = 1.2 mm, the system operated in the diffusive regime. In this regime, the spontaneous emission background was less evident, and the lasing threshold reduced to 38 mJ/cm$^2$ (figure 3.5).

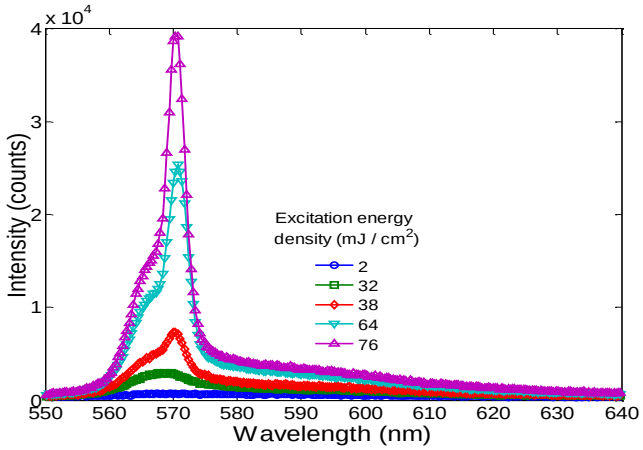


Figure 3.5 Emission intensity spectrum for random lasers containing Rh6G and $Al_2O_3$ nanoparticles ($3 \times 10^{11}$ cm$^{-3}$) with different excitation energy densities. A narrow lasing peak occurred at 38 mJ/cm$^2$. The lasing peak spectral width remained constant for lasing above threshold.

At the largest concentration of scatterers studied, ($1 \times 10^{12}$ cm$^{-3}$ and $l_s$ = 0.35 mm), most photons would experience multiple scattering before they leave the sample, which would elongate photon paths and increase feedback, reducing the stimulated emission threshold at 25 mJ/cm$^2$ as shown in figure 3.6.

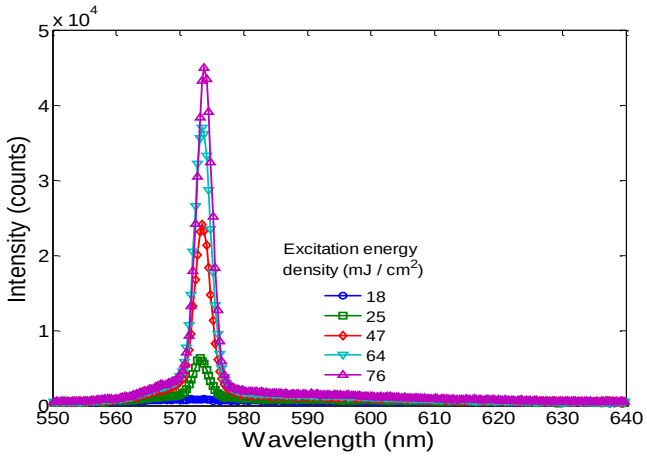


Figure 3.6 Emission intensity spectrum for random lasers containing Rh6G and $Al_2O_3$ nanoparticles ($1 \times 10^{12}$ cm$^{-3}$) with different excitation energy densities. A narrow lasing peak ~ 3 nm occurred at 25 mJ/cm$^2$. The lasing peak spectral width remained constant for lasing above threshold.

Figure 3.7 shows the amplitude of the peak of the emission spectrum for various nanoparticle concentrations in the spatial coherence measurement where the threshold excitation energy density decreased for increasing scatterer concentration.

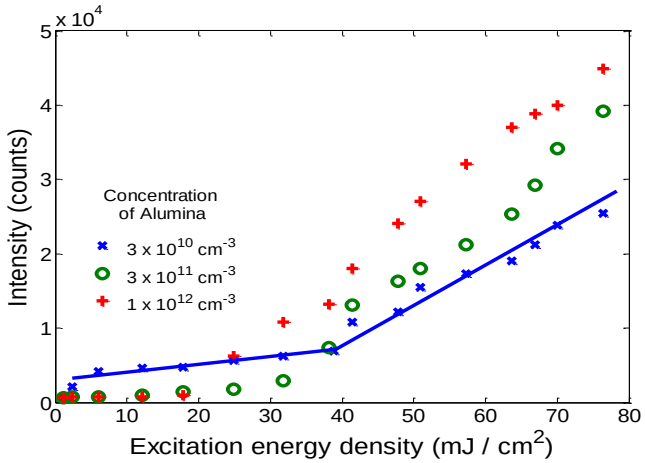


Figure 3.7 Emission peak intensity of random lasers containing Rh6G and $Al_2O_3$ nanoparticles with various concentrations of $Al_2O_3$ nanoparticles as a function of excitation energy density, collected concurrently with spatial coherence measurement. The blue line indicates the lasing threshold for $3 \times 10^{10}$ $cm^{-3}$ of $Al_2O_3$ nanoparticles. The uncertainty in these emission spectrum measurements was ± 4%.

The characteristics of the emission spectra and lasing threshold for the temporal coherence measurements are shown in figure 3.8. The fluorescence background and the lasing threshold reduce as the concentration of $Al_2O_3$ nanoparticles increases.

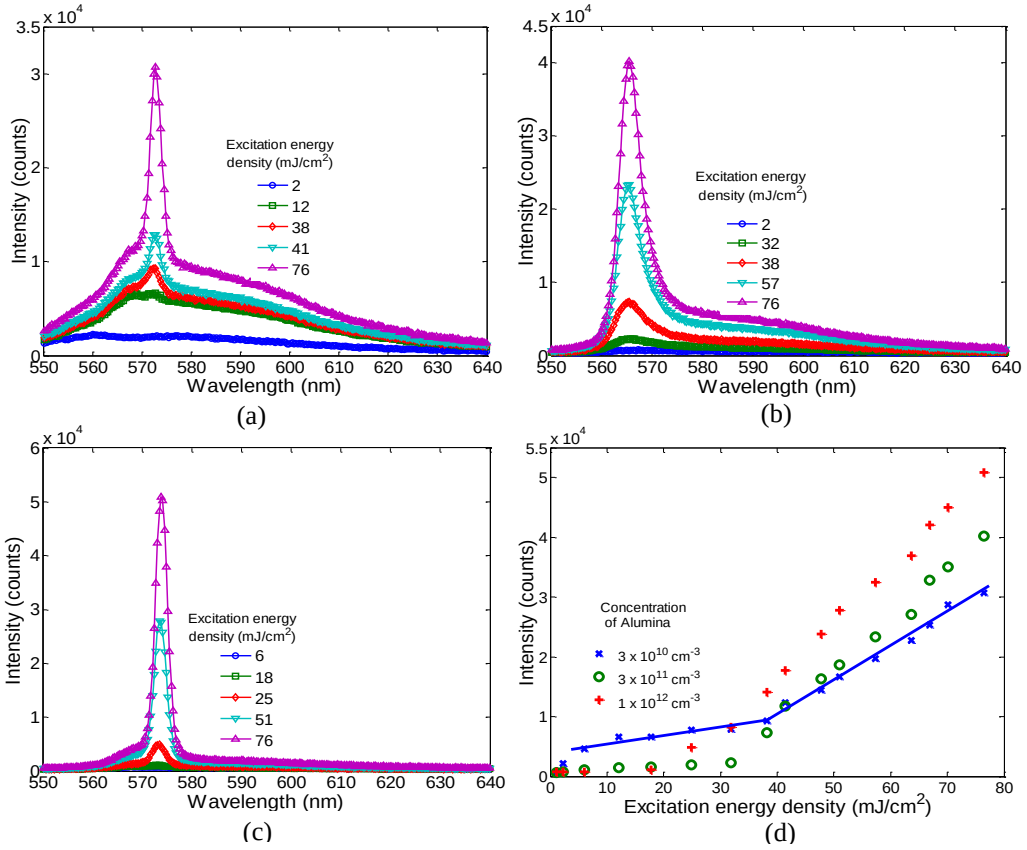


Figure 3.8 Emission intensity spectra for random lasers containing Rh6G and (a) $3 \times 10^{10}$ $cm^{-3}$, (b) $3 \times 10^{11}$ $cm^{-3}$ and (c) $1 \times 10^{12}$ $cm^{-3}$ of $Al_2O_3$ nanoparticles; (d) Emission peak intensity of random lasers containing Rh6G and various concentrations of $Al_2O_3$ nanoparticles as a function of excitation energy density, collected concurrently with temporal coherence measurement. The blue line indicates the lasing threshold for $3 \times 10^{10}$ $cm^{-3}$ of $Al_2O_3$. The uncertainty in these emission spectrum measurements was ± 4%.

## 3.3.2 Spatial coherence measurement

The fringe visibility of the central fringe was calculated from eq. (3.3) assuming the intensities on the two slits were equal. Interference fringe visibility is a maximum at the centre fringe, due to finite slit width and limited temporal coherence. Here, the slit width was fixed at 40 µm and the slit separation was varied from 100 to 300 µm. As seen in figures 3.9 and 3.10, the interference fringes below the lasing threshold had low visibility ($V < 0.05$) while the fringes above the lasing threshold were more distinct ($V > 0.2$) for $Al_2O_3$ nanoparticles with concentration of $3 \times 10^{10}$ $cm^{-3}$.

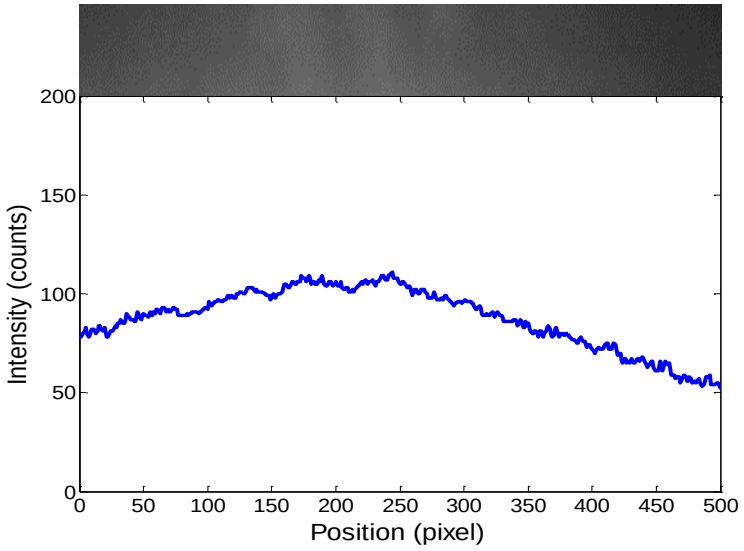


Figure 3.9 Interference fringes and intensity profile of spatial coherence for a random laser containing Rh6G and $Al_2O_3$ nanoparticles ($3 \times 10^{10}$ $cm^{-3}$) excited by 12 $mJ/cm^2$ (below lasing threshold). The slit separation was 100 µm.

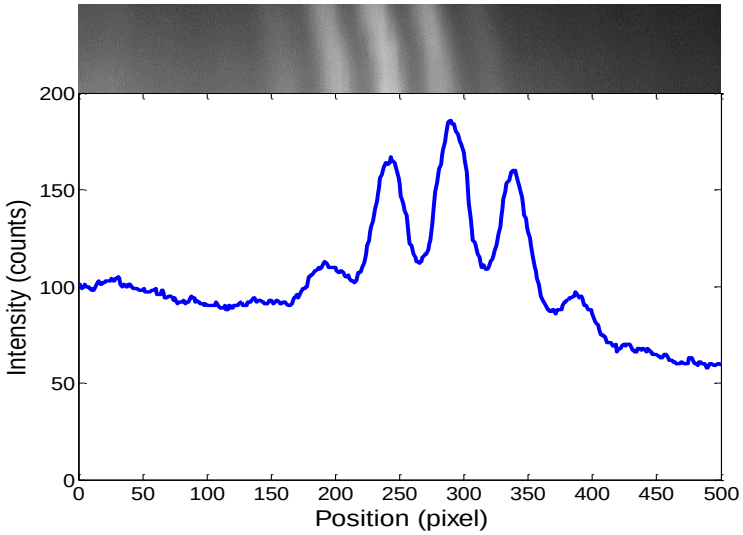


Figure 3.10 Interference fringes and intensity profile of spatial coherence for a random laser containing Rh6G and $Al_2O_3$ nanoparticles ($3 \times 10^{10}$ $cm^{-3}$) excited by 76 $mJ/cm^2$ (above lasing threshold). The slit separation was 100 µm.

From the intensity profile graphs of these images, the visibility for each image was plotted as a function of excitation energy density (figure 3.11). This figure compares the visibility of the central fringe for solutions with three particle concentrations when the excitation energy was increased. It shows that the visibility

rose linearly before the lasing threshold. Above the threshold energy, the visibility increased abruptly. Higher excitation energy produced higher gain for lasing. Furthermore, a higher concentration of $Al_2O_3$ nanoparticles gave increased coherence, with better visibility of interference fringes above the lasing threshold. The light was partially coherent as $V \ll 1$. Figure 3.11 also indicates the dependence of lasing threshold on the concentration of scatterers.

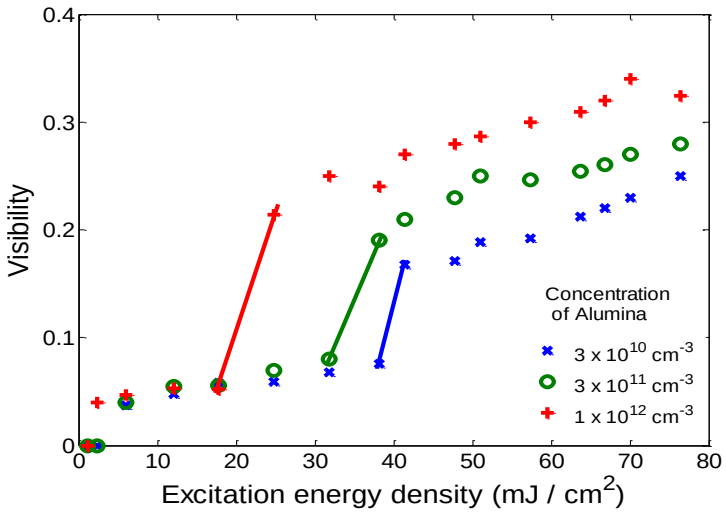


Figure 3.11 Visibility of spatial coherence fringes for random lasers as a function of excitation energy density for samples containing Rh6G and different concentrations of $Al_2O_3$ nanoparticles. The lines indicate the lasing threshold region with an abrupt increase in coherence.

Spatial coherence was evaluated as a function of the distance between emitting regions of the random laser. Redding *et al.* [73] studied this by varying the distance between a cuvette and a spherical lens and the distance between the lens and a double slit, and adjusting the magnification of their imaging optics so that points with varying separation were imaged onto the double slit. However, in this work, the distance between points on the emission spot was varied by varying the slit spacing (100 µm, 200 µm and 300 µm) with the same slit width (40 µm) for a concentration of $1 \times 10^{12}$ $cm^{-3}$ of $Al_2O_3$ nanoparticles.

The visibility as a function of excitation energy density for different slit separations plotted in figure 3.12 shows that the visibility is reduced when the slit separation increased. Light from more closely spaced positions in the gain region shows more spatial coherence as expected. The lasing thresholds for three different slit separations, shown by the lines in figure 3.12 were correlated with the lasing thresholds determined by the emission spectrum and temporal coherence measurements. From figures 3.11 and 3.12, the maximum visibility for the emission light was 0.34 and the random laser was partially coherent.

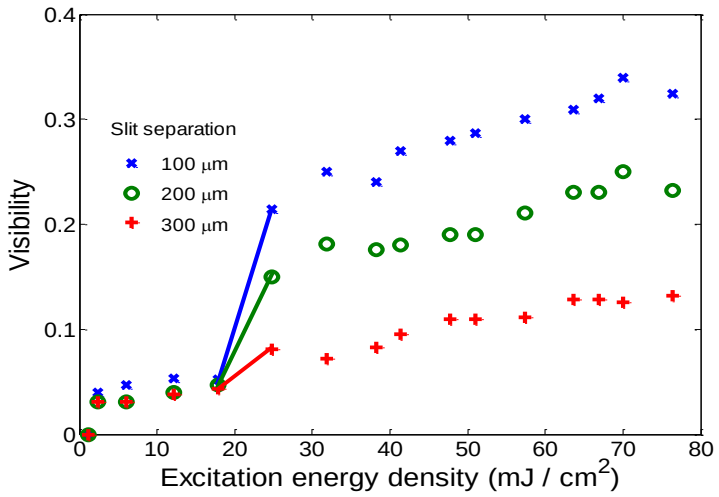


Figure 3.12 Visibility of spatial coherence fringes for random lasers as a function of excitation energy density for samples containing Rh6G and $Al_2O_3$ nanoparticles ($1 \times 10^{12}$ $cm^{-3}$) for three different slit separations. The lines indicate the lasing threshold region in each case.

### 3.3.3 Temporal coherence measurement

The temporal coherence was measured using the set up shown in figure 3.3. Fringe measurements are shown in figures 3.13 and 3.14 for excitation below and above lasing threshold. As the excitation energy density increased, the emission changed from broadband to a narrower line, with more pronounced fringes. By applying eq. (3.3) to figures 3.13 and 3.14, the visibility as a function of optical path difference (OPD) was plotted in figure 3.15, showing that above the threshold, the

fringe visibility doubled. However, only partially coherent light was measured with average visibility values less than 1. The random laser was an extended source and the large size of the pin hole selected light from different parts of the sample, so that $V \neq 1$ even for zero optical delay, due to the broad fluorescence dye emission spectrum and limited spatial coherence of the random laser [74, 75].

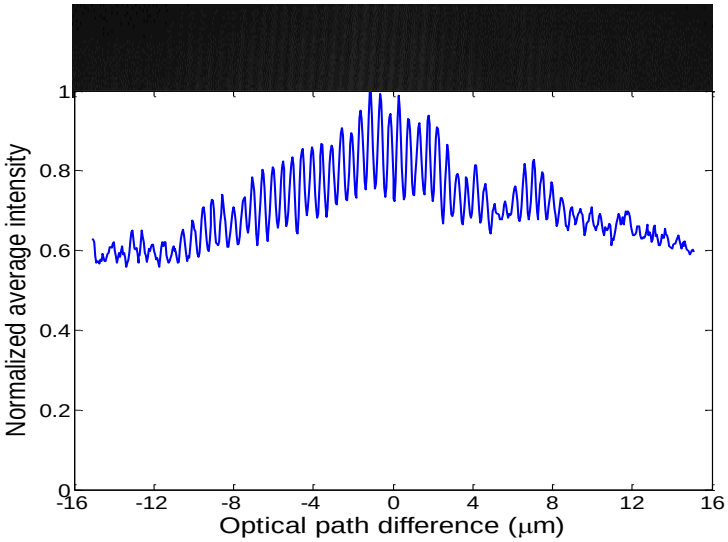


Figure 3.13 Interference fringes and intensity profile indicating temporal coherence for a sample with Rh6G and $Al_2O_3$ nanoparticles ($3 \times 10^{10}$ $cm^{-3}$) excited by 25 $mJ/cm^2$ (below lasing threshold). The average visibility was ~ 0.15.

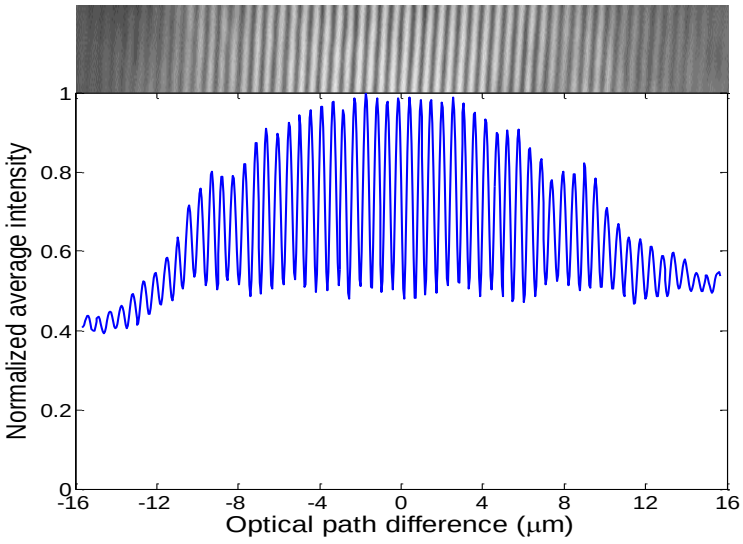


Figure 3.14 Interference fringes and intensity profile indicating temporal coherence for a random laser with Rh6G and $Al_2O_3$ nanoparticles ($3 \times 10^{10}$ $cm^{-3}$) excited by 67 $mJ/cm^2$ (above lasing threshold). The average visibility was ~ 0.35.

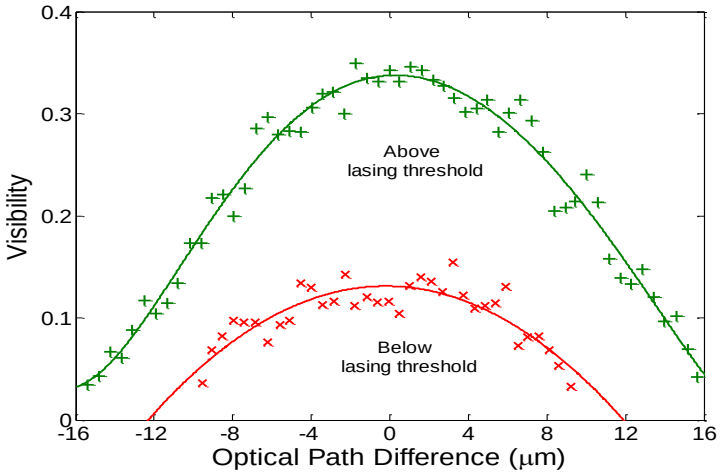


Figure 3.15 Visibility as a function of optical path difference for a random laser with Rh6G and $Al_2O_3$ nanoparticles ($3 \times 10^{10}$ $cm^{-3}$) above lasing threshold (67 $mJ/cm^2$) and below lasing threshold (25 $mJ/cm^2$). The lines are fitted to determine the FWHM.

The coherence length, $l_c$ describes the temporal coherence properties of random lasing, referring to the maximum optical path difference between two points of a light beam which retain a phase relationship (or can interfere to give fringes). It was measured as the full width at half maximum (FWHM) of the visibility curve [155] as shown in figure 3.15. Figure 3.16 depicts the coherence length as a function of pump energy per pulse for $3 \times 10^{10}$ $cm^{-3}$ of $Al_2O_3$ nanoparticles. The coherence length displays nonlinear behaviour as a function of pump energy density.

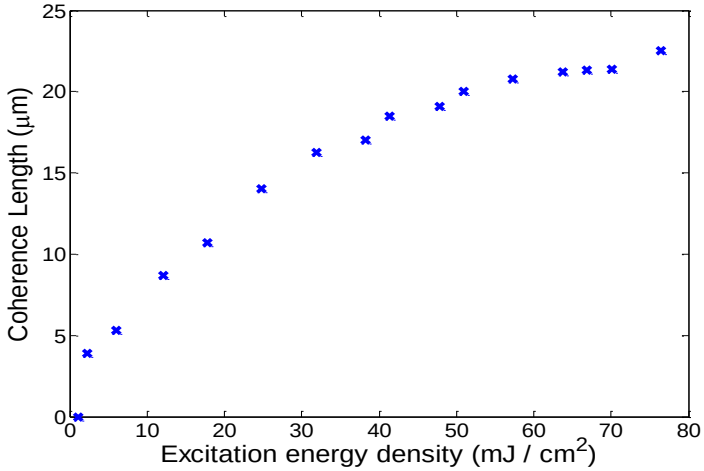


Figure 3.16 Coherence length as a function of the excitation energy density for random laser containing Rh6G and $Al_2O_3$ nanoparticles ($3 \times 10^{10}$ $cm^{-3}$). The coherence length increased nonlinearly.

## 3.4 Discussion

From the measurements of emission spectra and spatial coherence, the threshold was determined by the rapid change in emission peak intensity (figures 3.7 and 3.8 (d)) and fringe visibility (figures 3.11 and 3.12). The presence of a kink in the emission peak intensity and in the fringe visibility of spatial coherence define the random laser thresholds (~ 25 mJ/cm$^2$ for $1 \times 10^{12}$ cm$^{-3}$ of $Al_2O_3$, 38 mJ/cm$^2$ for $3 \times 10^{11}$ cm$^{-3}$ of $Al_2O_3$ and 41 mJ/cm2 for $3 \times 10^{10}$ cm$^{-3}$) which are quite similar for both measurements. The threshold also can be determined when a narrow emission peak appears on top of the fluorescence background as shown in figures 3.4 to 3.6. The coherence length (figure 3.16) shows a nonlinear trend as the laser makes a transition from spontaneous emission to stimulated emission, but the threshold behaviour is less evident as measured by coherence length in comparison with other parameters, as it is dominated by the broad fluorescence bandwidth at lower pump energy densities.

The threshold was significantly influenced by particle concentration, consistent with the spectral measurement results of Dice *et al.* [102]. The behavior of the random lasers in this chapter is consistent with that of random lasers with incoherent feedback reviewed in [1] where a narrow emission peak appears at the frequency of the gain maximum as the interference effects are averaged out during long excitation pulses.

Random dye lasers often exhibit a broad background emission spectrum [30, 47, 49, 54, 102]. The broad background emission was reduced for increased particle concentration and the emission spectrum narrowed without a significant broadband background for the highest particle concentration when pumped well above threshold. In this regime, as the transport length increased, the lasing threshold reduced. Figures

3.4 to 3.6 show that the emission peak intensity increased abruptly with a narrow linewidth (3 nm) emission peak at lasing threshold and above this threshold, increasing pump energy increased the emission intensity but the emission linewidth at the lasing peak remained constant. These results are comparable with results reported in Noginov *et al.* [49] where they discussed the effect of scattering on a random laser by titania nanoparticles with Rh6G. At small particle concentrations, photons have very short propagation paths in the gain medium and do not undergo strong amplification, leading to a narrow emission peak on top of the spontaneous emission background. However, at large particle concentrations, most photons experience multiple scattering paths which provide feedback, narrowing the emission spectrum as a whole and giving lower lasing threshold [49].

We studied the effect of scattering using dielectric nanoparticles (alumina) by varying the particle concentration, with fixed Rh6G concentration. The scattering contribution was varied independently of the gain medium. Particle concentration influenced the lasing threshold and emission intensity because scattering confined the pump light to a restricted volume and also more scattering gave longer light confinement inside the gain medium. When the particle concentration was varied from $3 \times 10^{10}$ $cm^{-3}$ to $1 \times 10^{12}$ $cm^{-3}$, the lasing threshold reduced and the emission intensity increased. A higher particle concentration provided stronger scattering and more feedback, resulting in a lower lasing threshold. Random lasers with lower particle concentrations have higher pump thresholds, since more gain is needed to compensate for insufficient scattering by nanoparticles.

In the spatial coherence measurements, the lasing thresholds as determined by the emission spectra (figure 3.4 to 3.6) and fringe visibility (figures 3.11 to 3.12) were

consistent. The fringe visibility increased substantially when a narrow emission peak appeared on top of the spontaneous emission band. This is consistent with the analysis by Redding *et al.* [73] on the spatial coherence of picosecond-pumped random lasers. They studied the effects of pump spot diameter and particle concentration on the spatial coherence of random dye lasers with polystyrene nanospheres and found that a larger pump area and a higher scattering strength resulted in reduced spatial coherence. Here, the spatial coherence was used to clarify the threshold properties of random lasers. From figure 3.12, the thresholds observed for all slit spacings were similar as the spatial coherence measurements were limited by the large pumped region.

The lasing threshold determined from the emission spectrum of figure 3.8 is more distinct than the nonlinear dependence of the temporal coherence observed in figure 3.16 for the random laser with Rh6G and $Al_2O_3$ nanoparticles ($3 \times 10^{10}$ $cm^{-3}$). The coherence length depends on the detailed emission spectrum of the system. At low pump energy density, the emission is dominated by the broadband, low temporal coherence fluorescence. At higher pump energy density, the narrow linewidth emission peak increases and begins to dominate the output spectrum, resulting in longer coherence lengths.

A single narrow emission peak (3 nm) appeared above threshold (figures 3.4 to 3.6) indicating that the laser was operating with incoherent feedback, also consistent with both coherence measurements where we obtained visibility less than 1. The emission peak for random lasers with incoherent feedback is expected to show a stable mean frequency when the centre frequency of the amplification line is sufficiently stable [1, 2]. Furthermore, the fringe patterns for both coherence measurements showed minimal variation (± 4%) in terms of the fringe position and visibility from

pulse to pulse as the interference effects were averaged out due to long excitation pulses, mentioned in [1, 2]. While there is expected to be a Fourier relationship between the spectral width and temporal coherence, consistent with the experimental observations, the spatial coherence properties do not necessarily correlate well with the beam divergence in an analogous fashion. The abrupt increase in spatial coherence for operation above threshold corresponds to a transition to an emitted wavefront that has reduced intra-pulse phase fluctuations, yet the wavefront itself remains highly complex, consistent with the scrambling expected for diffuse scattering.

## 3.5 Chapter 3 Summary

In conclusion, the threshold of random lasing has been determined by investigating the coherence and emission spectrum of the emitted light. Spatial measurement shows the same threshold as that obtained by measurement of the emission spectra while the nonlinearity of the coherence length dependence on pump excitation is consistent with a change from spontaneous emission to stimulated emission. The emission intensity increases rapidly and a narrow linewidth emission peak appears with sufficient pump energy density. The fluorescence background is relatively reduced when the particle concentration is increased substantially. Above threshold, the interference fringes increase abruptly in visibility, consistent with increased spatial and temporal coherence, corresponding with high emission intensity and narrow linewidth. Hence, coherence measurements confirm threshold behavior, consistent with the observed narrowing of emission spectra for random lasers in the weakly scattering to diffusive regime.

# Chapter 4

# Extended emission wavelength of random dye lasers by exploiting radiative and non-radiative energy transfer

In Chapter 4, we demonstrate long-wavelength operation (> 700 nm) of random dye lasers (using a Methylene blue dye) with the addition of Rhodamine 6G and titania, enabled by radiative and non-radiative energy transfer. The pump energy is efficiently absorbed and transferred to the acceptors, to support lasing in random dye lasers in the near infra-red. The optimum random laser performance with the highest emission intensity and the lowest lasing threshold was achieved for a concentration of Methylene blue as the acceptor equal to 6× the concentration of Rhodamine 6G (donor). Excessive levels of Methylene blue increased the lasing threshold and broadened the Methylene blue emission linewidth due to dye quenching from reabsorption. This is due to competition between the donor emission and energy transfer, and between absorption loss and fluorescence quenching. The radiative and

non-radiative energy transfer is analyzed as a function of the acceptor concentration and pump energy density, with consideration of the spectral overlap. The dependence of the radiative and non-radiative transfer efficiency on the acceptor concentration is obtained and the energy transfer parameters, including the radiative and non-radiative energy transfer rate constants ($K_R$ and $K_{NR}$), are investigated using Stern-Volmer analysis. The analysis indicates that radiative energy transfer is the dominant energy transfer mechanism in this system.

The results in Chapter 4 have been published as:

W. Z. Wan Ismail, E. M. Goldys and J. M. Dawes, "Extended emission wavelength of random dye lasers by exploiting radiative and non-radiative energy transfer," Applied Physics B: Lasers and Optics **122**, 1-9 (2016).

The first author (W. Z. Wan Ismail) set up and conducted the experiment, analyzed the experiment results and wrote the article. The other authors (E. M. Goldys and J. M. Dawes) supervised the first author in setting up the experiment, analysing and discussing the results and revising the article.

## 4.1 Introduction

Organic dyes such as Rhodamine are commonly used in random lasers due to their broad absorption spectra, high gain and compatibility with available pump wavelengths (such as 532 nm) while Methylene blue, Oxazine and Nile blue dyes are not compatible with blue and green pump light. Here, we combine these dyes in a single laser to extend the random laser emission to near infra-red wavelengths through the process of energy transfer.

Energy transfer (redistribution of excitation energy between a short wavelength absorber, the donor and a long wavelength acceptor, the emitter) is either radiative, where the donor molecule emits a photon which is subsequently absorbed by the acceptor molecule; or non-radiative, where the excited donor transfers its excitation energy to a ground-state acceptor through a non-radiative process. Non-radiative energy transfer is also known as Förster (fluorescence) resonance energy transfer (FRET) [9, 156, 157]. For both radiative and non-radiative energy transfer, significant overlap of the donor emission spectrum and the acceptor absorption spectrum is required to support long-range multipole interactions [9, 156, 157].

Energy transfer-based random lasing was introduced previously in refs. [62, 95, 108, 158]. Shi *et al.* [108] demonstrated cascaded radiative energy transfer between three different dyes in separate cuvettes. Luis *et al.* [95] and Alee *et al.* [158] studied FRET random lasers using mixtures of Rhodamine 6G / Nile blue and Coumarin / Rhodamine 6G respectively. Luis *et al.* [95] observed laser emission from a mirror cavity within the sample cell and Alee *et al.* [158] observed the enhancement of a FRET random laser by varying the concentration of scatterers. Lopez *et al.* [62] studied FRET random lasing by doping a DNA-lipid complex with two different dyes and tuning the emission wavelength by varying sphere diameters. They observed a narrow emission peak (~ 15 nm) at ~ 700 nm at the acceptor wavelength.

In this chapter, we report the following observations: (1) Random dye laser emission in the near infra-red (> 700 nm) with a narrow emission linewidth (~ 4 nm), ~ 3× narrower than reported in [62]. This was achieved in a random dye laser system incorporating Rhodamine 6G (Rh6G) / Methylene blue (MB) / titania pumped with 532 nm light. We attribute this infrared emission to energy transfer between Rh6G and

MB dye molecules. (2) We found that energy transfer influences the random lasing threshold, shifts the emission peak wavelength and changes the emission linewidth, depending on the dye concentration ratio. The optimum MB concentration was identified for a Rh6G concentration of $5 \times 10^{-4}$ M. (3) We analyzed energy transfer based on the radiative, dipole-dipole energy transfer and Stern-Volmer expressions, taking into account the acceptor concentration and energy density of the pump laser. Our analysis indicates that the radiative energy transfer efficiency dominates the non-radiative energy transfer efficiency for all acceptor concentrations.

## 4.2 Theoretical considerations

The radiative and non-radiative energy transfer in the system under consideration is analyzed using rate equations combined with Stern-Volmer plots. This allows us to estimate the radiative ($K_R$) and non-radiative ($K_{NR}$) rate constants. The rate equations of the donor-acceptor dye mixture at the lasing threshold are [9]:

$$\frac{dN_{1D}}{dt} = N_{0D}\sigma_{aD}W(t) - K_{NR}\, N_{1D}N_{0A} - \frac{N_{1D}}{\tau_D} \tag{4.1}$$

$$\frac{dN_{1A}}{dt} = N_{0A}\sigma_{aA}W(t) + (K_{NR}+K_R)\, N_{1D}N_{0A} - \frac{N_{1A}}{\tau_A} \tag{4.2}$$

$$N_D = N_{0D} + N_{1D} \tag{4.3}$$

$$N_A = N_{0A} + N_{1A} \tag{4.4}$$

where $N_{0D}$, $N_{1D}$, $N_{0A}$ and $N_{1A}$ are the population densities of Donor (D) and Acceptor (A) molecules in the ground (0) and excited (1) states respectively. $\sigma_{aD}$ and $\sigma_{aA}$ are the absorption cross sections for donors and acceptors at the pump wavelength (532 nm), $\tau_D$ and $\tau_A$ are the fluorescence lifetimes of the donor and acceptor without energy transfer and *W(t)* is the pump rate.

Dipole-dipole, dipole-quadrupole and quadrupole-quadrupole interactions among dye molecules may contribute to non-radiative energy transfer. We assume only dipole-dipole interactions. An oscillating dipole is generated when a fluorescent 'donor' is excited to resonate with a dipole of an 'acceptor' in the near field. The emission of the Rh6G fluorophores (donor) can couple to the excitation of the MB fluorophores (acceptor) when the acceptor dipole interacts with the donor dipole through non-radiative energy transfer [156]. The non-radiative energy transfer efficiency, $\eta_{NR}$ is given by [9, 159];

$$\eta_{NR} = \pi^{1/2} X \exp(X^2)(1 - \mathrm{erf}(X)) \tag{4.5}$$

where $X$ is the ratio of molar acceptor concentration [$A$], over the critical molar acceptor concentration $[A]_o$ as defined below.

($X = [A] / [A]_o$). The function erf ($X$) is given by;

$$\mathrm{erf}(X) = \frac{2}{\pi^{1/2}} \int_0^X \exp(-t^2)\, dt \tag{4.6}$$

and $[A]_o$ is [159];

$$[A]_o = \frac{3000}{2\pi^{\frac{3}{2}} \tilde{N} (R_0)^3} \text{ (in Molar, M)} \tag{4.7}$$

where $\tilde{N}$ is Avogadro's number and $R_o$ is the critical transfer distance of donor and acceptor molecules. $R_o$ is given by [9, 160];

$$R_o = \left(\frac{3000}{4\pi \tilde{N} [A]_{1/2}}\right)^{1/3} = \frac{7.35}{([A]_{1/2})^{1/3}} \text{ (in Angstroms, } \dot{A}) \tag{4.8}$$

where $[A]_{1/2}$ is the half-quenching concentration which can be obtained under the condition [9];

$$I_{DA} = I_D/2 \tag{4.9}$$

where $I_{DA}$ and $I_D$ are the emission intensities of the donor in the presence and absence of the acceptor respectively. According to the Förster energy transfer theory, $R_o$ (the Förster distance) is related to the energy transfer probability (rate), $P_{DA}$ as [9];

$$P_{DA} = \frac{1}{\tau_D}\left(\frac{R_0}{R}\right)^s \tag{4.10}$$

where $s$ is 6 for dipole-dipole, 8 for dipole-quadrupole and 10 for quadrupole-quadrupole interactions, $\tau_D$ is the fluorescence lifetime of the donor molecules without acceptors and $R$ is the average distance between the donor and acceptor.

The radiative energy transfer efficiency ($\eta_R$) is obtained from the total energy transfer efficiency, $\eta_T$ [9];

$$\eta_T = \eta_R + \eta_{NR} \tag{4.11}$$

where

$$\eta_R = 1 - \frac{I_{DA}}{I_D} \tag{4.12}$$

$$\eta_{NR} = 1 - \frac{\varphi_{DA}}{\varphi_D} \tag{4.13}$$

where $\varphi_{DA}$ and $\varphi_D$ are the quantum yields with and without acceptors. The radiative and non-radiative rate constants can be determined from Stern-Volmer plots, as shown by [9, 161];

$$\frac{I_D}{I_{DA}} = 1 + K_T\tau_D[A] \tag{4.14}$$

$$\frac{\varphi_D}{\varphi_{DA}} = 1 + K_{NR}\tau_D[A] \tag{4.15}$$

where $K_T$ and $K_{NR}$ are the total and non-radiative rate constants and [$A$] is the concentration of acceptors.

## 4.3 Experimental methods

### 4.3.1 Sample preparation

Methanol solutions with Rh6G (fixed concentration, $5 \times 10^{-4}$ M) and MB (various concentrations, $1 \times 10^{-4}$ to $9 \times 10^{-3}$ M) (Sigma Aldrich) in dye ratios ranging from 1:1 to 1:18 were added to titania nanoparticles, (200 nm particle diameter, number density $1 \times 10^{11}$ $cm^{-3}$) (Sigma Aldrich) and the solutions were placed in a cuvette (1 cm × 1 cm). Gain is provided by both dyes, while titania exhibits scattering effects due to its large refractive index contrast with the solvent, methanol (titania, 2.6 and methanol, 1.33). The transport mean free path, $l_t$ of the solution of titania nanoparticles without dyes, ~ 242 μm, was estimated from a Coherent Backscattering (CBS) experiment [44, 46, 131]. The systems operated in the diffusive regimes under the condition: the emission light wavelength, $\lambda < l_t < L$ [1] where $L$ is the dimension of the pumped region.

### 4.3.2 Optical measurements

The absorption and fluorescence spectra were measured using a Cary spectrophotometer (Varian Australia) and Fluorolog (Horiba Jobin Yvon) spectrofluorometer. For random laser measurements (figure 4.1), the samples were excited with a Q-switched, frequency-doubled Nd:YAG laser (532 nm, 10 Hz, 4 ns) with a 3 mm diameter excitation spot size at the sample ($L$) at an angle of 45$^o$ to the normal to the front face of the cuvette and the emission light was collected from the front face of the cuvette at 30$^o$ to the normal by a lens ($f$ = 5 cm) and measured by a fibre-coupled spectrometer (Ocean Optics Spectrometer (USB2000+UV-VS-ES) with a resolution ~ 1 nm). A thin teflon sheet inside the cuvette prevented back-reflection

from the cuvette's faces and a 532 nm edge filter blocked residual pump light from the spectrometer.

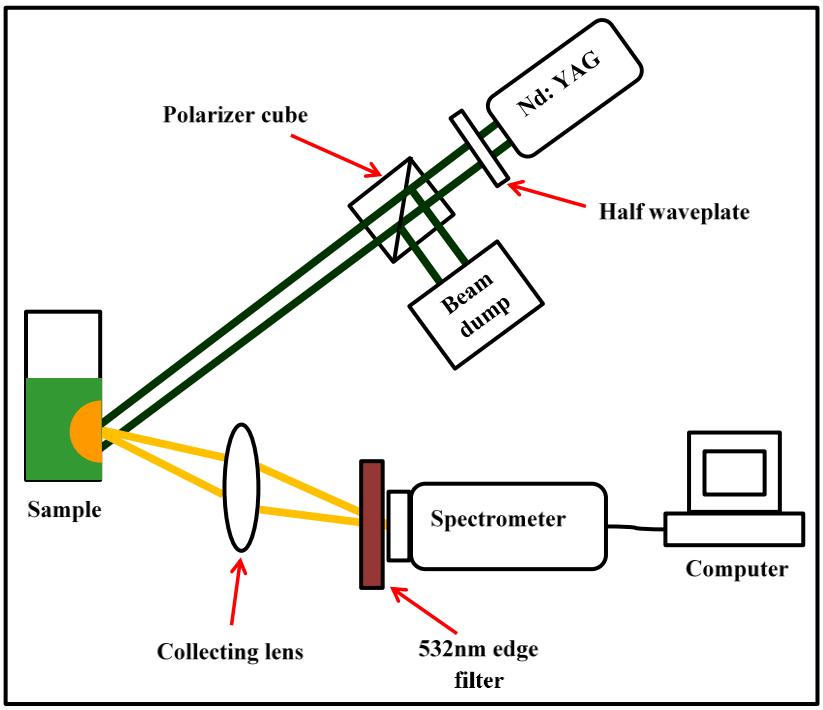


Figure 4.1 Random laser measurement

## 4.4 Experimental and theoretical results

### 4.4.1 Absorption and fluorescence spectra of donors and acceptors

The fluorescence and absorption spectra for both dyes are plotted in figure 4.2 (Rh6G and MB). This shows the spectral overlap between the donor fluorescence spectrum (Rh6G) and the acceptor absorption spectrum (MB) and indicates the possibility of energy transfer between these two dye molecules. MB has a fluorescence quantum yield of 4 % in water and a high proportion of dimer (with a characteristic absorption peak, $\lambda_{abs}$ ~ 590 nm) [162] as shown in figure 4.2. In contrast, the Rh6G quantum yield is substantially higher (95 %, [163]).

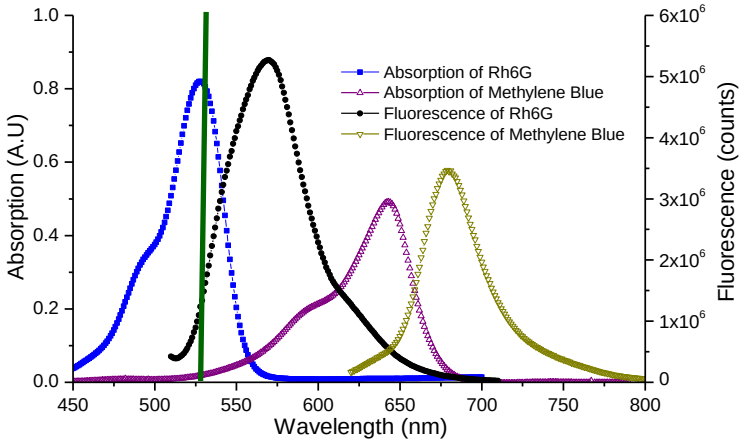


Figure 4.2 Absorption spectra of Rh6G (blue curve) and MB (purple curve); fluorescence spectra of Rh6G (black curve) and MB (olive curve). Both dyes have similar concentration, $5 \times 10^{-4}$ M. The green line shows the laser excitation at $\lambda \sim 532$ nm.

### 4.4.2 Spectral narrowing for random lasers based on dielectric nanoparticles

Due to the inefficient pump absorption of MB (see green line in figure 4.2), a random laser with MB dye and titania nanoparticles, pumped with 93 mJ/cm$^2$ does not reach lasing threshold. No spectral narrowing is observed in the MB / titania emission (figure 4.3 (a)). However, the addition of Rh6G allows this system to lase at ~ 710 nm with a low threshold. Below the lasing threshold (figure 4.3 (b)), the Rh6G emission intensity peaks at ~ 560 nm with no lasing emission at ~ 710 nm but when the system reaches threshold, it emits at ~ 710 nm (MB), with reduced Rh6G fluorescence.

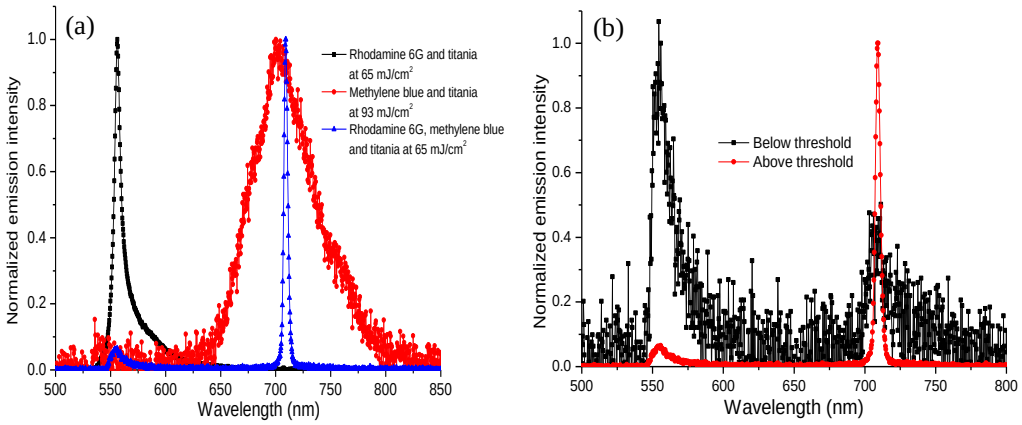


Figure 4.3 (a) The normalized emission spectra of Rh6G / titania, MB / titania and Rh6G / titania / MB random lasers. A Rh6G ($5 \times 10^{-4}$ M) / titania ($1 \times 10^{11}$ $cm^{-3}$) random laser is shown by the black curve. The emission from MB ($3 \times 10^{-3}$ M) / titania ($1 \times 10^{11}$ $cm^{-3}$) excited at 93 $mJ/cm^2$ is shown by the red curve. The emission from the Rh6G ($5 \times 10^{-4}$ M) / titania ($1 \times 10^{11}$ $cm^{-3}$) / MB ($3 \times 10^{-3}$ M) random laser is shown by the blue curve. (b) The normalized emission spectra of Rh6G ($5 \times 10^{-4}$ M) / titania ($1\times 10^{11}$ $cm^{-3}$) / MB ($3 \times 10^{-3}$ M) random lasers for below (37 $mJ/cm^2$) and above (65 $mJ/cm^2$) threshold.

### 4.4.3 Rhodamine 6G (Rh6G) emissions of Rh6G / Methylene blue (MB) / titania random lasers for low concentrations of MB ($1 \times 10^{-4}$ to $5 \times 10^{-4}$ M)

For Rh6G / MB titania random lasers with low MB concentrations ($1 \times 10^{-4}$ M to $5 \times 10^{-4}$ M), a narrow emission peak appears at ~ 560 nm instead of ~ 710 nm. Figure 4.4 shows the emission spectra of Rh6G ($5 \times 10^{-4}$ M) / MB ($5 \times 10^{-4}$ M) / titania ($1 \times 10^{11}$ $cm^{-3}$) random lasers, excited at ~ 42 $mJ/cm^2$. The emission intensity of Rh6G decreases and the Rh6G lasing threshold increases (figure 4.5) when the MB concentration is increased from $1 \times 10^{-4}$ M to $5 \times 10^{-4}$ M. This is attributed to the energy transfer from Rh6G to MB. Rh6G not only affects the MB emission but also its lasing threshold. For MB concentrations from $1 \times 10^{-4}$ M to $5 \times 10^{-4}$ M, Rh6G lasing is observed but no MB lasing is observed (figure 4.5). At these low MB concentrations, there is insufficient gain for MB, resulting in lasing at ~ 560 nm.

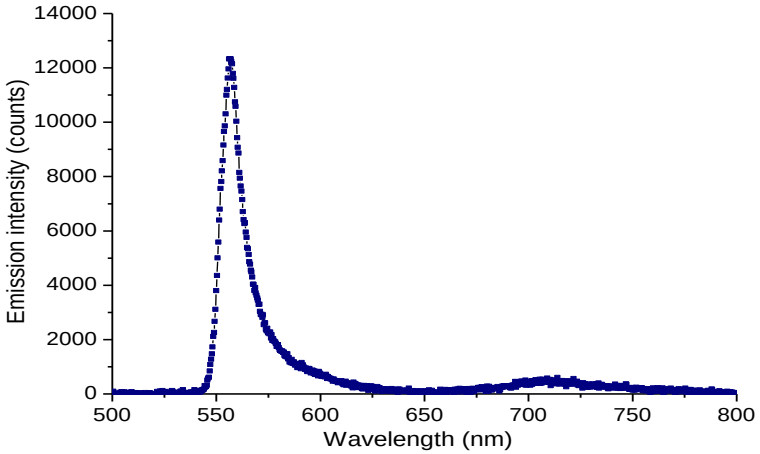


Figure 4.4 The emission spectra of Rh6G ($5 \times 10^{-4}$ M) / MB ($5 \times 10^{-4}$ M) / titania ($1 \times 10^{11}$ $cm^{-3}$) random lasers, excited at ~ 42 $mJ/cm^2$.

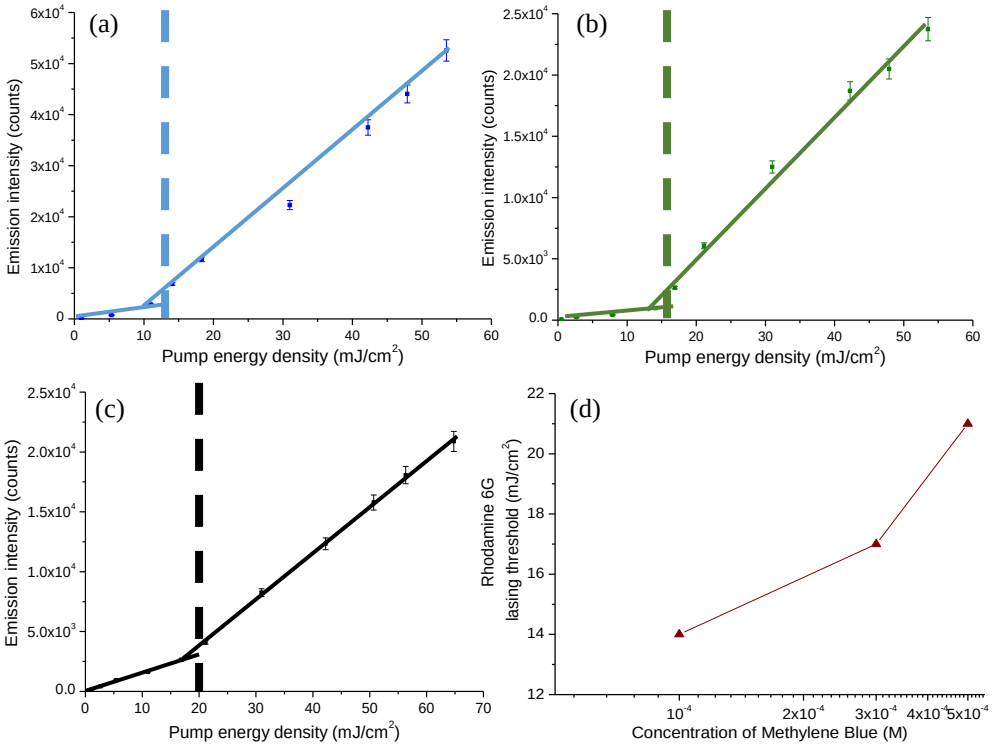


Figure 4.5 The emission peak intensity of Rh6G emissions for Rh6G / titania / MB random lasers at ~ 560 nm with fixed donor concentration ($5 \times 10^{-4}$ M) and various low concentrations of MB; (a) $1 \times 10^{-4}$ M, (b) $3 \times 10^{-4}$ M and (c) $5 \times 10^{-4}$ M. Figure 4.5(d) Comparison of Rh6G threshold of Rh6G / titania / MB random lasers for low concentrations of MB ($1 \times 10^{-4}$ M to $5 \times 10^{-4}$ M). The concentration of Rh6G is fixed at $5 \times 10^{-4}$ M. The straight lines show the nonlinear increase of emission intensity as a function of pump energy density and the dashed line is used to determine the threshold.

### 4.4.4 Methylene blue (MB) and Rhodamine 6G (Rh6G) emissions of R6G / MB / titania random lasers for increased concentrations of MB ($1 \times 10^{-3}$ to $9 \times 10^{-3}$ M)

Increasing the MB concentration to $1 \times 10^{-3}$ M produces lasing with a narrow emission peak at ~ 710 nm (figure 4.6) because the energy is efficiently transferred from the donor (Rh6G) to the acceptor (MB). For a MB concentration of $3 \times 10^{-3}$ M, the emission spectrum at ~ 560 nm substantially reduces (4× lower than that for 1 mM concentration MB) because the energy absorbed by the Rh6G dye is mostly transferred to the MB. Adding more MB broadens the emission at ~ 710 nm (figure 4.6 (c-e)). The MB emission spectrum for MB concentration above 12× Rh6G is broad (figure 4.6 (f)) as the lasing is not achieved even for high pump energy density. Both MB and Rh6G emissions reduce with increased MB concentration (figure 4.6 (c-e)).

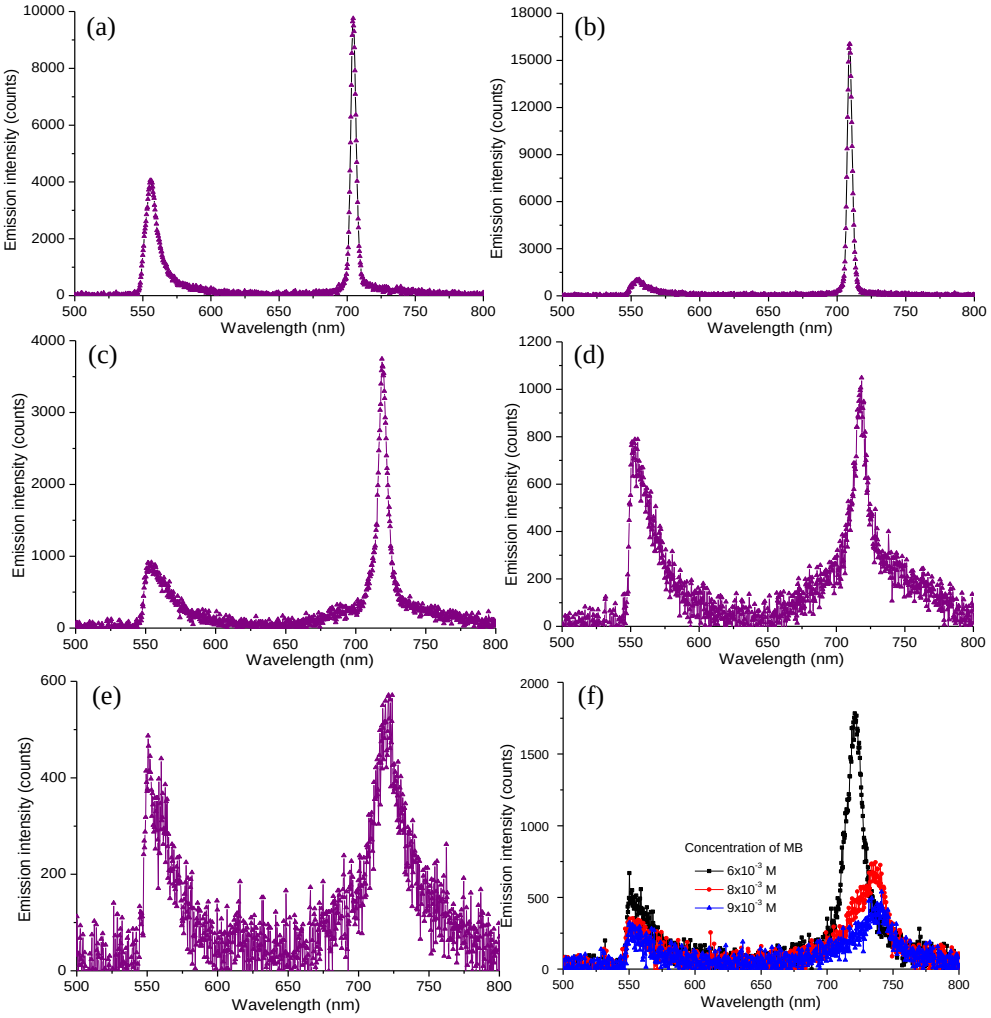


Figure 4.6 The emission spectra of Rh6G / MB / titania random lasers with fixed donor concentration ($5 \times 10^{-4}$ M) and varied acceptor concentrations; (a) $1 \times 10^{-3}$ M, (b) $3 \times 10^{-3}$ M, (c) $4 \times 10^{-3}$ M, (d) $5 \times 10^{-3}$ M and (e) $6 \times 10^{-3}$ M. All samples are excited at ~ 65 mJ/cm$^2$. Figure 4.6 (f) The emission spectra of Rh6G ($5 \times 10^{-4}$ M), titania ($1 \times 10^{11}$ cm$^{-3}$) / MB (12 to 18× concentration of Rh6G) at 85 mJ/cm$^2$.

When the MB concentrations increase from $1 \times 10^{-3}$ to $5 \times 10^{-3}$ M, we observe MB lasing (figure 4.7). Lasing thresholds for MB emission are clearly observed when the emission peak intensity increases nonlinearly with the pump energy density. The Rh6G emission intensity shows a linear increase with the pump energy density compared with the MB emission intensity, so no lasing threshold is evident for Rh6G emission and for MB concentrations above 12× Rh6G (figure 4.7).

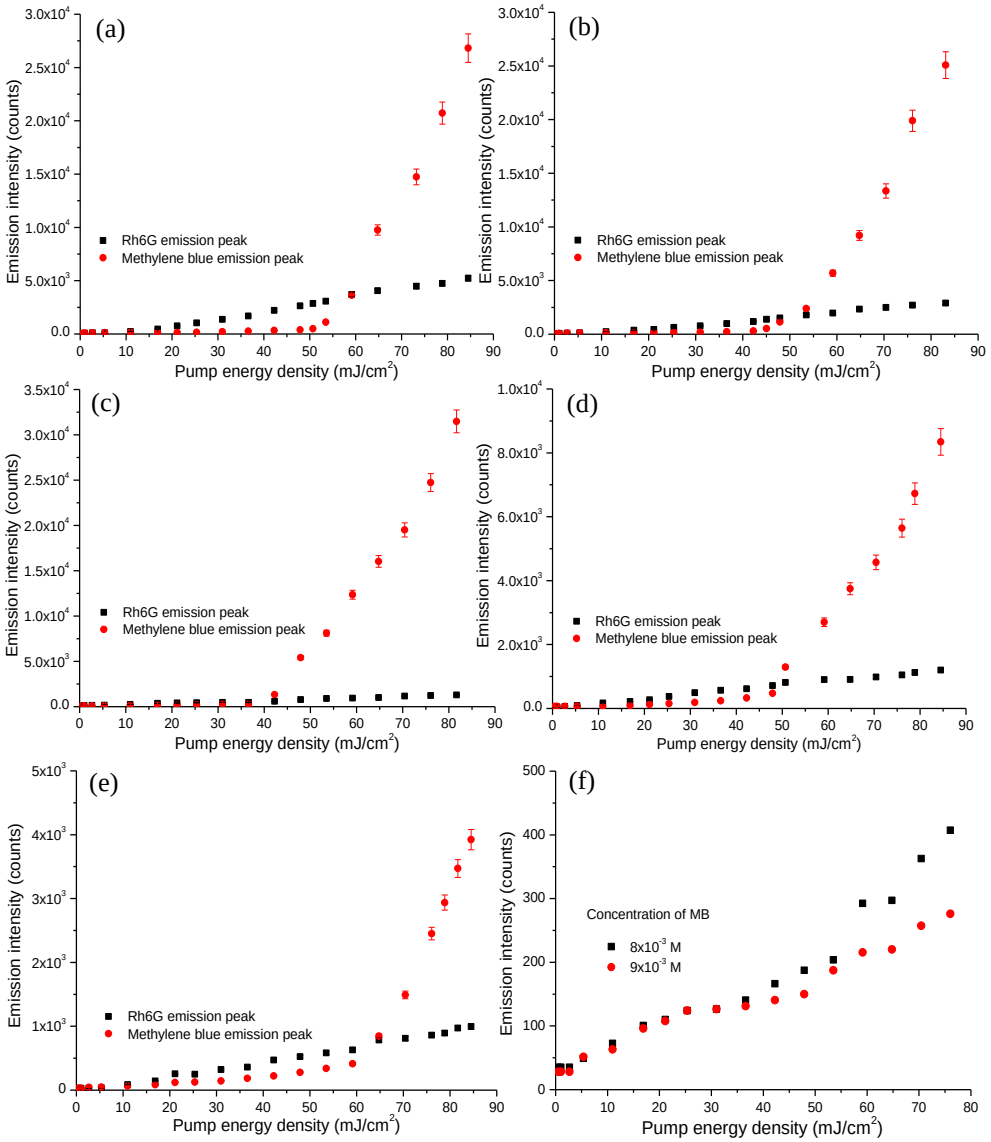


Figure 4.7 The emission peak intensity of Rh6G / titania / MB random lasers with fixed donor concentration ($5 \times 10^{-4}$ M) and various concentrations of acceptors; (a) $1 \times 10^{-3}$ M, (b) $2 \times 10^{-3}$ M, (c) $3 \times 10^{-3}$ M, (d) $4 \times 10^{-3}$ M and (e) $5 \times 10^{-3}$ M. Figure 4.7(f) The emission peak intensity of MB emission for Rh6G / titania / MB random lasers above 700 nm with fixed donor concentration ($5 \times 10^{-4}$ M) and increased concentration of MB (16 to 18× of concentration of Rh6G).

We find that the optimum MB concentration for our near infra-red random dye lasers should be 6× greater than the concentration of Rh6G (3 mM MB concentration). We believe the most relevant unit for the optimum concentration of the donor and acceptor dyes would be the dye concentrations. However in our case, both 3mM and 6× dye concentration are stated. The optimum MB concentration depends on the

concentration of the donor molecules. If we use a higher concentration of donor, we can determine a different optimum MB concentration.

The lasing thresholds of MB emission for different concentrations of MB are evident in figure 4.8 (a) where 3 mM of MB achieves the lowest lasing threshold in the present system. The corresponding slope of the threshold curves for 3 mM concentration MB is 1.3× and 3× higher than that for 2 mM and 4 mM concentration MB respectively (figure 4.8 (b)).

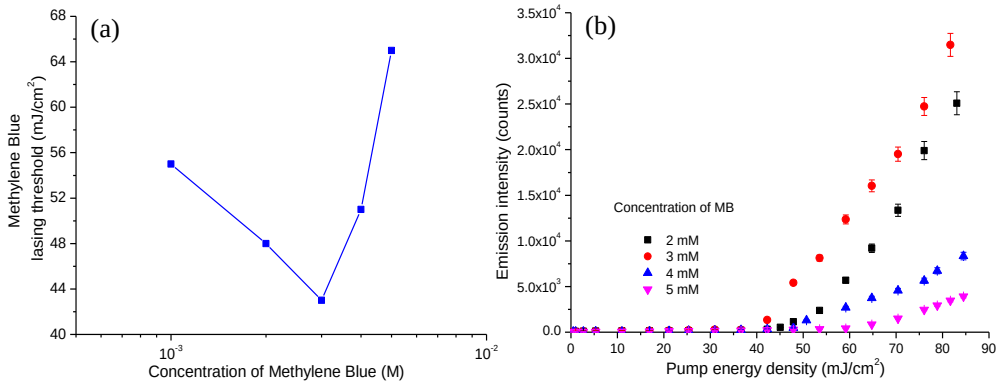


Figure 4.8 (a) Lasing thresholds of Rh6G / titania / MB random lasers (~ 710 nm emission) for increased MB concentrations ($1 \times 10^{-3}$ M to $5 \times 10^{-3}$ M). The concentration of Rh6G is fixed at $5 \times 10^{-4}$ M. (b) Comparison of threshold curves of Rh6G / titania / MB random lasers for MB emission at ~ 710 nm with fixed concentration of donor ($5 \times 10^{-4}$ M) and various concentrations of acceptors.

## 4.4.5 Energy transfer analysis

In this study, the $\eta_{NR}$ is calculated from eq. (4.5) with $[A_0]$, estimated as 0.56 M. The $\eta_{NR}$ increases linearly from 0.002 to 0.02 for MB concentrations $5 \times 10^{-4}$ to $5 \times 10^{-3}$ M. The radiative energy transfer efficiency, $\eta_R$ versus pump energy density is shown in figure 4.9; here $\eta_R$ increases with acceptor concentration. Figure 4.9 shows that $\eta_R$ is reduced for low MB concentration ($5 \times 10^{-4}$ M) compared with higher MB concentrations because there is no lasing emission at the acceptor wavelength (see figure 4.4). When the MB concentration is increased, the radiative energy transfer

efficiency approaches 1 following the appearance of emission peaks at ~ 710 nm (see figure 4.6). This shows that radiative energy transfer plays a crucial role in supporting lasing emission at the acceptor wavelength.

Kumar *et al.* [9] reported energy transfer from donors to acceptors for the situation when the concentration of donor ≥ concentration of acceptor and they observed negative slopes of $\eta_R$ as a function of pump energy density. In the present system, we observe positive slopes of $\eta_R$ as a function of pump energy density because the system operates in a different regime (concentration of donor ≤ concentration of acceptor). The positive slope arises due to the increased efficiency of energy transfer as a function of pump excitation since every pump photon can excite donor molecules which readily transfer the energy to an adjacent dye acceptor.

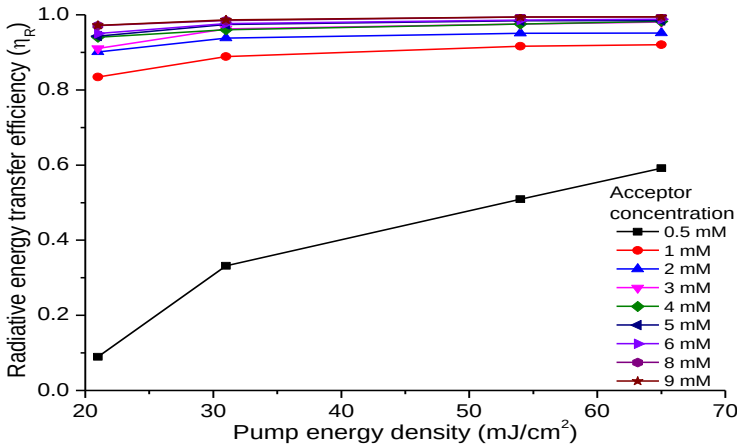


Figure 4.9 The estimated radiative energy transfer rate ($\eta_R$) for various acceptor concentrations in Rh6G / MB / titania random lasers based on different pump energy density.

Stern-Volmer plots (figures 4.10 and 4.11) are used to analyze the energy transfer in this system by calculating the radiative and non-radiative rate constants [9, 161]. Here, the fluorescence lifetime of the donor molecules without acceptors, $\tau_D$ is ~ 4 ns [8].

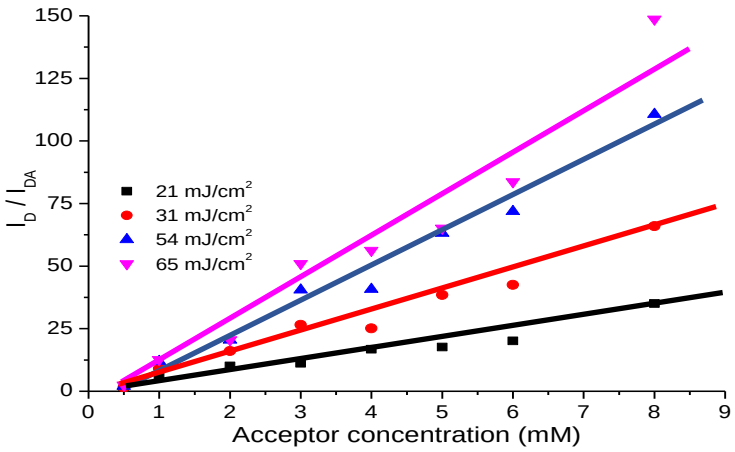


Figure 4.10 Measured $I_D / I_{DA}$ for various acceptor concentrations for different pump energy densities. The lines are fitted to the data for each pump energy density.

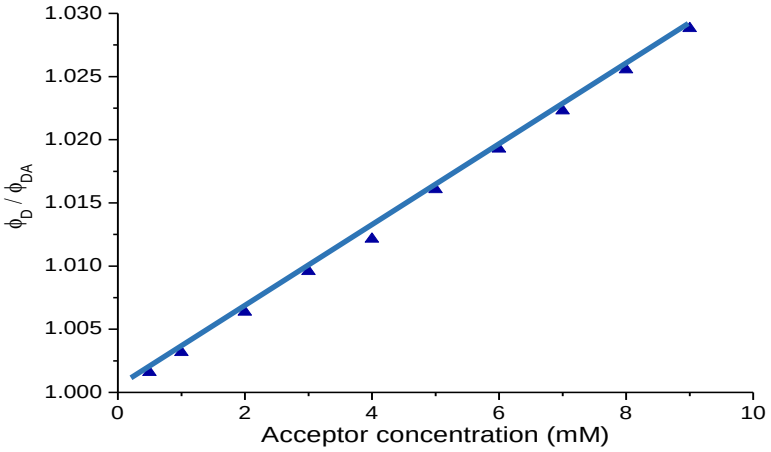


Figure 4.11 Calculated $\varphi_D / \varphi_{DA}$ versus various acceptor concentrations at 65 mJ/cm$^2$. The blue line is fitted to the data indicating a linear increase.

Both ratios $I_D$ / $I_{DA}$ and $\varphi_D$ / $\varphi_{DA}$ are linearly proportional to the acceptor concentration, consistent with the Stern-Volmer expressions, eq. (4.14) and eq. (4.15). $K_T$ and $K_{NR}$ values can be found from the gradient while $K_R$ can be calculated from $K_T = K_R + K_{NR}$. Here, $K_{NR}$ is estimated as $3 \times 10^{10}$ $M^{-1}s^{-1}$ and $K_R$ ranges from $7 \times 10^{11}$ to $4 \times 10^{12}$ $M^{-1}s^{-1}$ where $\tau_D \sim 4$ ns.

## 4.5 Discussion

### 4.5.1 Experiment and theoretical analysis

The energy transfer from Rh6G dye molecules (donor) to MB dye molecules (acceptor) can be described by both radiative and non-radiative processes evaluated from the rate equations and the Stern-Volmer plots. The optimum random laser performance is observed at an acceptor concentration of 3 mM. At this acceptor concentration, we calculate the radiative energy transfer efficiency to be almost ~ 1 while the non-radiative energy transfer efficiency is much less (~ 0.004). From the Stern-Volmer plots, the radiative energy transfer rate constant $K_R$ ($7 \times 10^{11}$ to $4 \times 10^{12}$ $M^{-1}s^{-1}$) is ~ 20× higher than $K_{NR}$ ($3 \times 10^{10}$ $M^{-1}s^{-1}$) for all measured pump levels, showing that radiative energy transfer dominates the energy transfer from Rh6G to MB dye molecules in this system.

### 4.5.2 FRET contribution in Rh6G / MB random lasers

Rh6G / MB / titania random lasers offer the probability of laser emission in both Rh6G and MB wavelength ranges. Because the Rh6G is a very efficient fluorescence emitter, it may lase over a wide range of conditions and transfer energy both radiatively and non-radiatively to MB which is a less efficient emitter.

We find at low MB concentrations ($1 \times 10^{-4}$ M to $5 \times 10^{-4}$ M), Rh6G lases and shows evidence of non-radiative energy transfer (with decreased Rh6G emission peak intensity and increased Rh6G threshold as a function of increased MB concentration) [62].

As the MB concentration is increased ($1 \times 10^{-3}$ M to $5 \times 10^{-3}$ M), lasing occurs at the MB wavelength since every pump photon contributes to more excitation of MB.

Laser emission develops at the MB emission peak and may compete with Rh6G for the available gain. At these MB / Rh6G concentration ratios, radiative energy transfer appears to dominate over non-radiative energy transfer as demonstrated by the radiative energy transfer efficiency for a concentration ≥ 1 mM (figure 4.9). In a mixture of two laser dyes, the Förster energy transfer occurs efficiently if the distance between the donor and acceptor is small < 30 $\dot{A}$ [164]. We estimate the average inter-molecular spacing ($\frac{1}{\sqrt[3]{N_T}}$, [158] ) is ~ 80 $\dot{A}$ where $N_T$ (total number density of donor and acceptor molecules) ~ $2.1 \times 10^{18}$ molecules/cm$^3$ when the MB concentration is 6× greater than the Rh6G concentration. At these concentrations, FRET may not be efficient for energy transfer. We note that it is challenging to create random lasers relying on the FRET mechanism with this pair of dyes due to their disparate fluorescence quantum yields.

### 4.5.3 Effects of energy transfer on emission intensity, emission linewidth and emission peak wavelength

Energy transfer affects the emission intensity of both donor (Rh6G) and acceptor (MB) (figures 4.4 and 4.6) since the emission intensity varies based on increasing MB concentrations. The emission intensity is quantitatively related to the radiative and non-radiative transfer efficiency. At $5 \times 10^{-4}$ M of MB concentration in Rh6G / MB / titania random lasers, the energy transfer from the donor to the acceptor is inefficient as emission occurs at the Rh6G emission wavelength but not the MB emission wavelength. At this MB concentration, the radiative and non-radiative energy transfer efficiencies are small ($\eta_R$ ~ 0.6 and $\eta_{NR}$ ~ 0.002). When more acceptor molecules (~ 3 mM of acceptor concentration) are added, the radiative and non-

radiative energy transfer rates increase, leading to higher emission intensity at the MB wavelength and reduced emission intensity at the Rh6G wavelength than $5 \times 10^{-4}$ M of MB concentration (figures 4.4 and 4.6). The emission intensity at the MB emission wavelength reaches the maximum value when most of the absorbed photons by MB are re-emitted (see figure 4.6 (b)). With increased MB concentration (4 mM as compared with 3 mM), self-quenching acceptor-acceptor interactions and re-absorption reduce the MB emission intensity (figure 4.6). Self-quenching arises with the increase of the non-radiative energy transfer efficiency [9].

The MB emission peak wavelength is red-shifted by about ~ 20 nm (from $1 \times 10^{-3}$ M to $6 \times 10^{-3}$ M) at higher MB concentrations, due to self-absorption of MB leading to red-shifted emission (figure 4.6). The intermolecular separation between Rh6G and the MB molecules reduces with increasing MB concentration.

### 4.5.4 Effect of energy transfer on lasing threshold

Radiative and non-radiative energy transfer also significantly influences the Rh6G / MB / titania random laser threshold. Higher non-radiative energy transfer leads to losses when the energy is released in the form of heat rather than light.

For lower MB concentration, when Rh6G dye molecules are not effectively pumping MB molecules, the lasing occurs at the Rh6G emission wavelength (figures 4.4 and 4.5). As the MB concentration increases, the MB molecules absorb Rh6G emission more effectively, resulting in sufficient gain for the MB to lase. Increasing acceptor concentration provides more gain for lasing, with a reduced lasing threshold (55 mJ/cm$^2$ for 1 mM of MB concentration to 43 mJ/cm$^2$ for 3 mM of MB concentration). However, excess acceptor molecules experience self-quenching,

which increases the lasing threshold (figures 4.7 and 4.8) or prevents lasing at the acceptor wavelength. Excess MB may also hinder efficient pump absorption by Rh6G, thus resulting in a higher lasing threshold.

## 4.6 Chapter 4 Summary

Random lasing emission with a narrow emission peak (~ 4 nm) beyond 700 nm is achieved by combining two dyes with scatterers. Methylene blue (MB) dye is a less efficient dye for random lasers excited with 532 nm green light but with the addition of Rhodamine 6G (Rh6G), MB can reach the laser threshold. For low MB concentrations ($1 \times 10^{-4}$ M to $5 \times 10^{-4}$ M), the random laser emission is from Rh6G at ~ 560 nm whereas for MB concentrations ($1 \times 10^{-3}$ M to $5 \times 10^{-3}$ M), the emission is from MB at ~ 710 nm. Both random laser emissions are affected by radiative and non-radiative energy transfer. The MB lasing emission intensity at ~ 710 nm is enhanced as the Rh6G emission intensity at ~ 560 nm reduces for MB concentrations from $1 \times 10^{-3}$ M to $5 \times 10^{-3}$ M. A MB concentration ($3 \times 10^{-3}$ M) at 6× the Rh6G concentration is needed to achieve optimum random lasing. The radiative and non-radiative energy transfer efficiencies are compared using Stern-Volmer plots. Both radiative and non-radiative energy transfers influence the lasing threshold and spectral emission of random lasers depending on the acceptor concentration. Radiative energy transfer dominates in the present systems since $K_R$ is 20 times higher than $K_{NR}$. Adding acceptors to facilitate energy transfer can improve the efficiency of random dye lasers but an excess concentration of acceptors leads to fluorescence quenching.

# Chapter 5

# Plasmonic enhancement of Rhodamine dye random lasers

Chapter 5 consists of two sections: 5.1 Colloidal-solution Plasmonic Rhodamine dye random lasers and 5.2 Solid-state Plasmonic Rhodamine dye random lasers. In Section 5.1, the passive scatterers were suspended in a dye-methanol solution whereas in Section 5.2, the scatterers / dyes were mixed in polymer solution and dried as a solid-state polymer film.

In this chapter, we demonstrated improved characteristics in Rhodamine dye random lasers with the addition of gold nanoparticles for both colloidal-solution and solid-state random dye lasers due to plasmonic effects. We observed contrasting trends of lasing threshold between random dye lasers incorporating dielectric and metal nanoparticles. The effects of gold nanoparticles in random dye lasers are discussed in the context of the tradeoff between local field enhancement and fluorescence quenching. Effects of film thickness, dye concentration and glass substrate on solid-state Rhodamine dye random lasers are also discussed.

Results in Section 5.1 Colloidal-solution Plasmonic Rhodamine dye random lasers have been published as:

W. Z. Wan Ismail, T. P. Vo, E. M. Goldys and J. M. Dawes, "Plasmonic enhancement of Rhodamine dye random lasers," Laser Physics **25**, 085001 (2015).

The first author (W. Z. Wan Ismail) set up and conducted the experiment, analyzed the experiment results and wrote the article. The second author (T. P. Vo) gave advice in the experimental method and the other authors (E. M. Goldys and J. M. Dawes) supervised the first author in setting up the experiment, analysing and discussing the results and revising the article.

## 5.1 Colloidal-solution Plasmonic Rhodamine dye random lasers

### 5.1.1 Introduction

Metallic nanoparticles within the laser medium (with a larger scattering cross section than dielectric particles of the same size [15, 39, 165]) concentrate the optical field near the nanoparticle surface, creating localized surface plasmons (LSPs). Their addition results in increased gain and enhanced laser performance [15, 39, 165]. Earlier work by Dice *et al.* [55] reported enhanced random laser emission with silver nanoparticles in a Rhodamine 6G (Rh6G) random dye laser. Meng *et al.* [37, 39] demonstrated the advantages of local field enhancement for gold / silver core shell nanoparticles in Rh6G dye lasers. However, a high concentration of metal nanoparticles not only increases the scattering strength but also increases the absorption loss and fluorescence quenching. The overlap of the plasmon resonance of metallic nanoparticles with the emission spectrum of the dye medium leads to both local field enhancement, increasing the dye excitation [37, 39] and fluorescence quenching or energy transfer, reducing the dye emission [11, 166]. Hence, the effect

on random lasing of combining metal nanoparticles with a specific dye is a balance between these competing effects.

In Section 5.1, we aim to improve the performance of random dye lasers by investigating the effects of spectral overlap, local field enhancement, fluorescence quenching and scattering / absorption from gold nanoparticles on the behavior of two different random dye lasers; Rh6G and Rhodamine 640 (Rh640). We report the following findings. (1) Rh6G random lasers with gold perform better than Rh6G random lasers with alumina in the weakly scattering regime. (2) Excessive gold reduces the performance of Rh6G random lasers because of fluorescence quenching due to strong spectral overlap of Rh6G fluorescence with the gold plasmon resonance. (3) Although Rh640 has less effective pump absorption at 532 nm than Rh6G, the addition of gold nanoparticles and consequent plasmonic effects, enhances the performance of the Rh640 random lasers.

## 5.1.2 Experimental methods

### 5.1.2.1 Sample preparation

The random dye laser samples were prepared as follows. Commercial dyes, Rh6G ($1 \times 10^{-3}$ M) and Rh640 ($1 \times 10^{-3}$ M and $2.2 \times 10^{-3}$ M) (Sigma Aldrich) were dissolved separately in methanol to provide the laser gain media. Alumina nanoparticles, average diameter ~ 150 nm (Sigma Aldrich) with final concentrations of $3 \times 10^{10}$ to $1 \times 10^{12}$ $cm^{-3}$ and gold nanoparticles, average diameter ~ 60 nm (Ted Pella) with final concentrations of $3 \times 10^{9}$ $cm^{-3}$ to $8 \times 10^{11}$ $cm^{-3}$ were mixed separately with the dye solutions. The gold nanoparticles were capped/stabilized with citrate and

have negative surface charges (Ted Pella data sheet). The scattering mean free path, $l_s$ was calculated based on [3, 28, 36-38];

$$l_s = 1/(\rho\sigma_s) \quad (5.1)$$

where $\rho$ is the particle concentration and $\sigma_s$ is the scattering cross section (estimated through Mie theory [35, 36, 41, 84, 154]), involving two regimes; the weakly scattering regime ($l_s \geq L$) and the diffusive regime ($L > l_s > \lambda$) [1, 3]. $L$ is the sample size (2 mm) and $\lambda$ is the emission wavelength. In this study, the scattering length, $l_s$ for nanoparticles at pump wavelength was varied from 0.35 mm to 111.1 mm. All samples were ultrasonically dispersed for 30 minutes before each experiment.

#### 5.1.2.2 Optical measurements

The same random laser experimental set up in Chapter 3 (3.2.2.3 Emission spectrum measurement) was used in this chapter. The random dye laser samples were placed in a quartz cuvette (1 cm × 1 cm) with a thin piece of teflon was positioned inside the cuvette. The samples were excited by a Q-switched frequency-doubled Nd:YAG laser at 45$^o$ from the normal to the cuvette face. The pump spot diameter was 2 mm and the dye laser emission from the front face of the cuvette was collected by a fibre coupled spectrometer. The absorption and fluorescence spectra were measured using a Cary spectrophotometer and Fluorolog spectrofluorometer.

### 5.1.3 Results

#### 5.1.3.1 Absorption and fluorescence spectra

Strong resonant coupling arises between the Rh6G and Rh640 and the gold nanoparticles due to the overlap of their respective absorption and fluorescence spectra, which is shown in figures 5.1 and 5.2. We observe that gold and Rh6G absorb

pump light more strongly than Rh640 and the pump absorption cross-section for Rh6G is ~ 2.2× greater than Rh640. The localized surface plasmon resonance (LSPR) peak for gold nanoparticles overlaps with the absorption and fluorescence spectra for both Rh6G and Rh640 respectively.

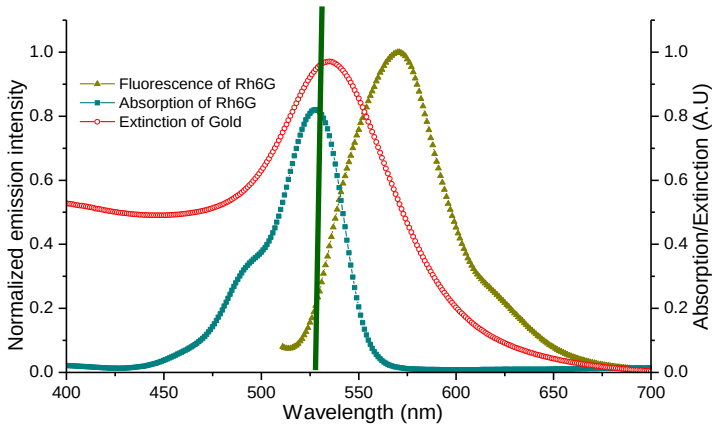


Figure 5.1 Fluorescence and absorption (extinction) spectra of Rh6G ($5 \times 10^{-4}$ M) and gold nanoparticles ($8 \times 10^{10}$ $cm^{-3}$). The fluorescence spectrum of Rh6G (gold curve) overlaps with the plasmon resonance of gold extinction (red curve). The straight green line shows the 532 nm excitation.

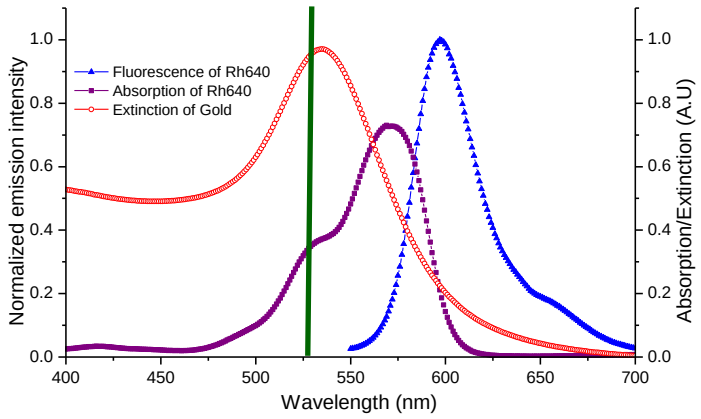


Figure 5.2 Fluorescence and absorption (extinction) spectra of Rh640 ($5 \times 10^{-4}$ M) and gold nanoparticles ($8 \times 10^{10}$ $cm^{-3}$). The fluorescence spectrum of Rh640 (blue curve) slightly overlaps with the plasmon resonance of gold extinction (red curve). The straight green line shows the 532 nm excitation.

### 5.1.3.2 Random dye lasers with alumina nanoparticles

Similar concentrations of dyes (Rh6G and Rh640) ($1 \times 10^{-3}$ M) with various concentrations of alumina ($3 \times 10^{10}$ to $1 \times 10^{12}$ nanoparticles per $cm^3$) were used. The

threshold characteristics of Rh6G / alumina random lasers in the weakly scattering and diffusive regimes were reported in Chapter 3 (Spectral and coherence signatures of threshold in random lasers). Higher emission intensity with reduced fluorescence background was obtained with higher alumina concentration. The emission spectra above threshold for different mean scattering lengths exhibit a narrow emission peak between 570 nm to 572 nm with some fluorescence background.

The Rh640 / alumina random laser emission spectra with increasing alumina concentrations are shown in figure 5.3 (a). There is still a pronounced fluorescence background for the highest concentration of alumina. The emission peak wavelength varies between 608 nm to 610 nm, but the spectral width narrows slightly with increased pump energy density. The full width at half maximum (FWHM) is larger than for the Rh6G / alumina random laser, decreasing from 15 nm ($3 \times 10^{10}$ and $3 \times 10^{11}$ $cm^{-3}$) to 6 nm ($1 \times 10^{12}$ $cm^{-3}$); (figure 5.3). The emission peak intensity increases with particle concentration and the lasing threshold is observed when emission peak intensity increases nonlinearly with the pump energy density (figure 5.3 (b)).

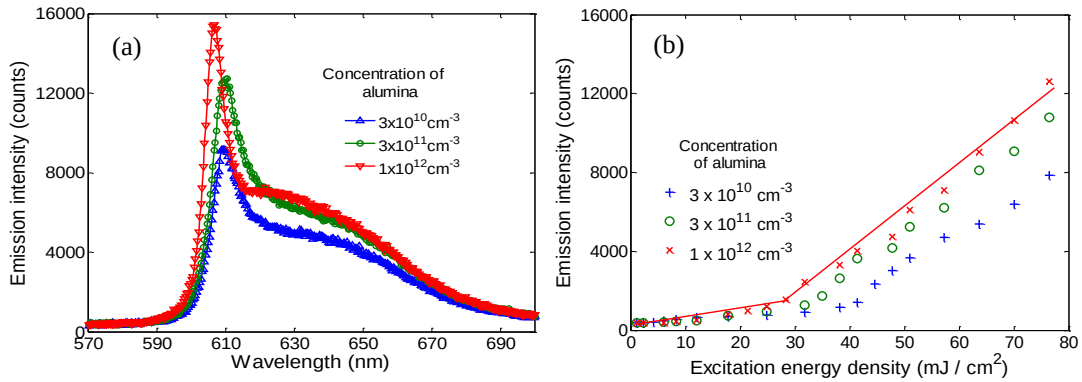


Figure 5.3 (a) Emission intensity spectra of Rh640 / alumina random lasers with different alumina concentrations ($3 \times 10^{10}$ to $1 \times 10^{12}$ $cm^{-3}$) at 83 $mJ/cm^3$ and (b) Emission peak intensity of Rh640 / alumina random lasers with various alumina concentrations as a function of excitation energy density. The red line indicates the lasing threshold for Rh640 / alumina random lasers with $1 \times 10^{12}$ $cm^{-3}$ of alumina. The uncertainty in these emission spectrum measurements was ± 3%.

The lasing threshold for both Rh6G / alumina and Rh640 / alumina random lasers decrease when the particle concentration is increased from $3 \times 10^{10}$ $cm^{-3}$ (weakly scattering regime) to $1 \times 10^{12}$ $cm^{-3}$ (diffusive regime) as shown in figure 5.4. The lowest threshold is achieved in random dye lasers with $1 \times 10^{12}$ $cm^{-3}$ of alumina concentration.

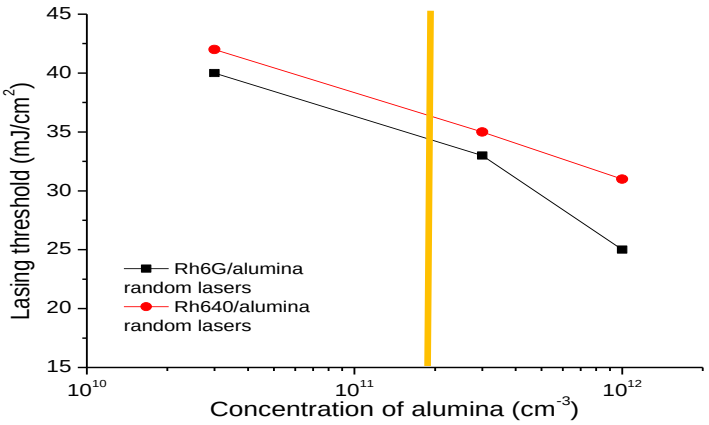


Figure 5.4 Lasing threshold versus particle concentrations for both random dye lasers with alumina. The vertical orange line indicates the transition from the weakly scattering regime to the diffusive regime at ~ 530 nm.

### 5.1.3.3 Random dye lasers with gold nanoparticles

The addition of gold nanoparticles to random dye lasers gives a narrow emission peak with a reduced fluorescence background even at low gold nanoparticle concentrations. A fixed concentration of dyes ($1 \times 10^{-3}$ M) with varied concentration of gold nanoparticles ($3 \times 10^{9}$ to $8 \times 10^{11}$ $cm^{-3}$) was used, unless otherwise stated.

We first discuss Rh6G ($1 \times 10^{-3}$ M) / gold ($8 \times 10^{10}$ $cm^{-3}$) random lasers which exhibit emission spectra with reduced background fluorescence and a narrow emission peak (3 nm) (figure 5.5).

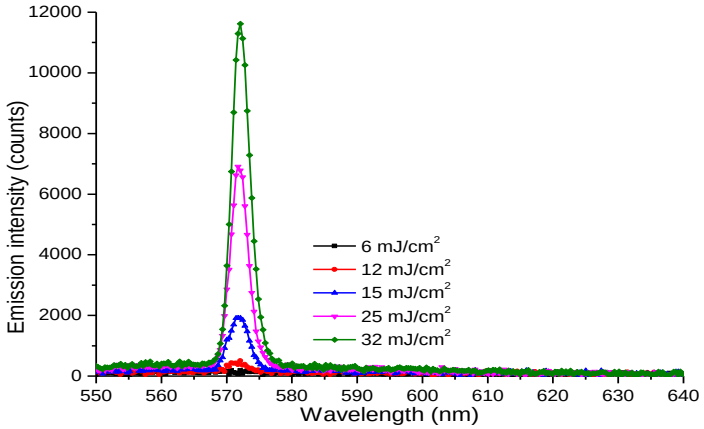


Figure 5.5 Emission intensity spectra of Rh6G ($1 \times 10^{-3}$ M) random lasers with gold nanoparticles ($8 \times 10^{10}$ $cm^{-3}$) pumped with different excitation energy densities. The lasing threshold is ~ 15 $mJ/cm^2$.

Figure 5.6 shows the variation of emission peak wavelength and lasing thresholds for Rh6G / gold random lasers with various gold concentrations. The emission peak wavelength is slightly changed between 570 nm to 572 nm for different excitation energy densities and particle concentrations, and is similar to that obtained from Rh6G / alumina random lasers. The random dye lasers can be divided into 2 regimes (as explained in Chapter 1 (Section 1.2.2.1)): the diffusive and the weakly scattering regimes (shown by the vertical orange line in figure 5.6) based on the concentration of gold nanoparticles. The threshold reduces in the weakly scattering regime with increasing gold, but it increases for samples in the diffusive regime. The lowest lasing threshold is observed for a gold concentration of $8 \times 10^{10}$ $cm^{-3}$.

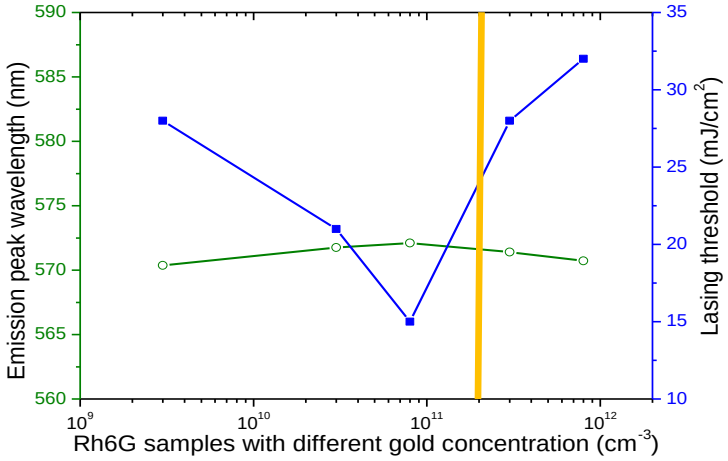


Figure 5.6 The emission peak wavelength (empty circles) and lasing thresholds (filled squares) of Rh6G ($1 \times 10^{-3}$ M) random lasers with various concentrations of gold nanoparticles. The emission peak wavelength is slightly changed between 570 nm to 572 nm. The lasing threshold is shown by the blue line with filled squares. The vertical orange line indicates the transition from the weakly scattering regime to the diffusive regime at ~ 530 nm.

We now discuss Rh640 / gold random lasers. As shown in figure 5.7, Rh640 ($1 \times 10^{-3}$ M) / gold ($8 \times 10^{10}$ cm$^{-3}$) random lasers show a narrow emission peak at 628 nm (~ 3 nm) above threshold, which is shifted with respect to the Rh640 / alumina random lasers, which operate at 610 nm (figure 5.3 (a)). The emission peak spectral width remains constant for lasing above threshold. Figure 5.7 shows a lasing threshold at ~ 12 mJ/cm$^2$.

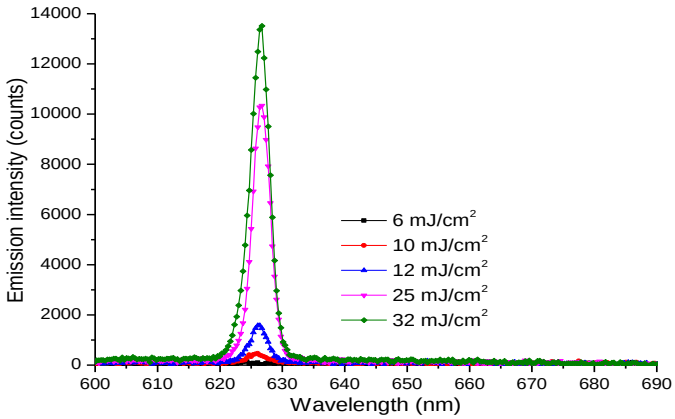


Figure 5.7 Emission spectra of Rh640 ($1 \times 10^{-3}$ M) random lasers with gold nanoparticles ($8 \times 10^{10}$ cm$^{-3}$) pumped with different excitation energy densities. The lasing threshold is ~ 12 mJ/cm$^2$.

The emission peak wavelength is red-shifted (from 621 nm to 631 nm) when the gold concentration increases from $3 \times 10^{9}$ to $8 \times 10^{11}$ $cm^{-3}$, as shown in figure 5.8. The lasing thresholds for Rh640 / gold random lasers are plotted in figure 5.8, indicating that the lowest lasing threshold occurs for $8 \times 10^{10}$ $cm^{-3}$ of gold nanoparticle concentration. Figure 5.8 also shows a similar trend with Rh6G / gold random lasers (as in figure 5.6) where the threshold decreases in the weakly scattering regime and increases in the diffusive regime.

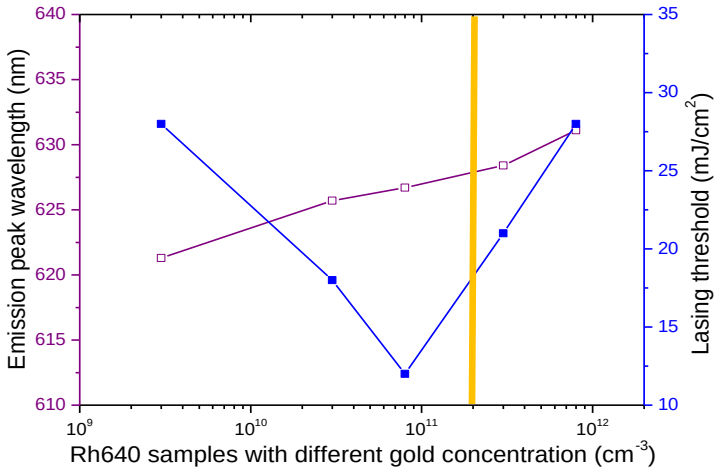


Figure 5.8 The emission peak wavelength (empty rectangles) and lasing thresholds (filled squares) of Rh640 ($1 \times 10^{-3}$ M) random lasers with various concentrations of gold nanoparticles. The emission peak is red-shifted when the gold concentration increases from $3 \times 10^{9}$ $cm^{-3}$ to $8 \times 10^{11}$ $cm^{-3}$. The lasing thresholds as a function of gold concentration are shown as filled squares with a blue line. The vertical orange line indicates the transition from the weakly scattering regime to the diffusive regime at ~ 530 nm.

For a more detailed comparison of Rh640 and Rh6G random lasers with similar absorbed pump energy, the concentration of Rh640 was increased to $2.2 \times 10^{-3}$ M compared with Rh6G ($1 \times 10^{-3}$ M), while the concentration of gold was varied from $3 \times 10^{9}$ to $8 \times 10^{10}$ $cm^{-3}$. This ensured similar pump absorption values and size of lasing regions. The emission spectra of Rh640 ($2.2 \times 10^{-3}$ M) / gold random lasers with different gold concentrations are shown in figure 5.9. The emission peak slightly shifts to a longer wavelength for increasing gold concentration, and also shifts (~ 3

nm) to a longer wavelength when the concentration of Rh640 increases from $1 \times 10^{-3}$ M (figure 5.7) to $2.2 \times 10^{-3}$ M (figure 5.9).

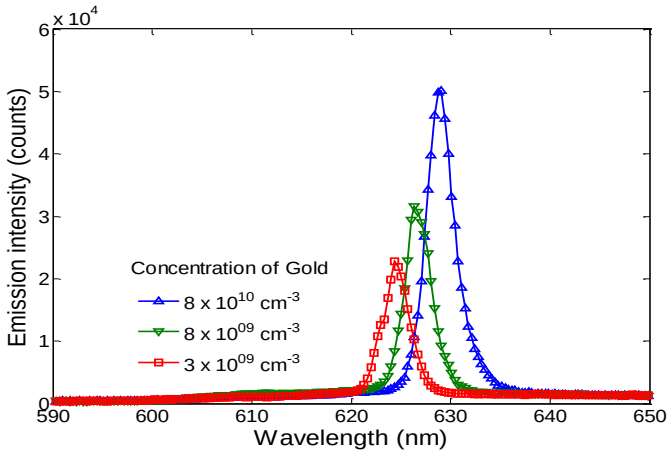


Figure 5.9 Emission intensity spectra for Rh640 ($2.2 \times 10^{-3}$ M) random lasers with various concentrations of gold nanoparticles and excitation energy density of 57 mJ/cm$^2$. The graph shows the emission peak movement to the shorter wavelength when the concentration of gold decreases from 8 $\times 10^{10}$ to 3 $\times 10^{9}$ cm$^{-3}$.

Figure 5.10 shows that the lasing threshold reduces and the emission peak intensity increases when the concentration of Rh640 increases from $1 \times 10^{-3}$ M to $2.2 \times 10^{-3}$ M. Rh640 random lasers ($2.2 \times 10^{-3}$ M) produce higher emission peak intensity and lower threshold than Rh6G ($1 \times 10^{-3}$ M) random lasers for equivalent pump energy absorption.

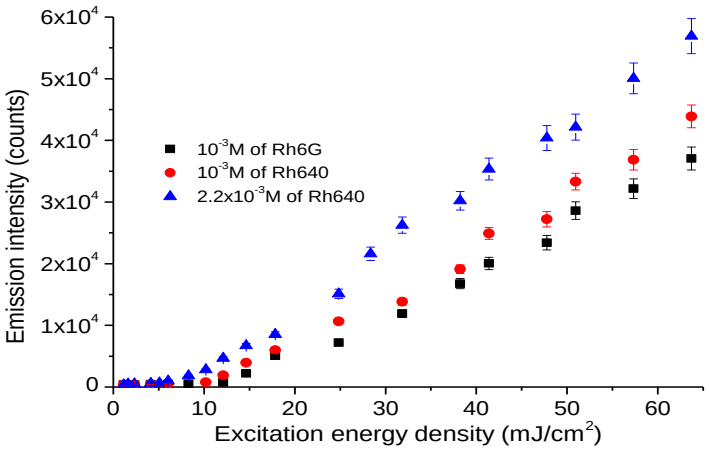


Figure 5.10 Emission peak intensity of random dye lasers (Rh640 ($1 \times 10^{-3}$ M and $2.2 \times 10^{-3}$ M) and Rh6G ($1 \times 10^{-3}$ M)) with similar gold concentration ($8 \times 10^{10}$ cm$^{-3}$).

## 5.1.4 Discussion

### 5.1.4.1 Dielectric nanoparticles in random dye lasers

Alumina nanoparticles are effective elastic scatterers and at large alumina concentrations, the lasing threshold is reduced. The scattering mean free path, $l_s$ at $\lambda$ = 530 nm for random dye lasers with alumina, ranges from 11.6 mm, in the weakly scattering regime ($l_s \geq L$) to 0.35 mm, in the diffusive regime ($L > l_s > \lambda$). When the scattering mean free path is decreased, the lasing threshold correspondingly decreases (figure 5.4). The refractive index of alumina is 1.77 [167] at $\lambda$ = 530 nm and refractive index of methanol is 1.33 giving a moderate refractive contrast that yields moderate scattering strength. Therefore, a high particle concentration is needed to provide adequate scattering to initiate random lasing.

In the Rh640 / alumina random lasers, the lasing threshold and the emission peak linewidth both reduce with increasing alumina concentration (figure 5.3 (a)). However, an increased alumina concentration ($1 \times 10^{12}$ $cm^{-3}$ of alumina) with Rh640 does not completely reduce the fluorescence background, unlike the behavior with Rh6G (as shown in Chapter 3).

### 5.1.4.2 Metal nanoparticles in random dye lasers

Addition of gold nanoparticles to random dye lasers increases the gain due to the enhanced local electric field near the surface of metal nanoparticles. In the weakly scattering and diffusive regimes, the scattering length $l_s$ at $\lambda$ = 530 nm for random dye lasers with gold nanoparticles is varied from 0.42 mm to 111.1 mm. We observe a higher emission peak intensity and reduced lasing threshold in random dye lasers using gold nanoparticles compared to random dye lasers using alumina in both regimes.

*5.1.4.2.1 Emission peak shift*

The emission peak is slightly varied between ~ 570 nm to 572 nm for Rh6G random lasers, as shown in figure 5.6. Rh6G and gold both absorb the pump light strongly, with resonant coupling due to spectral overlap, leading to maximum gain at the fluorescence peak [39] which then determines the wavelength of the emission [84].

Rh640 random lasers with metal nanoparticles have not been previously reported, possibly because the bichromatic emission of Rh640 tends to reduce the output intensity. The competition between monomer and dimer emitters is affected by dye and scatterer concentrations, type of scatterers and pump energy [168, 169] and these influence the lasing wavelength [64]. Differential absorption of the monomer and dimer emitted light by the gold nanoparticles shifts the lasing wavelength (~ 610 nm for Rh640 / alumina random laser to ~ 625 nm for Rh640 / gold random laser). Lagendijk *et al.* [64] observed the wavelength shift in Rh640 with the addition of Quinaldine Blue, (QB) (non-fluorescent dye). We observe the addition of gold to Rh640 random lasers reduces the fluorescence background.

*5.1.4.2.2 Spectral overlap*

The Rh6G absorption peak overlaps with the localized surface plasmon resonance of gold (figure 5.1) resulting in coupling between metal and fluorophores and hence localization of the pump light. However, excessive pump absorption by dye and gold nanoparticles may result in high absorption loss. Rh640 does not absorb the pump light efficiently, but the increase of pump absorption by gold nanoparticles can enhance Rh640 fluorescence. The strong spectral correlation between the dyes and gold nanoparticles shown in figures 5.1 and 5.2 can be related to the fluorescence

enhancement factor or apparent brightness *Y* of a fluorophore with metal nanoparticles given by [13, 14];

$$Y = \gamma_{ex}(\omega_{ex})Q_{EM}(\omega_{em}) \quad (5.2)$$

where $\gamma_{ex}(\omega_{ex})$ is the near-field excitation rate of the fluorophores at the excitation frequency $(\omega_{ex})$ and $Q_{EM}(\omega_{em})$ is the quantum yield for the far field emission at the emission frequency $\omega_{em}$. The excitation rate $\gamma_{ex}(\omega_{ex})$ depends on the spectral overlap of the plasmon resonance with the absorption spectrum of the dye while $Q_{EM}$ depends on both the radiative and non-radiative decay rates of the fluorophores. These competing effects lead to both increases and decreases in the fluorescence efficiency of nearby fluorophores [13].

Rh640 / gold random lasers produce narrow emission linewidth with less fluorescence background compared with Rh640 / alumina random lasers (figures 5.3 (a) and 5.7). Gold nanoparticles absorb the energy of the incident photons and couple with Rh640 dye molecules to localize the pump light [39, 54, 55]. Thus, Rh640 / gold random lasers exhibit reduced threshold compared with Rh640 / alumina random lasers. Spectral overlap of the gold plasmon resonance band with the dye emission spectrum produces a high output emission intensity with low threshold [47]. When they are excited resonantly, metal nanoparticles can act as nano-antennas [170, 171] and transfer pump energy non-radiatively to the surrounding fluorophores as well as scattering the fluorophores' emission. By increasing the concentration of Rh640 to 2.2 × $10^{-3}$ M, the pump absorption is increased. A small red shift in the emission wavelength is observed with increasing dye concentration, due to photon reabsorption with energy transfer among dye molecules [168, 172].

The overlap of the dye fluorescence spectrum with the gold extinction spectrum (figures 5.1 and 5.2) helps gold nanoparticles to couple to the dye molecules when they confine the emission light through local surface plasmon resonance, leading to intensified output emission, but such overlapping can also quench the dye emission [11, 13, 166] resulting in low emission intensity. There is a tradeoff between emission intensity enhancement and quenching that is controlled by the distance between the fluorophores and metal nanoparticles [11] which depends on the relative concentration of dyes and nanoparticles.

*5.1.4.2.3 Local electric field enhancement and fluorescence quenching*

The change in lasing threshold in random dye lasers with gold nanoparticles (figures 5.6 and 5.8) is correlated with fluorescence enhancement and quenching phenomena, depending on distance, *d*, between donor and acceptor [11, 39]. *d* also depends on dye and particle concentration [11, 166] and is proportional to the Förster distance ($R_o$) given by [11, 173, 174];

$$R_0 = 0.211\left[K^2 n^{-4} \varphi_{dye}\, J(\lambda)\right]^{1/6} \text{Å} \tag{5.3}$$

where $K^2$ is the orientation factor, $n$ is the refractive index of the medium, $\varphi_{dye}$ is the quantum efficiency of dye and $J(\lambda)$ is the overlap integral between the absorption peak of gold and the emission peak of the dye. In this study, we used $K^2 = 2/3$ assuming that both dyes and gold nanoparticles are freely rotating and isotropically oriented [11], $n = 1.33$, $\varphi_{\text{Rh6G,Rh640}} \sim 0.95$ [163] and $J(\lambda)$ for Rh6G and Rh640 can be determined from the measured spectra as shown in ref. [175].

In figure 5.6, the lowest lasing threshold for Rh6G / gold random lasers occurs at gold concentration $8 \times 10^{10}$ cm$^{-3}$ which corresponds to $R_0 \sim 6$ nm based on eq. (5.3). This indicates the optimal Förster distance between gold and Rh6G molecules for

lowest threshold. When Meng *et al*. [37] used silver-core-silica-shell nanoparticles, the distance between silver and Rh6G molecules was less than 5 nm to achieve the optimum lasing threshold due to the decreased overlap of the silver absorption spectrum with the fluorescence spectrum of Rh6G. Here, we estimated $R_0$ for Rh640 dye molecules and gold nanoparticles is ~ 4 nm for the optimum lasing threshold. The optimum lasing threshold for Rh640 / gold random lasers is 12 mJ/cm$^2$ versus 15 mJ/cm$^2$ for Rh6G / gold random lasers with $8 \times 10^{10}$ cm$^{-3}$ of gold nanoparticles. This is consistent with an increased $R_0$ = 6 nm for Rh6G / gold random lasers that possibly induces more quenching compared with $R_0$ = 4 nm for Rh640 / gold random lasers. The values of $R_0$ are based on eq. (5.3) with some assumptions in the equation which increase the uncertainty in this measurement. Increasing and decreasing gold concentrations can vary the effective dye-gold distance resulting in fluorescence enhancement and quenching.

The decrease of the lasing threshold is attributed to enhanced fluorescence due to the concentration of the local electric field induced by excited surface plasmons at the gold nanoparticles' surface. Emission from dyes is absorbed by the gold nanoparticles. The light is confined at the particle surface leading to a concentrated local electric field with increased localized absorption by the dye and thus more amplification [55] and effective gain [166, 176]. The enhancement of the local electric field near the surface of the gold nanoparticles in dye (Rhodamine B) was studied theoretically by Zhu *et al.* [166] where the local field factor (the ratio between the electric field around gold and the applied field) was calculated based on quasi-static theory for different dye shell thickness. They explained that the field factor increased when the dye molecules occurred near the gold nanoparticles' surface. The field factor

decreased with an increase in the dye shell thickness. This phenomenon enhances lasing in a regime where scattering events are rare.

The increase in the lasing threshold is attributed to fluorescence quenching between dye molecules due to non-radiative surface energy transfer from the excited dye to gold nanoparticles. The energy transfer rate / efficiency has a $1/d^4$ distance dependence, so non-radiative energy transfer and quenching only occur for dye molecules located close to the metal surface [11]. The addition of excessive gold nanoparticles increases the quenching rate in the system, leading to a higher threshold.

Thus, the initial reduction of the lasing threshold is because more dye molecules are found in the near field of the gold nanoparticles, leading to higher gain for lasing while the increased threshold at higher gold concentrations is attributed to quenching dye molecule emission.

*5.1.4.2.4 Scattering and absorption properties of gold nanoparticles*

Figures 5.6 and 5.8 show the emission peak wavelength and lasing threshold of random dye lasers with gold nanoparticles in the weakly scattering and diffusive regimes. In the weakly scattering regime, the threshold reduces with the increased gold concentration, but with further increased gold in the diffusive regime, the threshold increases. However, a different lasing threshold trend is observed in random dye lasers with alumina nanoparticles where the threshold decreases consistently with increased alumina concentration in the transition from the weakly scattering to the diffusive regime (figure 5.4). Multiple scattering events rarely occur in the weakly scattering regime compared to the diffusive regime, so there is a mechanism (plasmonics) other than scattering which contributes to the lasing in both regimes when gold nanoparticles are used.

The dependence of random lasing characteristics on the amount of gold nanoparticles can be explained based on scattering and absorption properties of gold nanoparticles by using Mie scattering theory (a brief introduction for Mie scattering theory is given in Chapter 1 (Section 1.2.2.1: Multiple Light Scattering) [35, 36, 41, 84]. The Mie extinction cross section ($\sigma_{eM}$) is the sum of the Mie absorption cross section ($\sigma_{aM}$) and the Mie scattering cross section ($\sigma_{sM}$). $\sigma_{eM}$, $\sigma_{aM}$ and $\sigma_{sM}$ are given by [35, 36, 41, 84];

$$\sigma_{eM} = \frac{\lambda^2}{2\pi n_m^2}\sum_{n=1}^{\infty}(2n+1)Re[a_n(mx,x) + b_n(mx,x)] \quad (5.4)$$

$$\sigma_{sM} = \frac{\lambda^2}{2\pi n_m^2}\sum_{n=1}^{\infty}(2n+1)\,[|a_n(mx,x)|^2 + |b_n(mx,x)|^2] \quad (5.5)$$

$$\sigma_{aM} = \sigma_{eM} - \sigma_{sM} \quad (5.6)$$

where $n_m$ and $\lambda$ refer to the refractive index of the surrounding medium and light wavelength, respectively. In the equations, $m = n_s/n_m$ and the size parameter is defined by $x = 2\pi n_m a/\lambda$, where $a$ and $n_s$ are the radius of the spherical particle and the complex refractive index respectively while $a_n$ and $b_n$ denote the scattering coefficients which can be found in ref. [41]. Here, we assume a spherical gold particle in a homogeneous medium (methanol) using a particle diameter, $a$ of 60 nm. The refractive index of gold, $n_s$ is obtained from Johnson and Christy [177].

Figure 5.11 shows the calculated variation of $\sigma_{eM}$, $\sigma_{sM}$ and $\sigma_{aM}$ of gold (~ 60 nm) and $\sigma_{sM}$ of alumina (~ 150 nm) with wavelength based on refs. [35, 36, 41, 84, 154]. In the visible, gold absorbs light more effectively than it scatters. In this calculation, the average diameter of alumina is ~ 150 nm and its refractive index is based on Dodge *et al.* [167]. Figure 5.11 shows that alumina does not exhibit absorption loss and has a similar scattering cross section with gold at the Rh6G emission peak (~ 570 nm).

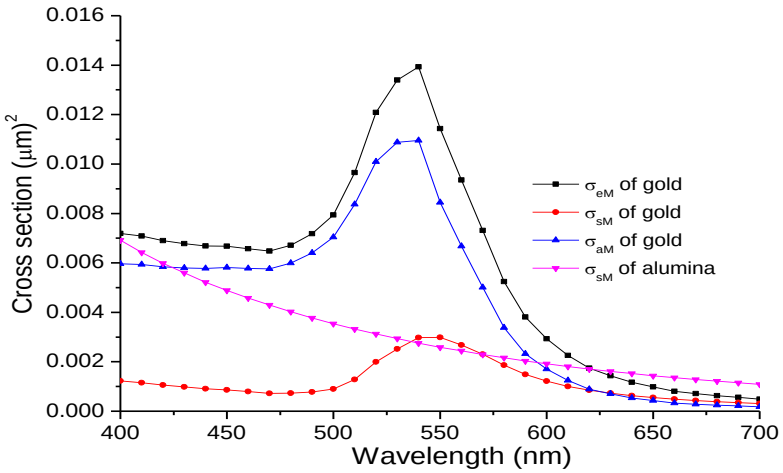


Figure 5.11. Estimation of scattering and absorption cross section of individual gold and alumina nanoparticles in methanol using Mie theory. While the absorption cross section of gold is larger than its scattering cross section, alumina does not absorb in the visible.

At the Rh640 emission peak (~ 620 nm), the scattering cross section for alumina is higher than that for gold nanoparticles. Although gold has a lower scattering cross section, gold significantly enhances the properties of random dye lasers compared to alumina. This suggests that the absorption properties of gold nanoparticles also affect the operation of random dye lasers [84]. Adding more gold nanoparticles increases the scattering but also increases the absorption loss (self-absorption effect), leading to random lasers with higher thresholds (figures 5.6 and 5.8). The spectral dependence of the absorption loss by gold nanoparticles contributes to the emission peak shift observed in Rh640 random lasers.

## 5.2 Solid-state Plasmonic Rhodamine dye random lasers

### 5.2.1 Introduction

Random dye lasers can also work in solid polymer films [47, 54]. In general, random lasers based on solid polymer films cannot be compared directly with random lasers based on colloidal solutions because they have different dimensionality, sample thickness, pump spot sizes and dynamics (moving particles in colloidal solutions instead of fixed particles' position in solid polymer film). There are some advantages of using solid polymer films compared to suspension of nanoparticles in dye solutions such as; ease of handling and prevention of flocculation and sedimentation. However, solid polymer films easily suffer from dye degradation problems due to photochemical changes under excitation. In dye solution samples, excess heat is redistributed and the gain medium is constantly renewed due to motion in the fluid [178]. Therefore, polymer films and single pulse pumping are preferred to avoid any damage to the films.

The objectives of this study are: (i) To observe spectral emission shape and lasing threshold trends in random lasers based on solid polymer films, (ii) To observe the effect of pump light penetration depth by studying different thickness of polymer films, (iii) To study the effect of glass substrate on random lasers.

Section 5.2 (Solid-state Rhodamine dye random lasers) describes my study of the effects of particle concentration, dye concentration, film thickness and glass substrate on solid-state random dye lasers. Sufficient particle and dye concentration are important to provide enough scattering and gain for solid-state Rhodamine dye lasers. Higher particle concentration (titania) provides more scattering leading to random dye lasers with decreased lasing threshold and emission spectra with less

fluorescence background. The effect of particle concentrations on random dye lasers is discussed in Chapter 3 (Spectral and coherence signatures of threshold in random lasers) and Section 5.1 (Colloidal-solution Plasmonic Rhodamine dye random lasers). High dye concentration produces a narrow emission peak. In solid film random dye lasers with metallic nanoparticles, a competing trend of lasing threshold is observed due to plasmonic and energy transfer effects (a similar trend is observed for colloidal metal-based random dye lasers (Section 5.1)). The effect of film thickness was studied by exciting drop- and spin-cast polymer films. Thicker polymer films produce narrow emission peaks and lasing thresholds compared to broad emission spectra for thin film because the thicker film provides larger pump penetration depth for better light confinement and higher gain. The glass substrate also provides better light confinement by reflecting the emission light into the films. Previous studies on solid-state random dye lasers [54, 179, 180] used nanoparticles with Rhodamine 6G (the gain medium) because the dye efficiently absorbs 532 nm pump light to provide sufficient gain to the system. In the present system, Rhodamine 640 was used with polyvinyl alcohol (PVA) and titania or gold to produce solid-state random dye lasers.

## 5.2.2 Experimental methods

### 5.2.2.1 Sample preparation (mixed nanoparticles in dye PVA films)

Titania nanoparticles, average diameter ~ 200 nm (Sigma Aldrich) ($1 \times 10^9$ to $2 \times 10^{11}$ $cm^{-3}$) and average diameter ~ gold, 60 nm (Ted Pella) ($5 \times 10^9$ to $5 \times 10^{11}$ $cm^{-3}$) were mixed separately with Rhodamine 640 ($5 \times 10^{-4}$ M) (Exciton) dissolved with PVA (0.05 g/ml) (Sigma Aldrich) in heated water (80 $^oC$). 1 ml of sample solution was drop-cast (spread) on a glass substrate (area ~ 4 cm × 2 cm) and dried at room

temperature for 24 hours (see figure 5.12). The film thickness was estimated as ~ 13 µm (measured by Alphastep profiler).

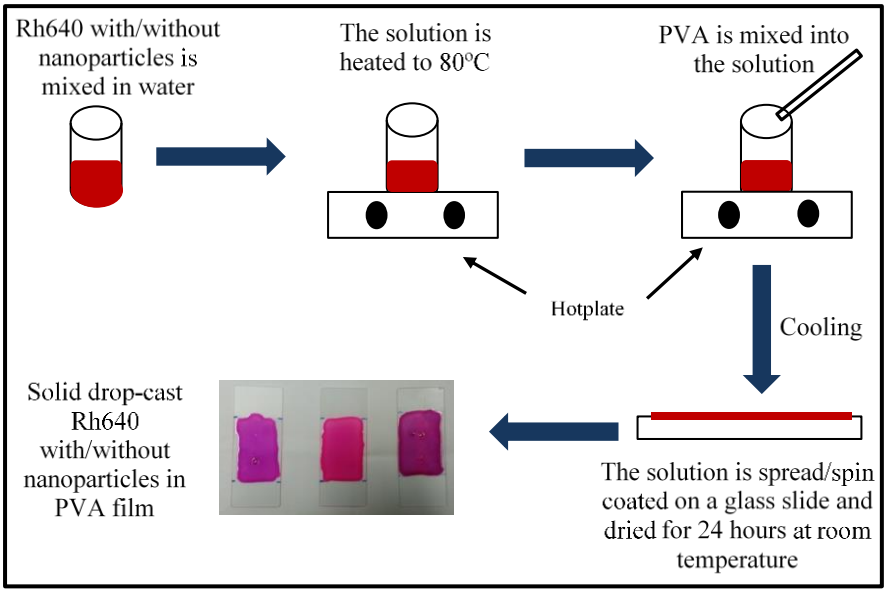


Figure 5.12 Preparation of Rh640 with / without nanoparticles mixed in PVA film.

To prepare thin PVA films, the sample solutions (Rhodamine 640 ($5 \times 10^{-4}$ M or $5 \times 10^{-3}$ M) with titania ($2 \times 10^{11}$ $cm^{-3}$)) were spin-coated with different speeds to obtain different PVA film thicknesses (< 5 µm). The film thickness is affected by spin-coating speed and different concentrations of PVA. Figure 5.13 shows the spin-coated Rh640 / nanoparticles in PVA film for different spin-coating speeds, various concentrations of Rhodamine 640 and PVA, with a fixed concentration of titania while Table 5.1 lists the thickness of the various PVA films shown in figure 5.13, measured by the Alphastep profiler. The particle and dye concentrations quoted in this section present the concentrations before drying the PVA films.

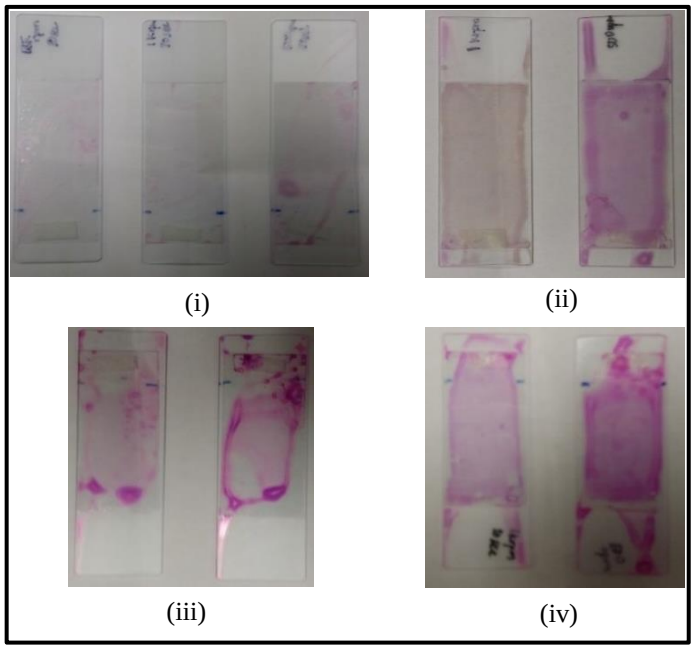


Figure 5.13 Solid spin-coated Rh640 / titania in PVA film with various spin-coating speeds, concentration of Rh640 and PVA; (i) Rh640 ($5 \times 10^{-4}$ M) / titania ($2 \times 10^{11}$ $cm^{-3}$) in PVA (0.05 g/ml film (1.5 krpm, 1 krpm, 500 rpm (left to right)), (ii) Rh640 ($5 \times 10^{-4}$ M) / titania ($2 \times 10^{11}$ $cm^{-3}$) in PVA (0.1 g/ml film (1 krpm, 500 rpm (left to right)), (iii) Rh640 ($5 \times 10^{-3}$ M) / titania ($2 \times 10^{11}$ $cm^{-3}$) in PVA (0.05 g/ml film (1 krpm, 500 rpm (left to right)) and (iv) Rh640 ($5 \times 10^{-3}$ M) / titania ($2 \times 10^{11}$ $cm^{-3}$) in PVA (0.1 g/ml film(1 krpm, 500 rpm (left to right)).

Table 5.1 Thickness estimation of PVA film measured by the Alphastep profiler for various spin-coating speeds, various concentrations of Rhodamine 640 and fixed concentration of titania ($2 \times 10^{11}$ $cm^{-3}$) before spreading on the glass slide.

| Concentration of Rh640 (M) | Concentration of PVA (g/ml) | Spin-coating speed (rpm/30 sec) | Thickness (μm ± 5 %) |
|---|---|---|---|
| $5 \times 10^{-4}$ M | 0.05 | 1.5 k | 0.1 |
| $5 \times 10^{-4}$ M | 0.05 | 1 k | 0.4 |
| $5 \times 10^{-4}$ M | 0.05 | 500 | 1.5 |
| $5 \times 10^{-4}$ M | 0.1 | 1 k | 3 |
| $5 \times 10^{-4}$ M | 0.1 | 500 | 6 |
| $5 \times 10^{-3}$ M | 0.05 | 1 k | 0.4 |
| $5 \times 10^{-3}$ M | 0.05 | 500 | 1.5 |
| $5 \times 10^{-3}$ M | 0.1 | 1 k | 3 |
| $5 \times 10^{-3}$ M | 0.1 | 500 | 6 |

### 5.2.2.2 Optical measurements

The random laser experimental set up was similar to that described in Chapter 4 (Section 4.3.2: Optical measurements). The middle region of the polymer film was

excited at an angle of 45° by a frequency-doubled Q-switched Nd:YAG laser (532 nm, 4 ns,10 Hz). The pump spot size on the sample was 3 mm. Single pulse pumping was used to focus the film so as to avoid damage to the film or degradation of the dye. The emitted light from the front face of the sample was collected by the same spectrometer at an angle of 30° and displayed in a computer for spectral analysis.

## 5.2.3 Results and discussion

### 5.2.3.1 Fluorescence of solid Rhodamine 640 film (drop-cast)

Figure 5.14 shows the emission spectra of the solid Rh640 PVA film without nanoparticles with increasing pump energy density. The emission spectra are broad (~ 50 nm linewidth) and no spectral narrowing is observed due to the absence of nanoparticles to provide feedback. The emission intensity increases as we increase the pump energy density due to amplified spontaneous emission (ASE). The ASE may also cause the growth of the emission peak at 640 nm as indicated in the black circle (figure 5.14).

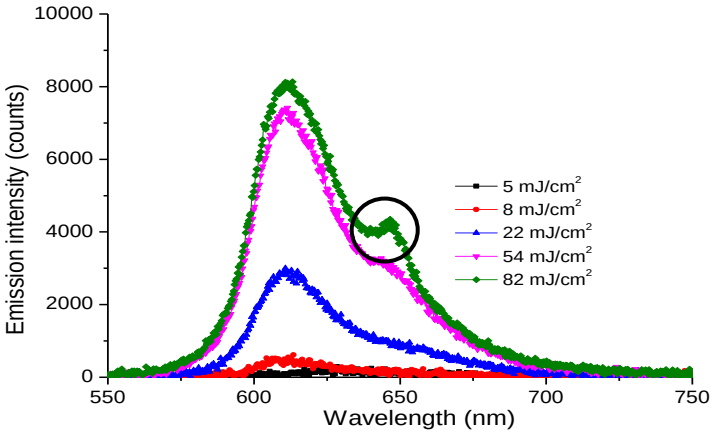


Figure 5.14 The emission spectra of Rh640 in solid PVA film (drop-cast) excited by Nd:YAG laser. The emission intensity increases gradually and the emission linewidth is broad (~ 50 nm) for all pump energy densities. The black circle shows the growth of emission peak at 640 nm.

#### 5.2.3.2 Solid Rhodamine 640 / titania random lasers (drop-cast)

Mixed Rhodamine 640 / titania in PVA films were prepared by drop-casting and the characteristics of random lasing were observed. Titania nanoparticles scatter the light to provide feedback for the random laser, leading to the occurrence of a narrow emission peak (4 nm) on top of the fluorescence spectrum (figure 5.15). An increasing density of titania nanoparticles gives more scattering (as discussed in Chapter 3). The large refractive index contrast between PVA and titania nanoparticles provides high scattering efficiency leading to spectral narrowing.

Emission spectra of solid Rh640 / titania random lasers for different pump energy densities and various concentrations are shown in figure 5.15. The fluorescence background reduces gradually when more titania nanoparticles are added to provide increased scattering and feedback. For the lowest concentration of titania ($1 \times 10^9$ $cm^{-3}$), the emission peak appears at ~ 650 nm and the emission peak blue-shifts with increased titania nanoparticle concentration. The shift is attributed to bichromatic emission from the Rh640 dye. The lasing threshold reduces and the emission peak intensity increases with higher scattering, as shown in figure 5.16. The effect of particle concentration on lasing threshold can be observed in figure 5.17 where a higher concentration of titania gives a lower lasing threshold. Effects of dielectric concentrations on the emission spectra and lasing threshold of solid-state random dye lasers are comparable with the colloidal-solution random dye lasers (Chapter 3). As we discussed in Chapter 3, the higher concentration of dielectric nanoparticles gives more scattering and leads to increased feedback in random dye lasers.

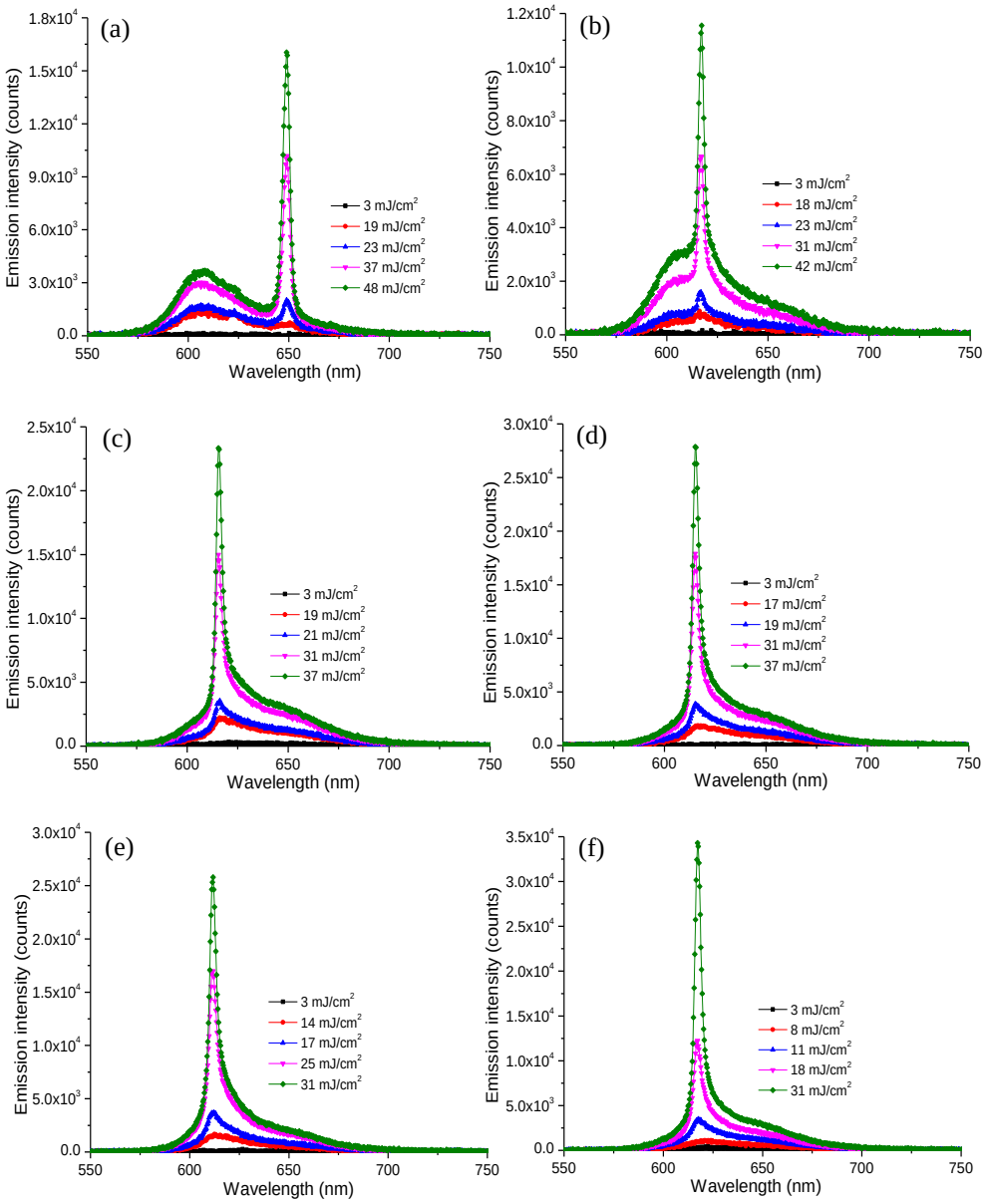


Figure 5.15 Emission spectra of solid Rh640 / titania (drop-cast) random lasers for different pump energy densities for titania concentrations (before drying the PVA film); (a) $1 \times 10^{9}$ $cm^{-3}$, (b) $5 \times 10^{9}$ $cm^{-3}$, (c) $1 \times 10^{10}$ $cm^{-3}$, (d) $5 \times 10^{10}$ $cm^{-3}$, (e) $1 \times 10^{11}$ $cm^{-3}$ and (f) $2 \times 10^{11}$ $cm^{-3}$. The lasing threshold is determined when a narrow emission peak appears on top of the fluorescence spectrum.

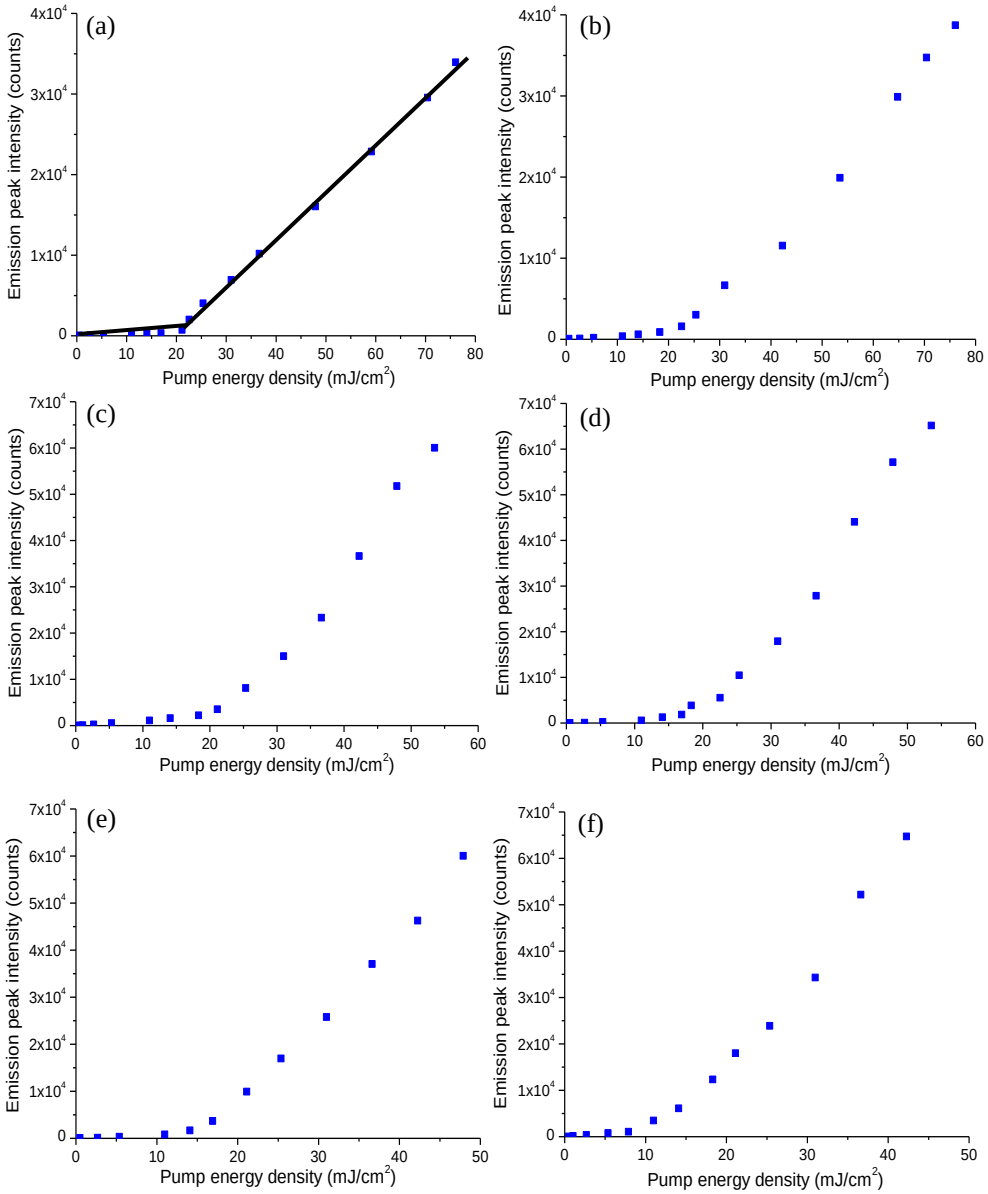


Figure 5.16 Emission peak intensity as a function of pump energy density of solid Rh640 / titania (drop-cast) random lasers for titania concentrations (before drying the PVA film); (a) $1 \times 10^9$ cm$^{-3}$, (b) $5 \times 10^9$ cm$^{-3}$, (c) $1 \times 10^{10}$ cm$^{-3}$, (d) $5 \times 10^{10}$ cm$^{-3}$, (e) $1 \times 10^{11}$ cm$^{-3}$ and (f) $2 \times 10^{11}$ cm$^{-3}$. The lasing threshold is determined when the emission peak intensity increases nonlinearly with the pump energy density (as shown by the black line in Figure 5.16 (a)). The lasing threshold reduces and the emission peak intensity increases with increased particle concentration.

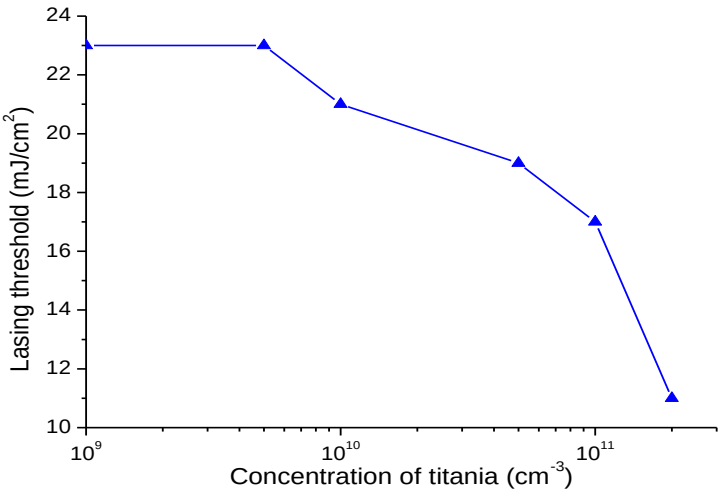


Figure 5.17 The dependence of solid Rh640 / titania (drop-cast) random lasing threshold on the concentration of titania. The lasing threshold reduces for increased concentration of titania.

### 5.2.3.2 Solid Rhodamine 640 / gold random lasers (drop-cast)

We observe plasmonic effects on the emission spectra and lasing threshold of solid-state random lasers incorporating gold nanoparticles ($5 \times 10^9$ to $5 \times 10^{11}$ cm$^{-3}$) which are within similar ranges of gold nanoparticles used in Section 5.1 and Rh640 dye ($5 \times 10^{-4}$ M). The dependence of emission spectra on pump energy density for solid Rh640 / gold random lasers is shown in figure 5.18. Broad emission spectra are observed below threshold and above threshold, a narrow emission peak with reduced background fluorescence appears at 650 nm for gold concentration $5 \times 10^9$ cm$^{-3}$. When the gold concentration is increased by a factor of 10, the fluorescence spectrum narrows above threshold. Increasing the gold concentration by a factor of 100 produces an emission peak at ~ 620 nm instead of ~ 650 nm, and the dye fluorescence background increases again. The increase of fluorescence background occurs possibly due to high absorption loss induced by gold nanoparticles. The emission peaks maintain the same wavelength for each pump energy density and are red-shifted slightly with the increased gold concentration. For a gold concentration of $2 \times 10^{11}$ cm$^{-3}$, two emission peaks appear at ~ 620 nm and ~ 650 nm above threshold. For the

highest gold concentration, ($5 \times 10^{11}$ $cm^{-3}$), the emission peak at ~ 620 nm dominates with no emission peak at ~ 650 nm. These phenomena are due to interactions between monomer and dimer molecules in Rh640 with gold nanoparticles [64, 168, 169]. Ad Lagendijk *et al.* [64] observed two emission peaks of Rh640 random lasers when a high concentration of Quinaldine blue (Qblue) was added to the Rh640 random lasers. In the present case, the emission peak intensity for Rh640 random lasers with high gold concentrations ($\geq 2 \times 10^{11} cm^{-3}$) reduces (figure 5.18) due to absorption by the gold nanoparticles, and resulting in fluorescence quenching. The competition in the emission between ~ 620 nm and ~ 650 nm may contribute to the reduced overall emission intensity for the Rh640 random lasers with high gold concentration. Fluorescence from Rh640 is enhanced by the addition of gold nanoparticles even without lasing. This is shown in figure 5.18 (f) in which Rh640 with gold nanoparticles gives stronger fluorescence emission than Rh640 without gold nanoparticles, when both are pumped below laser threshold.

The emission peak intensity as a function of pump energy density of solid Rh640 / gold random lasers is shown in figure 5.19. The lasing threshold is determined when the emission peak intensity starts to increase nonlinearly. The lasing threshold trend for solid Rh640 / gold random lasers, shown in figure 5.20, differs from that for solid Rh640 / titania random lasers. In the solid Rh640 / titania random lasers, the lasing threshold decreases gradually when more titania nanoparticles are added. The trend is solely influenced by scattering effects since titania nanoparticles are elastic scatterers for visible light. In solid Rh640 / gold random lasers, gold nanoparticles scatter and absorb the light concurrently leading to competing effects on lasing threshold (decreased and increased lasing threshold) for increased gold concentration.

For low gold concentrations, the small scattering effect is compensated by gain induced by plasmonic effects. The lowest lasing threshold is achieved at a gold concentration of $5 \times 10^{10}$ cm$^{-3}$ with optimum scattering and gain. For increased gold concentration, more absorption loss results in an increased lasing threshold.

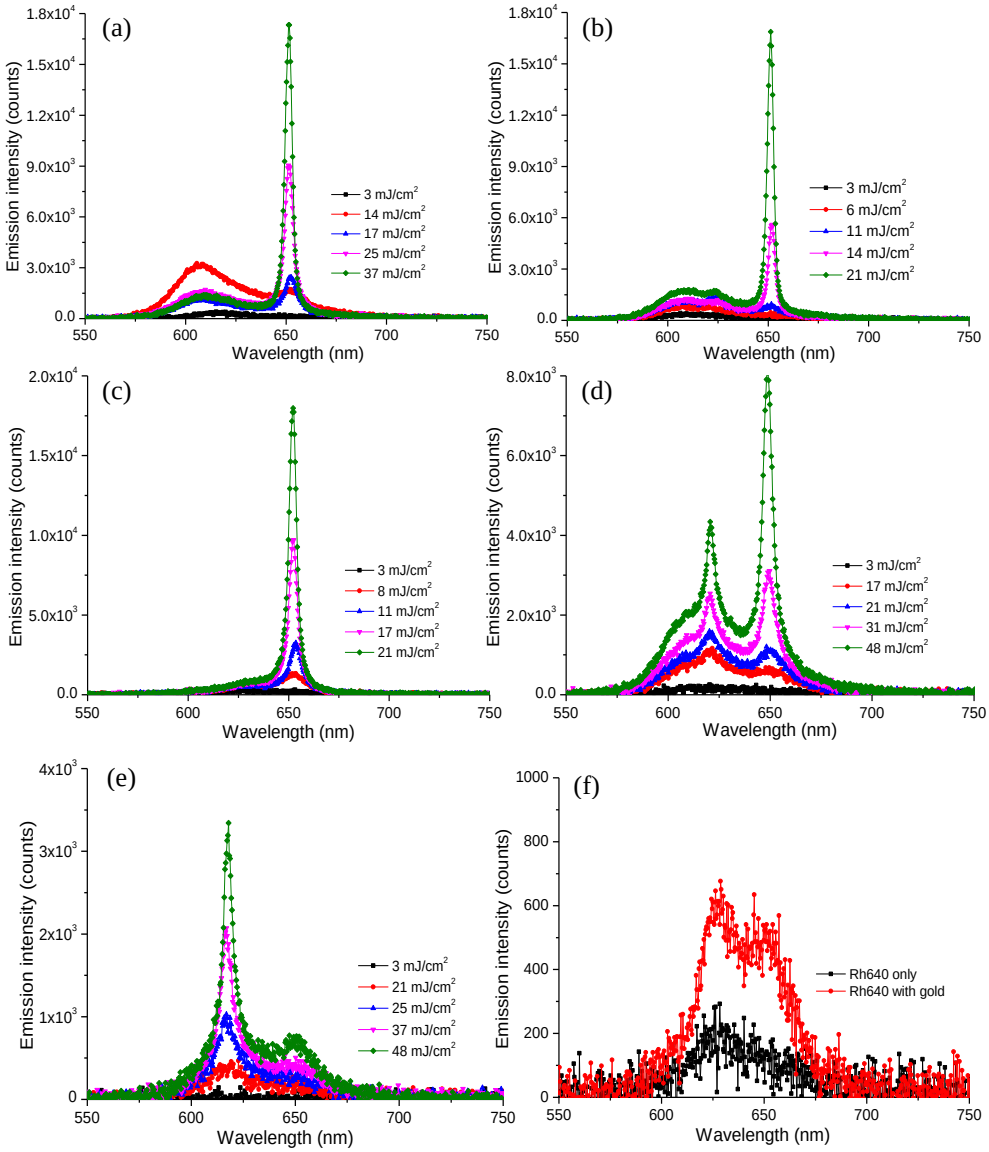


Figure 5.18 Emission spectra of solid Rh640 / gold (drop-cast) random lasers for different pump energy densities for gold concentrations (before drying the PVA film); (a) $5 \times 10^{9}$ cm$^{-3}$, (b) $2 \times 10^{10}$ cm$^{-3}$, (c) $5 \times 10^{10}$ cm$^{-3}$, (d) $2 \times 10^{11}$ cm$^{-3}$ and (e) $5 \times 10^{11}$ cm$^{-3}$. The lasing threshold is determined when a narrow emission peak appears on top of the fluorescence spectrum. Figure 5.18 (f) Comparison of emission spectra of Rh640 ($5 \times 10^{-4}$ M) with and without gold nanoparticles ($5 \times 10^{10}$ cm$^{-3}$) excited at 5 mJ/cm$^2$ (below threshold).

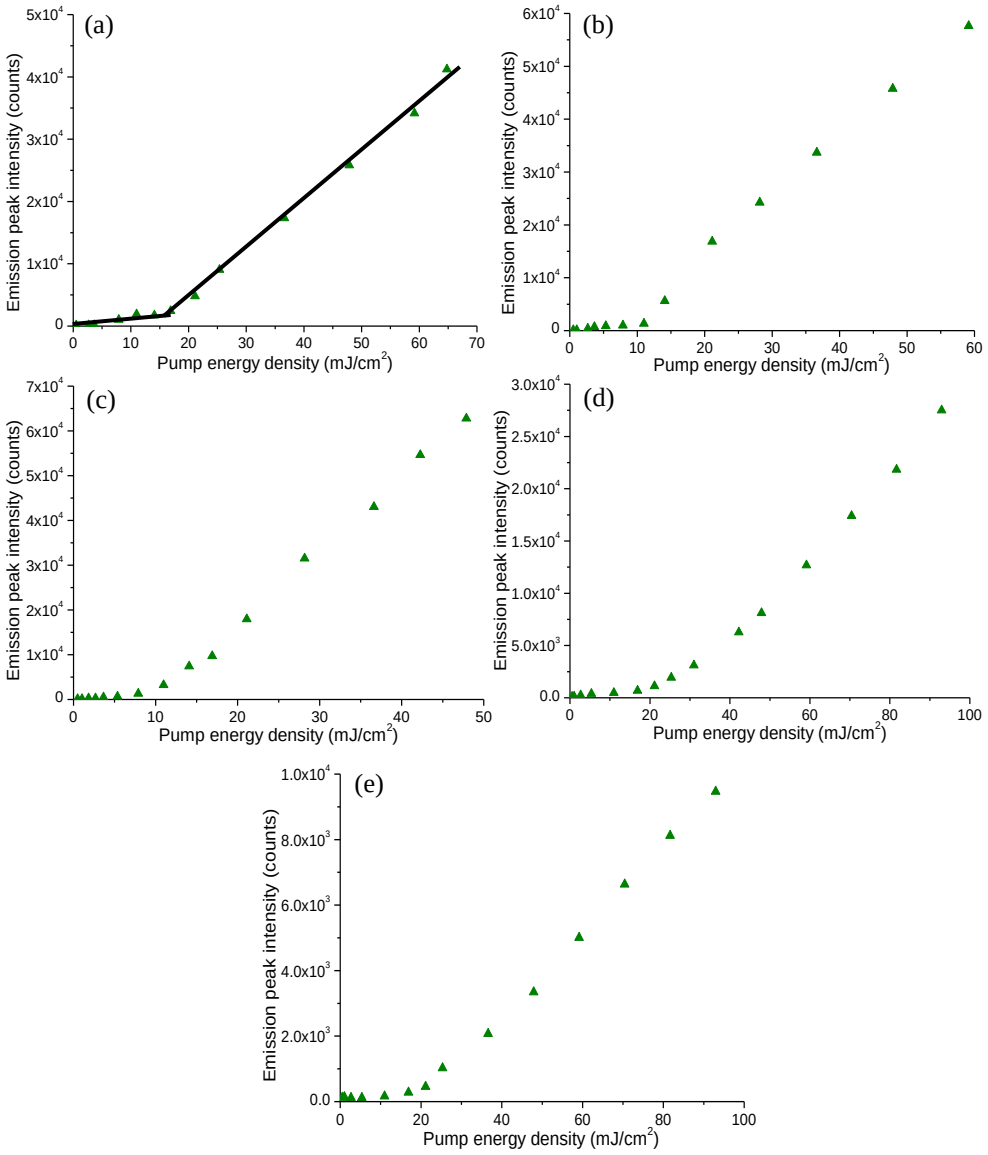


Figure 5.19 Emission peak intensity as a function of pump energy density of solid Rh640 / gold (drop-cast) random lasers for gold concentrations (before drying the PVA film); (a) $5 \times 10^9$ cm$^{-3}$, (b) $2 \times 10^{10}$ cm$^{-3}$, (c) $5 \times 10^{10}$ cm$^{-3}$, (d) $2 \times 10^{11}$ cm$^{-3}$ and (e) $5 \times 10^{11}$ cm$^{-3}$. The lasing threshold is determined when the emission peak intensity increases nonlinearly with the pump energy density (as shown by the black line in Figure 5.19 (a)).

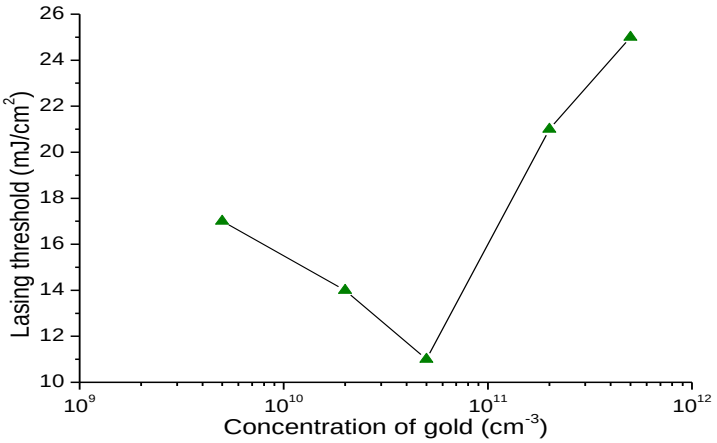


Figure 5.20 The dependence of solid Rh640 / gold (drop-cast) random lasing threshold on the concentration of gold where the lasing threshold reduces until it reaches the optimum threshold, 11 mJ/cm$^{-2}$ at $5 \times 10^{10}$ cm$^{-3}$ and increases back when higher gold concentration is used.

In addition, the spectral overlap of the plasmon resonance of the gold nanoparticles with the fluorescence spectrum of Rh640 suggests the possibility of plasmonic and non-radiative / resonant energy transfer effects. The emission light is absorbed by the gold nanoparticles to create plasmon excitation. The plasmon excitation results in local field enhancement in the dye, thus increasing the gain (figure 5.21). The emission peak intensity reduces significantly for solid Rh640 / gold random lasers with the highest gold concentration due to quenching of the dye emission. The quenching occurs due to non-radiative energy transfer from the excited Rh640 dye molecules to the gold nanoparticles due to absorption by the gold nanoparticles. The trade-off between plasmonic effects and resonant energy transfer leads to competing effects on the lasing threshold. These are also observed in colloidal-solution random dye lasers (Section 5.1).

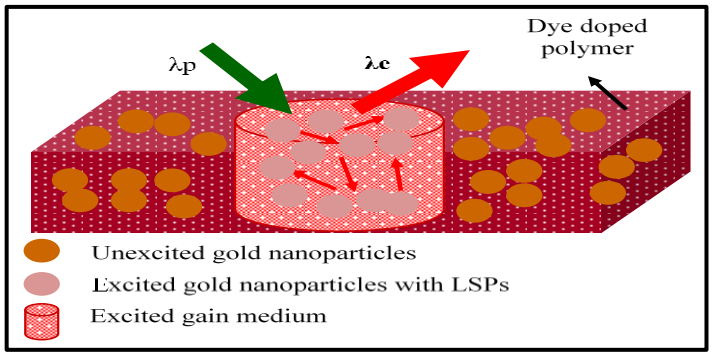


Figure 5.21 Localized surface plasmon (LSP) effects due to metal nanoparticles in dye-doped polymer film. Excitation of the gold nanoparticles increases local electromagnetic field, resulting in enhanced gain.

### 5.2.3.3 Solid Rhodamine 640 / titania random lasers (spin-cast / spin coated)

Spin-casting is used to produce thin and uniform polymer films. The film thickness was increased from 0.13 µm to 5 µm by varying the spin-casting speed and time and viscosity of the solution. The aim of this study was to investigate the effect of film thickness and dye concentration in random lasing. With 0.05 g / ml of PVA, 5 × $10^{-4}$ M of Rh640, 2 × $10^{11}$ $cm^{-3}$ of titania and spin coating speeds (500 rpm, 1 krpm and 1.5 krpm), solid thin films (< 1 µm) were produced. All three films when excited with high pump energy density (65 mJ / $cm^2$) did not exhibit narrow emission spectra, as shown in figure 5.22. The emission spectra are broad, ~ 40 nm for all three polymer films.

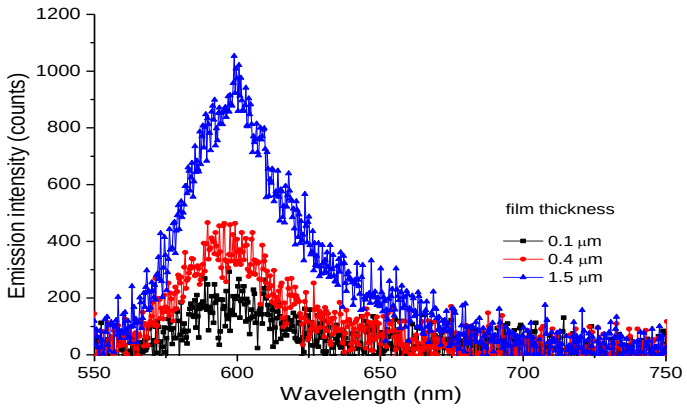


Figure 5.22 Emission spectra of solid Rh640 (5 × $10^{-4}$ M) / titania (2 × $10^{11}$ $cm^{-3}$) (spin-cast) random lasers for different film thickness excited with 65 mJ/$cm^2$.

For different positions on the PVA film, the emission spectra are quite similar indicating uniformity of the film (figure 5.23 (a)). When the film thickness was increased, the spectrum starts to narrow (figure 5.23). At a film thickness of ~ 6 µm (figure 5.23 (c)), the emission spectrum narrows down to ~ 20 nm, but there is no evidence of lasing.

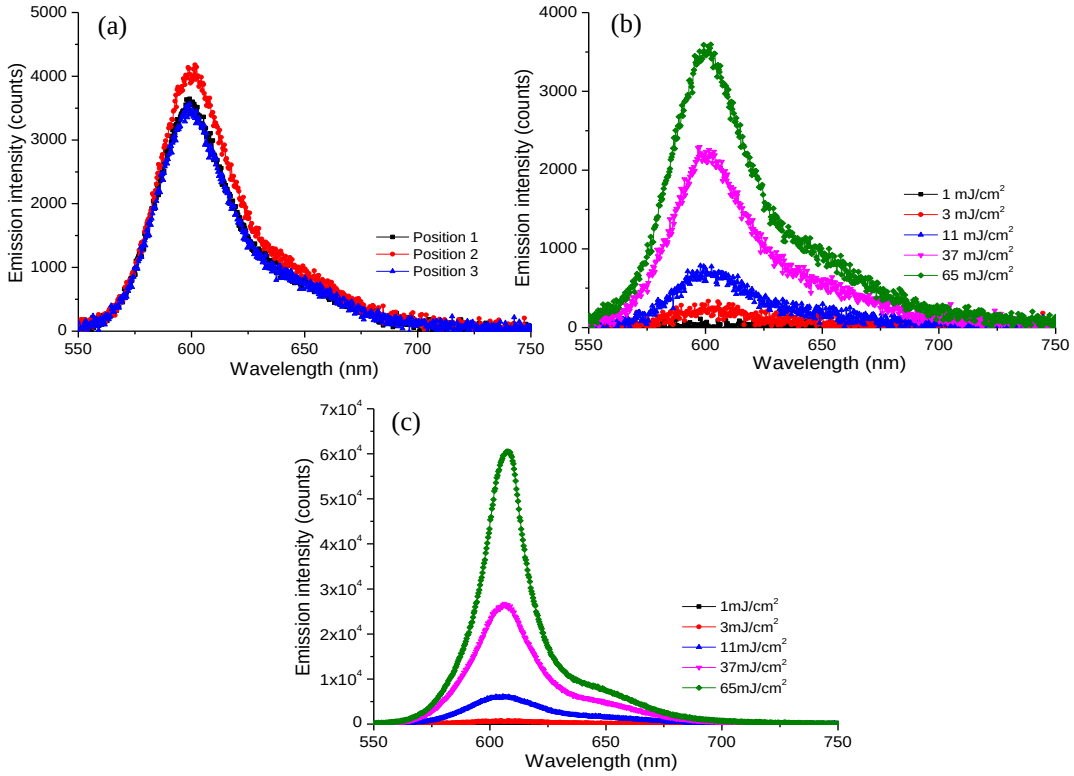


Figure 5.23 Emission spectra of solid Rh640 ($5 \times 10^{-4}$ M) / titania ($2 \times 10^{11}$ $cm^{-3}$) (spin-cast) random lasers for a film thickness of (a) 3 µm for three different positions on the PVA film excited with 65 $mJ/cm^2$, (b) 3 µm for different pump energy density and (c) 6 µm for different pump energy density.

To investigate the effect of dye concentration on the emission spectra and lasing threshold of random lasers based on mixed Rh640 / titania on thin films, the dye concentration was increased up to 10× ($5 \times 10^{-3}$ M) and the film thickness was varied from 0.4 µm to 6 µm. Broad emission spectra were observed for film thicknesses of 0.4 µm and 1.5 µm as shown in figure 5.24.

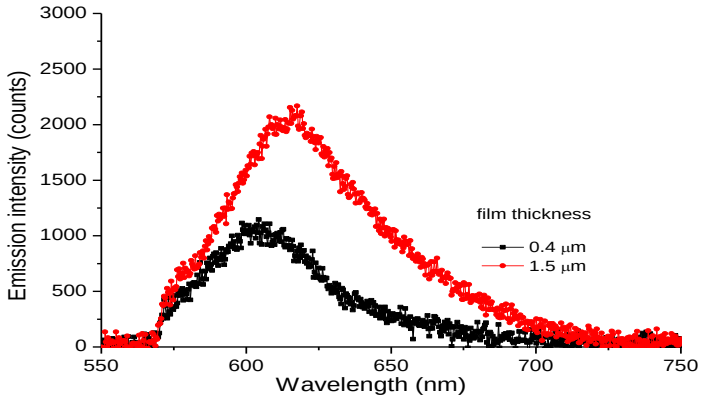


Figure 5.24 Emission spectra of solid Rh640 ($5 \times 10^{-3}$ M) / titania ($2 \times 10^{11}$ $cm^{-3}$) (spin-cast) random lasers for different film thickness excited with 65 $mJ/cm^2$.

Narrow emission spectra (4 nm) were observed for solid Rh640 with increased concentration ($5 \times 10^{-3}$ M) / titania ($2 \times 10^{11}$ $cm^{-3}$) (spin-cast) random lasers with film thicknesses of more than 3 μm. The normalized emission intensity below and above threshold for Rh640 ($5 \times 10^{-3}$ M) / titania ($2 \times 10^{11}$ $cm^{-3}$) random lasers is shown in figure 5.25, indicating spectral narrowing when the threshold is reached.

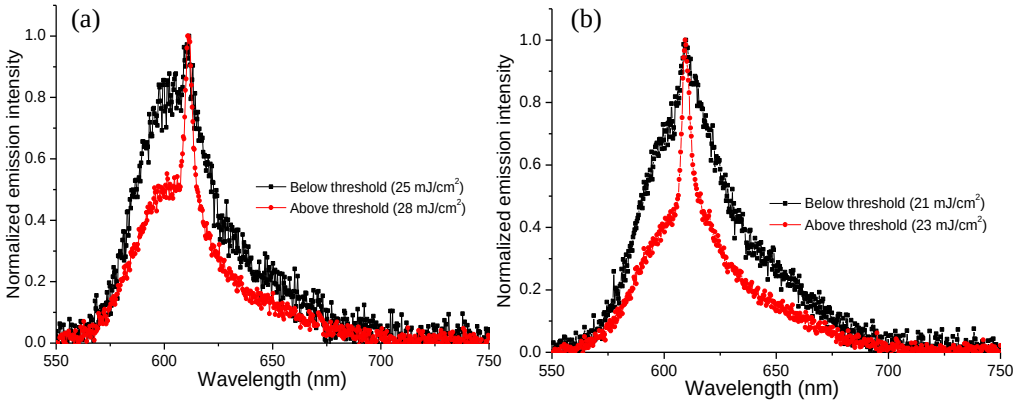


Figure 5.25 The normalized emission intensity of solid Rh640 ($5 \times 10^{-3}$ M) / titania ($2 \times 10^{11}$ $cm^{-3}$) (spin-cast) random lasers in PVA films below (black curve) and above threshold (red curve) for a film thickness of (a) 3 μm and (b) 6 μm in which a narrow emission peak appears when the lasing threshold is achieved.

The narrow emission peaks maintain the same wavelength and linewidth above threshold and the threshold is observed when there is a nonlinear increase of emission peak intensity with the pump energy density (figures 5.26 and 5.27). From both figures, we observe that solid random lasers with thicker films offer higher emission

peak intensity with lower threshold. It is evident that a high concentration of dye in a thicker film is needed to provide more gain to the solid random dye lasers. The spectral narrowing occurs due to better light confinement within a thicker film where the pump and emission light is multiply scattered and amplified before it emits from the gain medium. A thicker film contains more dye molecules and scatterers and thus more pump light is absorbed or trapped within the excited region. For thinner films, the pump light is less absorbed and the emission light is less scattered and amplified.

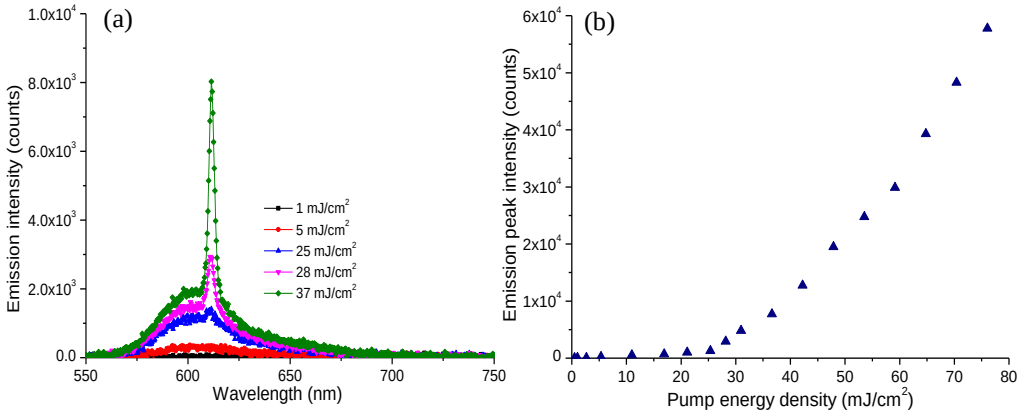


Figure 5.26 (a) Emission spectra and (b) Emission peak intensity of Rh640 ($5 \times 10^{-3}$ M) / titania ($2 \times 10^{11}$ $cm^{-3}$) random lasers for a film thickness of 3 µm. The lasing threshold is achieved when a narrow emission peak appears on top of the emission spectrum and the emission peak intensity increases nonlinearly with the pump energy density.

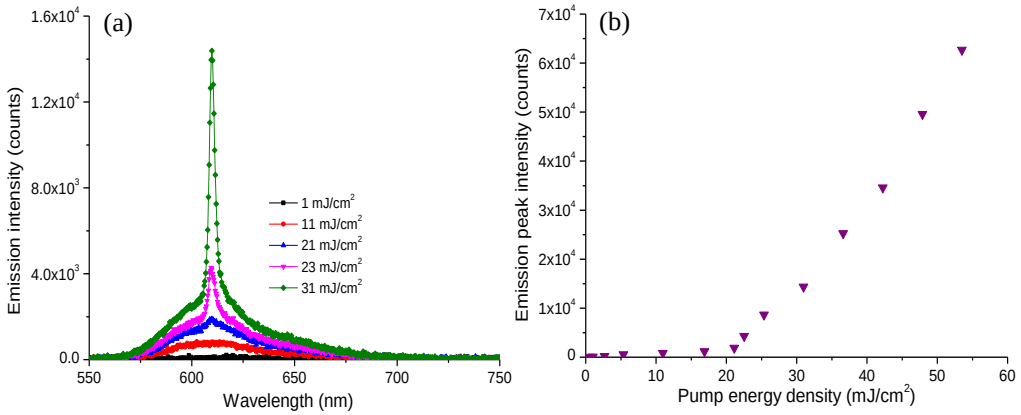


Figure 5.27 (a) Emission spectra and (b) Emission peak intensity of Rh640 ($5 \times 10^{-3}$ M) / titania ($2 \times 10^{11}$ $cm^{-3}$) random lasers for a film thickness of 6 µm. The lasing threshold is achieved when a narrow emission peak appears on top of the emission spectrum and the emission peak intensity increases nonlinearly with the pump energy density.

#### 5.2.3.4 Suspended membrane random lasers

Suspended membrane random lasers are obtained by peeling off the embedded Rh640 / nanoparticle films from the glass substrate. The films were prepared by the drop-casting method resulting in 13 μm-thick films, as films prepared by the spin-casting were difficult to peel. I maintained the experiment set up, in which the pump light excited the front of the film and the emitted light was collected by the spectrometer. By removing the film from the substrate, we can observe the effects of the glass substrate on the emission spectrum and lasing threshold of these solid-state random lasers. Figure 5.28 shows the emission spectra of suspended membrane Rh640 / titania random lasers for various concentrations of titania. The fluorescence background reduces when the particle concentration increases (similar to the behaviour of solid Rhodamine 640 / titania random lasers (figure 5.15)). The emission linewidth reduces from 10 nm to 5 nm when the titania concentration increases from $5 \times 10^{9}$ $cm^{-3}$ to $1 \times 10^{10}$ $cm^{-3}$. The emission peak wavelength red-shifts with the increased titania concentration.

The lasing thresholds of suspended membrane Rh640 / titania random lasers for various particle concentrations are shown in figure 5.29. In comparison with Rh640 / titania random lasers on the glass substrate (figure 5.17), suspended membrane Rh640 / titania random lasers have slightly higher lasing threshold than the solid Rhodamine 640 / titania random lasers (drop-cast). The glass substrate reflects light into the film so that the light is confined longer before it leaves the gain medium. Better light confinement enables higher gain in the system and reduced lasing threshold.

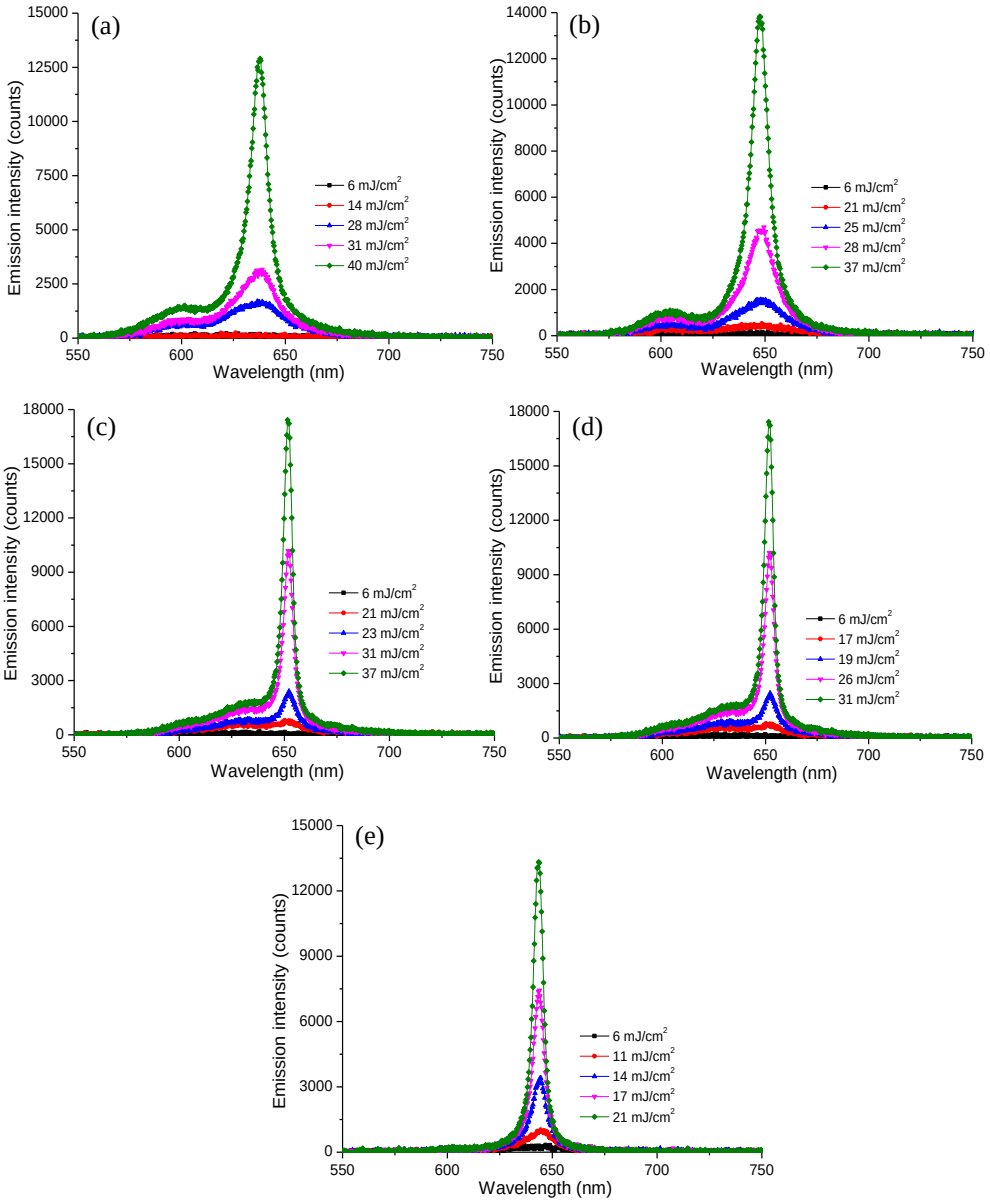


Figure 5.28 Emission spectra of solid suspended membrane Rh640 / titania random lasers for different pump energy densities for titania concentrations (before drying the PVA film); (a) $1 \times 10^{9}$ cm$^{-3}$, (b) $5 \times 10^{9}$ cm$^{-3}$, (c) $1 \times 10^{10}$ cm$^{-3}$, (d) $1 \times 10^{11}$ cm$^{-3}$ and (e) $2 \times 10^{11}$ cm$^{-3}$. The lasing threshold is determined when a narrow emission peak appears on top of the fluorescence spectrum.

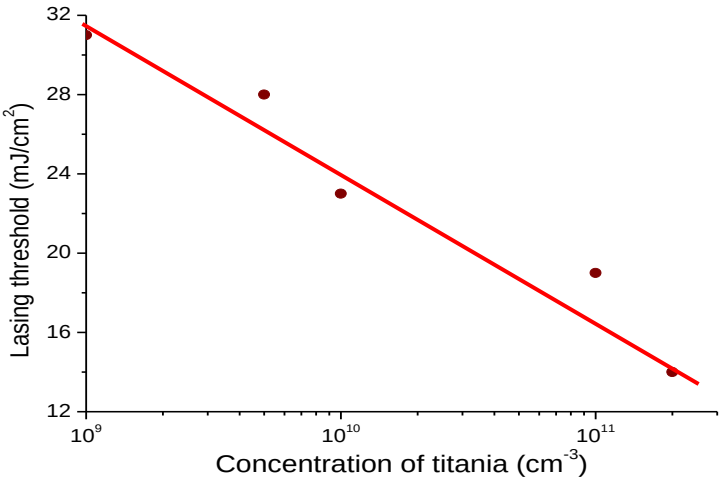


Figure 5.29 The dependence of solid suspended membrane Rh640 / titania random lasing threshold on the concentration of titania. The lasing threshold reduces for increased concentration of titania. The red line shows a linear decrease trend of lasing threshold.

The effect of the glass substrate is also observed in suspended membrane Rh640 / gold random lasers in terms of the emission spectra (figure 5.30) and lasing threshold (figure 5.31). In figure 5.30, we observe that the emission linewidth reduces and the emission intensity increases when the concentration of gold is increased up to $5 \times 10^{10}$ $cm^{-3}$. Adding more gold up to $5 \times 10^{11}$ $cm^{-3}$, the emission linewidth increases and the emission intensity reduces. The fluorescence background also increases when higher gold concentration is used. The lasing threshold is slightly higher than for Rh640 / gold random lasers on the glass substrate (figure 5.19 ) and the competing trends of lasing threshold with gold concentration are similar with Rh640 / gold random lasers on the glass substrate (figure 5.20). The reduced lasing threshold for Rh640 / gold random lasers on the glass substrate is consistent with the earlier results of ref. [61]. Dominguez *et al.* [61] observed fivefold reduction of lasing threshold for solid Rh6G / silver random lasers with an aluminium mirror which provides the external feedback for the laser emission.

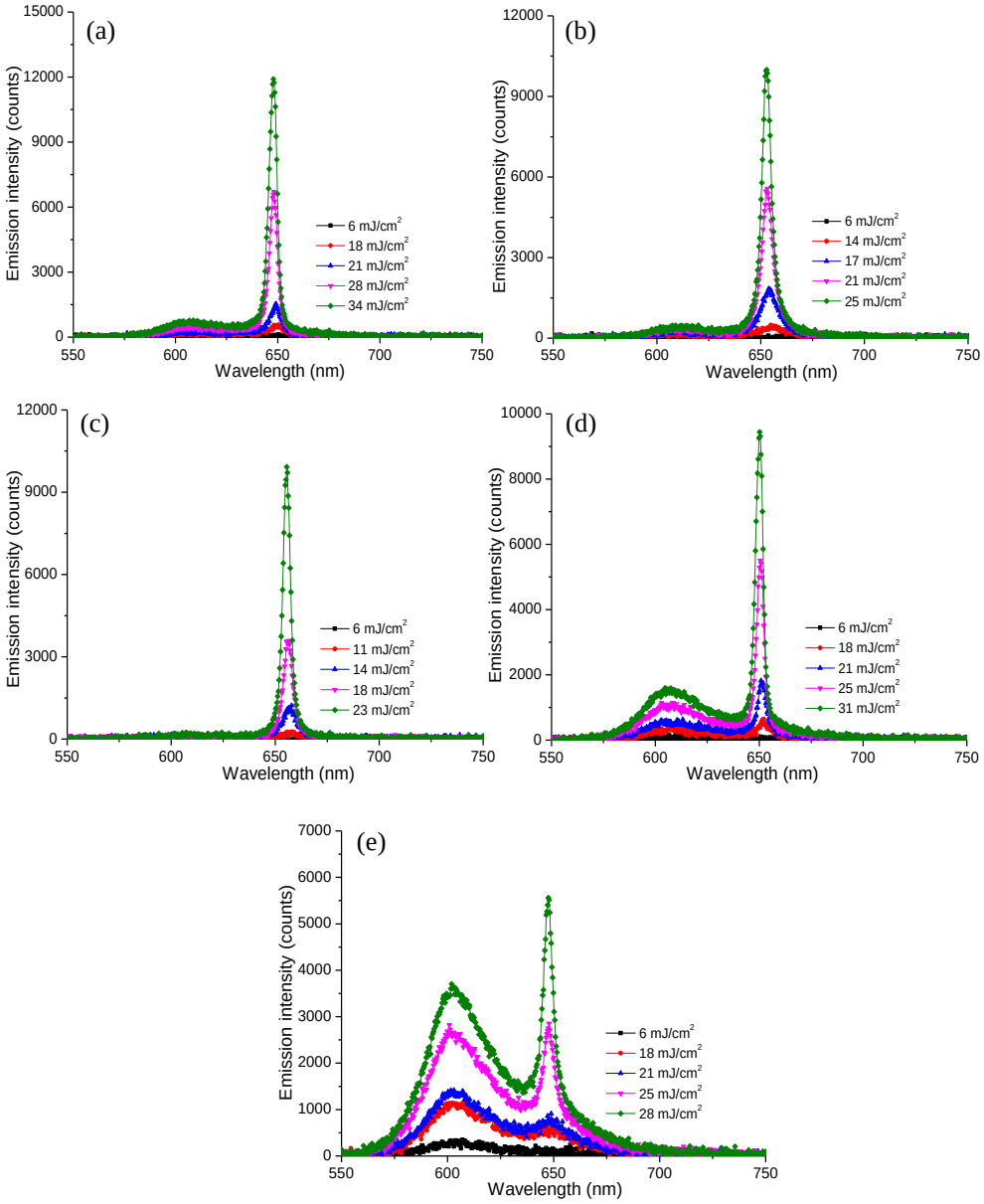


Figure 5.30 Emission spectra of solid suspended membrane Rh640 / gold random lasers for different pump energy densities for gold concentrations (before drying the PVA film); (a) $5 \times 10^{9}$ $cm^{-3}$, (b) $2 \times 10^{10}$ $cm^{-3}$, (c) $5 \times 10^{10}$ $cm^{-3}$, (d) $2 \times 10^{11}$ $cm^{-3}$ and (e) $5 \times 10^{11}$ $cm^{-3}$. The lasing threshold is determined when a narrow emission peak appears on top of the fluorescence spectrum.

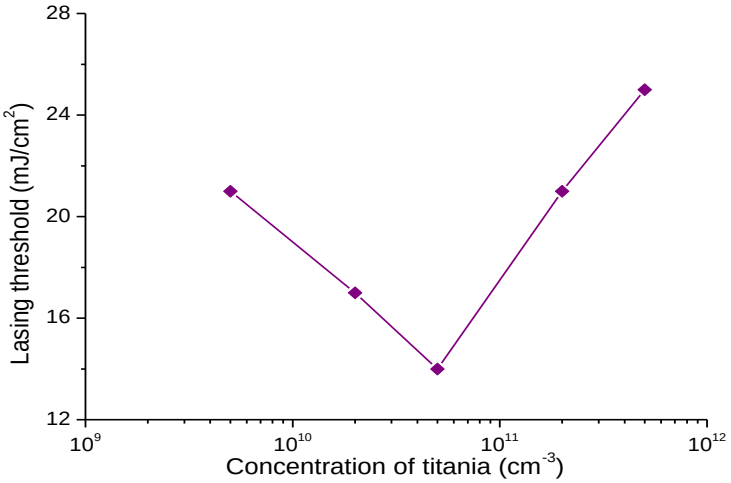


Figure 5.31 The dependence of solid suspended membrane Rh640 / gold random lasing threshold on the concentration of titania. The lasing threshold reduces for increased concentration of gold.

## 5.3 Chapter 5 Summary

We observe improved performance with lower lasing threshold, higher emission peak intensity and narrower emission linewidth for Rhodamine dye random lasers with relatively low concentrations of gold nanoparticles in comparison with dielectric scattering particles. These characteristics are observed through colloidal-solution and solid-state random lasers which are attributed to enhanced scattering and absorption of gold nanoparticles and increased spectral overlap between the dye fluorescence spectrum and the gold extinction spectrum, which induces localized surface plasmons and resonance energy transfer.

In colloidal-solution random dye lasers, more significant effects are observed in Rh640 random lasers than in Rh6G random lasers, in terms of fluorescence background and lasing threshold, due to reduced spectral overlap between the extinction spectrum of gold nanoparticles and the dye emission. The contrasting trends of lasing threshold can be seen between random dye lasers incorporating dielectric and metal nanoparticles in the diffusive regime.

We observe that the film thickness, glass substrate, particle concentration and dye concentration all affect the performance of solid state random lasers. Solid dielectric scatterer-based random dye lasers produce emission spectra with less fluorescence background, higher emission peak intensity and reduced lasing threshold with increased particle concentration. The higher dye concentration and thicker film provide higher gain for the random dye laser and narrow emission peaks are produced from films with film thicknesses above 3 μm (for a Rh640 dye concentration of $5 \times 10^{-3}$ M). Contrasting trends of lasing threshold are observed in solid metal particle-based random dye lasers, consistent with results for colloid metal-based random dye lasers (Section 5.1) due to plasmonic and energy transfer effects. Reflection of the pump and emission light from the glass substrate also affect the performance of random lasers by allowing a slightly lower threshold than the suspended membrane random lasers without the glass substrate.

The results and discussion reported in this chapter provide insights into the effects of plasmonic enhancement, dye concentration, film thickness and glass substrate on colloidal-solution and solid-state random dye lasers.

# Chapter 6

# Effects of metal-fluorophore distance and surface roughness on random lasers

In Chapter 6, we discuss two different types of random laser materials, namely silica-coated silver nanoparticles and lumpy bimetallic nanoparticles. These metal nanoparticles induce localized surface plasmons (LSPs) and scatter the light, affecting the gain and feedback of random lasers respectively. The main aim of this chapter is to study the effect of nanoparticle (metal)-fluorophore distance and surface roughness of nanoparticle scatterers on the performance of random lasers. This chapter is divided into two sections: 6.1 The effects of metal-fluorophore distance on plasmonic random lasers and 6.2 Random lasers with lumpy bimetallic nanoparticles. The experimental results shown in this chapter used the best sample that we produced. Better control of the sample production is needed in future to ensure the reproducibility of the experimental results for all samples[7].

[7] The synthesis of silver and silica-coated silver nanoparticles was based on the methods of Wei Deng (ARC Centre of Excellence for Nanoscale Biophotonics, Australia). Debra Birch provided access to the transmission electron microscope.

# 6.1 Surface plasmon effects on random lasers based on metal-fluorophore distance.

## 6.1.1 Introduction

Localized surface plasmons affect random laser characteristics depending on the properties of the metal nanoparticles; metal-fluorophore distance and particle concentrations. Silver and gold nanoparticles with various shapes [55, 112] are commonly used in random lasers due to their stability, ease of preparation and better performance than dielectric nanoparticles. Metal-based random lasers perform better in the weakly scattering regime than in the diffusive regime due to plasmon resonances whereas high metal nanoparticle concentrations lead to absorption loss and dye quenching [55]. Meng *et al.* [37] observed an increase of lasing threshold for picosecond-pulsewidth Rh6G / silica-coated silver random lasers.

We observed a narrow emission peak when Rh6G / silica-coated silver nanoparticle solution was excited with a nanosecond-pulsewidth laser, indicating incoherent feedback random lasing. The lasing threshold increases with increased silver-fluorophore distance and scattering strength. We observe a slight emission peak shift with the increase of the metal-fluorophore distance and there is a possibility to tune the emission wavelength slightly by varying the metal-fluorophore distance in these lasers.

## 6.1.2 Sample preparation and characterization

Silica-coated silver nanoparticles were prepared following the method of Deng *et al.* [133] and the sample was characterized using zetasizer (dynamic light scattering (DLS)) and transmission electron microscope (TEM) (see Section 2.1.2.4).

### 6.1.2.1 Synthesis of silver colloids

The citrate-reduction method was used to produce silver nanoparticles [133, 181, 182]. Silver nitrate aqueous solution was prepared by dissolving 0.009 g of silver nitrate ($AgNO_3$) (Sigma Aldrich) into 49 ml of deionized water. The solution was vigorously stirred (1000 rpm) and heated on a hot plate to boiling (100 $^oC$), confirmed by a thermometer (figure 6.1). concentration of particles. The concentration of silver nanoparticles was $3 \times 10^{-5}$ g/cm$^3$, equivalent to $6 \times 10^{10}$ cm$^{-3}$.

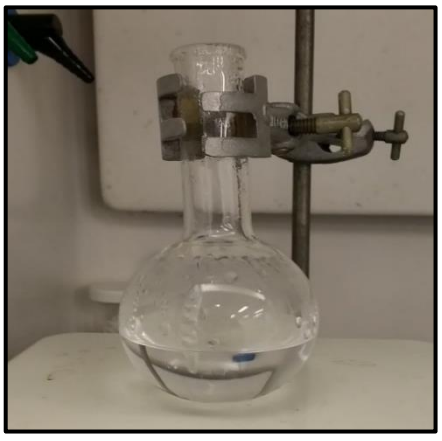

Figure 6.1 Silver nitrate aqueous solution was stirred and heated on a hotplate.

To the boiling silver nitrate aqueous solution, 1 ml of freshly prepared trisodium citrate (34 mM) (Sigma Aldrich) was added dropwise within 1 minute. The dropwise-addition is important in order to produce small-size silver nanoparticles. The solution started to change colour from transparent to light yellow after adding the trisodium citrate. Then, it changed to dark yellow / orange after 6 minutes and finally, to pale

green within 15 minutes (figure 6.2). The reaction solution was cooled at room temperature before centrifugation (by Eppendorf Mini Spin) using 500 rcf (relative centrifugal force) for 1 hour to remove larger silver colloids.

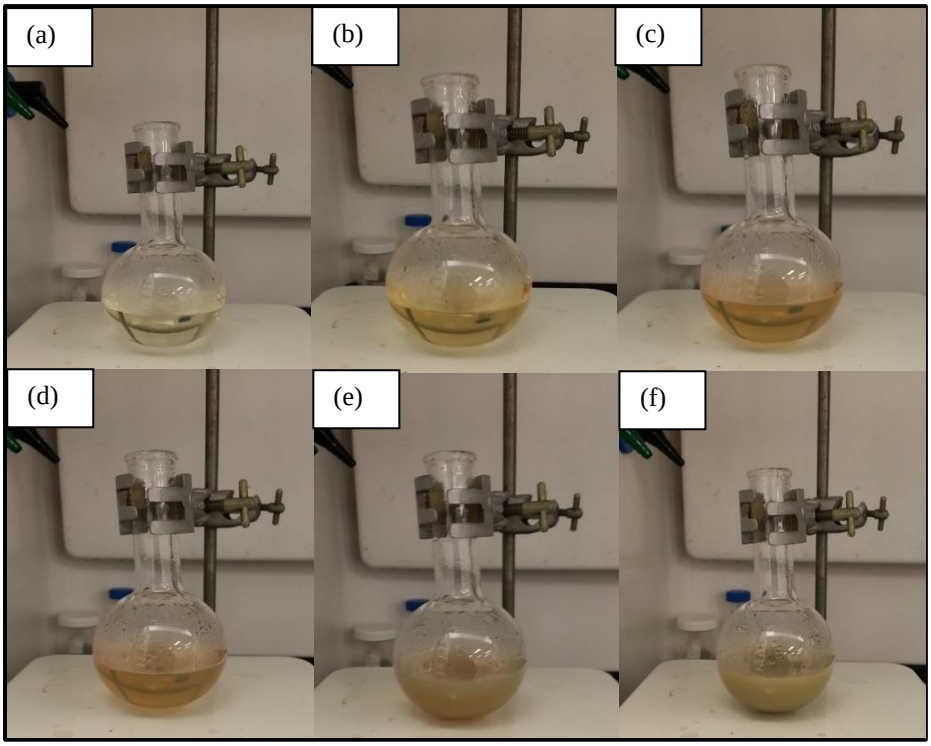


Figure 6.2 The colour of silver nitrate aqueous solution changes after adding trisodium citrate (a) 1 minute, (b) 3 minutes, (c) 6 minutes, (d) 8 minutes, (e) 12 minutes and (f) 15 minutes.

The supernatant silver colloid was taken and the size of the colloid was measured using the Zetasizer and TEM. Figure 6.3 shows the TEM images of the silver colloids after centrifugation with the estimated average silver diameter, 45 ± 2 nm (figure 6.3). To estimate the particle concentration, 1 ml of silver colloids was washed with deionized water and centrifuged using the highest speed, 14.1 krcf. The remaining sediment (silver nanoparticles) was dried in vacuum and weighed to estimate the

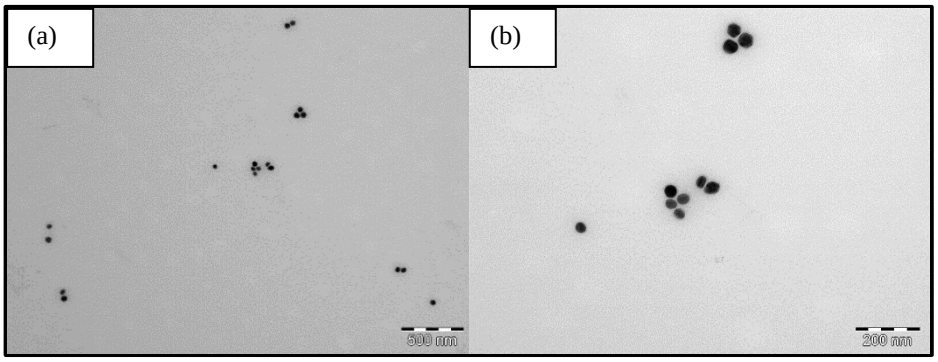


Figure 6.3 TEM image of silver colloids after centrifugation for 1 hour (10× dilution) with a scale bar (a) 500 nm and (b) 200 nm. From that figure, the size of nanoparticles were estimated as ~ 45 ± 2 nm.

### 6.1.2.2 Synthesis of silica-coated silver nanoparticles

Under vigorous stirring (1000 rpm) at room temperature, 5 ml of silver colloids in aqueous solution (average diameter ~ 45 ± 2 nm, $6 \times 10^{10}$ $cm^{-3}$) was mixed with ethanol (20 ml). Ammonium hydroxide (400 µl) was added to increase the ionic strength of the solution and catalyze the hydrolysis and condensation of the alkoxysilanes to prepare the silica coating [182]. 10 mM of tetraethyl orthosilicate (TEOS) in ethanol solution was added dropwise to the suspension. The volume of TEOS (10 mM) was varied from 350 µl to 700 µl to vary the silica shell thickness (more TEOS volume produces thicker silica shell). The mixed solution was stirred for 24 hours to produce silica-coated silver nanoparticles (figure 6.4). The final solution was twice washed with ethanol (centrifuged at 14.1 krcf for 10 minutes, supernatant was removed and the sediment was ultrasonically dispersed in ethanol) to remove TEOS traces and the silica-coated silver nanoparticles were suspended in ethanol for TEM and optical measurements. The solution concentration was estimated as ~ $6 \times 10^{-6}$ $g/cm^3$.

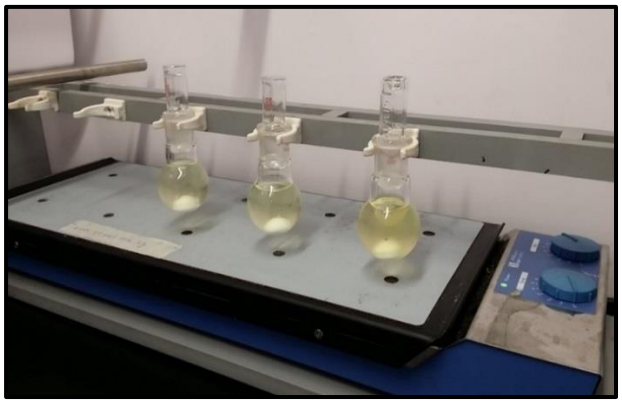

Figure 6.4 Stirring silver with ammonium hydroxide and TEOS on a multipoint stirring plate for 24 hours to make silica-coated silver nanoparticles

The TEM images of silica-coated silver nanoparticles for various silica shell thicknesses are presented in figure 6.5. For random laser measurements, Rhodamine 6G (Rh6G) ($5 \times 10^{-5}$ M) (Sigma Aldrich) was added to the silica-coated silver nanoparticle aqueous solution in a quartz cuvette (1 cm × 1 cm) to provide gain to the system.

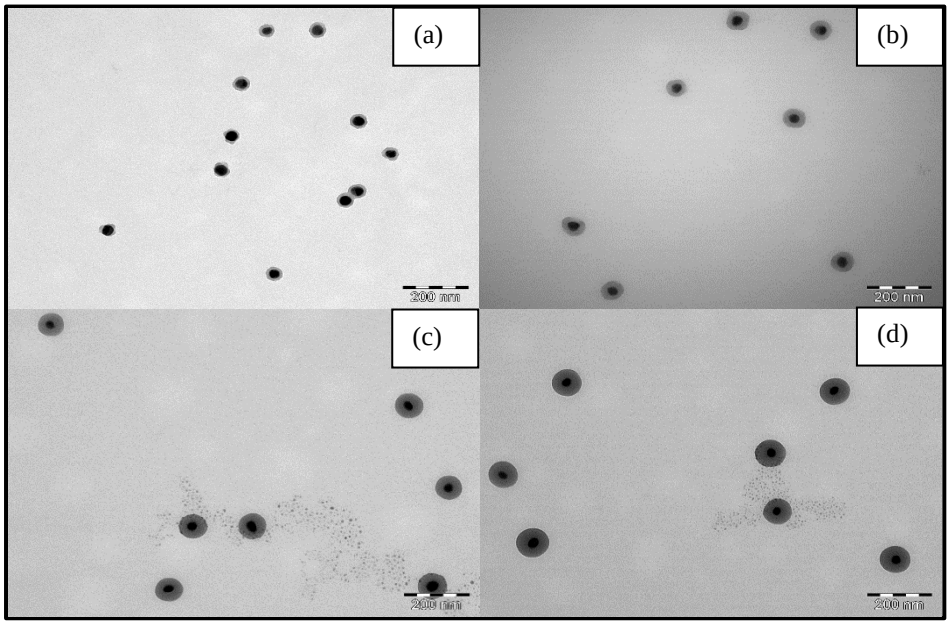


Figure 6.5 TEM images of silica-coated silver nanoparticles with various silica shell thicknesses (a) 8 nm, (b) 18 nm, (c) 22 nm and (d) 32 nm (10× dilution). The scale bar end to end is 200 nm.

The scattering mean free paths, $l_s$ of the silica-coated silver nanoparticle solutions were estimated to be from 42 cm to 18 cm based on $l_s = 1 / (\rho\sigma_s)$ [3, 28, 36-38] where $\rho$ and $\sigma_s$ correspond to the particle concentration and scattering cross section. The decreased $l_s$ was also observed in ref. [37]. As $l_s > L$ (sample size ~ 3 mm), the silica-coated silver nanoparticle solutions are in the weakly scattering regime [39]. The particle concentration, $\rho \sim 1.2 \times 10^{10}$ cm$^{-3}$. The scattering cross sections, $\sigma_s$ of the silica-coated silver nanoparticles for 0 to 32 nm of silica shell thickness with silver core, 45 nm were estimated to be $2 \times 10^{-12}$ cm$^2$ to $4.5 \times 10^{-12}$ cm$^2$ using ScatLab software[8] which uses Mie theory [35, 36, 41, 183].

### 6.1.3 Optical measurements

The absorption and fluorescence spectra were measured using a Cary spectrophotometer (Varian Australia) and Fluorolog spectrofluorometer (Horiba Jobin Yvon). The random laser experiments used the same set up, discussed in Chapter 4 (Section 4.3.2 Optical measurements).

### 6.1.4 Results and discussion

Figure 6.6 presents the extinction spectra of silica-coated silver nanoparticles with various silica shell thicknesses. With increased silica shell thickness, the extinction peak reduces and the extinction spectrum broadens. Shuford *et al.* [184] also observed the decrease of the extinction peak for increased silica shell thickness

[8]Prof. Francesco Ruffino (a Physics Professor at University of Catania, Italy) provided access to the Scatlab software to estimate the scattering cross section of the silica-coated silver nanoparticles.

with gold cores. Figure 6.7 shows the absorption and fluorescence spectra of Rh6G. By comparing both figures (figures 6.6 and 6.7), we observe the degree of overlap of the extinction spectra of silica-coated silver nanoparticles with the absorption and fluorescence spectra of Rh6G. The spectral overlap decreases with increased silica shell thickness.

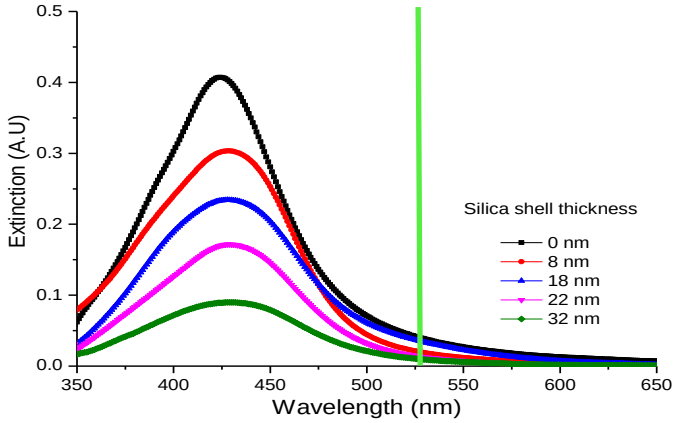


Figure 6.6 Extinction spectra of silica-coated silver nanoparticles with various silica-shell thicknesses. The vertical green line represents the pump excitation wavelength at ~ 532 nm.

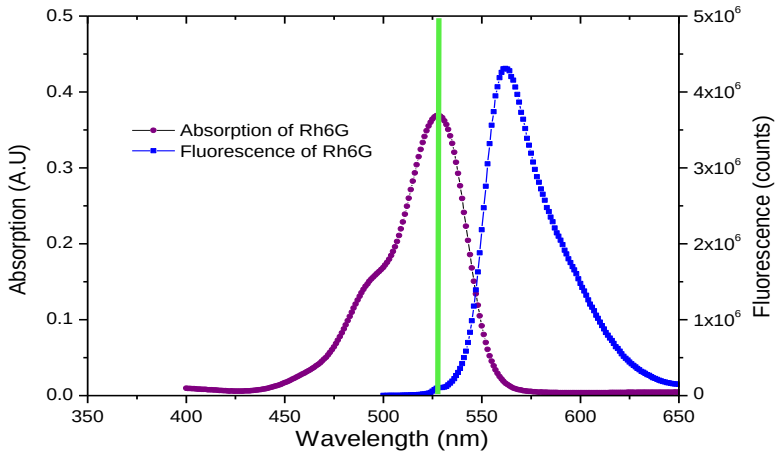


Figure 6.7 Absorption and fluorescence spectra of Rhodamine 6G. The vertical green line represents the pump excitation wavelength at ~ 532 nm.

Figure 6.8 (a) shows the emission spectra of the Rh6G / silver nanoparticle solutions. The emission intensity increases and the emission spectrum narrows with the increasing pump level (figure 6.8 (b)).

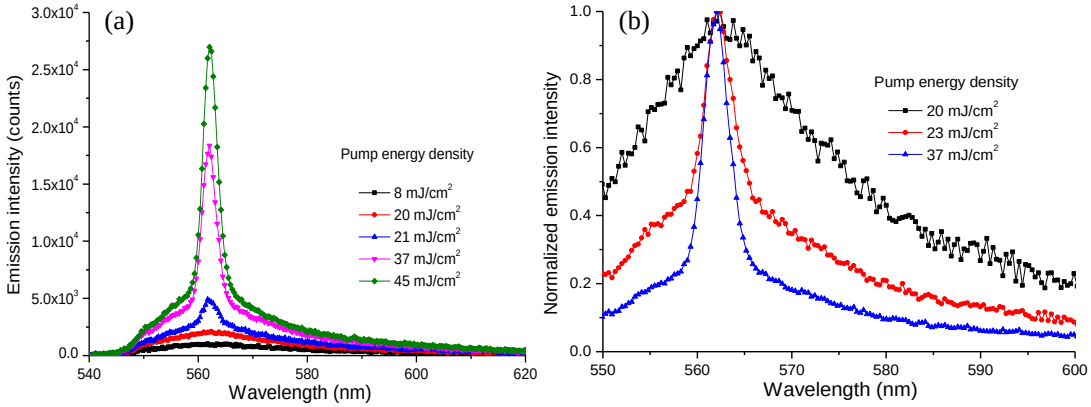


Figure 6.8 (a) Emission spectra and (b) Spectral narrowing of Rh6G / silver random lasers for increasing pump energy density.

Random lasing for Rh6G / silver nanoparticle solutions can be determined by the lasing threshold as shown in figure 6.9. The emission peak intensity increases nonlinearly for increasing pump level. For Rh6G / silica-coated silver random lasers, the lasing threshold increases and the emission peak intensity reduces with increased silica shell thickness (figure 6.9). The presence of a 'kink' in the emission peak intensity determines the lasing threshold as shown by the green line in figure 6.9.

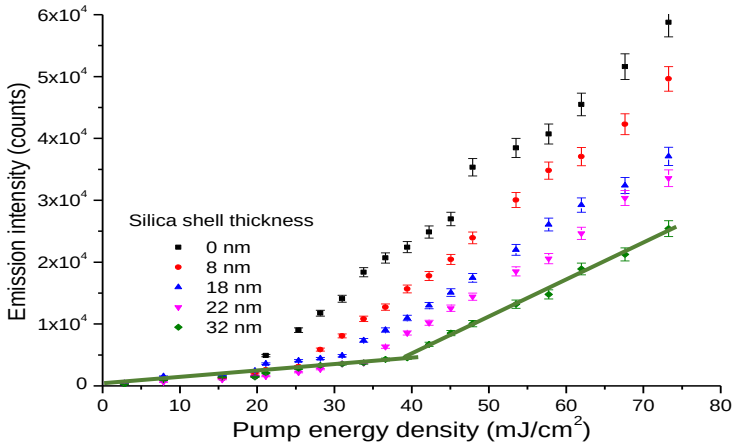


Figure 6.9 Emission peak intensity of Rh6G / silica-coated silver random lasers as a function of pump energy density. The green line is used to determine the lasing threshold.

The lasing threshold is also compared with the scattering mean free path, $l_s$. The lasing threshold increases as $l_s$ decreases with increased silica shell thickness (metal-fluorophore distance) as presented in figure 6.10.

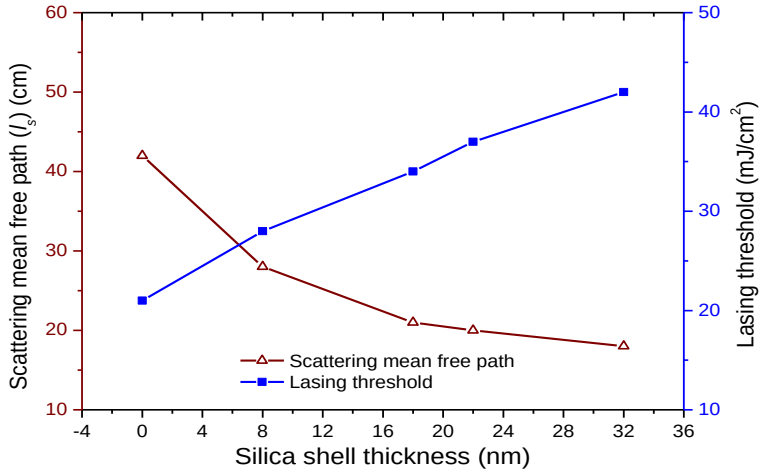


Figure 6.10 The scattering mean free path, $l_s$ (empty brown triangles) versus lasing thresholds (filled blue squares) of Rh6G / silica-coated silver random lasers with various silica shell thicknesses. The uncertainty of the silica shell thickness is ±1 nm.

The emission peak slightly blue-shifts from 562 nm (0 nm silica shell thickness) to 560 nm (32 nm silica shell thickness) for increased silica shell thickness as shown in figure 6.11.

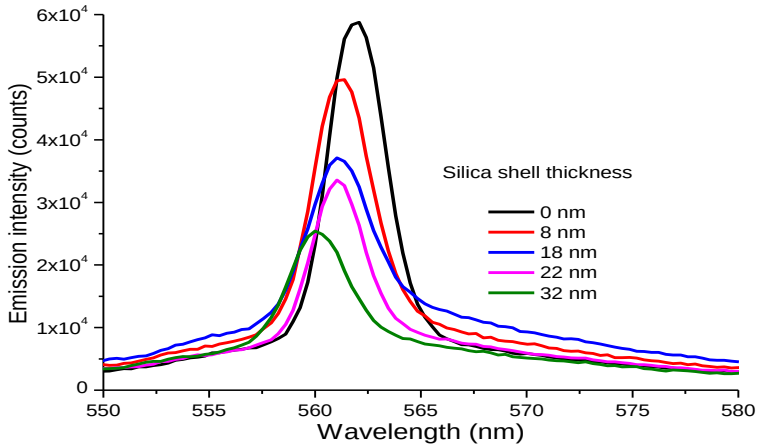


Figure 6.11 Emission spectra of Rh6G / silica-coated silver random laser with various silica shell thicknesses at 73 mJ/cm$^2$. The uncertainty of the silica shell thickness is ±1 nm.

Random lasing is observed in Rhodamine 6G / silica-coated silver nanoparticles with various silica-shell thicknesses. Silver nanoparticles not only scatter the light but also enhance the gain due to surface plasmon effects [54, 55]. The

decrease of the surface plasmon peaks with increased silica shell thickness, shown in figure 6.6, suggests that metal-fluorophore distance influences the surface plasmon effect. The surface plasmon effect can be estimated from the spectral overlap of the surface plasmon band with the absorption and / or fluorescence of the dye molecules (figure 6.6 and figure 6.7). As all samples are in the weakly scattering regime [39], we attribute the spectral narrowing in figure 6.8 to surface plasmon effects, where the local electric field is enhanced near the silver surface, leading to enhanced gain in the system. The enhanced gain compensates for the reduced scattering that occurs in the weakly scattering regime.

The local electric field enhancement near the metal surface is shown by simulation, using the discrete dipole approximation (DDA), as shown in figure 6.12 [37, 39]. When the metal-fluorophore distance increases (increased silica shell thickness), the local electric field intensity near the silica shell reduces, which results in less gain at the particle surface and an increased lasing threshold.

The increase of the lasing threshold with the increased scattering strength (figure 6.10) also shows that scattering is less important than surface plasmon effects in the metal-based random lasers. The inherent physics of this behavior is attributed to the modification of the pump rate, $\gamma_p$ and the absorption rate, $\gamma_{ab}$ as discussed in refs. [37, 39]. The magnitude of the pump rate, $\gamma_p$ depends on the incident laser field whereas the enhanced field due to the localized surface plasmons is based on the spatial distribution of the electric field intensity on the silica-coated silver nanoparticles. So, the magnitude of $\gamma_p$ declines as the molecule is far away (figure 6.12) [37]. The absorption rate, $\gamma_{ab}$ determines the energy transfer from molecules to metallic nanoparticles which influences the fluorescence properties. $\gamma_{ab}$ decreases as

the dye molecule is far away from the particle while the excessive $\gamma_{ab}$ near the metal surface is detrimental to lasing and leads to a high lasing threshold [37]. Thus, the decreased $\gamma_p$ and $\gamma_{ab}$ increases the lasing threshold of silver-based random dye lasers. Figure 6.12 shows that the local field at the surface of Au@$SO_2$ nanoparticles is largely modified by the dielectric spacer, indicating that the interactions between Au and Rh6G vary with *d*. The discrete dipole approximation calculation of electromagnetic field around metallic nanoparticle in figure 6.12 shows that when the silica thickness increases to 7.6 cm, the local field effect reduces which increases the lasing threshold. We believe that the local field enhancement still affects the random laser action, but not as much as gold without silica shell.

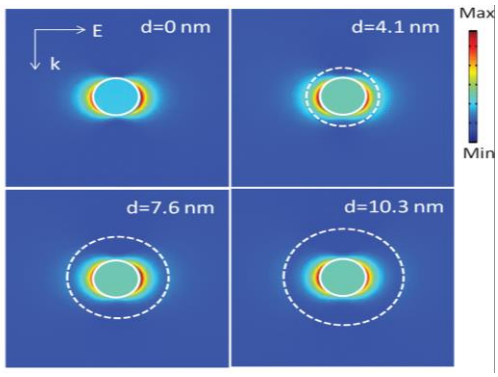


Figure 6.12 Spatial distribution of electric field intensity for silica-coated gold nanoparticles with increasing silica shell thicknesses, as shown by the discrete dipole approximation (DDA). The solid line and the dashed line present the core and shell of gold nanoparticles [39].

The metal-fluorophore distance may affect the emission peak shift, as shown in figure 6.11. The emission peak shifts possibly because the extinction peak reduces (figure 6.6) that leads to a decrease in light absorption. The competition between monomer and dimer emitters of dye may also influence the emission peak shifts [168, 169]. From the aforementioned results and discussion, it is clear that the performance of random lasers reduces (increased lasing threshold) when the dye molecules are distant from the metal nanoparticles.

## 6.2 Random lasers with lumpy bimetallic nanoparticles.

### 6.2.1 Introduction

The performance of random lasers can be influenced by the surface roughness of scatterers [58, 99, 108] as discussed in Chapter 1 (Section 1.2.5.4). Improved feedback can be provided by scattering induced by rough micron-scale grooves [99] or nano-rubbing induced cavities [58]. Random lasing can be observed in dye solution with metal nanowires in which nanowires act as nano-antennas to enhance plasmonic effects [60] and the emission wavelength range can be extended by introducing roughness to the silver nanowires [108]. Surface roughness affects the plasmonic properties of the metal nanoparticles by significantly enhancing local fields and plasmonic effects compared to smooth metal nanoparticles. This leads to peak-broadening and red-shifting of the single particle-plasmon resonances [185].

In this work, random lasing was realized in a dye solution (Rhodamine 640) with lumpy bimetallic nanoparticles (silver and gold) which induced incoherent random lasing with a narrow emission linewidth ~ 3 nm.

### 6.2.2 Sample preparation and characterization

Using boiled deionized water (38 ml), 2 ml of silver colloid aqueous solution (average diameter ~ 45 ± 2 nm, $6 \times 10^{10}$ $cm^{-3}$) (sample from Section 6.1) was added and followed by the addition of 0.009 g of silver nitrate (Sigma Aldrich). Then, 1 ml of 34 mM trisodium citrate (Sigma Aldrich) was added dropwise to the suspension which was kept boiling for 5 to 10 minutes leading to the formation of silver colloids with different core sizes. The silver colloid solution was cooled to room temperature

and was centrifuged for 500 rcf for 1 hour to remove larger silver nanoparticles (sediment). The supernatant was taken and centrifuged again for 5 krcf for 10 minutes to obtain smaller silver colloids. Then, the silver colloids were washed and dispersed in deionized water for further experiments.

The TEM images of the silver colloids are shown in figure 6.13. Slight aggregation is observed since the silver colloids are not diluted. The silver nanoparticle surface is smooth and the average diameter of the silver nanoparticles is ~ 30 ± 2 nm from TEM measurement. The particle concentration was estimated by drying and weighing the dried samples, which gives $2.2 \times 10^{-5}$ g/cm$^3$ or $1.1 \times 10^{11}$ cm$^{-3}$.

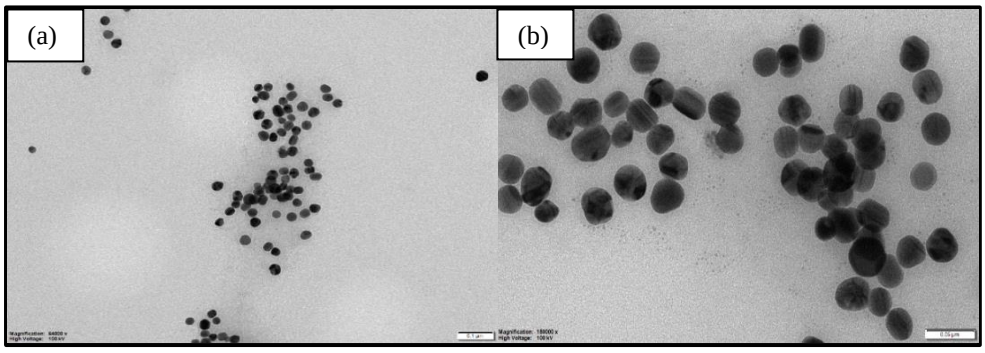


Figure 6.13 TEM images of silver nanoparticles ($1.1 \times 10^{11}$ cm$^{-3}$) with a scale bar of (a) 100 nm and (b) 50 nm.

To prepare lumpy bimetallic nanoparticles, the as-prepared silver nanoparticle solution was diluted (4×) and ultrasonically dispersed to prevent aggregation. 40 µl of gold (III) chloride trihydrate ($HAuCl_4$) (4.8 mM) (Sigma Aldrich) was added to the diluted silver nanoparticles ($2.8 \times 10^{10}$ cm$^{-3}$) in a mixed 0.25:0.75 water:ethanol solution and the solution was stored at room temperature overnight (12 hours) to ensure gold (Au) atoms epitaxially nucleated and grew on the surface of the silver (Ag) through galvanic replacement reactions [186]. The concentration of lumpy bimetallic nanoparticles was estimated as ~ $2.8 \times 10^{10}$ cm$^{-3}$.

Figure 6.14 shows the TEM image of the lumpy bimetallic nanoparticles. We observe the lumpy and rough surface of the bimetallic nanoparticles with the average diameter ~ 32 ± 2 nm and the nanogaps at the rough surface of the nanoparticles (figure 6.14 (inset)). Rhodamine 640 ($1 \times 10^{-4}$ M) was added to the lumpy bimetallic nanoparticle solution in a quartz cuvette (1 cm × 1 cm) for random laser studies.

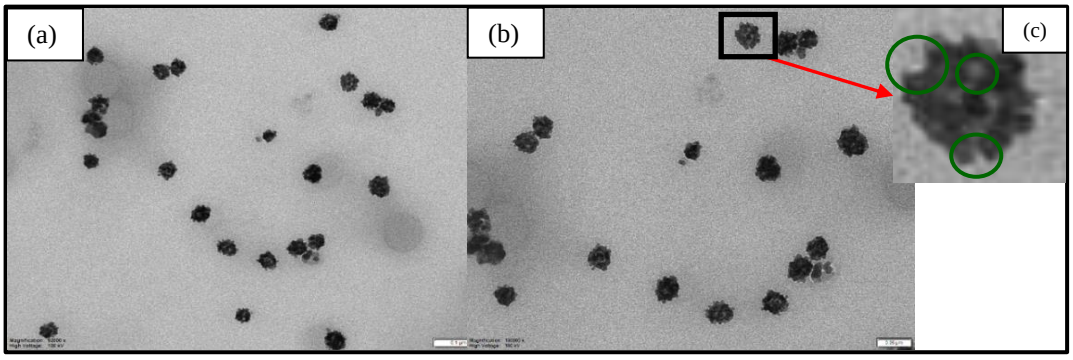


Figure 6.14 TEM images of lumpy bimetallic nanoparticles ($2.8 \times 10^{10}$ $cm^{-3}$) with a scale bar of (a) 100 nm, (b) 50 nm and (c) The enlarged view of a lumpy bimetallic nanoparticle. The green circles show the nanogaps.

The scattering mean free paths of silver and lumpy bimetallic nanoparticle solution, $l_s$ are estimated as ~ 446 cm and ~ 298 cm, based on $l_s = 1 / (\rho\sigma_s)$ [3, 28, 36-38] where $\rho$ and $\sigma_s$ refer to the number density of scatterers and scattering cross section respectively. $\sigma_s$ for silver and lumpy bimetallic nanoparticles are estimated as ~ $8 \times 10^{-14}$ $cm^2$ and ~ $1.2 \times 10^{-13}$ $cm^2$ at the optical wavelength of $\lambda$ ~ 600 nm calculated from Mie theory [35, 36, 41, 84, 154]. As $l_s >> L$ (sample size ~ 3 mm), the random lasers are in the weakly scattering regime [1, 39].

### 6.2.3 Optical measurements

The absorption and fluorescence spectra were measured using a Cary spectrophotometer and Fluorolog spectrofluorometer. The random laser experimental set up is similar to that in Chapter 4 (Section 4.3.2 Optical measurements).

### 6.2.4 Results and discussion

Figure 6.15 compares the extinction (absorption) spectra of silver and lumpy bimetallic nanoparticle solutions and the absorption and fluorescence spectra of Rhodamine 640. When Au atoms grow on the surface of the silver, the silver plasmon resonance peak shifts from 410 nm (orange curve) to 560 nm and broadens (red curve), thus producing a more effective overlap of the spectra of the lumpy bimetallic nanoparticles with the pump laser wavelength, absorption and fluorescence of Rhodamine 640 (Rh640).

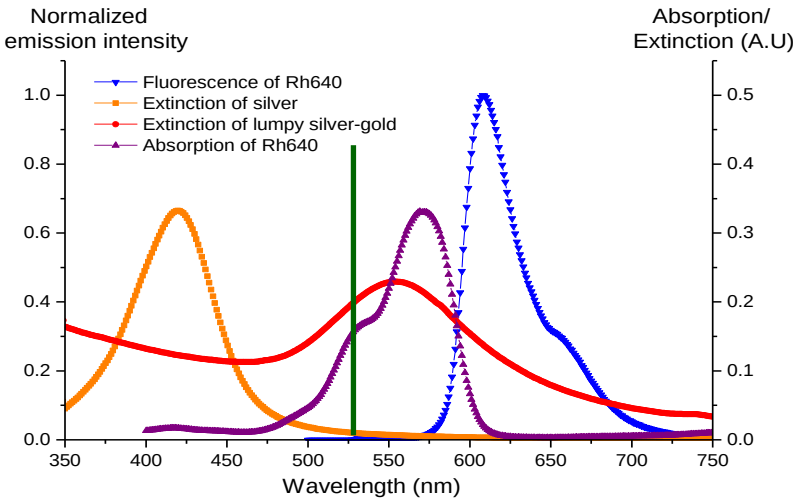


Figure 6.15 Extinction (absorption) spectra of silver and lumpy bimetallic nanoparticles (of Rhodamine 640) and fluorescence spectrum of Rhodamine 640: Extinction spectrum of silver (orange curve); extinction spectrum of lumpy bimetallic nanoparticles (red circle curve); absorption of Rhodamine 640 (purple triangle curve) and fluorescence spectrum of Rhodamine 640 (dark blue curve). The vertical line (dark green) indicates the pump laser wavelength.

Figures 6.16 (a) and 6.16 (b) present the emission spectra of Rh640 random lasers with silver nanoparticles and with lumpy bimetallic nanoparticles respectively. We observe distinctive spectral narrowing for the Rh640 / lumpy bimetallic random lasers (figure 6.16 (b)).

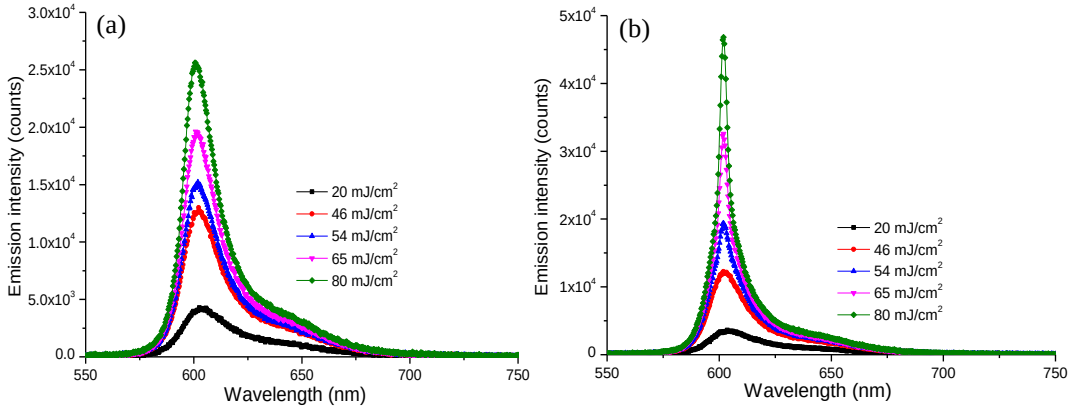


Figure 6.16 Emission spectra of (a) Rh640 ($1 \times 10^{-4}$ M) / silver and (b) Rh640 ($1 \times 10^{-4}$ M) / lumpy bimetallic random lasers.

Rh640 / lumpy bimetallic random lasers exhibit a lasing threshold at ~ 53 mJ/cm$^2$, as estimated from the abrupt increase of the emission peak intensity and the decrease of the emission linewidth (75 % of emission peak intensity) as shown in figure 6.17. Meanwhile, Rh640 / silver random lasers only produce a linear increase of the emission peak intensity and decrease of the emission linewidth (figure 6.17). The emission linewidth gradually decreases from 23 nm to 15 nm for Rh640 / silver random lasers while the emission linewidth abruptly decreases from 23 nm to 5 nm for Rh640 / lumpy bimetallic random lasers. We observe a nonlinear increase of the emission peak intensity and a step decrease of the emission linewidth with the pump level for Rh640 / lumpy bimetallic random lasers which were comparable with that reported in ref. [49, 53]. A sharp reduction of the emission linewidth indicates the onset of the stimulated emission [49]. Here, we estimate the lasing threshold from ~ 52 mJ/cm$^2$ to 55 mJ/cm$^2$ when the emission peak intensity starts to increase nonlinearly and emission linewidth decreases sharply (figure 6.17). Rh640 / lumpy bimetallic random lasers exhibit a clear threshold with an abrupt decrease of emission linewidth due to the surface roughness on lumpy bimetallic nanoparticles.

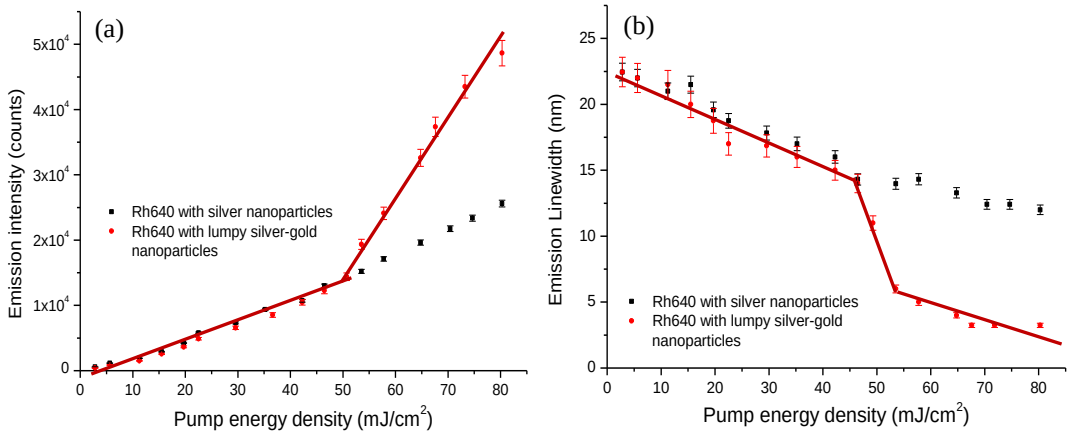


Figure 6.17 (a) Emission peak intensity and (b) Emission linewidth at 75% of emission peak intensity as a function of pump energy density for Rh640 ($1 \times 10^{-4}$ M) / silver and Rh640 / lumpy bimetallic random lasers. The lasing threshold is estimated when the emission peak intensity increase nonlinearly with the pump level or when the emission linewidth drops significantly as indicated by the brown line.

Spectral narrowing and lasing threshold are evidence of random lasing with incoherent feedback [1, 2]. The Rh640 with lumpy bimetallic nanoparticle random lasers exhibit these characteristics due to two factors: (1) surface roughness and (2) bimetallic nanoparticles.

(1) Comparing the silver nanoparticles with smooth surfaces (figure 6.13) to the lumpy bimetallic nanoparticles with rough, porous surfaces (figure 6.14), the roughness of the lumpy bimetallic nanoparticles is due to gold atoms attached to the silver surface. The dye molecules may be concentrated near the nanogaps and the nanogaps form energy "hotspot" which increase the local electromagnetic field [187].

(2) Silver nanoparticles have a surface plasmon band within range 350 nm to 500 nm with a plasmon peak at ~ 410 nm (figure 6.15) and this leads to almost negligible plasmon effects on the fluorescence spectrum of Rhodamine 640 whereas the plasmon resonance peak of the bimetallic nanoparticles red-shifts and broadens. The scattering mean free path of the silver nanoparticle solution, $l_s$ ~ 446 cm at $\lambda$ ~ 600 nm indicates the weakly scattering regime [1, 39] with less scattering. With

insufficient scattering and almost negligible plasmon effects to increase the gain, no random lasing is observed for the Rh640 / silver nanoparticle solution. In contrast, the lumpy bimetallic nanoparticles have a plasmon band in the visible range which overlaps effectively with the absorption and fluorescence of Rh640, and gives plasmonic enhancement to the Rh640 / lumpy bimetallic nanoparticle random lasers. Though the lumpy bimetallic nanoparticles are in the weakly scattering regime ($l_s \sim$ 298 nm at $\lambda \sim 600$ nm) [1, 39], the plasmon effects can compensate for the weak scattering and produce effective random lasing.

## 6.3 Chapter 6 Summary

We studied the effects of localized surface plasmons on the performance of random lasers to understand the influence of metal-fluorophore distance and surface roughness of nanoparticles. In both cases, we observed that the metal-fluorophore distance and the nanoparticle surface roughness modify the surface plasmon resonance band and thus influence the spectral overlap between the plasmon band and the absorption and / or fluorescence of the dye. Increasing the metal-fluorophore distance increases the random lasing threshold whereas introducing roughness on the scatterers reduces the threshold for random lasing.

# Chapter 7

# Dopamine sensing and measurements using random lasers

We developed a novel dopamine sensing and measurement technique based on aggregation of gold nanoparticles in random lasers. Dopamine combined with copper ions triggers the aggregation of gold nanoparticles and thus affects the performance of random lasers. Dopamine sensing can be achieved using four random lasing parameters which are sensitive to the presence of dopamine namely emission peak shift, emission linewidth, peak to background ratio and random lasing threshold. The dopamine is most sensitively detected by a change in the emission linewidth with a limit of detection of $1 \times 10^{-7}$ M, as well as by an increase in the lasing threshold. The dopamine concentration from $1 \times 10^{-7}$ M to $1 \times 10^{-2}$ M can be determined by calibrating with the laser threshold.

Results in Chapter 7 have been published as:

W. Z. Wan Ismail, G. Liu, K. Zhang, E. M. Goldys and J. M. Dawes, "Dopamine sensing and measurement using threshold and spectral measurements in random lasers," Optics Express **24** (2), A85-A91(2016).

The first author (W. Z. Wan Ismail) set up and conducted the experiment, analyzed the experiment results and wrote the article. The second author (G. Liu) suggested the measurement of dopamine and the third author (K. Zhang) gave advice in preparing the samples. The other authors (E. M. Goldys and J. M. Dawes) supervised the first author in setting up the experiment, analysing and discussing the results.

## 7.1 Introduction

Medical diagnostics and sensing are increasingly being achieved using light-based technologies. Vardeny *et al.* [92] applied random lasers to detect cancerous tissues. They soaked biological tissues extracted from human organs such as colon and kidney in Rhodamine 6G dye and created random lasers. The cancerous tissues-based random lasers showed more emission peaks than the normal tissue-based random lasers due to their more disordered structures.

Parkinson's and Huntington's disease are fatal diseases that can affect the human brain and a signature of these disease is changes in dopamine concentration [188-190]. Dopamine is a catecholamine neurotransmitter distributed in the brain tissues and body fluids of mammals [188]. It has important roles in the function of the central nervous, renal and cardiovascular systems. Cerebro-spinal fluid levels of neuronal metabolites of catecholamine provide neurochemical biomarkers of Parkinson's disease including dopamine and norepinephrine. The dopamine concentration in patients with Parkinson's disease is estimated within $0.11 \pm 0.04$ nmol/l [191]. A deficiency of dopamine in the brain leads to 'out of control' muscle activity in Parkinson's disease, while excessive dopamine leads to Huntington's

disease [188-190]. Therefore, the measurement of dopamine is significant in diagnosis, monitoring, prevention and treatment of these conditions.

Several authors have used optical methods to sense dopamine, including techniques based on nanoparticle aggregation [189] and colorimetric assays [192]. In particular, Su *et al.* [189] used copper ions to enhance the aggregation of gold nanoparticles by dopamine. The limit of detection was $2 \times 10^{-7}$ M, determined by a colour change and absorption peak shift. Chen *et al.* [192] used melamine-induced aggregation of gold nanoparticles to detect dopamine in a complex medium of human urine, where they achieved a limit of detection of 33 nM. The lowest detection limit of dopamine reported in the literature is 0.3 nM [190]. The detection mechanism in this work was based on fluorescence resonant energy transfer (FRET) from the silicon nanoparticles to dopamine.

This study demonstrates the first-time use of random lasers with incoherent feedback to detect dopamine based on dopamine-induced aggregation of gold nanoparticles. In random lasers, [2] random scatterers and gain media are mixed together. Light undergoes multiple scattering events in the random medium while it is simultaneously amplified by stimulated emission in the gain medium. Features of random lasing including the presence of laser emission, lasing threshold, polarization and coherence of emission are determined by properties such as plasmonic effects [39, 102]. While nanoparticle aggregation is widely exploited in biosensing, to the best of our knowledge, it has not been used to detect trace quantities of biomolecules in random lasers. We hypothesised that since multiple light scattering and gain are important in random lasers as they provide feedback and light amplification, the presence of analyte affecting nanoparticle aggregation may be detected via random

lasing. This is because the aggregation of nanoparticles may lead to sedimentation and it also reduces the number density of scatterers. When multiple light scattering is reduced due to reduced number density of scatterers, the feedback is also reduced which thus affects the random laser performance. Noginov *et al.* [193] observed an increased lasing threshold and reduced laser slope efficiency for aggregated silver nanoparticles in Rhodamine 6G dye lasers.

Dopamine detection using lasers could be a novel alternative to current techniques which involve chemical or biological effects, provided there is sufficient detection sensitivity. To explore this, we investigated different sensing parameters such as emission peak shift, emission linewidth, peak to background ratio and lasing threshold. We found that the aggregation results in an emission peak red-shift of ~ 1 nm and broadening of the emission linewidth. We also observed a decrease of the peak to background ratio and an increase of the lasing threshold with aggregation. In our system, the limit of dopamine detection is ~ $1 \times 10^{-7}$ M, higher than the estimated dopamine concentration in patients with Parkinson's disease [191]. The sensitivity of the dopamine detection can possibly be improved with higher power pump lasers but may also be limited by interference from other molecules. We were able to measure dopamine concentration based on the random lasing threshold over a wide dynamic range from $10^{-7}$ M to $10^{-2}$ M.

## 7.2 Experimental Methods

### 7.2.1 Sample preparation and characterization

Various concentrations of dopamine in water ($1 \times 10^{-8}$ to $1 \times 10^{-2}$ M) (Sigma Aldrich) were added to gold nanoparticles (the number density of scatterers, $\rho \sim 1.8 \times$

$10^{11}$ $cm^{-3}$, size ~ 20 nm) (Ted Pella) and stirred for 5 minutes to mix the sample before 0.15 mM copper (II) chloride (Sigma Aldrich) was added. Small sized gold nanoparticles were used to prevent precipitation or too-rapid aggregation with the dopamine. The concentration of copper (II) chloride was optimized to 0.15 mM because the aggregation of gold nanoparticles occurs with increased concentration of copper (II) chloride even without dopamine. The final solution was 0.35:0.65 methanol:water. The solution was stored at room temperature for 30 minutes to allow aggregation before recording the optical measurements. Rhodamine 640 (Exciton, $1 \times 10^{-4}$ M) was added as the random laser gain medium.

The scattering mean free path, $l_s = 1 / (\rho\sigma_s)$ [3, 28, 36-38], (Chapter 1: Section 1.2.2.1 Multiple light scattering (eq. 1.8)), for the gold nanoparticle solution with 0 M of dopamine is ~ 139 cm, where $\rho$ and $\sigma_s$ refer to the number density of scatterers and scattering cross section respectively. $\sigma_s$ is estimated as ~ $4 \times 10^{-14}$ $cm^2$ at the optical wavelength of $\lambda$ ~ 532 nm based on Mie theory [35, 36, 41, 84, 154]. As $l_s >> L$ (sample size ~ 3 mm), the random laser with gold nanoparticles and no dopamine is in the weakly scattering regime [1, 3, 39]. With added dopamine, the value of $l_s$ may increase due to reduced number density of scatterers.

We observed the aggregation of gold nanoparticles due to addition of dopamine and copper (II) chloride using transmission electron microscopy (TEM) (figure 7.1) (the TEM process was explained in Chapter 2 (Section 2.1.2.4: Characterization of ruby nanocrystals)). The size of the gold nanoparticles increases and the shape becomes irregular after aggregation, as shown in the TEM images in figure 7.1.

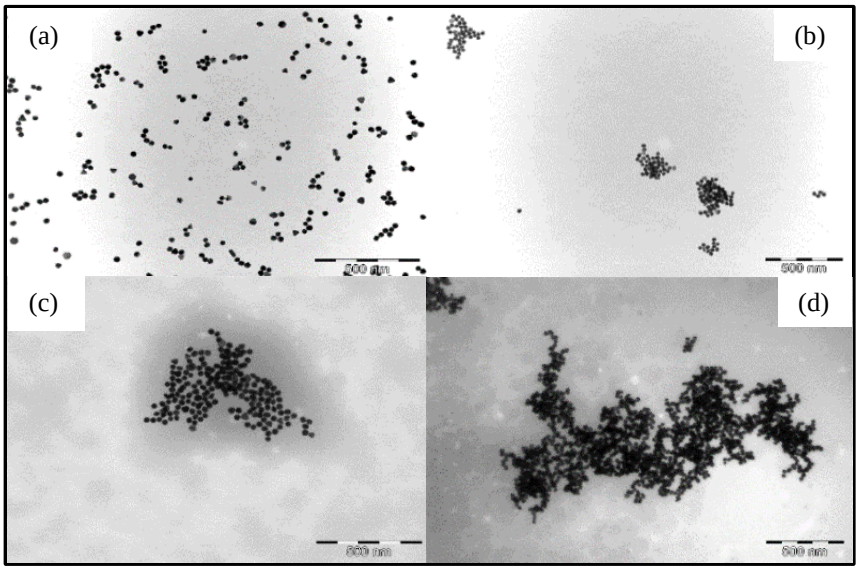


Figure 7.1 TEM of gold nanoparticles with 0.15 mM copper (II) chloride and (a) 0 M, (b) $1 \times 10^{-7}$ M, (c) $1 \times 10^{-5}$ M and (d) $1 \times 10^{-3}$ M of dopamine concentration. The scale bar end to end is 500 nm.

### 7.2.2 Optical measurements

The random laser measurements set up shown in Chapter 4 (Section 4.3.2 Optical measurements (figure 4.1)) was used in this chapter. The samples were excited with the Q-switched, frequency-doubled Nd:YAG laser at an angle of 45$^o$ to the normal to the front face of the cuvette and the emission light was collected from the front face of the cuvette at 30$^o$ to the normal by a lens ($f$ = 5 cm) and measured by a fibre-coupled spectrometer. The absorption / extinction spectra of the Rh640 / gold nanoparticles were measured by a Cary spectrophotometer (Varian) while the fluorescence was measured by Fluorolog spectrofluorometer (Horiba Jobin Yvon).

## 7.3 Results and discussion

### 7.3.1 Absorption and fluorescence spectra

The absorption spectra of Rh640 with and without dopamine / copper (II) chloride and the extinction spectra of gold nanoparticles with 0.15 mM of copper (II)

chloride are shown in figure 7.2. These graphs exhibit similar shapes so it appears that no aggregation is observed for Rh640 with dopamine (1 mM) and copper (II) chloride (0.15 mM) and gold nanoparticles with copper (II) chloride (0.15 mM).

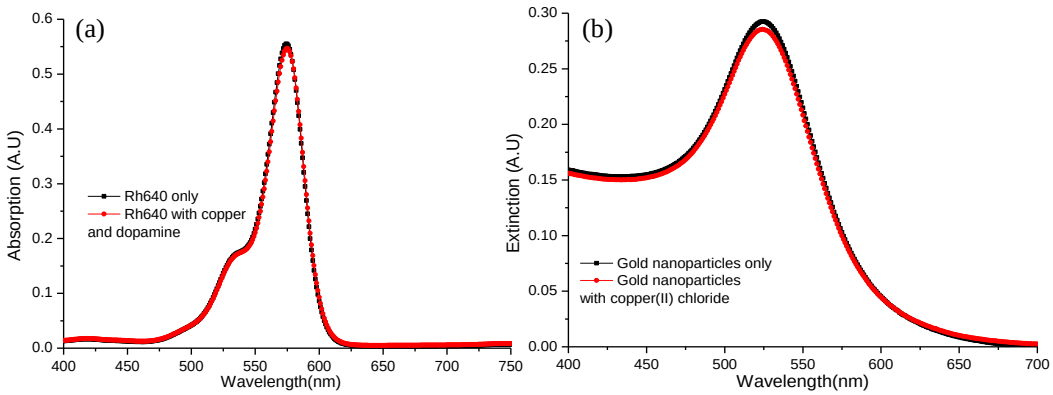


Figure 7.2 (a) Absorption spectra of Rh640 with and without copper (II) chloride (0.15 mM) and dopamine (1 mM) and (b) Extinction spectra of gold nanoparticles with and without copper (II) chloride (0.15 mM). No aggregation / coupling between dye and dopamine or copper is observed for both samples as the absorption and extinction spectra are quite similar.

Figure 7.3 presents the extinction spectra for gold nanoparticle solutions for varying concentrations of added dopamine. This figure shows that dopamine red-shifts the extinction peak of the gold nanoparticles and the shoulder starts to appear at 650 nm at a dopamine concentration of $1 \times 10^{-7}$ M. The extinction spectra of the gold nanoparticles change their shape when the gold nanoparticles aggregate [189]. The extinction spectra (figure 7.3) show that the extinction peak at ~ 530 nm decreases and shifts to the longer wavelength, which is indicative of aggregation. With more dopamine, increased aggregation of the gold nanoparticles leads to further wavelength shift in the extinction spectrum. The red-shifted extinction peak was also observed by Su *et al.* [189]. Figure 7.4 shows that gold / dopamine with copper (II) chloride shifts the extinction peak faster than gold / dopamine without copper (II) chloride. The gold extinction peak at 530 nm decreases and the extinction peak at 650 nm due to the

aggregated gold nanoparticles starts to increase with the addition of copper (II) and dopamine.

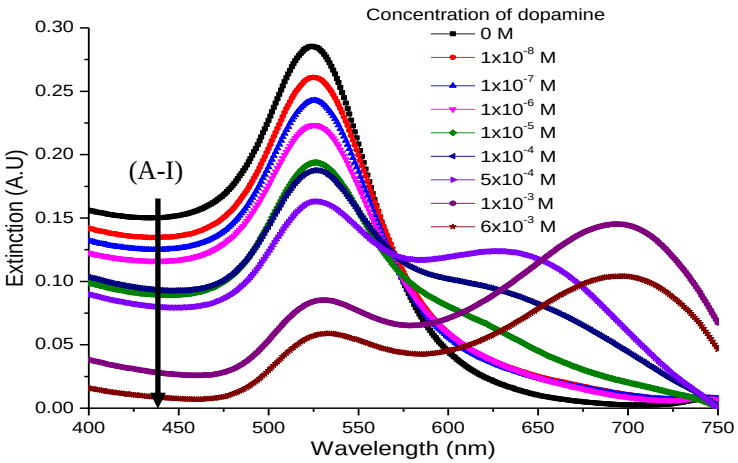


Figure 7.3 Extinction spectra of gold nanoparticle solutions ($1.8 \times 10^{11}$ $cm^{-3}$, ~ 20 nm) with varied dopamine concentrations (A-I) and 0.15 mM of copper (II) chloride without Rh640. From A to I, the concentrations of dopamine are 0, 0.01, 0.1, 1, 10, 100, 500, 1000 and $6000 \times 10^{-6}$ M. The solvent is methanol-water mixture (0.35:0.65). The aggregation of gold nanoparticles is seen when the extinction peak shifts to the longer wavelength due to addition of dopamine. The red shift occurs as the copper ions stimulate the gold aggregation by dopamine. Adding dopamine to gold nanoparticles leads to aggregation of gold nanoparticles.

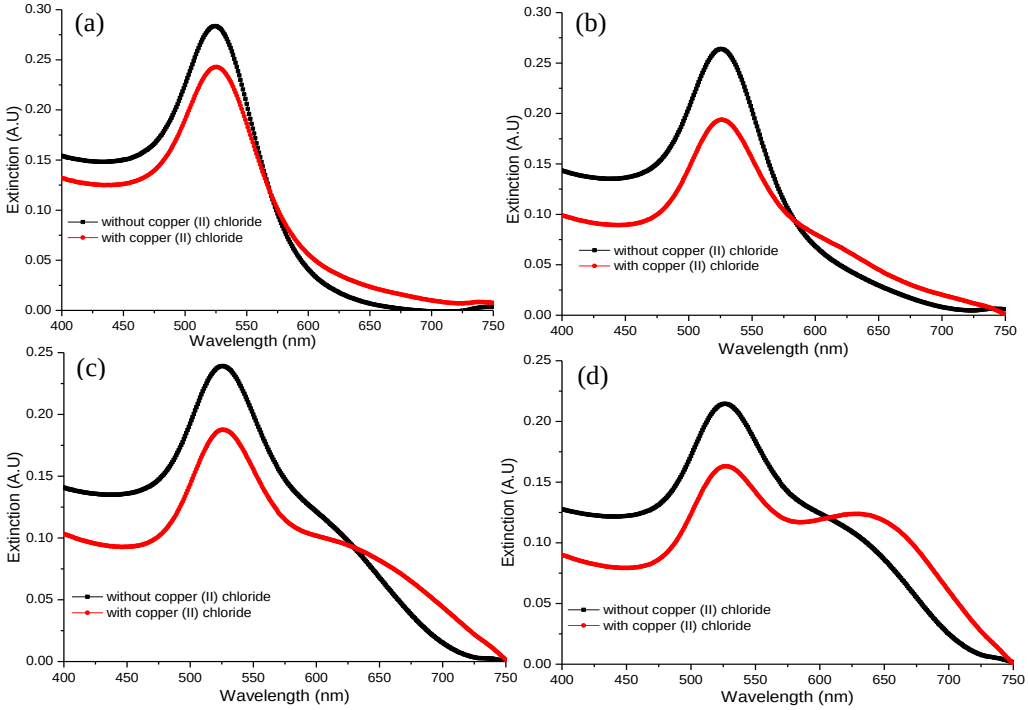


Figure 7.4 Comparison of extinction spectra of gold nanoparticles with (a) $1 \times 10^{-7}$ M, (b) $1 \times 10^{-5}$ M, (c) $1 \times 10^{-4}$ M, (d) $5 \times 10^{-4}$ M of dopamine and with / without 0.15 mM copper (II) chloride (without Rh640). Adding copper ions enhances the aggregation.

### 7.3.2 Dopamine sensing and measurement by random lasers

All samples were separately excited by the frequency doubled laser, Nd:YAG laser (532 nm, 10 Hz, 4 ns). The Rh640 / Dopamine / Copper (II) Chloride samples for different pump energy densities exhibit broad spectra as shown in figure 7.5. With no gold particles, there was no scattering and no laser operation.

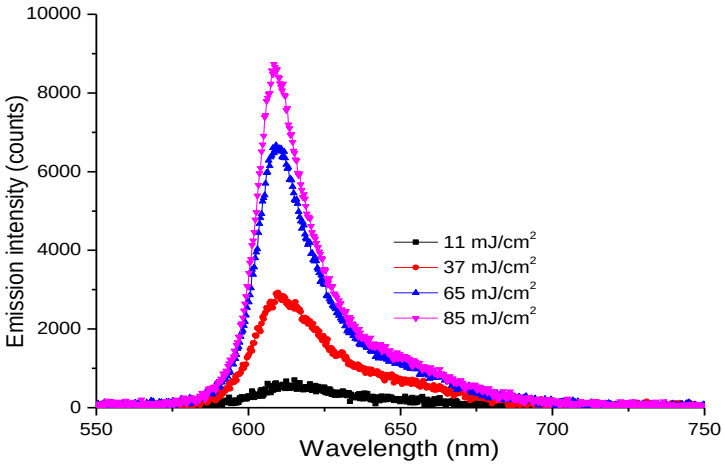


Figure 7.5 Broadband emission spectra of Rhodamine 640 ($1 \times 10^{-4}$ M) / dopamine (1 mM) / Copper (II) Chloride (0.15 mM) without gold nanoparticles for various pump energy densities. The emission linewidth at 50 % of emission peak intensity for emission spectrum (85 mJ/cm$^2$) is 40 nm.

Gold nanoparticles provide scattering for the feedback mechanism in random lasers. Figure 7.6 shows the emission spectra of Rh640 / gold nanoparticles with various concentrations of dopamine and a fixed concentration of Copper (II) Chloride (0.15 mM). A narrow emission peak appears when the lasing threshold is achieved. In figure 7.6 (f), broad emission spectra are observed for all pump levels and no random lasing occurs.

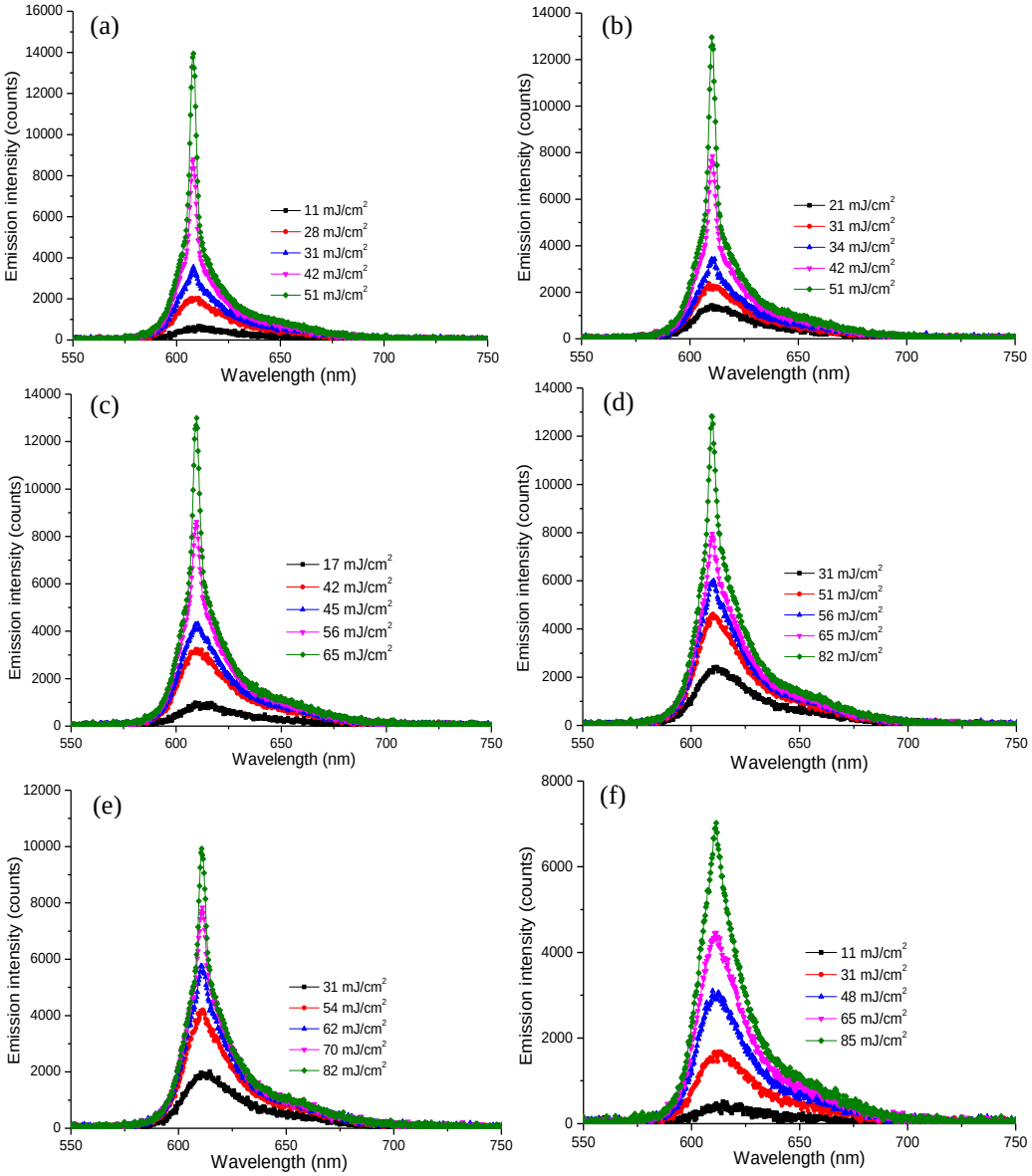


Figure 7.6 Emission spectra of Rh640 / gold random lasers with copper (II) chloride (0.15 mM) and varied concentrations of dopamine; (a) 0 M, (b) $1 \times 10^{-7}$ M, (c) $1 \times 10^{-5}$ M, (d) $5 \times 10^{-4}$ M, (e) $6 \times 10^{-3}$ M and (f) $1 \times 10^{-2}$ M for different pump energy densities. The emission spectra narrows (4 nm) when the lasing threshold is achieved. No spectral narrowing is observed for the highest concentration of dopamine, figure (f).

The emission peak red-shifts when the gold particle aggregation occurs for a concentration of $1 \times 10^{-7}$ M of dopamine as shown in figure 7.7. In figure 7.7 (a), the emission peak shift cannot be seen clearly for the low pump energy density, 31 mJ/cm$^2$ because the threshold is not yet reached for some dopamine concentrations but when the pump energy density is increased (figure 7.7 (c-d)), the emission peak shift is

clearly observed. The emission wavelength shift is small (less than 1 nm) for all concentrations of dopamine. The aggregation of gold nanoparticles also affects the linewidth of the emission spectra (figure 7.7) as the emission spectrum broadens for all concentrations of dopamine from $1 \times 10^{-7}$ M at low pump energy density, 31 mJ/cm$^2$. When the pump energy density increases up to 48 mJ/cm$^2$, the emission spectrum broadens from $3 \times 10^{-6}$ M. For 85 mJ/cm$^2$, spectral narrowing was observed for all concentrations of dopamine.

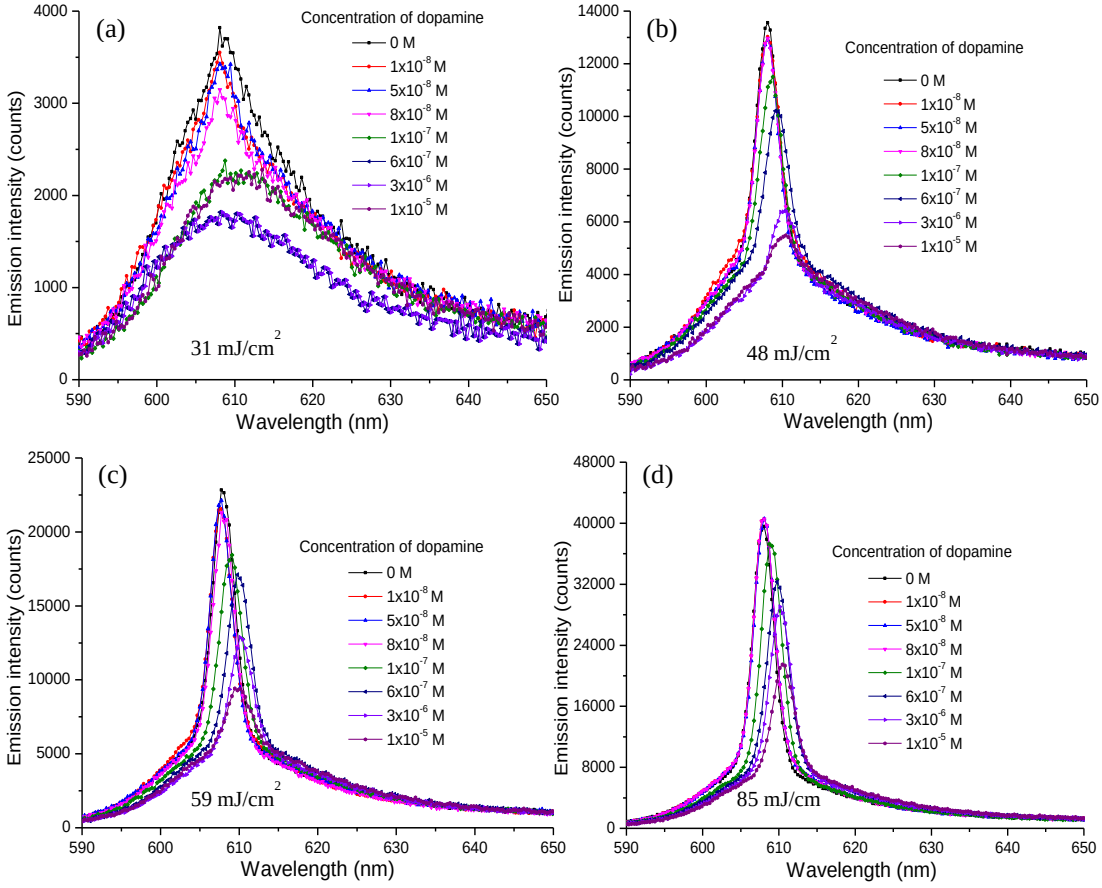


Figure 7.7 Emission spectra of Rh640 / gold random lasers with copper (II) chloride (0.15 mM) and various concentrations of dopamine pumped with (a) 31 mJ/cm$^2$, (b) 48 mJ/cm$^2$, (c) 59 mJ/cm$^2$ and (d) 85 mJ/cm$^2$.

The random lasing threshold for Rh640 / gold / dopamine is shown in figure 7.8 for various concentrations of dopamine. The emission peak intensity increases

nonlinearly with the pump energy density as shown in figure 7.8. Figure 7.8 shows that the lasing threshold for 0 to 8 × $10^{-8}$ M of dopamine is quite similar and the threshold increases from 1 × $10^{-7}$ M. The emission peak intensity decreases and the lasing threshold increases when the concentration of dopamine is increased.

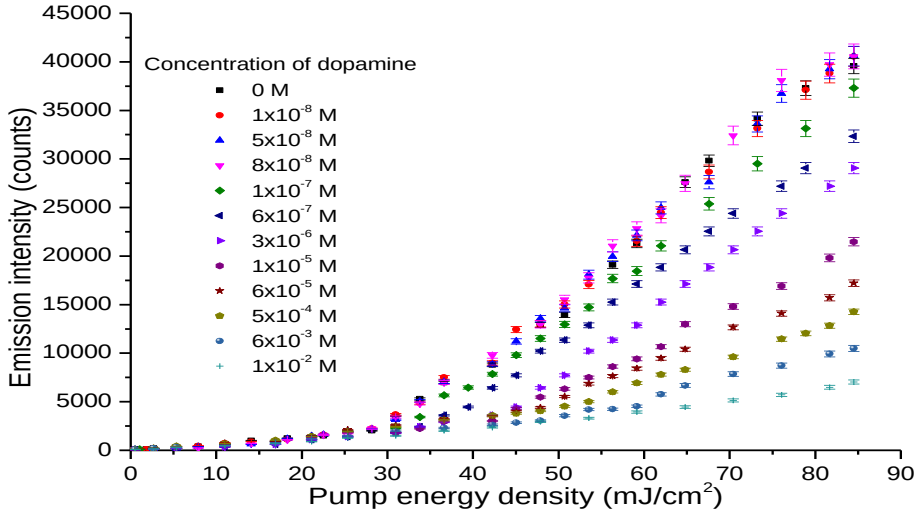


Figure 7.8 Emission peak intensity of Rh640 / gold random lasers with copper (II) chloride (0.15 mM) and various concentrations of dopamine versus pump energy density. The lasing threshold is determined when the emission peak intensity increases nonlinearly with the pump energy density.

Random lasing can be used to detect dopamine through the aggregation of gold nanoparticles, enhanced by copper ions. In this study, the dopamine detection limit using random lasing is ~ 1 × $10^{-7}$ M based on several sensing parameters such as emission peak shift, linewidth, emission peak intensity to background ratio and lasing threshold transition.

Dopamine triggers aggregation of gold nanoparticles because dopamine molecules are adsorbed onto the surface of the gold nanoparticles by electrostatic adhesion. Addition of copper (II) chloride assists the aggregation of gold nanoparticles by dopamine through interactions between $Cu^{2+}$ ions with the amino and hydroxyl groups of the dopamine molecules. Figure 7.3 shows the spectral absorption of gold

with dopamine shifts with the addition of copper (II) chloride. The $Cu^{2+}$ ions serve as a selective "discriminator and linker" at high gold nanoparticle concentrations, changing the colour of their solutions from wine red to blue [189] due to aggregation.

The first signature of dopamine is a small emission peak wavelength shift, plotted in figure 7.9. The small change in emission peak wavelength of the Rh640 / gold / copper (II) chloride random lasers occurs as the size and shape of the gold nanoparticles change due to aggregation, resulting in changes to the localized surface plasmons and energy transfer process [13, 14, 39, 189]. Thus, the emission peak red-shifts (< 1 nm) with increased concentration of dopamine above the limit of detection of $1 \times 10^{-7}$ M.

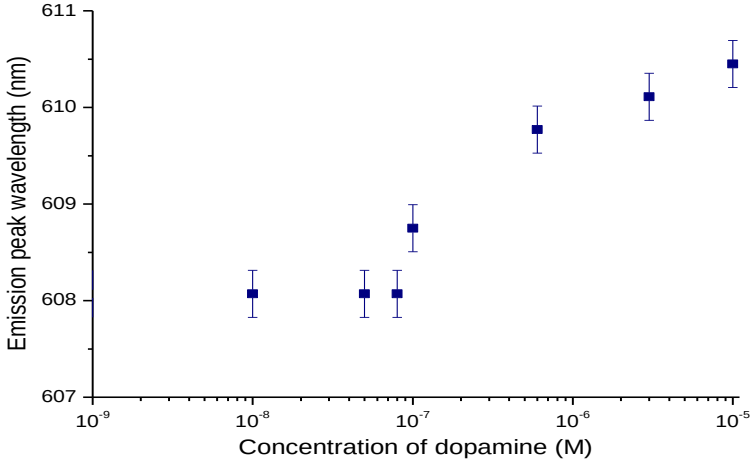


Figure 7.9 The emission peak wavelength of Rh640 / gold / copper (II) chloride random lasers for various concentrations of dopamine, excited with 85 mJ/cm$^2$. The emission peak wavelength red-shifts for above $10^{-7}$ M of dopamine concentration.

The second indicator of dopamine detection by random lasing is determined through the emission linewidth changes of Rh640 / gold / copper (II) chloride for various concentrations of dopamine estimated at 90 % of emission peak intensity, as shown in figure 7.10. This analysis was done at a low pump energy, 31 mJ/cm$^2$ where

Rh640 / gold / copper (II) chloride random lasers with ≥ 1 × $10^{-7}$ M of dopamine showed broad spectra and no lasing. The emission linewidth increased when the concentration of dopamine was increased from 8 × $10^{-8}$ to 1 × $10^{-7}$ M.

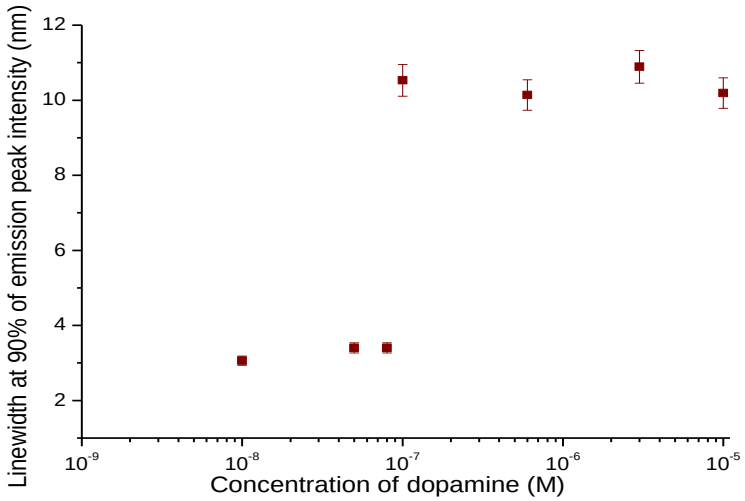


Figure 7.10 The emission linewidth of Rh640 / gold / copper (II) chloride random lasers for various concentrations of dopamine at 90% of emission peak intensity, excited with 31 mJ/cm$^2$. The emission linewidth shows a huge jump, 7 nm when the concentration of dopamine was increased from 8 × $10^{-8}$ to 1 × $10^{-7}$ M.

Furthermore, we observed that the random lasing peak intensity to background ratio is also a signature of the presence of dopamine (figure 7.11). The peak to background ratio drops from 20 (8 × $10^{-8}$ M of dopamine) to 14 (1 × $10^{-7}$ M of dopamine) for low pump energy density excitation (31 mJ/cm$^2$). For high pump energy density excitation (85 mJ/cm$^2$), the peak to background ratio decreases from 270 (8 × $10^{-8}$ M of dopamine) to 250 (1 × $10^{-7}$ M of dopamine), indicating the limit of dopamine detection to be 1 × $10^{-7}$ M. Rh640 / gold / copper (II) chloride / dopamine random lasers pumped with 85 mJ/cm$^2$ show the peak to background ratio is 10× higher than 31 mJ/cm$^2$ as the emission intensity is higher at high pump energy density.

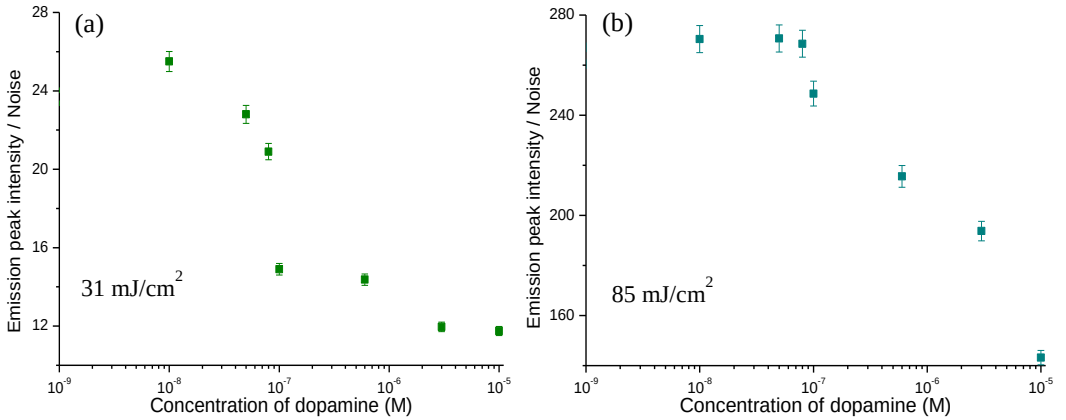


Figure 7.11 Emission peak intensity to background ratio of Rh640 / gold / copper (II) chloride random lasers with various concentrations of dopamine excited with (a) 31 mJ/cm$^2$ and (b) 85 mJ/cm$^2$.

The final parameter which can be exploited for dopamine detection by random lasing is the lasing threshold (figure 7.12). The lasing threshold increases as the gold nanoparticles aggregate, which leads to reduced number density of scatterers and increased particle size. Larger gold nanoparticles precipitate and the reduced number density of the nanoparticles affects the threshold. The dopamine limit of detection (in the range from $8 \times 10^{-8}$ to $1 \times 10^{-7}$ M) was determined from the increased lasing threshold from 31 to 35 mJ/cm$^2$. As the gold nanoparticle / copper (II) chloride solution without dopamine lases in the weakly scattering regime [39], the aggregation of gold nanoparticles significantly increases the scattering mean free path leading to inadequate feedback with higher lasing threshold. The decrease of the localized surface plasmon (LSP) peak at the excitation wavelength as shown in figure 7.3 may also contribute to the reduced emission intensity and increased lasing threshold. Figure 7.12 also allows the characterization of the concentration of dopamine from a concentration of $1 \times 10^{-7}$ M to $1 \times 10^{-2}$ M using the observed trend with the laser threshold. A large dynamic range of dopamine concentration (from $1 \times 10^{-7}$ M to $1 \times 10^{-2}$ M) may be measured by calibrating against the lasing threshold as indicated by the red line in figure 7.12.

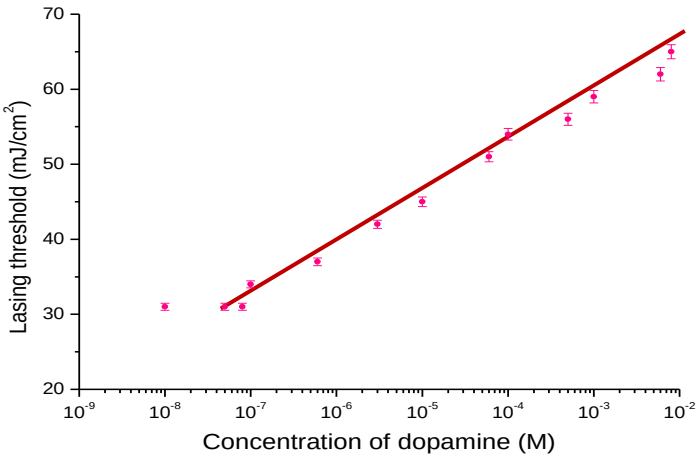


Figure 7.12 Comparison of lasing threshold of Rh640 / gold random lasers for various concentrations of dopamine with copper (II) chloride. The dark red line shows the concentration of dopamine (~1 × $10^{-7}$ M to 1 × $10^{-2}$ M) measured by the lasing threshold.

These results taken together indicate that the limit of dopamine detection using random lasing in this system is ~ 1 × $10^{-7}$ M, as determined through several sensing parameters such as emission peak shift, linewidth, emission peak / noise and lasing threshold.

## 7.4 Chapter 7 Summary

We demonstrated a useful application for random lasers with incoherent feedback to measure very low dopamine concentration through aggregation of gold nanoparticles, enhanced by copper ions. The detection indicators are the emission peak shift, emission peak linewidth, emission peak intensity to background ratio and lasing threshold with a dopamine detection limit of ~ 1 × $10^{-7}$ M. The best parameter for dopamine sensing using this random laser scheme is the change in emission peak linewidth. The dopamine concentration can be measured from the lasing threshold over a large dynamic range from 1 × $10^{-7}$ M to 1 × $10^{-2}$ M. Studies incorporating dopamine in buffer solutions consistent with clinical requirements are needed to demonstrate that this technique is suitable for clinical applications.

# Chapter 8

# Conclusions and future work

This research project has aimed to provide experimental characterizations of random lasers incorporating various materials. This thesis is divided into six main chapters. It presents the effects of particle / dye concentration, localized surface plasmons, energy transfer, surface roughness, metal-fluorophore distance and aggregation of nanoparticles on the emission, lasing threshold and the coherence of the random lasing output. No random lasing was observed from ruby nanoparticles or zinc oxide nanorods, as there was insufficient gain. Thus, we focused on random dye lasers containing dielectric and metal scattering particles, which allow independent control of the scattering and gain in the random laser system. We were able to understand the characteristics of these incoherent random dye lasers in terms of emission and lasing threshold so as to identify the factors which contribute to produce an efficient random laser to be used for a medical sensing application.

We observed the spectral and coherence signatures of random laser (Rhodamine 6G with alumina nanoparticles) thresholds operating in the weakly scattering and diffusive regimes, which are distinguished by their average scattering lengths of the light. The lasing threshold occurs when a narrow emission peak appears, the emission intensity increases nonlinearly, and the visibility of interference fringes

increases abruptly with adequate pump energy density. At threshold, the spatial and spectral coherence both increase above the coherence of the background fluorescence, consistent with stimulated emission. The resulting partial coherence suggests a combination of coherent stimulated emission with incoherent fluorescence background.

This thesis also demonstrated that radiative and non-radiative energy transfer from Rhodamine 6G (donor) to Methylene blue (acceptor) can extend the wavelength range of the random lasers, analogously with standard mixed dye lasers. In this case, radiative energy transfer is the dominant mechanism contributing to lasing operation. Radiative and non-radiative energy transfer also influence the lasing threshold and the emission spectrum of random dye lasers.

The properties of dielectric-based random lasers may be compared with those of metal-based random lasers to see the effects of localized surface plasmons, absorption and fluorescence quenching from metal nanoparticles. The addition of gold, rather than dielectric nanoparticles to random dye lasers can improve their efficiency. However, the concentration of gold nanoparticles must be selected carefully due to the competing effects of fluorescence quenching and gain enhancement due to localized surface plasmons and energy transfer. Further, the metal-fluorophore distance and the particle surface roughness enhance the localized surface plasmons, and contribute to the efficiency of the random laser. Finally, we used the effect of gold nanoparticle aggregation in random lasers to develop a novel dopamine detection and measurement scheme.

This thesis combines techniques and approaches from chemistry, physics and optics, in nanoparticle preparation, optical characterization of the random lasers, and

chemical preparation of the scattering solutions, with the goal, to demonstrate features of random lasers and a potential application of random lasers. It shows that ball milling is a useful and economical technique to produce nanoscale particles. Although we did not obtain random lasing from ruby nanocrystals or ZnO nanorods, our studies of fluorescence and analysis of the available gain for effective population inversion for the ruby nanocrystals lay the foundation for future studies.

The studies of the ruby nanocrystals demonstrate how critical gain is for lasing. Increasing the concentration of the ruby nanocrystals not only increases the gain but also the scattering, so it increases the possibility of excitation and emission light to be scattered out of the pumped region resulting in higher loss. Ruby's three level laser scheme also creates additional losses due to self-absorption. As the gain in our ruby nanocrystals was insufficient to balance the loss, lasing was not achieved.

In random dye lasers, the amount of gain is independent of the scattering. Increasing the dye concentration increases the absorption of the pump light, and increasing the concentration of nanoparticles provides better light confinement in the excited region. When gain is sufficient to compensate the loss, lasing can be achieved easily. Appropriate laser energy is also needed to excite the gain medium. Thus, we need a suitable pump laser, sufficient dye concentration and scattering to produce efficient random lasers.

In addition, gain can be enhanced by metal nanoparticles through localized surface plasmon effects. When the absorption spectrum of the gold nanoparticles overlaps with the absorption and fluorescence spectra of the dye molecules, the emitted light can be confined at the surface of the particles resulting in enhancement of the local electric field and increasing the optical gain for the laser. Therefore, metal

nanoparticles can assist lasing in the weakly scattering (low particle concentration) regime of random dye lasers. Rhodamine dyes (Rhodamine 640 and Rhodamine 6G) are efficient dyes for gold nanoparticles as the absorption / fluorescence spectra of the dyes have good overlap with those of the gold nanoparticles. However, greater spectral overlap also supports fluorescence resonance energy transfer, which eventually leads to quenching of the dye. Therefore, the trade-off between local field enhancement and dye quenching in metal-based random lasers produces competing effects on the lasing threshold. This trade-off may also enable Rhodamine 640 / gold random lasers to perform better than Rhodamine 6G / gold random lasers.

Localized surface plasmon effects are enhanced by surface roughness of metal nanoparticles and the strength of the interaction with the dye depends on the metal-fluorophore distance. Increasing the metal-fluorophore distance reduces the plasmonic contribution, leading to a higher random lasing threshold. The roughness on the metal surface can effectively trap dye molecules in gaps on the particle surface to form energy 'hotspots' which enhances the local electric field interacting with these molecules.

Understanding the properties of random lasers using various materials enables the appropriate choice of materials for the dopamine sensing random lasers. Gold (rather than silver) nanoparticles were used for dopamine sensing. Dopamine aggregates the gold nanoparticles when its amino group and hydroxyl groups are adsorbed on the surface of the gold nanoparticles. Adding copper ions enhances the aggregation as the copper ions serve as a selective ''discriminator and linker'' for dopamine detection [189]. We have shown that measuring the effect of the aggregation of gold nanoparticles on random dye laser properties can be used to sense dopamine

more sensitively than directly measuring the aggregation by colorimetry. The dopamine can be sensed using four different random lasing parameters; emission peak shift, emission linewidth, peak to background ratio and lasing threshold. We can estimate the concentration of dopamine from $1 \times 10^{-7}$ M to $1 \times 10^{-2}$ M by calibrating with the lasing threshold. There is scope to improve the sensitivity of dopamine detection and measurement using random lasers as an alternative to chemical methods [190, 192].

In future, we plan to improve our random laser dopamine sensor to incorporate phosphate-buffered saline (PBS) solutions, better suited to clinical applications. Since the gold nanoparticles may aggregate in the PBS, pH control is also needed. Previously we used a large sample volume (a cuvette) for the random laser measurements. To reduce the required sample volumes, we will place the samples on concave microscope slides with a single depression well in the middle of the slides. Alternatively, we can use liquid-filled hollow core fibres to create 1-dimensional random lasers. These enable the use of smaller volumes of sample, and reduce the threshold by confining the pump and emission light as they are guided within the fibre. Guiding can be achieved with a contrast of the refractive index between the random laser solution and the hollow core fibre cladding. Better light confinement may increase the sensitivity of dopamine-sensing random lasers to permit a lower detection limit for dopamine ($<10^{-7}$ M). We have chosen Rhodamine dyes to provide the gain as the dyes have high quantum yield [163]. However, we can also opt for other dyes which suit the gold surface plasmon resonance spectrum. Finally, random fibre lasers with plasmonic effects [112, 113] offer decreased lasing threshold and improved output power, and could be used effectively with a variety of low-gain laser materials.

# References


1. H. Cao, "Lasing in random media," Waves Random Media **13**, R1-R39 (2003).
2. D. S. Wiersma, "The Physics and applications of random lasers," Nature Physics **4**, 359-367 (2008).
3. F. Luan, B. Gu, A. S. L. Gomes, K. T. Yong, S. Wen and P. N. Prasad, "Lasing in nanocomposite random media," Nanotoday **10**, 168-192 (2015).
4. I. Johnson and M. T. Z. Spence, *Molecular probes Handbook, A guide to Fluorescent Probes and Labeling Technologies* (Life Technologies Corporation, 2010).
5. J. R. Lakowicz, *Principles of Fluorescence Spectroscopy* (Springer, 2006).
6. A. L. P. Nery, R. M. Liegel and C. Fernandez, "Fluorescence and Chemiluminescence:Teaching Basic Principles by Simple Demonstration Experiment," Chemical Education Journal **13**, 13-22 (2009).
7. B. Valeur and M. N. Berberan-Santos, *Molecular Fluorescence: Principles and Applications* (Wiley, 2012).
8. A. Penzkofer and Y. Lu, "Fluorescence quenching of Rhodamine 6G in methanol at high concentration," Chemical Physics **103**, 399-405 (1986).
9. G. A. Kumar and N. V. Unnikrishnan, "Energy transfer and optical gain studies of FDS:RhB dye mixture investigated under cw laser excitation," Journal of Photochemistry and Photobiology A: Chemistry **144**, 107-117 (2001).
10. F. Theodor, "Intermolecular energy migration and fluorescence," Analytical Physics **2**, 55-75 (1948).
11. T. Sen, S. Sadhu and A. Patra, "Surface energy transfer from Rhodamine 6G to gold nanoparticles: A spectroscopic ruler," Applied Physics Letter **90**, 043104 (2007).
12. E. Dulkeith, A. C. Morteani, T. Niedereichholz, T. A. Klar and J. Feldmann, "Fluorescence quenching of dye molecules near gold nanoparticles: Radiative and nonradiative effects," Physical Review Letters **89**, 203002 (2002).
13. Y. Chen, K. Munechika and D. S. Ginger, "Dependence of fluorescence intensity on the spectral overlap between fluorophores and plasmon resonant single silver nanoparticles," Nano Letters **7** (3), 690-696 (2007).
14. T. Nakamura and S. Hayashi, "Enhancement of dye fluorescence by gold nanoparticles: Analysis of particle size dependence," Japanese Journal of Applied Physics **44** (9A), 6833-6837 (2005).
15. M. L. Brongersma and P. G. Kik, *Surface Plasmon Nanophotonics* (Springer, 2007).
16. J. M. Pitarke, V. M. Silkin, E. V. Chulkov and P. M. Echenique, "Theory of surface plasmons and surface-plasmon polaritons," Reports on Progress in Physics **70**, 1-87 (2007).
17. S. A. Maier, *Plasmonics: Fundamentals and Applications* (Springer, 2007).
18. C. Kittel, *Introduction to solid state physics* (Wiley, 2005).
19. K. A. Willets and R. P. Van Duyne, "Localized surface plasmon resonance spectroscopy and sensing," Annual Review of Physical Chemistry **58**, 267-297 (2007).
20. S. A. Maier and H. A. Atwater, "Plasmonics: Localization and guiding of electromagnetic energy in metal / dielectric structures," Journal Of Applied Physics **98**, 011101 (2005).
21. K. Munechika, Y. Chen, J. M. Smith and D. S. Ginger, "Importance of spectral overlap: Fluorescence enhancement by single metal nanoparticles" in *Metal-Enhanced Fluorescence* (Wiley, 2010).

22. W. Zhang and B. T. Cunningham, "Fluorescence enhancement by a photonic crystal with a nanorodstructured high index layer," Applied Physics Letters **93**, 133115 (2008).
23. X. Li, Y. He, T. Zhang and L. Que, "Aluminum oxide nanostructure-based substrates for fluorescence enhancement," Optics Express **20**, 21272 (2012).
24. T. Wang, J. Costan, A. Centeno, J. S. Pang, D. Darvill, M. P. Ryana and F. Xie, "Broadband enhanced fluorescence using zinc oxide nanoflower arrays," Journal of Materials Chemistry C **3**, 2656-2663 (2015).
25. R. Paschotta, *Field Guide to Lasers* (SPIE, 2008).
26. D. S. Wiersma, "Laser physics: The smallest random laser," Nature **406,** 132-135 (2000).
27. R. V. Ambartsumyan, N. G. Basov, P. G. Kryukov and V.S. Letokhov, "A laser with a nonresonant feedback," IEEE J. Quantum Electronics **QE-2**, 442–446 (1966).
28. V. S. Letokhov, "Stimulated emission of an ensemble of scattering particles with negative absorption," JETP Letters **5** (8), 212 (1967).
29. C. Gouedard, D. Husson, S. Sauteret, F. Auzel and A. Migus, "Generation of spatially incoherent short pulses in laser-pumped neodymium stoichiometric crystals and powders," Journal of Optical Society of America B **10**, 2358-2363 (1993).
30. N. M. Lawandy, R. M. Balachandran, S. L. Gomes and E. Sauvain, "Laser action in strongly scattering media," Nature **368**, 436-438 (1994).
31. D. Zhang, B. Cheng, J. Yang, Y. Zhang, W. Hu and Z. Li, "Narrow-bandwidth emission from a suspension of dye and scatterers," Optical Communication **118**, 462-465 (1995).
32. G. V. Soest, M. Tomita and A. Lagendijk, "Amplifying volume in scattering media," Optics Letters **24**, 306-308 (1999).
33. D. S. Wiersma and A. Lagendijk, "Light diffusion with gain and random lasers," Physical Review E **54** (4), 4256-4265 (1996).
34. R. M. Balachandran, N. M. Lawandy and J. A.Moon, "Theory of laser action in scattering gain media," Optics Letters **22**, 319-321 (1997).
35. C. F. Bohren and D. R. Huffman, *Absorption and scattering of light by small particles* (Wiley, 1998).
36. H. C. van de Hulst, *Light Scattering by Small Particles* (Dover Publications, 1981).
37. X. Meng , K. Fujita , S. Murai, T. Matoba and K. Tanaka, "Plasmonically controlled lasing resonance with metallic-dielectric core-shell nanoparticles," Nano Letters **11**, 1374-1378 (2011).
38. X. Meng, K. Fujita, S. Murai and K. Tanaka, "Coherent random lasers in weakly scattering polymer films containing silver nanoparticles," Physical Review A **79**, 053817 (2009).
39. X. Meng, K. Fujita, Y. Moriguchi, Y. Zong and K. Tanaka, "Metal–Dielectric Core–Shell Nanoparticles: Advanced Plasmonic Architectures Towards Multiple Control of Random Lasers," Advanced Optical Materials **1** (8), 573-580 (2013).
40. X. Wu, *Study of lasing in random and periodic systems* (Northwestern University, 2007).
41. A. J. Cox, A. J. DeWeerd and J. Linden, "An experiment to measure Mie and Rayleigh total scattering cross sections," American Journal Physics **70**, 620-625 (2002).
42. R. Corey, M. Kissner and P. Saulnier, "Coherent backscattering of light," American Journal of Physics **63**, 560-564 (1995).
43. M. A. Noginov, *Solid-State Random Laser* (Springer, 2005).
44. M. P. Van Albada and A. Lagendijk, "Observation of weak localization of light in a random medium," Physical Review Letters **55** (24), 2692-2695 (1985).
45. P. E. Wolf and G. Maret, "Weak localization and coherent backscattering of photons in disordered media," Physical Review Letters **55**, 2696-2698 (1985).

46. M. B. van der Mark, M. P. van Albada, and A. Lagendijk, "Light scattering in strongly scattering media:Multiple scattering and weak localization," Physical Rview B **37**, 3575-3592 (1988).
47. T. Zhai, X. Zhang, Z. Pang, X. Su, H. Liu, S. Feng and L. Wang, "Random Laser Based on Waveguided Plasmonic Gain Channels," Nano Letters **11**, 4295-4298 (2011).
48. T. Zhai, J. Chen, L. Chen, J. Wang, L. Wang, D. Liu, S. Li, H. Liu and X. Zhang, "A plasmonic random laser tunable through stretching silver nanowires embedded in a flexible substrate," Nanoscale **7**, 2235-2240 (2015).
49. J. Kitur, G. Zhu, M. Bahoura and M. A. Noginov, "Dependence of the random laser behavior on the concentrations of dye and scatterers," Journal of Optics **12**, 024009 (2010).
50. Y. C. Chen, C. S. Wang, T. Y. Chang, T. Y. Lin, H. M. Lin and Y. F. Chen, "Ultraviolet and visible random lasers assisted by diatom frustules," Optics Express **23** (12), 16224-16231 (2015).
51. W. L. Sha, C. H. Liu and R. R. Alfano, "Spectral and temporal measurements of laser action of Rhodamine 640 dye in strongly scattering media," Optics Letters **19** (23), 1922-1924 (1994).
52. H. Cao, Y. G. Zhao, S. T. Ho, E. W. Seelig, Q. H. Wang and R. P. H. Chang, "Random Laser Action in Semiconductor Powder," Physical Review Letters **82** (11), 2278-2281 (1999).
53. J. Yi, G. Feng, L. Yang, K. Yao, C. Yang, Y. Song, S. Zhou, "Behaviors of the Rh6G random laser comprising solvents and scatterers with different refractive indices," Optics Communications **285**, 5276-5282 (2012).
54. O. Popov, A. Zilbershtein and D. Davidov, "Random lasing from dye-gold nanoparticles in polymer films: Enhanced gain at the surface-plasmon-resonance wavelength," Applied Physics Letters **89**, 191116 (2006).
55. G. D. Dice, S. Mujumdar and A. Y. Elezzabi, "Plasmonically enhanced diffusive and subdiffusive metal nanoparticle-dye random laser," Applied Physics Letter **86**, 131105 (2005).
56. C. S. Wang, H. Y. Lin, T. H. Lin and Y. F. Chen, "Enhancement of Random Lasing Assisted by Light Scattering and Resonance Energy Transfer Based on ZnO/SnO Nanocomposites," AIP Advances **2**, 012133 (2012).
57. H. Cao, J. Y. Xu, S. H. Chang and S. T. Ho, "Transition from amplified spontaneous emission to laser action in strongly scattering media," Physical Review E **61** (2), 1985-1986 (2000).
58. L. Sznitko, K. Cyprych, A. Szukalski, A. Miniewicz and J. Mysliwiec, "Coherent–incoherent random lasing based on nano-rubbing induced cavities," Laser Physics Letters **11**, 045801 (2014).
59. T. Zhai, Y. Zhou, S. Chen, Z. Wang, J. Shi, D. Liu, and X. Zhang, "Pulse duration dependent and temperature tunable random lasing in a weakly scattering structure formed by speckles," Physical Review A **82**, 023824 (2010).
60. Z. Wang, X. Shi, S. Wei, Y. Sun, Y. Wang, J. Zhou, J. Shi and D. Liu, "Two-threshold silver nanowire-based random laser with different dye concentrations," Laser Physics Letters **11**, 095002 (2014).
61. C. T. Dominguez, R. L. Maltez, R. M. S. dos Reis, L. S. A. de Melo, C. B. de Araújo and A. S. L. Gomes, "Dependence of random laser emission on silver nanoparticle density in PMMA films containing Rhodamine 6G," Journal of Optical Society of America B, **28** (5), 1118-1123 (2011).
62. J. F. Galisteo-López, M. Ibisate and C. López, "FRET-tuned resonant random lasing," Journal of Physical Chemistry C **118**, 9665-9669 (2014).
63. S. Gottardo, R. Sapienza, P. D. Garcia, A. Blanco and D. S. Wiersma, "Resonance-driven random lasing," Nature Photonics **2**, 429-432 (2008).

64. R. G. S. El-Dardiry and A. Lagendijk, "Tuning random lasers by engineered absorption," Applied Physics Letter **98** (16), 161106 (2011).
65. T. Nakamura, B. P. Tiwari and S. Adachi, "Control of random lasing in ZnO/$Al_2O_3$ nanopowders," Applied Physics Letters **99**, 231105 (2011).
66. S. Cavalieri and D. S. Wiersma, "Temperature-controlled random laser action in liquid crystal infiltrated systems," Physical Review A **66**, 056612 (2002).
67. Q. Song, L. Liu, L. Xu, Y. Wu and Z. Wang, "Electrical tunable random laser emission from a liquid-crystal infiltrated disordered planar microcavity," Optics Letters **34**, 298-300 (2009).
68. H. K. Liang, S. F. Yu and H. Y. Yang, "Directional and controllable edge-emitting ZnO ultraviolet random laser diodes," Applied Physics Letters **96**, 101116 (2010).
69. R. Paschotta, "Coherence" in *Encyclopedia of Laser Physics and Technology* (Wiley, 2008).
70. M. Born and E. Wolf, *Principles of Optics: Electromagnetic Theory of Propagation, Interference and Diffraction of Light* (Cambridge University Press, 1999).
71. H. Cao, Y. Ling, J. Y. Xu, C. Q. Cao and P. Kumar, "Photon Statistics of Random Lasers with Resonant Feedback," Physcial Review Letters **86** (20), 4524-4527 (2001).
72. G. Zacharakis, N. A. Papadogiannis, G. Filippidis, and T. G. Papazoglou, "Photon statistics of laserlike emission from polymeric scattering gain media," Optics Letters **25** (12), 923-925 (2000).
73. B. Redding, M. A. Choma and H. Cao, "Spatial coherence of random laser emission," Optics Letters **36** (17), 3404-3406 (2011).
74. M. A. Noginov, S. U. Egarievwe, N. E. Noginova, H. J. Caulfield and J. C. Wang, "Interferometric studies of coherence in a powder laser," Optical Material **12**, 127–134 (1999).
75. V. M. Papadakis, S. Andreas, A. Demetrios, H. A. Spiros, E. P. Giannelis and D. G. Papazoglou, "Single-shot temporal coherence measurements of random lasing media," Journal of Optical Society of America B **24** (1), 31-36 (2007).
76. S. Knitter, M. Kues and C. Fallnich, "Emission polarization of random lasers in organic dye solutions," Optics Letters **37** (17), 3621-3623 (2012).
77. F. Yao, W. Zhou, H. Bian, Y. Zhang, Y. Pei, X. Sun and Z. Lv, " Polarization and polarization control of random lasers from dye-doped nematic liquid crystals," Optics Letters **38**, 1557-1559 (2013).
78. H. Cao, "Random Lasers: Development, Features and Applications," Optics and Photonics News **38**, 24-29 (2005).
79. L. Yang, G. Feng, J. Yi, K. Yao, G. Deng and S. Zhou, "Effective random laser action in Rhodamine 6G solution with Al nanoparticles," Applied Optics **50** (13), 1816-1821 (2011).
80. J. Andreasen, A. A. Asatryan, L. C. Botten, M. A. Byrne, H. Cao, L. Ge, L. Labonté, P. Sebbah, A. D. Stone, H. E. Türeci, and C. Vanneste, "Modes of random lasers," Advances in Optics and Photonics **3**, 88-127 (2011).
81. C. T. Dominguez, Y. Lacroute, D. Chaumont, M. Sacilotti, C. B. de Araújo and A. S. L. Gomes, "Microchip random laser based on a disordered $TiO_2$-nanomembranes arrangement," Optics Express **20** (16), 17380-17385 (2012).
82. O. Svelto, S. Taccheo, C. Svelto, "Analysis of amplified spontaneous emission: some corrections to the Linford formula," Optics Communications **149**, 277-282 (1998).
83. C. T. Dominguez, M. d. A. Gomes, Z. S. Macedo, C. B. de Araújo and A. S. L. Gomes, "Multi-photon excited coherent random laser emission in ZnO powders," Nanoscale **7**, 317 (2015).
84. T. Nakamura, S. Sonoda and S. Adachi, "Plasmonic control of ZnO random lasing characteristics," Laser Physics Letters **11**, 016004 (2014).
85. C. T. Dominguez, M. S. Vieira, R. M. Oliveira, M. Ueda, C. B. de Araújo and Anderson S. L. Gomes, "Three-photon excitation of an upconversion random laser in

ZnO-on-Si nanostructured films," Journal of Optical Society of America B **31** (8), 1975-1980 (2014).
86. J. Bing, A. R. Warrier and C. Vijayan, "Raman mode random lasing in ZnS-B-carotene random gain media," Applied Physics Letters **102**, 221105 (2013).
87. T. Takahashi, T. Nakamura and Sadao Adachi, "Blue-light-emitting ZnSe random laser," Optics letters **34** (24), 3923-3925 (2009).
88. M. A. Noginov, G. Zhu, I. Fowlkes and M. Bahoura, "GaAs random laser," Laser physics Letters **1**, 291-293 (2004).
89. M. Bahoura, K. J. Morris and M. A. Noginov, "Threshold and slope efficiency of $Nd_{0.5}La_{0.5}Al_3(BO_3)_4$ ceramic random laser: effect of the pumped spot size," Optics Communications **201**, 405-411 (2002).
90. R. Niyuki, H. Takashima, H. Fujiwara and K. Sasaki, "Annealing temperature dependence of random lasing properties in a diamond nanoparticle film in *Proceeding of SPIE* (SPIE, 2015).
91. Y. J. Lu, C. X. Shan, Z. X. Zhou, Y. L. Wang, B. H. Li, J. M. Qin, H. A. Ma, X. P. Jia, Z. H. Chen and D. Z. Shen, "Electrically pumped random lasers with p-diamond as a hole source," Optica **6**, 558-562 (2015).
92. R. C. Polson and Z. V. Vardeny, "Random lasing in human tissues," Applied Physics Letter **85** (7), 1289-1291 (2004).
93. Q. Song, Z. Xu, S. H. Choi, X. Sun, S. Xiao, O. Akkus and Y. L. Kim, "Detection of nanoscale structural changes in bone using random lasers" Biomedical Optics Express **1** (5), 1401-1407 (2010).
94. C. S. Wang, T. Y. Chang, T. Y. Lin and Y. F. Chen, "Biologically inspired flexible quasi-single-mode random laser: An integration of pieris canidia butterfly wing and semiconductors," Scientific Reports **4**, 6736 (2014).
95. L. Cerdán, E. Enciso, V. Martín, J. Bañuelos, I. López-Arbeloa, A. Costela and I. García-Moreno, "FRET assisted laser emission in colloidal suspensions of dye-doped latex nanoparticles," Nature Photonics **6**, 621-626 (2012).
96. L. Cerdán, A. Costela, E. Enciso and I. García-Moreno, "Random lasing in self-assembled dye-doped latex nanoparticles: Packing density effects," Advanced Functional Materials **23**, 3916-3924 (2013).
97. A. Costela, I. Garcia-Moreno, L. Cerdan, V. Martin, O. Garcia and R. Sastre, "Dye-Doped POSS Solutions: Random nanomaterials for laser emission," Advanced Materials **21**, 4163-4166 (2009).
98. J. Liu, P. D. Garcia, S. Ek, N. Gregersen, T. Suhr, M. Schubert, J. Mørk, S. Stobbe and P. Lodahl, "Random nanolasing in the Anderson localized regime," Nature Nanotechnology **9**, 285-289 (2014).
99. Y. Chen, J. Herrnsdorf, B. Guilhabert, Y. Zhang, I. M. Watson, E. Gu, N. Laurand and M. D. Dawson, "Colloidal quantum dot random laser," Optics Express **19** (4), 2996-3003 (2015).
100. A. K. Augustine, P. Radhakrishnan, V. P. N. Nampoori and M. Kailasnath, "Enhanced random lasing from a colloidal CDSe quantum dot-Rh6G system," Laser Physics Letters **12**, 025006 (2015).
101. A. Samanta,Y. Zhou, S. Zou, H. Yan, and Y. Liu, "Fluorescence quenching of quantum dots by gold nanoparticles: A potential long range spectroscopic ruler," Nano Letters **14**, 5052-5067 (2014).
102. G. D. Dice and A. Y. Elezzabi, "Random lasing from a nanoparticle-based metal–dielectric–dye medium," Journal of Optics A:Pure and Applied Optics **9**, 186-193 (2007).
103. M. I. Stockman, "SPASER explained," Nature photonics **2**, 327-329 (2008).
104. S. F. Yu, C. Yuen, S. P. Lau, W. I. Park, and G. C. Yi, "Random laser action in ZnO nanorod arrays embedded in ZnO epilayers," Applied Physics Letters **84** (17), 3241-3243 (2004).

105. J. Ziegler, M. Djiango, C. Vidal, C. Hrelescu and T. A. Klar, "Gold nanostars for random lasing enhancement," Optics Express **23** (12), 15152-15159 (2015).
106. E. Hao and G. C. Schatz, "Electromagentic fields around silver nanoparticles and dimers," Journal of Chemical Physics **120**, 357-366 (2004).
107. K. D. Tomsia and E. M. Goldys, "Gold and silver nanowires for fluorescence enhancement" in *Nanowires-Fundamental Research* (Intech, 2011).
108. X. Shi, Y. Wang, Z. Wang, S. Wei, Y. Sun, D. Liu, J. Zhou, Y. Zhang and J. Shi, "Random lasing with a high quality factor over the whole visible range based on cascade energy transfer," Advanced Optical Materials **2** (1), 88-93 (2014).
109. I. Viola, N. Ghofranih, A. Zacheo, V. Arima, C. Contib and G. Gigli, "Random laser emission from a paper-based device," Journal of Materials Chemistry C **1**, 8128-8133 (2013).
110. M. V. dos Santos, C. T. Dominguez, J. V. Schiavon, H. S. Barud, L. S. A. de Melo, S. J. L. Ribeiro, A. S. L. Gomes and C. B. de Araújo, "Random laser action from flexible biocellulose-based device," Journal of Applied Physics **115**, 083108 (2014).
111. C. J. S. de Matos, L. d. S. Menezes, A. M. Brito-Silva, M. A. M. Ga´mez, A. S. L. Gomes, and C. B. de Araújo, "Random fibre laser," Physcial Review Letters **99** (15), 153903 (2007).
112. S. Li, L. Wang, T. Zhai, Z. Xu, Y. Wang, J. Wang and X. Zhang, "Plasmonic random laser on the fibre facet," Optics Express **23** (18), 23985-23991 (2015).
113. Z. Hu, Y. Liang, K. Xie, P. Gao, D. Zhang, H. Jiang, F. Shi, L. Yin, J. Gao, H. Ming and Q. Zhang, "Gold nanoparticle-based plasmonic random fibre laser," Journal of Optics **17**, 035001 (2015).
114. S. Sebastian, C. L. Linslal, C. P. G. Vallabhan, V. P. N. Nampoori, P. Radhakrishnan and M. Kailasnath, "Random lasing with enhanced photostability of silver nanoparticle doped polymer optical fibre laser," Laser Physics Letters **11**, 055108 (2014).
115. Y. Yonenaga, R. Fujimura, M. Shimojo, A. Kubono and K. Kajikawa, "Random laser of dye-injected holey photonic-crystal fibre," Physical Review A **92**, 013824 (2015).
116. M. Gagné and R. Kashyap, "Demonstration of a 3 mW threshold Er-doped random fiber laser based on a unique fiber Bragg grating," Optics Express **17**, 19067-19074 (2009).
117. R. C. Polson and Z. V. Vardeny, "Cancerous tissue mapping from random lasing emission spectra," Journal of Optics **12**, 024010 (2010).
118. Z. N. Wang, Y. J. Rao, H. Wu, P. Y. Li, Y. Jiang,X. H. Jia and W. L. Zhang, "Long-distance fibre-optic point-sensing systems based on random fibre lasers," Optics Express **20** (16), 17695-17700 (2012).
119. B. Redding, M. A. Choma and H. Cao, "Speckle-free laser imaging using random laser illumination," Nature Photonics **6**, 355-359 (2012).
120. B. Redding, S. F. Liew, R. Sarma and H. Cao, "Compact spectrometer based on a disordered photonic chip," Nature Photonics **7**, 746-751 (2013).
121. T. H. Maiman, "Stimulated Optical Radiation in Ruby," Nature **187**, 493-494 (1960).
122. T. H. Maiman, R. H. Hoskins, I. J. D'Haenens, C. K. Asawa and V. Evtuhov, "Stimulated optical emission in fluorecent solids. II. Spectroscopy and stimulated emission in ruby. Physical Review," **123** (4), 1151-1157 (1961).
123. C. Pflitsch, R. A.Siddiqui and B. Atakan, "Phosphorescence properties of sol-gel derived ruby measured as functions of temperature and $Cr^{3+}$ content," Applied Physics A **90**, 527-532 (2008).
124. A. M. Edmonds , M. A. Sobhan , V. K. A. Sreenivasan , E. A. Grebenik , J. R. Rabeau, E. M. Goldys and A. V. Zvyagin, "Nano-ruby: A promising fluorescent probe for background-free cellular imaging," Particle and Particle Systems Characterization **30**, 506-513 (2013).

125. P. Balaz, "Chapter 2: High Energy Milling" in *Mechanochemistry in Nanoscience and Minerals Engineering* (Springer, 2008).
126. I. Ozdemir, S. Ahrens, S. Mucklich, B. Wielage, "Nanocrystalline Al–$Al_2O_{3p}$ and $SiC_p$ composites produced by high-energy ball milling," Journal of Materials Processing Technology **205**, 111-118 (2008).
127. W. A. W. Razali, V. K. A. Sreenivasan, E. M. Goldys and A. V. Zvyagin, "Large-scale production and characterization of biocompatible colloidal nanoalumina," Langmuir **30**, 15091-15101 (2014).
128. S. Ghanizadeh, X. Bao, B. Vaidhyanathan, J. Bineer, "Synthesis of nano α-alumina powders using hydrothermal and precipitation routes: a comparative study," Ceramics International **40**, 1311-1319 (2014).
129. P. Manivasakan, A. Karthik, V. Rajendran, "Mass production of $Al_2O_3$ and $ZrO_2$ nanoparticles by hot-air spray pyrolysis," Powder Technology **234**, 84-90 (2013).
130. V. A. Martinez, J. H. J. Thijssen, F. Zontone, W. van Megen and G. Bryant, "Dynamics of hard sphere suspensions using dynamic light scattering and X-ray photon correlation spectroscopy: Dynamics and scaling of the intermediate scattering function," Journal of Chemical Physics **134**, 054505 (2011).
131. W. Brown and K. Mortensen, *Scattering in polymeric and colloidal systems* (Gordon and Breach Science, 2000).
132. F. T. Carmona, C. G. Segundo, N. C. Espitia and J. H. Cordero, "Angular distribution of random laser emission," Optics Letters **39** (3), 655-658 (2014).
133. W. Deng, D. Jin, K. D. Tomsia, J. Yuan, J. Wu and E. M. Goldys, "Ultrabright Eu-Doped Plasmonic Ag@$SiO_2$ Nanostructures:Time-gated Bioprobes with single particles sensitivity and negligible background," Advanced Materials **23**, 4649-4654 (2011).
134. T. Zeng, Y. Hu, N. Wang, C. Xia, S. Li, Y. Zu, L. Liu, Z. Yao, Y. Zhao and H. C. Wu, "Effects of different metal ions on the fluorescence of CdSe/ZnS quantum dots capped with various thiolate ligand," Physical Chemistry Chemical Physics **15**, 18710-18715 (2013).
135. T. S. Lim, C. C. Fu, K. C. Lee, H. Y. Lee, K. Chen, W.F. Cheng, W. W. Pai, H. C. Chang and W. Fann, "Fluorescence enhancement and lifetime modification of single nanodiamonds near a nanocrystalline silver surface," Physical Chemistry Chemical Physics **11**, 1508-1514 (2009).
136. W. Koechner, *Solid-State Laser Engineering* (Springer, 1999).
137. M. J. Choi, K. E. McBean, P. H. R. Ng, A. M. McDonagh, P. J. Maynard, C. Lennard and C. Roux, "An evaluation of nanostructured zinc oxide as a fluorescent powder for fingerprint detection," Journal of Materials Science **43** (2), 732-737 (2007).
138. H. Hong, J. Shi, Y. Yang, Y. Zhang, J. W. Engle, R. J. Nickles, X. Wang and W. Cai, "Cancer-targeted optical imaging with fluorescent zinc oxide nanowires," Nano Letters **11** (9), 3744-3750 (2011).
139. M. H. Huang, S. Mao, H. Feick, H. Yan, Y. Wu, H. Kind, E. Weber, R. Russo, and P. Yang, "Room-temperature ultraviolet nanowire nanolasers," Science **292**, 1897-1899 (2001).
140. G. C. Yi, C. Wang and W. I. Park, "ZnO nanorods: synthesis, characterization and applications," Semiconductor Science and Technology **20**, S22-S34 (2005).
141. S. H. Yi, S. K. Choi, J. M. Jang, J. A Kim, W. G. Jung, "Low-temperature growth of ZnO nanorods by chemical bath deposition," Journal of Colloid and Interface Science **313** (2), 705-710 (2007).
142. P. C. Stark, *Characterization of random lasers made from dyes, ZnO nanorods and nanoparticles in polymer films* (Macquarie University, 2013).
143. T. L. Tan, C. W. Lai and S. B. Abd Hamid, "Tunable band gap energy of Mn-doped ZnO nanoparticles using the coprecipitation technique," Journal of Nanomaterials **2014**, 371720 (2014).

144. S S. Bishnoi, R. Das, P. Phadke, R. K. Kotnala and S. Chawla, "Enhanced visible fluorescence in highly transparent Al-doped ZnO film by surface plasmon coupling of Ag nanoparticles," Journal Of Applied Physics **116**, 164318 (2014).
145. R. Das, P. Phadke, N. Khichar and S. Chawla, "Plasmonic enhancement of dual mode fluorescence in a silver nano-antenna–ZnO:$Er^{3+}$ hybrid nanostructure. Journal of Materials Chemistry C **2**, 8880-8885 (2014).
146. R. Niyuki, H. Takashima, H. Fujiwara and K. Sasaki, "Ultraviolet random lasing from a diamond nanoparticle film," Applied Physics Letters **105**, 011112 (2014).
147. H. Fujiwara, R. Niyuki, Y. Ishikawa, N. Koshizaki, T. Tsuji and K. Sasaki, "Low-threshold and quasi-single-mode random laser within a submicrometer-sized ZnO spherical particle film," Applied Physics Letters **102**, 061110 (2013).
148. D. Anglos, A. Stassinopoulos, R. N. Das, G. Zacharakis, M. Psyllaki, R. Jakubiak, R. A. Vaia,E. P. Giannelis and S. H. Anastasiadis, "Random laser action in organic-inorganic nanocomposites" Journal of Optical Society of America B **21** (1), 208-213 (2004).
149. M. A. Noginov, N. E. Noginova, H. J. Caulfield, M. M. Venkateswarlu, T. Thompson and V. Ostroumov, "Short pulsed stimulated emission in the powders of $NdAl_3(BO_3)_4$, $NdSc_3(BO_3)_4$,and $Nd:Sr_5(PO_4)_3F$ laser crystals," Journal of Optical Society of America B **13**, 2024-2033 (1996).
150. P. Solarz, "Investigation of a random lasing in $K_5PrLi_2F_{10}$ powders," Optical Materials **34**, 1497-1499 (2012).
151. Y. T. Chen and Y. F. Chen, "Enhanced random lasing in ZnO nanocombs assisted by Fabry-Perot resonance," Optics Express **19** (9), 8728 (2011).
152. S. H. Cheng, Y. C. Yeh, M. L. Liu, C. W. Chen Y. F. Chen, "Enhancement of laser action in ZnO nanorods assisted by surface plasmon resonance of reduced graphene oxide nanoflakes," Optics Express **20** (S6), 799-805 (2012).
153. H. Cao, Y. Ling, J. Y. Xu, A. L. Burin, R. P. H. Chang, "Review on latest developments in random lasers with coherent feedback," Journal of Physics A: Mathematical and General **38**, 10497–10535 (2005).
154. S. Prahl, "Mie Scattering Calculator," http://omlc.org/calc/mie_calc.html (2012).
155. B. E. A. Saleh and M. C. Teich, "Statistical Optics" in *Fundamental of Photonics* (Wiley, 1991).
156. B. W. van der Meer, G. Coker and S. Y. Chen, *Resonance Energy Transfer:Theory and Data* (Wiley, 1994).
157. D. L. Andrews, "A unified theory of radiative and raditionless molecular energy transfer," Chemical Physics **135**, 195-201 (1989).
158. K. S. Alee, S. Barik, S. Mujumdar, "Förster energy transfer induced random lasing at unconventional excitation wavelengths," Applied Physics Letter **103**, 221112 (2013).
159. M. A. Ali and S. A. Ahmed, "Comprehensive examination of radiationless energy transfer models in dyes: Comparisons of theory and experiment," Journal of Chemical Physics **90**, 1484-1491 (1989).
160. C. Lin and A. Dienes, "Study of excitation transfer in laser dye mixtures by direct measurement of fluorescence lifetime," Journal Of Applied Physics **44**, 5050-5052 (1973).
161. J. R. Lakowicz, *Principles of fluorescence* (Springer, 1999).
162. J. P. Tardivo, A. D. Giglio, C. S. de Oliveira, D. S. Gabrielli, H. C. Junqueira, D. B. Tada, D. Severino, R. d. F. Turchiello, M. S. Baptista, "Methylene blue in photodynamic therapy: From basic mechanisms to clinical applications," Photodiagnosis and Photodynamic Therapy **2** (3),175-191 (2005).
163. R.F. Kubin and A.N. Fletcher, "Fluorescence quantum yields of some rhodamine dyes," Journal of Luminescence **27**, 455-462 (1983).

164. R. Ghazya, S. A. Zimb, M. Shaheena, F. El-Mekaweya, "Experimental investigations on energy-transfer characteristics and performance of some laser dye mixtures," Optics and Laser Technology **34**, 99-105 (2002).
165. J. A. Schuller, E. S. Barnard, W. Cai, Y. C. Jun, J. S. White and M. L. Brongersma, "Plasmonics for extreme light concentration and manipulation," Nature Materials **9**, 193-204 (2010).
166. J. Zhu, K. Zhu and L. Q. Huang, "Using gold colloid nanoparticles to modulate the surface enhanced fluorescence of Rhodamine B," Physics Letters A **372**, 3283-3288 (2008).
167. I. H. Malitson and M. J. Dodge, "Refractive Index and Birefringence of Synthetic Sapphire," Journal of Optical Society of America **62**, 1405 (1972).
168. M. A. F. de Souza and A. Lencina, "Controlling bichromatic emission in scattering gain media," Optics Letters **31** (9),1244-1246 (2006).
169. R. B. Silva, A. F. Silva, A. M. B. Silva and C. B. De Araujo, "Bichromatic Random laser from a powder of Rhodamine-doped-sub-micrometer silica particles," Journal Of Applied Physics **115**, 043515 (2014).
170. E. Heydari, R. Flehr and J. Stumpe, "Influence of spacer layer on enhancement of nanoplasmons-assisted random lasing," Applied Physics Letters **102**, 133110 (2013).
171. S. Kuhn, U. Hakanson, L. Rogonete and V. Sandoghdar, "Enhancement of single moelcule fluorescence using a gold nanoparticle as an optical nanoantenna," Physical Review Letters **97**, 017402 (2006).
172. R. M. Balachandran and N. M. Lawandy, and J. A. Moon, "Understanding bichromatic emission from scattering gain media," Optics Letters **21** (19), 1603-1605 (1996).
173. J. R. Lackowicz, *Principles of Fluorescence Spectroscopy* (Springer, 2006).
174. P. Selvin, *Fluorescence Resonance Energy Transfer* (Academic Press, 1995).
175. S. Preus, "Calculate spectral overlap integral in FRET," http://www.fluortools.com/software/ae/documentation/tools/j (2015).
176. M. Futamata, Y. Maruyama and M. Ishikawa, "Local electric field and scattering cross section of Ag nanoparticles under surface plasmon resonance by finite differece time domain method," Journal of Physical Chemistry B **107**, 7607-7617 (2003).
177. P. B. Johnson and R. W. Christy, "Optical constants of the noble metals," Physical Review B **6**, 4370-4379 (1972).
178. A. Costela, L. Cerdan, I. G. Moreno, "Solid state dye lasers with scattering feedback," Progress in Quantum Electronics **37**, 348-382 (2013).
179. X. Meng, K. Fujita, Y. Zong, S. Murai and Katsuhisa Tanaka, "Random lasers with coherent feedback from highly transparent polymer films embedded with silver nanoparticles," Applied Physics Letters **92**, 201112 (2008).
180. O. Popov, A. Zilbershtein and D. Davidov, "Enhanced amplified emission induced by surface plasmons on gold nanoparticles in polymer random lasers," Polymer for advanced technologies **18**, 751-755 (2007).
181. L. Rainville, M. C. Dorais and D. Boudreau, "Controlled synthesis of low polydispersity Ag@$SiO_2$ core–shell nanoparticles for use in plasmonic applications," RSC Advances **3**, 13953-13960 (2013).
182. E. Mine, A. Yamada, Y. Kobayashi, M. Konno and L. M. Liz-Marzán, "Direct coating of gold nanoparticles with silica by a seeded polymerization technique," Journal of Colloid and Interface Science **264** (2), 385-390 (2003).
183. F. Ruffino, A. Pugliara, E. Carria, C. Bongiorno and M. G. Grimaldi, "Light scattering calculations from Au and Au/$SiO_2$ core/shell nanoparticles," Physica E **47**, 25-33 (2013).
184. C. E. Rayford II, G. Schatz and K. Shuford, "Optical Properties of Gold Nanospheres," Nanoscape **2** (1), 27-33 (2005).

185. J. Rodrı´guez-Ferna´ndez, A. M. Funston, J. Pe´rez-Juste, R. A. Alvarez-Puebla, L. M. Liz-Marza and P. Mulvaney, "The effect of surface roughness on the plasmonic response of individual sub-micron gold spheres," Physical Chemistry Chemical Physics **11**, 5909-5914 (2009).
186. L. Au, X. Lu and Y. Xia, "A comparative study of galvanic replacement reactions involving Ag nanocubes and $AuCl_2^-$ or $AuCl_4^-$," Advanced Materials **20** (13), 2517-2522 (2008).
187. X. Shi, Y. Wang, Z. Wang, Y. Sun, D. Liu, Y. Zhang, Q. and J. Shi, "High performance plasmonic random laser based on nanogaps in bimetallic porous nanowires," Applied Physics Letters **103**, 023504 (2013).
188. R. M. Wightman, L. J. May and A. C. Michael, "Detection of dopamine dynamics in the brain," Analytical Chemistry **60** (13), 769A-793A (1988).
189. H. Su, B. Sun, L. Chen, Z. Xu and S. Ai, "Colorimetric sensing of dopamine based on the aggregation of gold nanoparticles induced by copper ion," Analytical Methods **4** (12), 3981-3986 (2012).
190. X. Zhang, X. Chen, S. Kai, H. Y. Wang, J. Yang and F. G. Wu, "Highly sensitive and selective detection of dopamine using one-pot synthesized highly photoluminescent silicon nanoparticles," Analytical Chemistry **87** (6), 3360-3365 (2015).
191. D. S. Goldstein, C. Holmes and Y. Sharabi, "Cerebrospinal fluid biomarkers of central catecholamine deficiency in Parkinson's disease and other synucleinopathies," Brain **135**, 1900-1913 (2012).
192. Z. Chen, C. Zhang and C. Wang, "A colorimetric assay of dopamine utilizing melamine modified gold nanoparticle probes," Analytical Methods **7** (3), 838-841 (2015).
193. M. A. Noginov, G. Zhu, M. Bahoura, C. E. Small, C. Davison, J. Adegoke, V. P. Drachev, P. Nyga and V. M. Shalaev, "Enhancement of spontaneous and stimulated emission of a Rhodamine 6G dye by an Ag aggregate," Physical Review B **74**, 184203 (2006).

# Appendices

## A1 Inductively coupled plasma mass spectrometry (ICP MS)

A ruby crystal was placed inside the laser sample chamber that is connected to the ICP via plastic tubing. The sample chamber was evacuated to remove air, which would put out the plasma. A cycle of removing the air, and replacing it with Helium was repeated 10 times. After this, the sample chamber was connected to the ICP and helium flowed through the sample chamber. The sample position for ablation was chosen and a mass spectrometer (Agilent 7700 series) was activated until it was ready to receive the signals. The mass spectrometer collected data for 60 seconds prior to the laser turning on, measuring the gas background, which was subtracted from the part of the signal collected with the laser turned on. The sample was ablated with a UV excimer laser (193 nm, 5 Hz, 7 ns). Electrons were stripped off the argon atoms, forming argon ions when a spark was applied to the argon flowing through the ICP torch. This process ran continuously during the analytical session. The laser converted the solid into small particles that were carried into the torch by the helium carrier gas and once the elements in the sample were converted into ions, they were then brought into the mass spectrometer via the interface cones. The mass spectrometer detected the ions, counted them and save the raw data. Data reduction was done using the Glitter software (developed by GEMOC).

The calibration standards were measured to convert the raw counts measured by the mass spectrometer to concentrations. The calibration standard was well characterised, with accurately known concentrations of a wide range of elements and this allowed us to quantify the rest of the analyses in the run. The reference material was also well characterised, and was analysed as an unknown. The results of the analysis of the reference material were compared to published values to assess the quality of the analyses for the run in progress. The signal from the spectrometer was interpreted using Glitter software that gives the estimation in concentration, parts per millions (PPM).

# A2 Emission from nanodiamonds

## Introduction

Electrically pumped random lasing from p-type diamond has been realized by Ying *et al.* [91]. Here, we only observed fluorescence from nanodiamond. The emission spectra from diamond nanocrystals (synthesized in University of Technology Sydney by Igor Aharonovich's research group) were studied by mixing the nanodiamonds with different concentrations of gold nanoparticles. The diamond nanocrystals with concentration of $5 \times 10^{12}$ $cm^{-3}$ and 100 nm diameter, were suspended in an aqueous solution. A TEM image of the nanodiamonds, is shown in figure A2.1 (a). Since the quantity of diamond nanocrystals was limited, only a few experiments were conducted. The colloidal nanodiamond solution was placed in the 1 cm × 1 cm cuvette and excited using a similar system to that for the ruby nanocrystals. Various concentrations of gold nanoparticles ($3 \times 10^{9}$ to $3 \times 10^{11}$ $cm^{-3}$), 60 nm diameter were mixed with the colloidal nanodiamond solution. The emission spectra were averaged for 10 seconds to reduce the noise.

## Results and discussion

The excitation and fluorescence of the colloidal nanodiamonds, measured by a Fluorolog spectrofluorometer (Horiba Jobin Yvon) show that the nanodiamonds can be excited with green light (532 nm) but the optimum excitation is 630 nm. The emission spectrum is broad and has emission peak at 675 nm (figure A2.1 (b)).

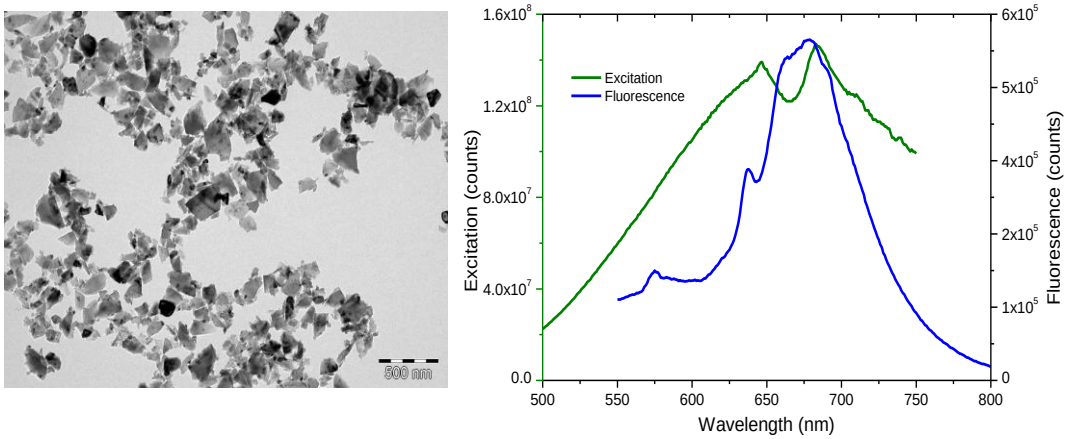


(a) (b)

Figure A2.1 (a) TEM image of colloidal nanodiamonds; (b) Excitation and emission of nanodiamonds measured by a Fluorolog spectrofluorometer (Horiba Jobin Yvon) (1 nm resolution).

The colloidal nanodiamonds ($5 \times 10^{12}$ $cm^{-3}$) were excited by a frequency doubled Nd:YAG nanosecond pulsed laser (532 nm, 10 Hz, 4 ns) and the emission spectra are shown in figure A2.2. The emission spectra are broad at high pump energy density. The emission spectra are averaged to reduce the noise. No spectral narrowing is observed and the emission spectra have a peak at 610 nm. The emission intensity increases when the excitation energy density increases. The effect of gold nanoparticles on the emission spectra of the nanodiamonds is shown in figure A2.3. As the concentration of gold was increased from $3 \times 10^{9}$ $cm^{-3}$ to $3 \times 10^{11}$ $cm^{-3}$, no obvious emission spectral changes can be observed with the addition of gold nanoparticles to the nanodiamond solutions. However, the addition of gold nanoparticles increases the emission peak intensity in comparison with nanodiamond solutions only (figures A2.2 to A2.3). This is because gold nanoparticles localize the pump light and increase the gain provided by the nanodiamonds, resulting in high emission intensity. With a concentration of $3 \times 10^{11}$ $cm^{-3}$ (figure A2.3 (c)), the emission peak intensity reduces slightly due to excessive absorption losses.

The nanodiamond fluorescence was enhanced after depositing the particles on a silver film. We attributed the enhancement to surface plasmon resonance (SPR) and this is consistent with the observations in figures A2.2 to A2.3. For all concentrations of gold nanoparticles, the emission intensity increases gradually with increased excitation energy density.

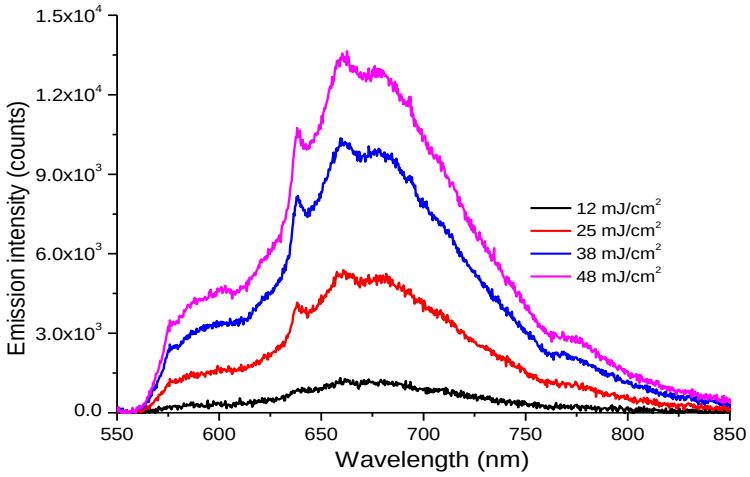


Figure A2.2 Emission spectra of colloidal nanodiamonds in an aqueous solution ($5 \times 10^{12}$ cm$^{-3}$) excited by Nd:YAG nanosecond pulsewidth laser. Higher excitation energy density gives higher emission.

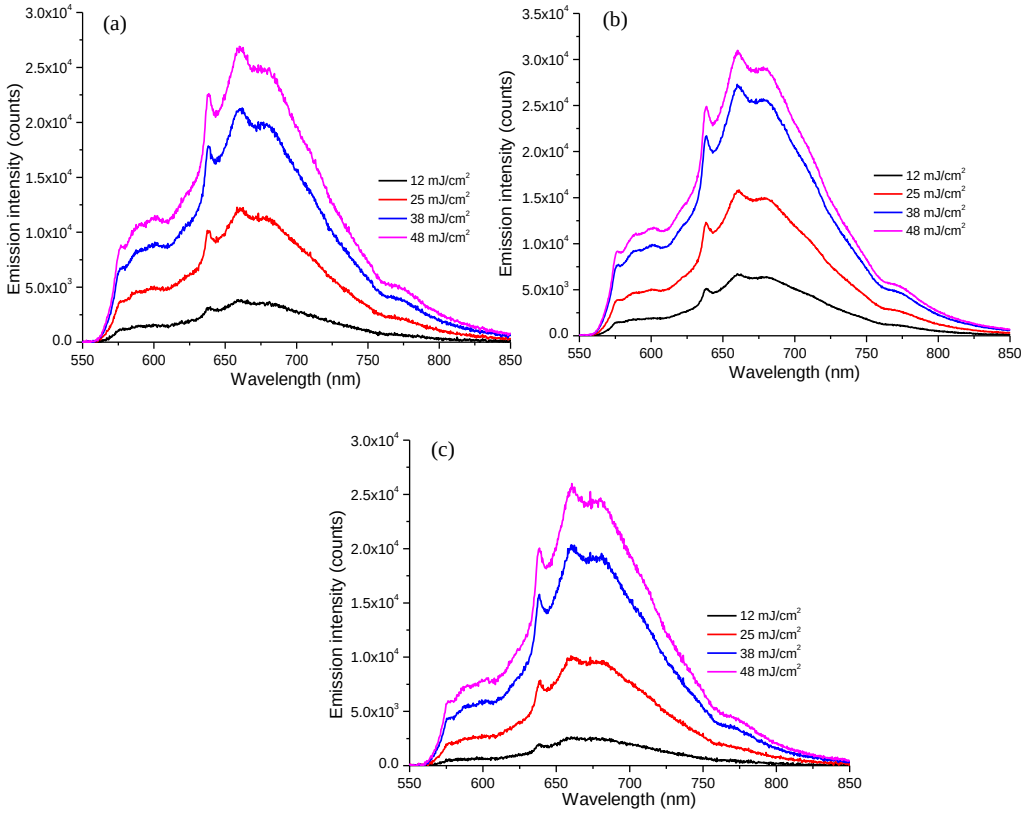


Figure A2.3 Emission spectra of colloidal nanodiamonds in an aqueous solution ($5 \times 10^{12}$ cm$^{-3}$) excited by Nd:YAG nanosecond pulsewidth laser with gold concentrations (a) $3 \times 10^{9}$ cm$^{-3}$ (b) $3 \times 10^{10}$ cm$^{-3}$ and (c) $3 \times 10^{11}$ cm$^{-3}$. The emission peak intensity is slightly higher for colloidal nanodiamonds with a gold concentration $3 \times 10^{10}$ cm$^{-3}$ compared to the others. No spectral narrowing is observed.

## A3 Glossary of acronyms

| | |
|---|---|
| Ag | Silver |
| $AgNO_3$ | Silver nitrate |
| $Al_2O_3$ | Aluminium oxide or Alumina |
| Al | Aluminium |
| ASE | Amplified spontaneous emission |
| Au | Gold |
| BC | Bacterial cellulose |
| CBS | Coherent backscattering |
| CCD | Charge-coupled device |
| CNR | Contrast-to-noise ratio |
| Cr | Chromium |
| $CrO_3$ | Chromium trioxide |
| DDA | Discrete dipole approximation |
| DLS | Dynamic light scattering |
| EDS | Energy-dispersive X-Ray |
| EM | Electromagnetic |
| FBG | Fibre Bragg Grating |
| FRET | Fluorescence (Förster) resonance energy transfer |
| FWHM | Full width at half maximum |
| GaAs | Gallium arsenide |
| GaN | Gallium nitride |
| $HAuCl_4$ | Gold (III) chloride |
| HEBM | High-energy ball milling |
| HMT | Hexamethylenetetramine |
| ICPMS | Inductively coupled plasma mass spectrometry |
| ITO | Indium tin oxide |
| LED | Light emitting diode |
| LSPR | Localized surface plasmon resonance |
| LSPs | Localized surface plasmons |
| MB | Methylene blue |
| MgO | Magnesium oxide |
| Nd:YAG | Neodymium-doped yttrium aluminium garnet |
| ND | Neutral density |
| OPD | Optical path difference |
| PBS | Phosphate-buffered solution |
| PCF | Photonic crystal fibre |
| PPM | Parts per millions |
| PVA | Polyvinyl alcohol |
| QB | Quinaldine blue |
| Rh6G | Rhodamine 6G |
| Rh640 | Rhodamine 640 |
| Rpm | Revolutions per minute |
| Rcf | Relative centrifugal force |
| SEM | Scanning electron microscope |
| SPASER | Surface plasmon amplification by stimulated emission of radiation |
| SPs | Surface plasmons |
| SPR | Surface plasmon resonance |
| SPPs | Surface plasmon polaritons |
| TEM | Transmission electron microscope |
| TEOS | Tetraethyl orthosilicate |
| $TiO_2$ | Titanium dioxide or Titania |
| ZNH | Zinc nitrate hexahydrate |
| ZnO | Zinc oxide |
| ZnS | Zinc sulphide |
| ZnSe | Zinc selenide |
| $ZrO_2$ | Zirconium oxide |

# A4 Glossary of symbols

| | |
|---|---|
| $h\nu$ | Photon energy |
| $Q$ | Quantum yield |
| $\Gamma$ | Emissive rate |
| $\lambda$ | Wavelength |
| $\tau_D$ | Donor fluorescence lifetime |
| $\tau_A$ | Acceptor fluorescence lifetime |
| $k_{nr}$ | Non-radiative decay rate |
| $\eta_{nr}$ | Non-radiative efficiency |
| $\eta_r$ | Radiative efficiency |
| $\eta_T$ | Total energy transfer efficiency |
| $K_{NR}$ | Non-radiative rate constant |
| $K_R$ | Radiative rate constant |
| $R_o$ | Förster distance |
| $R$ | Average distance between the donor and the acceptor |
| $P_{DA}$ | Energy transfer rate |
| $N_D$ | Population densities of donor |
| $N_A$ | Population densities of acceptor |
| $\varepsilon(\omega)$ | A complex dielectric constant |
| $l_s$ | Scattering mean free path |
| $l_t$ | Transport mean free path |
| $l_{amp}$ | Amplification length |
| $l_g$ | Gain length |
| $L$ | Sample size |
| $\lambda$ | Light wavelength |
| $\sigma_s$ | Scattering cross section |
| $\sigma_{sR}$ | Rayleigh scattering cross section |
| $\sigma_{sM}$ | Mie scattering cross section |
| $\sigma_{aM}$ | Mie absorption cross section |
| $\sigma_{eM}$ | Mie extinction cross section |
| $\sigma_{sG}$ | Geometrical scattering cross section |
| $\Theta_w$ | Width of backscattering cone |
| $g_{0(max)}$ | Maximum gain coefficient |
| $E_{ex}$ | Maximum energy for a complete inversion |
| $E_{ab}$ | Absorbed pump energy required to obtain threshold |
| $I$ | Average intensity |
| $V$ | Visibility |